Modelling water and energy balance of the land-atmosphere system using high resolution remote sensing data

C. Cammalleri

tutor:

Dr. G. Ciraolo
Università degli Studi di Palermo, Dip. di Ingegneria Civile, Ambientale e Aerospaziale, Palermo, Italy.

co-tutor:

Prof. C. Agnese
Università degli Studi di Palermo, Dip. dei Sistemi Agro-Ambientali, Palermo, Italy.

supervisors at ARS-USDA:

Dr. M.C. Anderson
U.S. Dept. of Agriculture, Agricultural Research Service, Hydrology and Remote Sensing Laboratory, Beltsville, MD, USA.

Dr. W.P. Kustas
U.S. Dept. of Agriculture, Agricultural Research Service, Hydrology and Remote Sensing Laboratory, Beltsville, MD, USA.

DOTTORATO DI RICERCA IN
INGEGNERIA IDRAULICA ED AMBIENTALE
XXII Ciclo

UNIVERSITÀ DEGLI STUDI
DI PALERMO
Dip. Ingegneria Civile,
Ambientale e Aerospaziale

Sedi Consorziate:

UNIVERSITÀ DEGLI STUDI
DI MESSINA
Dip. Ingegneria Civile

A thesis presented to the graduate school
of the University of Palermo in partial fulfilment
of the requirements for the degree of
Doctor of Philosophy

Tesi per il conseguimento del titolo di
Dottore di Ricerca

Modelling Water and Energy Balance of the Land-Atmosphere System Using High Resolution Remote Sensing Data

Carmelo Cammalleri

Tutor:
Dr. Giuseppe CIRAOLO

Co-tutor:
Prof. Carmelo AGNESE

Coordinatore del dottorato:
Prof. Enrico NAPOLI

Palermo, febbraio 2011

Settore Scientifico-Disciplinare Costruzioni Idrauliche e Marittime e Idrologia (ICAR/02)

Cammalleri, C.

"Modelling Water and Energy Balance of the Land-Atmosphere System Using High Resolution Remote Sensing Data"
Università degli Studi di Palermo, Facoltà di Ingegneria
Dottorato di Ricerca in Ingegneria Idraulica ed Ambientale - XXII Ciclo
(2008–2010)

Subject headings: hydrology, micro-meteorology, remote sensing, evapotranspiration.

Cover picture: Vincent Van Gogh (June, 1889) - Olive trees with the Alpilles in the background.

Io sono me più
il mio ambiente, e se
non preservo quest'ultimo
non preservo me stesso.
J. O. Gasset

Sommario

La rilevanza assunta dal risparmio della risorsa idrica negli ultimi anni ha spinto verso una corretta quantificazione delle perdite legate al processo evapotraspirativo, al fine di una gestione parsimoniosa della risorsa stessa. In particolare nei sistemi agricoli soggetti a stress severo, sia la misura che la stima dell'evapotraspirazione (ET) ad un'adeguata risoluzione spaziale e temporale sono uno dei principali problemi da affrontare per la comunità scientifica. Recentemente, le tecniche di telerilevamento sono divenute un ulteriore strumento a supporto della modellistica idrologica distribuita; in particolare, le immagini acquisite nelle onde corte e nell'infrarosso termico risultano essere di notevole interesse. In questo contesto, i due scopi principali di questa ricerca sono stati: la quantificazione dell'accuratezza delle misure micro-meteorologiche in sistemi agricoli vegetati con colture alte e sparse; e l'analisi dei modelli basati su dati telerilevati per la stima di ET ad alta risoluzione spaziale e temporale. L'area di studio è caratterizzata da un tipico clima Mediterraneo e da colture olivicole, e si trova localizzata nei pressi di Castelvetrano (Italia). Quest'area è stata oggetto nella primavera-estate 2008 di una campagna di misura mediante istallazioni *eddy covariance* e scintillometrica, e, contestualmente, dall'acquisizione di 7 immagini multi-spettrali ad alta risoluzione. L'analisi delle misure micro-meteorologiche ha permesso di quantificare l'accordo tra le due tecniche e ha portato allo sviluppo di un nuovo approccio di calibrazione dei dati scintillometrici. Inoltre, alcune ipotesi alla base della stima dei flussi giornalieri sono state discusse in dettaglio. L'analisi degli algoritmi per la simulazione dei processi di scambio nel continuo suolo-pianta-atmosfera è stata focalizzata: i) sulle stime *hot-spot* di ET mediante un approccio di bilancio energetico residuale, ii) sulla stima in continuo di ET alla scala di campo mediante diversi approcci. Quest'ultima analisi ha evidenziato i buoni risultati del modello accoppiato energetico/idrologico per la stima dei flussi di acqua ed energia sia a scala oraria che giornaliera. Infine, l'applicabilità di due approcci di *data assimilation* è stata testata utilizzando sia osservazioni artificiali che reali.

Abstract

In view of the increased relevance of water saving issues in the last decades, the correct quantification of water loss due to evapotranspirative process became fundamental for a parsimonious management of this resource. Especially in agricultural systems subjected to severe water stress, both the measurement and the modelling of evapotranspiration (ET) at adequate temporal and spatial resolution, are important topics for the hydrologist scientific community. Recently, the remote sensing techniques provide an additional tool to support the hydrologic spatially distributed models; in particular, images acquired in the short-wave and the thermal spectral regions have quite interesting applications. Within this framework, the two principal aims of this work were: to quantify the accuracy of surface energy fluxes measured by micro-meteorological techniques in sparse tall vegetated system; and to analyze the capability of remote sensing-based approach to retrieve ET at high temporal and spatial resolution. The selected test site was an area characterized by Mediterranean climate and olive crops, located near Castelvetrano (Italy). This area, during the spring-summer period in 2008, was interested by *in-situ* measurements campaigns with eddy covariance and scintillometer instruments, and, contextually, by the acquisition of 7 high resolution multi-spectral images. The analysis of micro-meteorological measurements allows to evaluate the agreement between these techniques in the study site, also by means of a novel algorithm for the elaboration of scintillometer data. Moreover, some fundamental hypothesis of daily fluxes estimation was critically discussed. The analysis of the algorithms for the simulation of the exchange processes in the continuum soil-plant-atmosphere was focused on: i) the retrieval of hot-spot ET maps by means of residual energy balance approach and ii) the continuous ET estimation at field scale using different approaches. This latter analysis highlights the good performance of a coupled energy/hydrological model for the assessment of energy and water fluxes at both hourly and daily scale. Finally, the applicability of two data assimilation schemes was tested using both artificial and real observations.

Contents

List of Figures

List of Tables

List of Symbols

Symbol	Units	Description
a		wind speed exponential profile extinction factor, pag. 55
c_g		fraction of $R_{n,s}$ which is convert into G_0, pags. 44, 44
c_p	[J kg^{-1} K^{-1}]	specific heat of air at constant pressure
d_0	[m]	zero plane displacement length, pag. 53
d_r		inverse of the square relative distance earth-sun, pag. 18
d_{z1}	[m]	surface layer thickness, pag. 70
d_{z2}	[m]	root zone thickness, pag. 70
e	[kPa]	water vapour pressure in the atmosphere
e_0	[kPa]	water vapour pressure at the exchange height, pag. 64
e_a	[kPa]	actual water vapour pressure in the atmosphere
e_c	[kPa]	water vapour pressure in the canopy, pag. 64
e_s	[kPa]	water vapour pressure in the soil, pag. 64

Symbol	Units	Description
f_c		fractional vegetation coverage at nadir, pag. 160
f_B	[m^{-4}]	Hill bump in the dissipation range, pags. 88, 89, 94
f_T		dimensionless group for T_* computation, pags. 81, 92, 92, 93
f_ϵ		dimensionless group for ϵ computation, pags. 81, 92, 92
g	[m s^{-2}]	standard gravitational acceleration
h_c	[m]	canopy height
h_p		variance reduction in kernel smoothing of parameter, pag. 140
k_v		von Karman constant, pag. 49
l_0	[m]	inner scale, pags. 88, 94
q	[kg kg^{-1}]	specific water vapour concentration in the air, pag. 48
q_0	[kg kg^{-1}]	specific water vapour concentration at the exchange height, pag. 49
r_a	[s m^{-1}]	aerodynamic resistance for heat and water vapour transfer with $z_{0h} = z_{0m}$, pag. 63
r_{ah}	[s m^{-1}]	aerodynamic resistance for heat and water vapour transfer, pag. 59
r_c	[s m^{-1}]	stomatal resistance, pag. 74
r_i		surface reflectance at the i-th spectral band, pag. 29
r_s	[s m^{-1}]	resistance to heat flow in the boundary layer above the soil surface, pags. 65, 65
r_{ss}	[s m^{-1}]	soil resistance to vapour flux, pags. 73, 73
r_x	[s m^{-1}]	resistance of the canopy boundary layer, pag. 64

Symbol	Units	Description
s	[rad]	surface slope, pag. 18
t	[s]	time
$u(z)$	[m s^{-1}]	horizontal wind speed at height z, pags. 49, 52, 54, 55, 56
u_c	[m s^{-1}]	wind speed at the top of the canopy, pag. 54
u_s	[m s^{-1}]	wind velocity just above the soil surface ($z = 0.1$ m), pag. 65
u_*	[m s^{-1}]	friction velocity, pags. 48, 58, 84
w_l	[m]	mean leaf size, pag. 55
z	[m]	vertical distance/direction
z_{0h}	[m]	roughness length for heat transfer, pag. 57
z_{0m}	[m]	roughness length for momentum transfer, pag. 53
z_{0v}	[m]	roughness length for water vapour transfer, pag. 57
z_d	[m]	crown bottom height, pag. 56
z_m	[m]	eddy correlation/scintillometer measurement height, pag. 96
z_q	[m]	height of measurements of atmospheric water content, pag. 59
z_s	[m]	height above the soil where is minimal the effect of soil surface roughness, pag. 54
z_u	[m]	height of measurements of wind speed, pag. 58
z_T	[m]	height of measurements of air temperature, pag. 59
z^*	[m]	Elevation of the roughness sub-layer, pag. 93
B_{12}	[m$^{-11/3}$]	covariance of the two beam amplitudes of the scintillometer, pag. 89

Symbol	Units	Description
B^{-1}		dimensionless bulk parameter (inverse of Stanton number), pag. 57
C_1		relative depth of soil influenced by the surface external hydrological forces, pag. 71
C_2		parameter to characterise the velocity at which the water profile is restored to its equilibrium, pag. 72
C_n^2	[$m^{-2/3}$]	structure parameter of the refractive index of air, pag. 90
C_s	[J kg^{-1} K^{-1}]	soil specific heat, pag. 42
C_T^2	[K^2 $m^{-2/3}$]	structure parameters of the temperature, pags. 90, 91
CR		surface energy balance closure ratio, pag. 106
D	[m]	damping depth, pag. 43
D_s	[m^2 s^{-1}]	soil thermal diffusivity, pag. 42
DOY		day of the year
E_s	[mm s^{-1}]	soil evaporation, pags. 63, 63, 70, 132
ET	[mm s^{-1}]	actual evapotranspiration, pag. 3
ET_0	[mm s^{-1}]	reference evapotranspiration, pag. 61
$ET_{0,24}$	[mm d^{-1}]	daily reference evapotranspiration, pag. 128
ET_{24}	[mm d^{-1}]	daily evapotranspiration, pags. 122, 122, 122
ET_c	[mm s^{-1}]	canopy evapotranspiration, pags. 63, 63, 70, 132
ET_p	[mm s^{-1}]	potential evapotranspiration, pag. 61, 126
F	[m]	first Fresnel zone, pag. 88
G_0	[W m^{-2}]	soil heat flux in surface, pags. 39, 43, 44, 45, 45, 45

Symbol	Units	Description
$G_{0,24}$	[W m^{-2}]	daily soil heat flux in surface, pags. 45, 46
H	[W m^{-2}]	sensible heat flux, pags. 48, 59, 84, 86, 92, 120
H_c	[W m^{-2}]	sensible heat flux in canopy layer, pags. 62, 63
H_s	[W m^{-2}]	sensible heat flux in soil layer, pags. 62, 63
H_{sc}	[J m^{-3} K^{-1}]	soil volumetric heat capacity, pag. 42
I_r	[mm s^{-1}]	irrigation rate
K_c		crop coefficient, pags. 61, 130
K_{cb}		basal crop coefficient, pag. 61
K_e		coefficient for soil evaporation, pag. 61
K_r		dimensionless evaporation reduction coefficient, pags. 61, 132
K_s		water stress coefficient, pags. 62, 126, 132
K_{sat}	[m s^{-1}]	soil saturated hydraulic conductivity
K_{TOA}	[W m^{-2}]	solar constant, pag. 17
$K_i^{\downarrow}$	[W m^{-2} sr^{-1} μm^{-1}]	extraterrestrial radiance in the i-th narrowband, pag. 29
L	[m]	Monin-Obukhov length, pag. 51
L_0	[m]	outer scale, pag. 88
L_a	[W m^{-2}]	radiation emissions from atmosphere, pag. 36
L_c	[W m^{-2}]	radiation emissions from canopy, pag. 36
L_n	[W m^{-2}]	long-wave net radiation, pags. 33, 130
$L_{n,c}$	[W m^{-2}]	long-wave net radiation in canopy layer, pag. 35
$L_{n,s}$	[W m^{-2}]	long-wave net radiation in soil layer, pag. 35

Symbol	Units	Description
L_s	[W m^{-2}]	radiation emissions from soil, pag. 36
LAI	[m^2 m^{-2}]	leaf area index, pag. 161
LAI$_c$	[m^2 m^{-2}]	leaf area index refereed to vegetated region, pag. 35
$L^{\downarrow}$	[W m^{-2}]	downward long-wave radiation, pag. 29
$L^{\uparrow}$	[W m^{-2}]	upward long-wave radiation, pag. 29
NDVI		normalised difference vegetation index, pag. 160
P	[m]	scintillometer path length, 87
P_a	[kPa]	atmospheric pressure
P_e	[mm s^{-1}]	precipitation rate infiltrating into the soil, pag. 72
P_r	[mm s^{-1}]	total precipitation rate
Q	[mm s^{-1}]	drainage to soil beneath the rooting zone, pag. 72
R_a	[W m^{-2}]	extraterrestrial solar radiation, pag. 17
R_n	[W m^{-2}]	total net radiation, pag. 16
$R_{n,24}$	[W m^{-2}]	daily net radiation, pag. 36
$R_{n,c}$	[W m^{-2}]	net radiation in canopy layer, pag. 32
$R_{n,lw24}$	[W m^{-2}]	daily long-wave net radiation, pag. 38
$R_{n,s}$	[W m^{-2}]	net radiation in soil layer, pag. 32
R_s	[W m^{-2}]	incoming solar radiation, pag. 23
$R_{s,24}$	[W m^{-2}]	daily total solar radiation, pag. 37
R_{so}	[W m^{-2}]	clear-sky solar radiation, pags. 20, 22
$R_{so,24}$	[W m^{-2}]	daily clear-sky solar radiation, pag. 38
$R^{\uparrow}$	[W m^{-2} sr^{-1} μm^{-1}]	upwelling radiance, pag. 25
S	[J m^{-2}]	heat storage in canopy and air, pag. 15
S_n	[W m^{-2}]	short-wave net radiation, pag. 33
$S_{n,c}$	[W m^{-2}]	short-wave net radiation in canopy layer, pag. 34

Symbol	Units	Description
$S_{n,s}$	[W m^{-2}]	short-wave net radiation in soil layer, pag. 34
S_r		degree of saturation, pag. 40
T_0	[K]	aerodynamic temperature at source height, pags. 63, 116
T_a	[K]	air temperature at height z_T
$T_{a,m}$	[K]	daily average air temperature, pag. 38
$T_{a,\min}$	[K]	daily minimum air temperature, pag. 38
$T_{a,\max}$	[K]	daily maximum air temperature, pag. 38
$T_{a,\text{Dis-A}}$	[K]	air temperature diagnosed by ALEXI, pag. 124
$T_{a,\text{IC}}$	[K]	TSEB internal-scene calibrated air temperature, pag. 117
T_c	[K]	canopy surface temperature, pag. 115
T_{deep}	[K]	soil temperature at the deep where the daily temperature fluctuations can be assumed negligible, pag. 43
T_s	[K]	soil surface temperature, pag. 116
T_{RAD}	[K]	surface radiometric temperature, pag. 162
$T_{\text{RAD},m}$	[K]	daily average surface radiometric temperature, pag. 38
T_*	[K]	temperature scale, pag. 91
W_c	[mm]	canopy water storage, pag. 72
α		surface albedo, pags. 25, 25, 28, 29, 161
$\overline{\alpha}$		average daytime albedo, pag. 36
α_c		canopy albedo, pag. 27
α_p		shrinkage factor in kernel smoothing of parameter, pag. 140

Symbol	Units	Description
$\alpha_{\text{P-T}}$		Priestley-Taylor coefficient, pag. 114
α_s		soil albedo, pag. 27
β		Bowen ratio, pag. 66
β_0		extinction coefficient for hyperbolic-cosine profile, pag. 55
γ	[kPa K^{-1}]	psychrometric constant, pag. 59
ϵ	[m^2 s^{-3}]	dissipation rate of the kinetic energy of the turbulence, pags. 80, 91, 91
ϵ_0		surface emissivity, pags. 30, 31
ϵ_c		canopy emissivity, pag. 30
ϵ_s		soil emissivity, pag. 30
ϵ'		apparent atmospheric emissivity, pags. 30, 30
ζ	[m]	height above the zero plane displacement, pag. 51
θ	[m^3 m^{-3}]	actual volumetric soil water content, pag. 69
θ_1	[m^3 m^{-3}]	surface soil water content, pag. 70
θ_2	[m^3 m^{-3}]	mean root zone water content, pag. 70
θ_a	[K]	air potential temperature, pag. 48
θ_{cr}	[m^3 m^{-3}]	critical water content at which plant stress starts, pag. 74
θ_{fc}	[m^3 m^{-3}]	soil water content at field capacity, pag. 69
θ_{sat}	[m^3 m^{-3}]	saturation volumetric water content, pags. 41, 69
θ_{wl}	[m^3 m^{-3}]	soil water content at wilting point, pag. 69
ϑ	[rad]	observation zenith angle, pag. 25
κ		radiation extinction coefficient, pags. 32, 34

Symbol	Units	Description
κ_L		long-wave extinction coefficient, pag. 35
λ	[J kg^{-1}]	latent heat of vaporisation
λ_g	[W m^{-1} K^{-1}]	soil thermal conductivity, pag. 40
λ_{wl}	[μm]	spectral wavelength
λE_s	[W m^{-2}]	latent heat flux in soil layer, pags. 63, 63
λET	[W m^{-2}]	latent heat flux, pags. 48, 59, 84
λET_c	[W m^{-2}]	latent heat flux in canopy layer, pags. 63, 63
ξ	[rad]	surface aspect, pag. 18
ρ	[kg m^{-3}]	air density
ρ_s	[kg m^{-3}]	soil bulk density, pag. 41
ρ_w	[kg m^{-3}]	water density, pag. 69
σ	[W m^{-2} K^{-4}]	Stefan-Boltzmann constant, pag. 29
σ_{uw}	[m^2 s^{-2}]	covariance between horizontal and vertical wind speeds, pag. 84
σ_{wq}	[m s^{-1}]	covariance between vertical wind speed and water vapour concentration, pag. 84
σ_{wT}	[m s^{-1} K]	covariance between vertical wind speed and temperature, pag. 84
τ_{sw}		broadband short-wave atmospheric transmissivity for generic conditions, pag. 25
τ_{swo}		broadband short-wave atmospheric transmissivity for cloud-free conditions, pags. 20, 20, 24
ϕ_h		dimensionless buoyancy influences factors for heat, pags. 51, 81
ϕ_m		dimensionless buoyancy influences factors for momentum, pags. 51, 81

Symbol	Units	Description
ϕ_v		dimensionless buoyancy influences factors for water vapour, pag. 51
φ	[rad]	observation azimuth angle, pag. 25
ω	[rad]	hour angle, pag. 19
ω_0	[rad]	sunset/sunrise hour angle, pag. 38
Δ	[kPa K^{-1}]	slope of saturation curve
ΔT_0	[K]	correction to linear approximation of T_0, pag. 116
ΔT_c	[K]	correction to linear approximation of T_c, pag. 115
Λ		evaporative fraction, pag. 67
Ξ		Kalman gain matrix, pags. 137, 140
Φ_h		temperature profile adiabatic correction factors, pag. 52
Φ_m		wind speed profile adiabatic correction factors, pag. 52
$\Omega(\theta_s)$		clumping factor, pag. 35

List of Acronyms

Acronym	Description
ABL	Atmospheric Boundary Layer, pag. 46
AHS	Airborne Hyperspectral Scanner, pag. 31
ALEXI	Atmosphere-Land Exchange Inverse, pag. 111
ASTER	Advanced Spaceborne Thermal Emission and Reflection Radiometer, pag. 6
DIFA	*DIgitalizzazione della Filiera Agroalimentare* – research project, pag. 158
DSLF	Down-welling Surface Long-wave radiation Flux (LSA SAF product), pag. 166
DSSF	Down-welling Surface Short-wave radiation Flux (LSA SAF product), pag. 166
E	Effciency Index of Nash and Sutcliffe, pag. 278
EC	Eddie Correlation/Covariance, pag. 82
ECMWF	European Centre for Medium-range Weather Forecast, pag. 121
EUMESAT	European Organisation for the Exploitation of Meteorological Satellites, pag. 6
FVC	Fraction of Vegetation Coverage (LSA SAF product), pag. 165
G	Green spectral region, pag. 158
GOES	Geostationary Operational Environmental Satellite, pag. 6

Acronym	Description
IA	Willmott's Index of Agreement, pag. 278
IBL	Internal Boundary Layer, pag. 83
IC	Internal Calibration (of TSEB), pag. 117
IL	Inertial Sub-Layer, pag. 46
LAS	Large Aperture Scintillometer, pag. 90
LSA SAF	Land Surface Analysis Satellite Application Facility, pag. 23
LSM	Land Surface Model, pag. 110
LST	Land Surface Temperature (LSA SAF product), pag. 166
MAD	Mean Absolute Difference, pag. 277
ML	Mixing Layer, pag. 46
MODIS	MODerate resolution Imaging Spectroradiometer, pag. 6
MOST	Monin-Obukhov Similarity Theory, pag. 50
MSG	Meteosat Second Generation, pag. 6
NIR	Near Infra-Red spectral region, pags. 5, 158
NWC SAF	Nowcasting and Very Short Range Forecasting Satellite Application Facility, pag. 23
OSI SAF	Ocean and Sea Ice Satellite Application Facility, pag. 23
PM	Penman-Monteith, pag. 60
R	Red spectral region, pag. 158
RE	Relative Error, pag. 278
RMSD	Root Mean Square Difference, pag. 278
RS	Remote Sensing, pag. 5
RS-L	Roughness Sub-Layer, pag. 46
RWS	Radio Wave Scintillometer, pag. 90
SAS	Small Aperture Scintillometer, pag. 90
SEB	Surface Energy Balance, pag. 15
SEBAL	Surface Energy Balance Algorithm for Land, pag. 45

Acronym	Description
SEBS	Surface Energy Balance System, pag. 45
SEVIRI	Spinning Enhanced Visible and Infrared Imager, pag. 6
SIAS	*Servizio Informativo Agrometeorologico Siciliano* (Agrometeorological service of the Sicilian Region), pag. 144
SL	Surface Layer, pag. 46
SPA	Soil-Plant-Atmosphere continuum, pag. 2
SVAT	Soil-Vegetation-Atmosphere Transfer, pag. 110
TIR	Thermal Infra-Red spectral region, , pag. 5
TKE	Turbulent Kinetic Energy, pag. 79
TSEB	Two Source Energy Balance, pag. 111
VIS	VISible spectral region, pag. 5
XLAS	eXtra Large Aperture Scintillometer, pag. 90

Chapter 1

Introduction and background

1.1 Overview and problem statement

1.1.1 The challenge of water scarcity

Water is widely accepted as one of the most important resource of the planet, for this reason it is considered a priority issue for suitable development of a region.

The water demand has doubled in the last 50 years and the forecast on precipitation for the 21st century suggests significant reduction in water availability in the Mediterranean area (UNEP/MAP-PlanBleu, 2009); for this reason the planning for the use of this resource should be accurately revised as a consequence of its increasing scarcity.

The correct quantification of the water resource availability becomes largely important for agricultural, civil and industrial activities, and with the observed reduction in availability the competition among the different demanding sectors drastically increases. In this context, the agricultural sector in Mediterranean region shows a vulnerability, especially due to the high water demand during the irrigation season, which in the last years reached the 70% of total water availability (UNEP/MAP-PlanBleu, 2009). This is mainly due to the necessity to keep productive the agricultural landscape by reducing the water deficit by means of tangible contribution

of irrigation practise.

Sensible improvements in saving water used for agricultural purpose can be obtained by identifying the cropped areas under water stress or disease conditions, providing information useful to support water management practise.

However, right now, the assessment of water losses, at local, regional or global scale, represents one of the main issues of the hydrology due to the high spatial variability of this physical quantity. In fact, the factors involved in its spatial distribution are numerous, including: meteorological variability, morphological characteristics, land use, soil pedology and hydrological proprieties.

Due to the complex interaction observed among these factors, the more recent activities in this research field were focused on multi-disciplinary approaches, which include, with different degree of complexity, all the main factors involved in the water loss process.

In this reference frame, the numerous efforts performed by the scientific community in the last two decades to provide a suitable tool at support of the quantification of crop water loss are largely justified. Despite that, because of the complexity of the relevant processes, more steps should be realized to understand and model these mechanisms in the land-atmosphere system, expecially in areas characterized by complex vegetation structure, as sparse tall crops, typical of Mediterranean regions.

1.1.2 Interactions in the land-atmosphere system

The system constituted by the land and the surrounding atmosphere can be thought as a continuum, where fluxes of mass and energy directly connect the system components. Generally, the land is constituted by a mixture of soil and plants, directly in contact with the lower atmosphere environment; for this reason, it is common refereeing to the SPA (Soil-Plant-Atmosphere) continuum, and this micro-environment is also known as biosphere.

The SPA is generally interested by many processes and various interactions, which make complex the modelling without an interdisciplinary approach. Also the measurement of exchange processes in the SPA is difficult because of the spatial variability in vegetation and/or terrain and turbulent nature of the processes in the lower atmosphere.

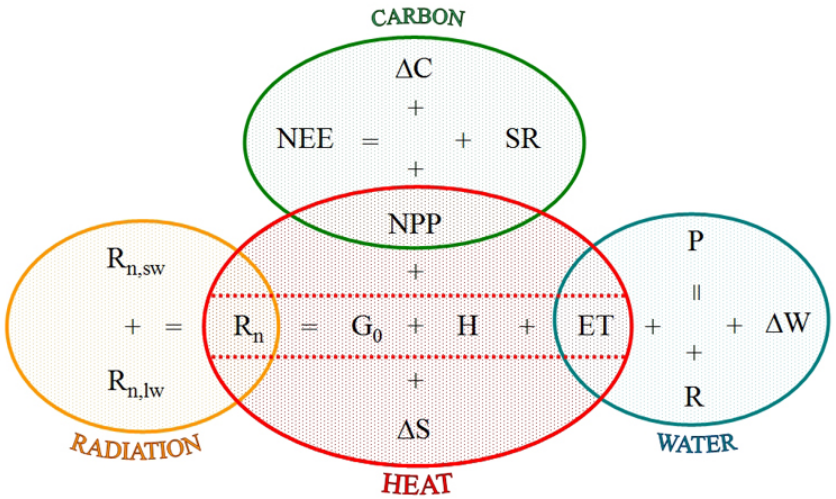

Figure 1.1: Schematic representation of the main balances in the SPA continuum. The red circle highlights the heat balance, the blue circle highlights the water balance, the orange circle highlights the radiative balance and the green circle highlights the carbon balance. The overlap regions empathise the inter-connections between the single budget equations.

One of the most adopted approach to analyse the interaction in the SPA is the use of conservation (or balance) law. Figure 1.1 shows the main balance equations, which represent the equilibrium between the incoming and outgoing mass (water, carbon) and energy (heat, radiation) fluxes.

The radiation balance (orange circle in Figure 1.1) describes the transfer of energy due to the radiative processes. The net amount of radiant energy available at the surface (commonly named net radiation, R_n) can be easily associated to the net amounts in the short-wave (sw) and long-wave (lw) spectrum regions.

The water balance (blue circle in Figure 1.1) schematizes the water storage in the soil (ΔW) as an equilibrium between the incoming term (net precipitation, P) and the outgoing fluxes directed to the atmosphere (evapotranspiration, ET) and in the deep soil (drainage and runoff, R).

Analogously, the carbon cycle (green circle in Figure 1.1) can be schematically represented as a budget between source, soil/plant respiration (SR), and sink, net photosynthesys (NPP), generating the net ecosystem

exchange (NEE) (which can be positive or negative) and a CO_2 storage in the system (ΔC).

As well highlighted by Figure 1.1, the central role on the SPA exchange processes is up to the heat balance (also commonly named energy balance), which is the key in the interconnection of the budgets in the biosphere.

In particular, the role of latent heat flux (or evapotranspiration) in this budget is to control the heating/cooling of the system by disposing/subtracting energy amounts to sensible heat, representing besides the main water loss of the hydrological balance.

Focusing the attention on the energetic process, the amounts of energy involved in the carbon cycle are generally smaller than the ones related to the other considered processes, suggesting the possibility to neglect it. Additionally, it is important to highlight how there are also others exchange processes in the SPA, as: nutrients, aerosol, pollutants (e.g., ozone), but these are secondary from an energetic point of view.

On the basis of these considerations, and assuming the heat and radiation budgets as an unique course, is possible to focus the attention on SPA interaction between energy and water balances.

This strong connection between the surface energy and water budgets suggested in the past to explore the possibility to infer the actual evapotranspiration by means of the quantification of the energy utilized by the system to change the state of water from liquid to vapour.

All the earlier applications of this theory, since the first on water body evaporation (Penman, 1948), adopt this framework to model the evaporation without involving the surface water budget. In successive extrapolations for natural surfaces, as fully or partially vegetated ones, scientists noted that several spatially and temporally dynamic feedback mechanisms between evaporation and the land surface (e.g., surface albedo and rooting depth) were present.

An important progress was made in the understanding of local-scale evaporation processes through improvements in micro-meteorological observation techniques as Bowen ratio, eddy correlation and scintillometry. However, such observations only represent local processes and can not be extended to large areas because of the land surface heterogeneity and the dynamic nature of the heat transfer processes (French *et al.*, 2005).

Moreover, despite the micro-meteorological measurements are consid-

ered (even if not easy) at least routine in homogeneous terrain (Lloyd, 1995), several authors have point out the attentions on the problematics related to the heterogeneous terrain (Garratt, 1978; Tsvang *et al.*, 1991).

For all these reasons, to adequately capture these feedbacks on both large areas and local-scale, a number of models were developed (Noilhan and Planton, 1989; Schelde *et al.*, 1997; Shuttleworth and Wallace, 1985) that account for atmospheric demands, surface radiation budget and water availability, as well as a range of biological and physical interactions (Kalma *et al.*, 2008). These efforts drove to the commonly acceptance of this interdisciplinary approaches to assess the evapotranspiration in a wide range of land conditions. However, the application of these methodologies on large areas, especially in the 80s, was extremely limited by the scarcity of spatially distributed information required from these models.

1.1.3 The contribute of remote sensing

The numerous factors involved in the evapotranspiration process, partially introduced in the previous subsections, cause an extreme spatial variability of this hydrological quantity, suggesting the use of spatially distributed approaches to accurately assess it.

Nevertheless, a considerable lack in the availability of large area hydrological parameters strongly limited in the past the applicability of spatially distributed models, despite the widely accepted needs in hydrological modelling since the early 70s (Freeze and Harlan, 1969).

To support these applications, in the last 20 years the increased availability of new technologies in remote sensing (RS) of the earth strongly encouraged the spatially distributed applications for hydrological variables assessment.

In fact, these observations, differently from the common *in-situ* measurements, are intrinsically characterized by a spatial variability and, generally, represent wide areas including the inaccessible one.

Since 80s, worldwide Government organizations supported numerous projects to remotely observe the land surface in different region of the electromagnetic spectrum; in the hydrological framework, the availability of passive data acquired in the short-wave (visible, VIS, and near-infrared, NIR) and long-wave (thermal-infrared, TIR) regions of the spectrum are of particular interest.

The first one because the sensitivity to land surface characteristics such as vegetation coverage, albedo; the second one thanks to the potentiality to provide spatially distributed observation of land surface temperature, directly connected with the thermodynamic equilibrium related with the energy budget (Schmugge *et al.*, 2002).

Nowadays, the availability of remotely-sensed data in short- and long-wave regions encompass a wide variety of sensors, characterized by different spatial and temporal resolutions. A detailed, but not exhaustive review, can be found in `http://en.wikipedia.org/wiki/List_of_Earth_observation_satellites`.

As well known, the Landsat series represents the longest running enterprise for acquisition of imagery of Earth from space. The ETM+ sensor on board of the last version of this satellite (the 7^{th}, launched in the 1999) provides acquisitions in 7 spectral bands; including 4 bands in the visible near-infrared and 2 bands in the middle-infrared (30 m spatial resolution) and 1 band in thermal infrared (60 m spatial resolution). The temporal resolution of this satellite is of 16 days, due to the polar sun-synchronous orbit at an elevation of about 705 km (`http://landsathandbook.gsfc.nasa.gov/handbook.html`).

For global applications in European and Africa areas, the MSG (Meteosat Second Generation) satellite, developed by ESA (European Space Agency) in close cooperation with EUMETSAT (European Organisation for the Exploitation of Meteorological Satellites), provides high temporal (15 min) observations in both visible and infrared by means of SEVIRI (Spinning Enhanced Visible and Infrared Imager) sensor (Aminou, 2002). The geostationary orbit of MSG satellite allows this extremely high temporal resolution, to the detriment of spatial resolution (of about 3.5 km in Italy). Similar data for the U.S. continent are provided by GOES (Geostationary Operational Environmental Satellite) series.

Another two widely adopted sensors are the MODIS (MODerate resolution Imaging Spectroradiometer) and ASTER (Advanced Spaceborne Thermal Emission and Reflection Radiometer) ones, on board of Terra satellite (MODIS is also on board of Aqua satellite).

The MODIS sensor performs acquisitions at moderate spatial resolution (250 m in the VIS and 1 km in the TIR) once at day (Masuoka *et al.*, 1998). Differently, the ASTER images are characterized by a detailed spatial

resolution (15 m in VIS and 90 m in TIR bands) but only via on-demand request of acquisitions, with a maximum temporal resolution of 16 days in full mode (Abrams and Hook, 2002).

It is important to stress how the reported temporal resolutions correspond to a theoretical one obtainable only in absence of cloud coverage. In the practical applications, the effective temporal resolution is generally lower than the theoretical one especially during the cloudy winter period.

Moreover, as highlighted by this brief overview, there is a significant gap between the desired resolutions and the practical scale at which processes should be represented. Methods to address spatial and temporal disparities between landscape heterogeneity and sensor and model resolution are limited, since widely accepted theory of scaling in hydrology does not yet exist (Beven and Fisher, 1996), especially for the land surface temperature (see e.g., Kustas *et al.*, 2003; Mostovoy *et al.*, 2008; Vazifedoust *et al.*, 2009).

In this context, high resolution on-demand airborne campaigns could provide an useful support in understanding the processes at adequate spatial scale with the desired temporal resolution, overtaking the limitation of satellite overpass frequency.

In fact, in agricultural applications, hydrological balance should be resolved at field scale, and at least with daily frequency, in order to be a valid support in the optimization of irrigation practise, thus avoiding waste of water resource.

Continuous land surface modelling, which introduces remotely observed information acquired in the short-wave range (Boulet *et al.*, 2000; Olioso *et al.*, 1995; van der Keur *et al.*, 2001), avoiding the limitations related to cloud coverage by means of de-clouded products obtained from temporal mosaicking of a set of consecutive images. This procedure is allowed by the slight temporal trend in the observed characteristics (e.g., vegetation density). Despite that, these approaches do not take advantage of the precious information acquired in the thermal bands. Moreover, the requirement of soil hydraulic/hydrological characteristics, difficult to be retrieved from remotely sensed data, makes the use of these approach problematic for wide area applications.

On the contrary, residual energy balance models (Bastiaanssen *et al.*, 1998a; Norman *et al.*, 1995; Su, 2002) allow the assessment of actual

evapotranspiration without involving the water balance, thanks to the introduction of remotely observed surface temperature. However, these approaches suffer of the above introduced limited availability of high temporal and spatial resolutions thermal data, requiring the use of "data filling" procedure to continuously assess the evapotranspiration.

1.2 Thesis objectives

As introduced in the previous sub-sections, the open topics related to the modelling of water and energy balance in the SPA are numerous, yet, and under investigation by worldwide experimental research projects.

The main goal of this thesis is to address some key arguments related to the field scale modelling and measuring of main energy and water balance components in a typical Mediterranean agricultural landscape.

In particular, the surface energy fluxes partitioning and the connections with actual evapotranspiration will be investigated at both high temporal and spatial resolution by means of *ad hoc* airborne remote sensing acquisitions and contextual in field campaigns. The principal research activities can be subdivided in two main lines:

- measurements of energy fluxes in sparse tall agricultural systems by means of micro-meteorological techniques, as scintillometry and eddy correlation;

- modelling of actual evapotranspiration by means of remote sensing-based approaches.

Regarding the first points, the key goal is the analysis of the reliability of micro-meteorological derived fluxes in systems characterized by heterogeneity at the scale of 10^0–10^1 m, as the tree crops typical of Mediterranean environment (e.g., olive, vineyard). This analysis, in addition to test the effective complexity of the micro-meteorological measurements in these particular system, allows to define the uncertainties related to the *in-situ* measurements, in order to provide a point of reference useful to quantify and evaluate the performance of the remote sensing-based models.

In this context, two different techniques were analyzed, the consolidated eddy correlation and the relative new scintillometry. In this analysis, par-

ticular attention was dedicated to the reliability of heat flux measurements and surface energy budget closure.

As regards to the SPA system modelling, the attentions were focused on both the residual energy budget approach and the land surface interaction models. The availability of high spatial resolution images (characterized by pixel dimension lower than the average heterogeneity scale) allows, first of all, to analyze some fundamental hypotheses of the so-called residual two-source models. Moreover, different methodologies to assess field scale actual evapotranspiration at hourly/daily temporal scale were critically compared, adopting the micro-meteorological observations as validation data sources.

The final aim of the work is to provide confirmations, supported by practical evidences, on the applicability of remote sensing-base technique in the framework of high temporal and spatial resolution modelling of water and energy balance also in areas characterized by sparse crops and high water stress conditions.

1.3 Outline

This thesis is organized into 9 chapters, the first and the latter report the introduction and the conclusions of the work, respectively. The remaining chapters can be schematically subdivided in three main parts: the first part is relative to the theoretical background, the second one deals with the description of available materials and adopted methodologies and the last one describes the applications of the experimental applications and modelling.

Introduction

In the **Chapter 1** (this chapter) the key problematics of the water scarcity and the enhancements in spatially distributed hydrological models, related to increasing remote sensing data availability, are briefly introduced. The main research objectives of the research are also reported, with the addition of this outline of the thesis structure.

Part I: Theoretical Background

The theoretical background part is constituted by the **Chapter 2**, where the theoretical basis of the surface energy budget are reported, including the description and modelling of the main balance components as: net radiation, soil heat flux, and heat and water vapour fluxes. Moreover, the connections between energy and water balance are highlighted with particular regards to the effects of water flow in the soil on evapotranspiration process.

Part II: Materials and Methods

The materials and methodologies part represents the core of the thesis, where the methodologies adopted in the observation of surface energy fluxes and in the modelling of exchange processes are described.

In particular, **Chapter 3** describes the eddy correlation and the scintillometry techniques for heat fluxes observation, and the model adopted for the footprint detection. The problematic related to the balance closure check Are also introduced.

Instead, **Chapter 4** reports the description of the applied remote sensing-based approaches, distinguish among residual surface energy budget, approaches based on water stress indices and modelling of land-atmosphere interactions.

In the **Chapter 5** the descriptions of the study area and the experimental installations are reported. The elaborations of the remotely sensed images, including airborne and satellite data, with particular attention on the retrieval of the parameters of hydrological interest (e.g., albedo, leaf area index, vegetation indices) are also discussed. More details on the pre-processing of airborne imagery, data calibrations and geometric corrections, are reported in **Appendix A**.

Part III: Applications and Results

The applications and results part is the main component of the thesis, where all the results obtained from the applications of the previously introduced methodologies were tested and critically analyzed, also by means of objective criteria based on the computation of the statistical indices described in **Appendix B**.

In the **Chapter 6** the preliminary analysis of the micro-meteorological measures is reported, focusing the attention principally on the sensible heat flux assessment by means of eddy covariance and scintillometry techniques in an olive orchard. The measures were also used to assess the uncertainties associated to the fluxes observations, at both hourly and daily scale, in this specific experimental site.

Chapter 7 reports the results of the applications of residual energy balance two-source model by means of the airborne images. In particular, the problems related to the in-canopy wind profile and the uncertainties in surface temperature retrieval were investigated in the case of sparse tall crops. The results were validated adopting the measurements retrieved by micro-meteorological measurements as described in the previous chapter.

Chapter 8 describes the applications of several methodologies to assess actual evapotranspiration at (at least) daily temporal scale in the olive grove experimental site. The critical analysis of the models performances was performed by means of a validation using observed fluxes (from micro-meteorological installations) and also in terms of model *vs.* model comparison. The degree of complexity of the different methodologies (in terms of data requirements) was also taken into account in the analysis, in order to emphasize the characteristics of each approach.

Conclusions

Finally, in the **Chapter 9** the main results and findings of the research are summarized, including also recommendations for further works and possible future advances.

Part I

Theoretical Background

Chapter 2

The surface energy budget

As reported in Fig. 1.1, the surface energy balance (SEB) equation, under the hypothesis of negligible horizontal advection, reads:

$$\frac{\partial S}{\partial t} = R_n - G_0 - H - \mathrm{NPP} - \lambda ET = 0 \tag{2.1}$$

where $\frac{\partial S}{\partial t}$ [W m^{-2}] represents the heat storage in canopy and air, R_n [W m^{-2}] is the net radiation density, G_0 [W m^{-2}] is the soil heat flux density, H [W m^{-2}] is the sensible heat flux density, the heat exchange between surface and atmosphere caused by their temperature gradient, NPP [W m^{-2}] is the net plant photosynthesis and λET [W m^{-2}] is the latent heat flux density, which represents the energy amount used for the surface evaporation and plant transpiration processes.

Adding the hypothesis that canopy and air storage and the energy required for photosynthesis are negligible, the energy budget equation can be written in the well-known form:

$$R_n - G_0 - H - \lambda ET = 0 \tag{2.2}$$

By convention, R_n is considered positive when radiation is directed downwards in the surface, while G_0, H and λET are considered positive when directed away from the land surface. Additionally, despite the terms

in Eq. (2.2) represent flux density, is common practise to adopt the name energy flux.

The Eq. (2.2) represents the energy conservation principle applied to the entire SPA system. Analogous equations can be derived for the specific components, such soil and canopy:

$$R_{n,s} - G_0 = H_s + \lambda E_s \tag{2.3a}$$
$$R_{n,c} = H_c + \lambda E T_c \tag{2.3b}$$

where the sub-scripts "s"and "c" denote the fluxes relative to the sub-layer soil and canopy.

The Eqs. (2.3) highlight how the energy balance equations of a mixed surface allow to split λET in the contributes of soil (λE_s) and canopy (λET_c), related to the evaporation and transpiration processes, respectively.

The next sub-sections focus the attention on the description of the terms in Eqs. (2.2) and (2.3), with particular regards to the partition in vegetation and soil components.

2.1 Net radiation

The net radiation, R_n, is the result of the radiative budget at the land surface, generally expressed by the interactions described in Fig. 1.1.

The radiation balance consists of two main parts, namely, the short-wave radiation balance, S_n, and the long-wave radiation balance, L_n. The distinction between shortwave (0.3-2.5 μm) and long-wave (3-100 μm) is suggested by the different diurnal behaviour of the two components, as highlighted in the next sub-sections.

On the basis of this scheme, the overall radiation balance may be described by the equation:

$$R_n = (1 - \alpha)R_s + L^{\downarrow} - L^{\uparrow} \tag{2.4}$$

where α is the surface albedo, R_s [W m^{-2}] is the incoming solar radiation, $L^{\downarrow}$ [W m^{-2}] is the downward long-wave radiation and $L^{\uparrow}$ [W m^{-2}] is the upward long-wave radiation.

2.1.1 Solar radiation modelling

The amount of emitted solar radiation that reaches the land surface is controlled, at global scale, by the relative location earth-sun and by the characteristics of the atmosphere (Iqbal, 1983). However, at local scale, the radiation is also controlled by surface slope, aspect and elevation (Allen *et al.*, 2006). Additionally, in land surface systems constituted by a mixture of canopy and soil, the interception of the light by canopy leaves, and the fraction transmitted to the soil, directly influences many processes (e.g., photosynthesis), as well as in the partition between evaporation from soil and transpiration from leaves (Campbell and Norman, 1998).

Generally, over inclined surfaces, the incoming radiation consists of the sum of three components:

- direct (beam) radiation, which represents the portion of solar radiation that is not absorbed or scattered by the atmosphere;
- diffuse radiation, which is originated from the solar beam, but is scattered toward the surface;
- reflected radiation, which is a small component reflected from surfaces in view of the inclined surface.

The analytical calculation of the total amount of incoming radiation is commonly carried out only for clear-sky conditions, starting from the computation of the extraterrestrial solar radiation, and then correcting that by the atmospheric influence.

Extraterrestrial solar radiation

The extraterrestrial solar radiation, R_a [W m^{-2}], at any daylight time, can be computed using the relationship:

$$R_a = K_{\mathrm{TOA}} d_r \cos(\theta_s) \tag{2.5}$$

in which K_{TOA} is the solar constant (1367 W m^{-2}), d_r is the inverse of the square relative distance earth-sun in astronomical units and θ_s [rad] is solar incident angle relative to the normal to the surface.

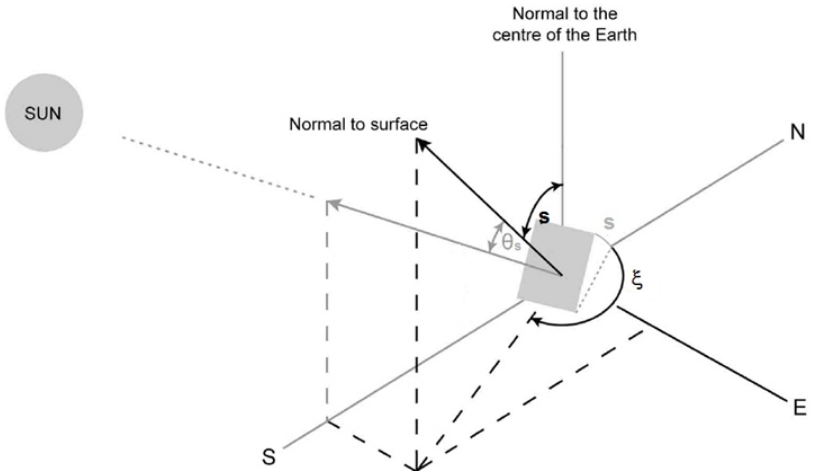

Figure 2.1: Scheme of tilted surface generically oriented.

The term d_r can be calculated using the relationship proposed by Duffie and Beckman (1980):

$$d_r = 1 + 0.033 \cos\left(\mathrm{DOY}\frac{2\pi}{365}\right) \tag{2.6}$$

where DOY is the day of the year.

The incidence angle of the solar beam can be computed, for a sloping surface generally oriented (Figure 2.1), by means of the equation (Garner and Ohmura, 1968):

$$\begin{aligned}\cos(\theta_s) = &\sin(\delta)\sin(\phi)\cos(s)\\ &-\sin(\delta)\cos(\phi)\sin(s)\cos(\xi)\\ &+\cos(\delta)\cos(\phi)\cos(s)\cos(\omega)\\ &+\cos(\delta)\sin(\phi)\sin(s)\cos(\xi)\cos(\omega)\\ &+\cos(\delta)\sin(\xi)\sin(s)\sin(\omega)\end{aligned} \tag{2.7}$$

where δ [rad] is the solar declination, ϕ [rad] is the latitude (positive for the northern hemisphere and negative for the southern hemisphere), s [rad] is the surface slope, where $s = 0$ for horizontal and $s = \pi/2$ for vertical slope, ξ [rad] is the surface aspect angle, where $\xi = 0$ for slope oriented

due south, $\xi = -\pi/2$ for slopes oriented due east, $\xi = +\pi/2$ for slopes oriented due west and $\xi = \pm\pi$ for slopes oriented due north, and ω [rad] is the hour angle, assuming values equal to 0 at the solar noon, positive values in the afternoon and negative value in the morning.

The solar declination is a function of DOY by means of the relationship:

$$\delta = 0.409 \sin\left(\frac{2\pi}{365}\mathrm{DOY} - 1.39\right) \tag{2.8}$$

For hourly (or shorter periods) applications of Eq. (2.5), ω can be computed as a function of the local time, according to the ASCE-EWRI (2005) formulation:

$$\omega = \frac{\pi}{12}\left[(t + 0.06667(L_z - L_m) + S_c) - 12\right] \tag{2.9}$$

where t [s] is the standard clock time, L_z [deg] is the longitude of the centre of the local time zone (west of Greenwich: e.g., $L_z = 345°$for Rome), L_m [deg] is the longitude of the site (west of Greenwich) and S_c [h] is the seasonal correction for solar time, defined as:

$$S_c = 0.1645 \sin(2b_s) - 0.1255 \cos(b_s) - 0.0250 \sin(b_s) \tag{2.10}$$

with:

$$b_s = \frac{2\pi(\mathrm{DOY} - 81)}{364} \tag{2.11}$$

The Eq. (2.7) can be simplified in a number of instances. When the surface is flat ($s = 0$), therefore Eq. (2.7) becomes ($\theta_s = \theta_{\mathrm{hor}}$):

$$\cos(\theta_{\mathrm{hor}}) = \sin(\delta)\sin(\phi) + \cos(\delta)\cos(\phi)\cos(\omega) \tag{2.12}$$

instead, when the surface is tilted towards the equator (e.g., facing south in the northern hemisphere) Eq. (2.7) reads ($\theta_s = \theta_N$):

$$\cos(\theta_N) = \sin(\delta)\sin(\phi - s) + \cos(\delta)\cos(\phi - s)\cos(\omega) \tag{2.13}$$

The values of θ_s returned by Eqs. (2.7), (2.12) and (2.13) are useful only when $|\omega| < |\omega_0|$, with ω_0 [rad] defined as the sunset/sunrise hour angle (see sub-section 2.1.5). In the other instances the incoming solar radiation is assumed equal to 0.

Clear-sky solar radiation

Usually, the clear-sky solar radiation, R_{so} [W m^{-2}], is simulated using the relationship:

$$R_{so} = \tau_{swo} R_a \tag{2.14}$$

where τ_{swo} is the broadband short-wave atmospheric transmissivity for cloud-free conditions.

Following the simplified methodology proposed by Allen *et al.* (1998), τ_{swo} ca be computed as follow:

$$\tau_{swo} = 0.75 + 2 \cdot 10^{-5} z \tag{2.15}$$

where z [m] represents the elevation above the sea level.

A more detailed approach, proposed by Allen (1996) and successively updated by ASCE-EWRI (2005), suggests to calculate separately the transmissivity for beam and diffuse radiations:

$$\tau_{swo} = K_{Bo} + K_{Do} \tag{2.16}$$

where K_{Bo} is the clearness index for direct beam radiation and K_{Do} is the index for diffuse radiation.

ASCE-EWRI (2005) proposed a procedure for K_{Bo} computation, based on the form of the equation introduced by Majumdar *et al.* (1972):

$$K_{Bo} = 0.98 \exp\left[\frac{-0.00146 P_a}{K_t \cos(\theta_s)} - 0.075\left(\frac{W}{\cos(\theta_s)}\right)^{0.4}\right] \tag{2.17}$$

in which K_t is an empirical turbidity coefficient, $0 < K_t \leq 1$, where $K_t = 1$ for clear air (typical of regions of agricultural and natural vegetation) and $K_t = 0.5$ for extremely turbid or polluted air, P_a [kPa] is the atmospheric pressure, and W [mm] is the equivalent depth of precipitable water in the atmosphere.

In the ASCE-EWRI (2005) procedure W is computed following Garrison and Adler (1990) as:

$$W = 0.14 e_a P_a + 2.1 \tag{2.18}$$

where e_a [kPa] is the actual vapour pressure in the atmosphere.

The direct component of global radiation, R_{Bo} [W m^{-2}], can be computed as:

$$R_{Bo} = K_{Bo} R_a \tag{2.19}$$

taking into account the effects of sun angle, elevation, and water vapour content of the effective optical mass of the atmosphere (Allen *et al.*, 2006).

The diffuse radiance over a generically inclined surface under clear sky conditions is computed starting from the corresponding value for a horizontal surface, $R_{Do_{\mathrm{hor}}}$ [W m^{-2}]:

$$R_{Do_{\mathrm{hor}}} = K_{Do_{\mathrm{hor}}} R_{a_{\mathrm{hor}}} \tag{2.20}$$

in which $R_{a_{\mathrm{hor}}}$ [W m^{-2}] is the extraterrestrial solar radiation received on a horizontal surface, computed by means of Eqs. (2.5) and (2.12), and $K_{Do_{\mathrm{hor}}}$ is the diffuse radiation index for a horizontal surface. Continuing to follow the ASCE-EWRI (2005) procedure, $K_{Do_{\mathrm{hor}}}$ is computed as a function of the corresponding direct beam coefficient, using the relationships developed by Boes (1981):

$$K_{Do_{\mathrm{hor}}} = \begin{cases} 0.35 - 0.36 K_{Bo_{\mathrm{hor}}} & K_{Bo_{\mathrm{hor}}} \geq 0.15 \\ 0.18 + 0.82 K_{Bo_{\mathrm{hor}}} & 0.065 < K_{Bo_{\mathrm{hor}}} < 0.15 \\ 0.10 + 2.08 K_{Bo_{\mathrm{hor}}} & K_{Bo_{\mathrm{hor}}} \leq 0.065 \end{cases} \tag{2.21}$$

where $K_{Bo_{\mathrm{hor}}}$ is the clearness index for horizontal surface, computed by means of Eq. (2.17) with $\theta_s = \theta_{\mathrm{hor}}$ (using the Eq. (2.12)).

The empirical coefficients in Eq. (2.21) were retrieved by ASCE-EWRI based on 49 locations across the U.S. (Allen *et al.*, 2006). Furthermore, the results found by ASCE-EWRI (2005) well agree with data from Liu and Jordan (1960) as well as Boes (1981).

Even though the Eqs. (2.21) were developed for both cloud-free and cloudy conditions, its accuracy is high only for clear or near clear sky conditions (Allen *et al.*, 2006).

The diffuse irradiance on an inclined surface under clear sky conditions, R_{Do} [W m^{-2}], is then computed as a fraction, f_i, of $R_{Do_{\mathrm{hor}}}$:

$$R_{Do} = f_i R_{Do_{\mathrm{hor}}} \tag{2.22}$$

A number of models for f_i computations were proposed in the literature due to the empiricism adopted to modelling the process (Perez *et al.*, 1990). In particular, diffuse models for slopes surface are generally subdivided between isotropic and anisotropic, where isotropic models assume that diffuse radiation has the same intensity from all directions (Allen *et al.*, 2006).

Isotropic approaches (Duffie and Beckman, 1980) estimate f_i as a simple function of the cosine of slope. For example, the formulation proposed by Tian *et al.* (2001):

$$f_i = 0.75 + 0.25\cos(s) - \frac{0.5s}{\pi} \tag{2.23}$$

approximates the solution found by Revfeim (1978) averaging the general cosine function and using a simple linear function of the slope.

Despite the assumption of isotropic diffuse radiation is less accurate of anisotropic one, especially for clear sky conditions (Perez *et al.*, 1990), isotopic models are largely applied.

Reflected radiance from surfaces in view of the inclined surface is estimated if known the average albedo (see section 2.1.2 for his definition) and the average incident radiation (beam+diffuse) of the surrounding surface. This contribute becomes significant only in mountainous regions (characterised by high slope surfaces) (Tian *et al.*, 2001). Due to the relative small amount of this component for agricultural areas, the reflected radiance is generally neglected in the practical applications.

On the basis of these considerations, R_{so} for a generic slope is finally calculated as:

$$R_{so} = K_{Bo}R_a + (f_i R_{Do_{\mathrm{hor}}})R_{a_{\mathrm{hor}}} \tag{2.24}$$

In order to use the radiations obtained by the above described procedures in energy balance modelling, it is common to re-project solar radiation in terms of energy per horizontal equivalent surface, $R_{s_{\mathrm{eq,hor}}}$ [W m^{-2}], as:

$$R_{s_{\mathrm{eq,hor}}} = \frac{R_s}{cos(s)} \tag{2.25}$$

in which R_s referees to all the radiation components (e.g., beam, diffuse, clear-sky, etc.). For this reason, all the radiations recalled in the next-sections refer always to horizontal equivalent value, even if missing the corresponding sub-script.

Solar radiation in practical applications

For the common remote sensing-based applications, generally realised under clear-sky conditions, the incoming radiation can be assumed almost equal to the clear sky value ($R_s = R_{so}$).

In case of generic atmospheric conditions (non-clear sky), R_s can be computed yet by means of Eq. (2.14), assuming the atmospheric transmissivity corresponding to the effective atmospheric conditions. However, in the practical applications, the use of Eq. (2.14) is rarely adopted (especially for short time, hourly, periods), preferring to acquire R_s measurements by means of meteorological stations. In this case, R_{so} values should plot as an upper envelope for measured R_s, and it is useful for checking calibration on instruments and for *in-situ* data quality controls.

Recently, geostationary satellites (e.g., GOES and MSG) increase the availability of remotely sensed estimation of R_s, in a wider range of meteorological conditions, due to the capability to obtain reliable estimation of cloud coverage conditions.

For European area (and also Africa and South America), MSG provides estimations of the down-welling surface short-wave radiation flux (namely DSSF) by means of the algorithm implemented in the LSA SAF (Land Surface Analysis Satellite Application Facility) system (LSASAF, 1994).

This algorithm uses three SEVIRI bands (0.6 μm, 0.8 μm and 1.6 μm) and it is largely based on the methodology adopted by Mètèo-France in the framework of OSI (Ocean and Sea Ice) SAF (Brisson *et al.*, 1999).

The computation of the total incoming solar radiation is based on the Eq. (2.14), in which τ_{sw} is computed differently if the pixel is marked as clear or cloudy (Figure 2.2).

The information on cloud cover is provided by the cloud mask software that was developed by the NWC (Nowcasting and Very Short Range Forecasting) SAF, which is integrated in the LSA SAF system.

In the case of clear pixels the effective atmospheric transmittance is

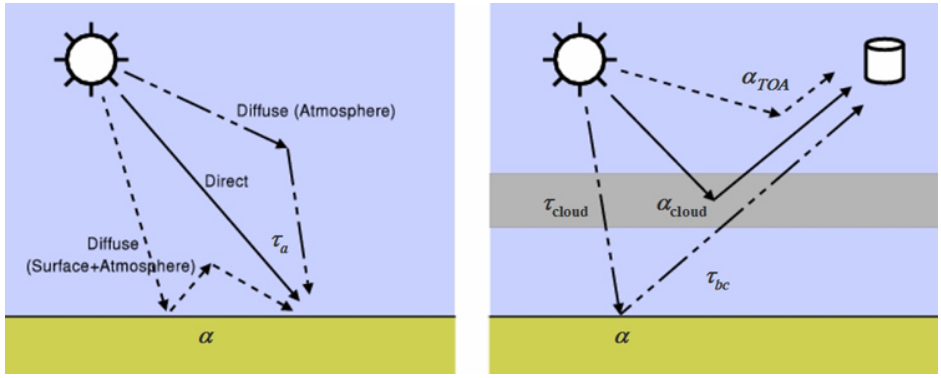

Figure 2.2: Scheme illustrating main elements of the clear (left) and cloudy sky (right) DSSF estimation methods (LSASAF, 1994).

computed as ($\tau_{sw} = \tau_{swo}$):

$$\tau_{swo} = \frac{\tau_a}{1 - \alpha\alpha_a} \tag{2.26}$$

where τ_a represents the apparent transmittance of the atmosphere and quantifies the contribution to the surface flux by the direct radiation as well as the diffuse radiation, and α_a is the spherical albedo of the atmosphere. Equation (2.26) results from a geometric series taking into account an infinite number of scattering orders between land surface and atmosphere (LSASAF, 1994).

The term τ_a is computed, following Frouin *et al.* (1989), as:

$$\tau_a = \exp(-\tau_{\mathrm{H_2O}}) \exp(-\tau_{\mathrm{O_3}}) \exp(-\tau_{\mathrm{A+CO_2+O_2}}) \tag{2.27}$$

with $\tau_{\mathrm{H_2O}}$, $\tau_{\mathrm{O_3}}$ and $\tau_{\mathrm{A+CO_2+O_2}}$ computed as a function of water vapour column density, total ozone content of the atmosphere, solar zenith angle, and a visibility factor (V, fixed to a value of 20 km).

The spherical albedo of the atmosphere is also parameterised as a function of visibility according to Frouin *et al.* (1989):

$$\alpha_a = 0.088 + \frac{0.456}{V} \tag{2.28}$$

Finally, the surface albedo is taken from the LSA SAF near-real time albedo product (LSASAF, 2005).

For cloudy pixels the DSSF estimates relies on a simplified physical description of the radiation transfer in the cloud-atmosphere-surface system (LSASAF, 1994) according to Brisson *et al.* (1999) and Gautier *et al.* (1980). It assumes that the whole pixel is covered by an homogeneous cloud layer, and then the effective transmittance, τ_{sw} (not in clear-sky), is given by:

$$\tau_{sw} = \frac{\tau_a \tau_{\text{cloud}}}{1 - \alpha \tau_{bc} \alpha_{\text{cloud}}} \tag{2.29}$$

where in the numerator, differently from clear-sky conditions, the cloud transmittance, τ_{cloud}, appears. The denominator assumes a similar significance as in Eq. (2.26), and quantifies multiple scattering between the surface and the bottom of the cloud. In this equation α_{cloud} denotes the albedo of the cloud, and τ_{bc} represents the transmittance of the atmosphere between the surface and the cloud layer.

The cloud characteristics (τ_{cloud} and α_{cloud}) are retrieved from SEVIRI measured spectral reflectances starting from the top-of-atmosphere albedo and applying the spectral conversion relations proposed by Clerbaux *et al.* (2005) and the angular reflectance model of Manalo-Smith *et al.* (1998).

2.1.2 Surface albedo

The surface albedo, α (also named short-wave reflectivity), represents the ratio between the outgoing and the incoming radiation in the whole short-wave range. While the reflectance, r, is commonly refereed to a specific wavelength, the albedo is the spectral integrated value, as expressed by the relationship:

$$\alpha = \frac{1}{R_s} \int_0^{2\pi} \int_0^{\pi/2} \int_{0.3}^{2.5} R^{\uparrow}(\vartheta, \varphi, \lambda_{\text{wl}}) \cos\vartheta \sin\vartheta \, \mathrm{d}\vartheta \mathrm{d}\varphi \mathrm{d}\lambda_{\text{wl}} \tag{2.30}$$

where $R^{\uparrow}(\vartheta, \varphi, \lambda_{\text{wl}})$ [W m^{-2} sr^{-1} μm^{-1}] is the reflected radiance, function of observation zenith angle, ϑ [rad], azimuth angle, φ [rad], and wavelength, λ_{wl} [μm].

Adopting the common assumption of "lambertian" behaviour of the observed surface, the Eq. (2.30) can be simplified as:

$$\alpha = \frac{\pi}{R_s} \int_{0.3}^{2.5} R^{\uparrow}(\lambda_{\text{wl}}) \mathrm{d}\lambda_{\text{wl}} \tag{2.31}$$

in which the term π represents the result of the integration in the upper hemisphere volume.

The albedo of different land surface is strongly influenced by a number of factors, mainly represented by the amount of cover, colour of soil or vegetation, roughness of the surface, water content (Campbell and Norman, 1998). Also water surfaces are characterised by a wide range of variability of α, depending on solute content.

Additionally, especially for tall sparse canopies and water surfaces, albedo depend strongly on solar zenith angle. In the first case (tall sparse crop) mainly due to the different penetration of sun rays during the day; in the second one, due to the different behaviour of these surfaces to direct and scattered sky radiation inputs (Robinson, 1966). A further factor which is responsible for the α diurnal variation is the difference in incident radiation spectral composition during the day; in fact, the incident radiation contains a higher proportion of short-wave radiation as the elevation of the sun increases. The effect of the wavelength dependence on α shows a trend toward an increase in albedo with decreasing sun elevation (Robinson, 1966).

For the above mentioned reasons, generally the daytime course of α assumes an almost constant value during the hours across midday, and higher value just after(before) the sunrise(sunset), with the typical "U" shape.

Additionally, for bare soil it is possible to affirm that the increase of water content causes a reduction in the albedo, because the albedo of water is lower than the soil surface one.

Albedo modelling in canopy-soil system

The albedo modelling, in the generic case of not dense canopy system, needs to take into account the radiation reflected from the soil, the transmission of beam radiation (including its scattered component) and the radiation re-reflected from the leaves in the foliage space (Campbell and Norman, 1998).

Despite the values of soil albedo, α_s, vary as a function of surface soil moisture (primarily), texture, plant residue, etc., generally its modelling for practical biophysic applications is realised by means of a simple relationship:

$$\alpha_s = \frac{\alpha_{s,\mathrm{vis}} + \alpha_{s,\mathrm{nir}}}{2} \tag{2.32}$$

where the soil albedo in the visible, $\alpha_{s,\mathrm{vis}}$, and near-infrared, $\alpha_{s,\mathrm{nir}}$, wavelengths are set equal to a constant value of 0.15 and 0.25, respectively (M.C. Anderson, personal communication).

As regard of the canopy albedo, α_c, the approach proposed by Campbell and Norman (1998) (in Chapter 15), also adopted in the Cupid model (Norman and Campbell, 1983), is widely used:

$$\begin{aligned}\alpha_c = & \frac{(W_{D,\mathrm{vis}}\alpha_{cD,\mathrm{vis}} + W_{B,\mathrm{vis}}\alpha_{cB,\mathrm{vis}})}{2} \\ & + \frac{(W_{D,\mathrm{nir}}\alpha_{cD,\mathrm{nir}} + W_{B,\mathrm{nir}}\alpha_{cB,\mathrm{nir}})}{2}\end{aligned} \tag{2.33}$$

where $W_{D,\mathrm{vis}}$, $W_{B,\mathrm{vis}}$, $W_{D,\mathrm{nir}}$ and $W_{B,\mathrm{nir}}$ are the weighting factors for diffuse visible radiation, beam visible radiation, diffuse near infrared radiation and beam near-infrared radiation, respectively; $\alpha_{cD,\mathrm{vis}}$, $\alpha_{cB,\mathrm{vis}}$, $\alpha_{cD,\mathrm{nir}}$ and $\alpha_{cB,\mathrm{nir}}$ are canopy albedo for diffuse visible radiation, beam visible radiation, diffuse near infrared radiation and beam near-infrared radiation, respectively.

The weighting factors in Eq. (2.33) assume generally values of 0.2 and 0.8 for diffuse and beam visible radiation, respectively, and 0.1 and 0.9 for diffuse and beam near-infrared radiation, respectively (Campbell and Norman, 1998).

The different components of canopy albedo can be computed using the following relationship (Monteith, 1973):

$$\alpha_{cX,\mathrm{y}} = \frac{r_{cX,\mathrm{y}} + \eta_{cX,\mathrm{y}}}{1 + r_{cX,\mathrm{y}}\eta_{cX,\mathrm{y}}} \tag{2.34}$$

in which the albedo for diffuse ($X = D$) and beam ($X = B$) radiation in visible (y = vis) and near-infrared (y = nir) spectral regions are computed using the corresponding reflectance and η parameter values.

The formulations adopted for η parameters computation differ for direct and diffuse radiation. In particular, for beam radiation η is a function of the vegetation extinction coefficient for beam radiation, K_{Be}:

$$K_{Be} = \frac{\sqrt{X^2 + \tan^2(\theta_s)}}{X + 1.774(X + 1.182)^{-0.733}} \tag{2.35}$$

where X is the ratio of average area of canopy elements projected onto the horizontal surface to the average area of canopy elements projected onto the vertical surface. For a spherical leaf angle distribution, $X = 1$ (Campbell and Norman, 1998).

Instead, η values for diffuse radiation is a function of the vegetation extinction coefficient for diffuse radiation, K_{De}, which, for spherical leaf angle distribution, can be computed as (Campbell and Norman, 1998):

$$K_{De} = 0.82 - 0.18 \log(\text{LAI}) \tag{2.36}$$

where LAI [m^2 m^{-2}] represents the leaf area index.

It is interesting to notice how this approach highlights the variability of beam albedo during the day, by means of θ_s which appears in Eq. (2.35), differently from diffuse albedo.

The above described approach suffers of an expensive requirement of input parameters, primarily due to the extreme detailed knowledge of canopy structure.

More details on in-canopy radiation extinction are reported in subsection 2.1.4.

Remotely sensed-based albedo estimation

Thanks to the remote sensing capability to observe the energy reflected by surfaces in defined portion of the electromagnetic spectrum, a number of study in the past (Brest and Goward, 1992; Li and Leighton, 1992; Price, 1990; Saunders, 1990) have focused the attention on the retrieving of short-wave albedo using a combination of narrowband reflectances (Liang, 2004).

Starting from the α definition under "lambertian" surface hypothesis (Eq. (2.31)), and subdividing the incoming solar radiation in its spectral contribution (Epema, 1990), the albedo definition reads:

$$\alpha = \pi \sum_{\lambda_{\text{wl}}=\lambda_1}^{\lambda_{\text{wl}}=\lambda_N} \frac{R^{\uparrow}(\lambda_{\text{wl}})}{K^{\downarrow}(\lambda_{\text{wl}}) d_r \cos(\theta_s)} \tag{2.37}$$

where $K^{\downarrow}(\lambda_{\text{wl}})$ [W m^{-2} sr^{-1} μm^{-1}] is the incoming extraterrestrial radiance at the wavelength λ_{wl}, whereas λ_1 and λ_N [μm] are the extremes of numerical integration.

On the basis of these hypotheses, and introducing the surface reflectance acquired by the sensor in specific narrowband, r_i, the albedo can be computed as:

$$\alpha = \sum_{i=1}^{N} r_i w_1 \tag{2.38}$$

where N represents the number of sensor bands in the short-wave, and w_i are weighting factors defined as:

$$w_i = \frac{K_i^{\downarrow}}{\sum_{i=1}^{N} K_i^{\downarrow}} \tag{2.39}$$

in which the incoming extraterrestrial radiance in the specific narrowband, $K_i^{\downarrow}$ [W m^{-2} sr^{-1} μm^{-1}], is derived from the theoretical extraterrestrial solar spectrum. This weighted linear combination approach (Price, 1990) assumes that the surface-level radiation and extraterrestrial radiation have similar behaviour.

Another approach is based on a simple multi-regression analysis between up-welling and down-ward fluxes, retrieved by atmospheric transfer simulations or from *in-situ* measurements, in a wide range of atmospheric conditions and surface types (Liang, 2004). This approach allowed to retrieve the regression coefficients for a number of operational sensors (e.g., MSG, MODIS, Landsat, etc.).

2.1.3 Long-wave radiation modelling

Differently from short-wave radiation, mainly related to the solar daily and seasonal cycles, the long-wave components of the ratiative budget is related to the radiation emitted by the atmosphere and land surface.

These amounts of energy can be easily computed on the basis of the Stefan-Boltzmann law applied to grey (nonblack) bodies. On the basis of this preface, the net long-wave budget equation for a generic surface reads:

$$L_n = L^{\downarrow} - L^{\uparrow} = \epsilon_0 \epsilon' \sigma T_a^4 - \epsilon_0 \sigma T_{\mathrm{RAD}}^4 \tag{2.40}$$

where σ is the Stefan-Boltzmann constant (5.67×10^{-8} W m^{-2} K^{-4}), ϵ_0 is the surface emissivity, ϵ' is the apparent atmospheric emissivity, T_a [K] is the air temperature and T_{RAD} [K] is the surface radiometric temperature.

Several formulation were proposed in the past decades for computing estimates of atmospheric emissivity. A simple semi-empirical relationship, for clear-sky conditions, is the one proposed by Bastiaanssen (1995) for the western Egypt:

$$\epsilon' = 1.08(-\ln \tau_{swo})^{0.265} \tag{2.41}$$

A physically based expression, developed by Brutsaert (1982) on the basis of an integration over the slab layers of a stratified atmosphere, reads:

$$\epsilon' = 1.23\left(\frac{e_a}{T_a}\right)^{1/7} \tag{2.42}$$

The reasoning of this formulation is that atmospheric thermal radiation is primarily a function of the water vapour concentration in the first few hundred meters of the atmosphere (Campbell and Norman, 1998).

The surface emissivity is used to take into account the difference between natural surfaces and theoretical black body. Since land natural surfaces are generally constituted by a mixture of bare soil and vegetation, therefore ϵ_0 can be assumed to be a linear combination between soil emissivity, ϵ_s, and canopy emissivity, ϵ_c (Sobrino and Raissouni, 2000):

$$\epsilon_0 = \epsilon_c f_c + \epsilon_s(1 - f_c) + d\epsilon \tag{2.43}$$

where f_c is the fractional vegetation coverage and $d\epsilon$ is a term which takes into account the cavity effect due to surface roughness.

The term $d\epsilon$ is negligible for flat surfaces, but in heterogeneous landscape this term assumes significant values, and can be calculated as:

$$d\epsilon = (1 - \epsilon_s)(1 - f_c)F'\epsilon_c \tag{2.44}$$

where F' is a shape factor (Sobrino *et al.*, 1990), ranging between 0 and 1, depending on the geometrical distribution of the surface. When Eqs. (2.43) and (2.44) are used for remotely sensed applications, a mean value

for F' is chosen, due to the impossibility to estimates this parameter from remote sensing data.

For a long-wave broadband applications, as in the Eq. (2.40), the soil and canopy emissivity are assumed equal to 0.97 and 0.98, respectively. In the case of application of Eq. (2.43) for remote sensing thermal data calibration, ϵ_s and ϵ_c values for specific wavelengths can be derived by the values suggested by Sobrino *et al.* (2007) for different operational satellite and airborne sensors.

In particular, the simple expressions derived for the 5 bands of ASTER sensor by Sobrino *et al.* (2007) are useful also for other sensors characterised by similar wavebands. These relationships assume the linear form:

$$\epsilon_0 = a_\epsilon + b_\epsilon f_c \tag{2.45}$$

where the parameters a_ϵ and b_ϵ were defined by Sobrino *et al.* (2007) for each ASTER bands, and also adapted for some airborne sensors (e.g., Airborne Hyperspectral Scanner, AHS) and field instruments (e.g., CIMEL 312 -1 and -2).

Table 2.1 reported the values suggested by the authors for a_ϵ and b_ϵ parameters for ASTER, AHS and CIMEL 312-1 sensors.

The above described method is valid only for land surface; for water bodies an approximate emissivity value of 0.99 can be assumed for both broad and narrow band applications.

2.1.4 Soil-canopy radiation partitioning

As previously highlighted in albedo modelling (sub-section 2.1.2), the analysis of the interaction between canopy and soil is fundamental in the partition between evaporation from soil and transpiration from leaves, especially for surfaces charachrezied by sparse canopy or low density vegatation.

Radiation, Φ_0, propagating through a homogeneous medium that attenuates the beam, suffers of a decrease in flux density well described by Beer's law (Figure 2.3):

$$\Phi = \Phi_0 \exp(-\kappa x_z) \tag{2.46}$$

where Φ is the attenuated flux density, x_z [m] is the beam travel the distance in the medium, and κ is the extinction coefficient.

Table 2.1: Parameters for surface emissivity estimation using the approach suggested by Sobrino *et al.* (2007) for the ASTER, AHS and CIMEL 312-1 thermal bands.

Sensor	Band	Range [μm]	a_ϵ	b_ϵ
ASTER	10	8.12-8.47	0.946	0.044
	11	8.47-8.82	0.949	0.041
	12	8.92-9.27	0.941	0.049
	13	10.25-10.95	0.968	0.022
	14	10.95-11.65	0.970	0.020
AHS	71	8.18	0.945	0.045
	72	8.66	0.967	0.023
	73	9.15	0.971	0.019
	74	9.60	0.969	0.021
	75	10.07	0.974	0.016
	76	10.59	0.979	0.011
	77	11.18	0.980	0.010
	78	11.78	0.981	0.009
	79	12.35	0.985	0.005
	80	12.95	0.985	0.005
CIMEL 312-1	1	8.00-14.00	0.962	0.021
	2	11.96	0.976	0.008
	3	10.80	0.969	0.013
	4	8.82	0.946	0.036

This law is strictly applied only for wavebands narrow enough that κ remains relatively constant. However, if changes in κx_z are small, the Eq. (2.46) can still give a good approximation, as commonly happen for solar radiation in the atmosphere.

Frequently, Beer's law is applied to direct model the divergence of net radiation in the canopy foliage space as (Anderson *et al.*, 1997):

$$R_{n,s} = R_n \exp(-\kappa \mathrm{LAI}) \tag{2.47a}$$

$$R_{n,c} = R_n[1 - \exp(-\kappa \mathrm{LAI})] \tag{2.47b}$$

where the extinction coefficient can be computed as $\kappa = 0.6/\sqrt{2\cos(\theta_s)}$.

These relationships are a modification of the formulations proposed by Norman *et al.* (1995), where the effect of solar zenith angle was neglected ($\sqrt{2\cos(\theta_s)} = 1$) and the extinction coefficient was assumed equal to 0.45.

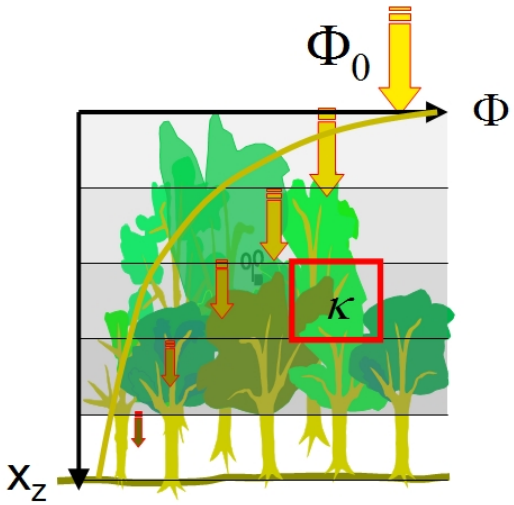

Figure 2.3: Graphical exemplification of Beer's law (redraw from Schmid, H.P.).

Following Anderson *et al.* (1997) the value 0.6 is used, in order to obtain for low solar zenith angle ($< 30°$) values of $\kappa \approx 0.45$, in the midway between its likely limits (0.3 to 0.6) (see Ross, 1981).

A more physically-based approach to estimate the divergence of R_n is based on the separate analysis of the transmission of short-wave, S_n, and long-wave, L_n, net radiation:

$$R_{n,s} = S_{n,s} + L_{n,s} \tag{2.48a}$$

$$R_{n,c} = S_{n,c} + L_{n,c} \tag{2.48b}$$

This approach is discussed separately for short-wave and long-wave components in the following sub-sections.

Short-wave divergence in canopies

Given that Beer's law is not strictly applied to the net radiation, the extinction coefficient for beam radiation, K_{Be}, can be estimated under the hypothesis of randomly distributed leaves in space (Campbell and Norman, 1998) using the Eq. (2.35).

Since diffuse radiation comes from all directions, it is attenuated differently from beam radiation, the extinction coefficient for diffuse radiation, K_{De}, must be computed differently from K_{Be}, by means of Eq. (2.36).

As highlighted by both Eqs. (2.35) and (2.36), extinction coefficients are strongly influenced by canopy structure and leaf angles distribution. Additionally, for canopies characterised by low foliage density, radiation reflected from soil and re-reflected from the leaves is not negligible, making more complex the modelling.

For a defined crop type (if known canopy structure and leaves average orientation) diffuse and beam extinction coefficients assume: the first a constant value, the second a simple function of solar zenith angle. In order to simplify the computation for practical applications in wide areas, similarly to the approach adopted by Anderson *et al.* (1997), the divergence of the total solar radiation in canopy and soil components can be modelled as:

$$S_{n,s} = (1 - \alpha_s) R_s \exp(-\kappa \mathrm{LAI}) \tag{2.49a}$$

$$S_{n,c} = (1 - \alpha_c) R_s [1 - \exp(-\kappa \mathrm{LAI})] \tag{2.49b}$$

where κ is computed as described above for Eq. (2.47).

The described simple radiative exchange schemes are valid, as mentioned, only for canopies with leaves that are randomly distributed throughout the canopy space (Campbell and Norman, 1998). When leaves are not randomly distributed in space, a number of models (e.g., Gijzen and Goudriaan, 1989) to estimate radiation extinction for sparse crops have been developed. However, these models are generally rather complex, requiring additional information about the surface not available operationally (Kustas and Norman, 1999).

For practical application, an alternative approach is to take into account the effect of this heterogeneity introducing a correction factor in the exponential decay equations by replacing LAI with $\Omega(\theta_s)$LAI; where $\Omega(\theta_s)$ is the clumping factor that is a function of the solar zenith angle (Chen and Cihlar, 1995).

The clumping factor takes into account reduced extinction through a clumped canopy compared to uniformly distributed vegetation, making possible to extend the formulations generated for random canopies to heterogeneous ones. Generally, for common agricultural species $\Omega(\theta_s) \leq 1$.

To compute the clumping factor, Campbell and Norman (1998) suggest the following semi-empirical expression:

$$\Omega(\theta_s) = \frac{\Omega(0)}{\Omega(0) + \big[1 - \Omega(0)\big] \exp\big[-2.2(\theta_s)^{p_0}\big]} \tag{2.50}$$

where $\Omega(0)$ is the clumping factor for a nadir solar zenith angle, and p_0 is an empirical expression given by:

$$p_0 = 3.8 - 0.46\frac{h_c}{s_{\text{row}} f_c} \tag{2.51}$$

where h_c [m] is the canopy height, and s_{row} [m] is the mean row spacing of the crops.

The clumping factor for a nadir solar zenith angle ca be computed as:

$$\Omega_0 = -\frac{\ln(T_v)}{0.5\text{LAI}} \tag{2.52}$$

in which T_v is the fraction of total transmission of radiation to the surface, gave by:

$$T_v = f_c \exp(-0.5\text{LAI}_c) + (1 - f_c) \tag{2.53}$$

where LAI_c [m^2 m^{-2}] is the LAI refereed to the vegetated region (leaf area per projection of canopy crow), estimable as: $\text{LAI}_c = \text{LAI}/f_c$.

In this thesis, excepting when explicitly declared, the term LAI refers to the clumped value, $\Omega(\theta_s)$LAI.

Long-wave partitioning

The long-wave balance, separately for canopy and soil systems, can be derived by the simple formulation proposed by Ross (1975). This formulation was derived using a single exponential equation to estimate the transmission for both soil and canopy layer (Kustas and Norman, 1999):

$$L_{n,s} = \exp(-\kappa_L \text{LAI}) L_a + [1 - \exp(-\kappa_L \text{LAI})] L_c - L_s \tag{2.54a}$$

$$L_{n,c} = [1 - \exp(-\kappa_L \text{LAI})][L_a + Ls - 2Lc] \tag{2.54b}$$

where κ_L is the long-wave extinction coefficient (≈ 0.95), similar to the extinction coefficient for diffuse radiation under low vegatation coverage

(Campbell and Norman, 1998), and L_a, L_c and L_s [W m^{-2}] are the emissions from atmosphere, canopy and soil, respectively.

The emissions L_a, L_c and L_s are computed from the Stefan-Boltzmann law as:

$$L_a = \epsilon' \sigma T_a^4 \tag{2.55a}$$

$$L_s = \epsilon_s \sigma T_s^4 \tag{2.55b}$$

$$L_c = \epsilon_c \sigma T_c^4 \tag{2.55c}$$

where the terms T_s and T_c [K] represent the soil and canopy surface temperature, respectively.

The emissivity of canopy and soil surfaces in Eq. (2.55) can be assumed equal to the values reported in sub-section 2.1.3, instead ϵ' can be computed via Eq. (2.41) or (2.42).

2.1.5 Daily estimation

Estimation of net radiation at daily scale is generally carried out by means of a numerical integration of the previous mentioned approaches (applied at hourly scale), or adopting a relationship formally similar to Eq. (2.4):

$$R_{n,24} = (1 - \overline{\alpha}) R_{s,24} - R_{n,lw24} \tag{2.56}$$

where $R_{s,24}$ [W m^{-2}] is the daily total solar radiation, $R_{n,lw24}$ [W m^{-2}] is the daily long-wave net radiation, and $\overline{\alpha}$ is the average daytime surface albedo.

Generally, despite the considerations on daily variability of α (see sub-section 2.1.2), daily averaged value is assumed equal to the value at midday.

This assumption is justified by the relative small amount of incoming radiation in correspondence of sunrise and sunset time.

Daily solar radiation

The daily calculation of incoming solar radiation, $R_{s,24}$ [W m^{-2}], is realised according to Eq. (2.14) with the following time integration:

$$\begin{aligned} 2\int_{\omega_1}^{\omega_2}\cos(\theta_s)\mathrm{d}\omega = & \\ & \sin(\delta)\sin(\phi)\cos(s)(\omega_2-\omega_1) \\ & -\sin(\delta)\cos(\phi)\sin(s)\cos(\xi)(\omega_2-\omega_1) \\ & +\cos(\delta)\cos(\phi)\cos(s)(\sin(\omega_2)-\sin(\omega_1)) \\ & +\cos(\delta)\sin(\phi)\sin(s)\cos(\xi)(\sin(\omega_2)-\sin(\omega_1)) \\ & -\cos(\delta)\sin(\xi)\sin(s)(\cos(\omega_2)-\cos(\omega_1)) \end{aligned} \tag{2.57}$$

where ω_1 and ω_2 [rad] are the beginning and ending sun-hour angles.

Combining Eqs. (2.14) and (2.57) the following relationship is obtained:

$$R_{s,24} = \tau_{sw} K_{\mathrm{TOA}} d_r \int_{\omega_1}^{\omega_2}\cos(\theta_s)\mathrm{d}\omega \tag{2.58}$$

For horizontal surface ω_1 and ω_2 are set equal to $-\omega_s$ and ω_s, corresponding to the sunset time angle calculated as:

$$\omega_s = \arccos(-\tan(\delta)\tan(\phi)) \tag{2.59}$$

For a sloping surface the sun-hour angle where the solar beam first strikes or last strikes the slope occurs when $\cos(\theta_s) = 0$ (Allen *et al.*, 2006). Under this hypothesis in Eq. (2.7), it is possible to derive other two "candidates" for sunrise and sunset hour angles. In particular, if surface is tilted from the horizontal and facing the equator, the sunset angle, $\omega_s^{'}$ [rad], is given by:

$$\omega_s^{'} = \arccos(-\tan(\delta)\tan(\phi - s)) \tag{2.60}$$

In this case the sunrise and sunset angles still remain numerically equal (in absolute value).

For generically oriented surfaces the two angles, $\omega_s^{"}$ [rad], are not the same, and the computation is more complex, and taking into account also the effect of surface aspect (Allen *et al.*, 2006).

The effective sunset/sunrise hour angles, ω_0, used as integration limits of Eq. (2.57), are derived as:

$$\omega_0 = \min(\omega_s, \omega_s^{'}, \omega_s^{"}) \tag{2.61}$$

The integration of Eq. (2.57) and application of Eq. (2.14) presume that there is a single, continuous direct beam period during the day; this is generally valid for west, south and east facing slopes (in the northern hemisphere). In areas having steep slopes away from the sun, is possible to identify situations where the sun beam strikes the surface during two separate periods. The procedure adopted to take into account this possibility is reported in detail in Allen *et al.* (2006).

Also in this case, using a clear-sky transmittance in Eq. (2.14) the obtained radiation is a clear-sky daily radiation, $R_{so,24}$. The effective $R_{s,24}$ value can be obtained from Eqs. (2.14) and (2.57) only using the effective daily transmittance value.

Daily long-wave radiation

For daily meteorological applications, net long-wave radiation, $R_{n,lw24}$ [W m^{-2}], can be computed taking into account the role assumed by atmospheric humidity and cloudiness.

For grass crop, supposing that the concentration of the other (than water vapour) absorbers are constant, $R_{n,lw24}$ can be modelled by the relationship (Allen *et al.*, 1998):

$$R_{n,lw24} = \sigma \left[\frac{T_{a,\max}^4 + T_{a,\min}^4}{2} \right] f_{\text{cloud}} f_{\text{w}} \tag{2.62}$$

where $T_{a,\max}$ and $T_{a,\min}$ [K] are the maximum and minimum daily air temperature respectively, f_{cloud} is the cloud factor, and f_{w} is the correction for air humidity.

The cloud factor can be assumed equal to:

$$f_{\text{cloud}} = \left(1.35 \frac{R_{s,24}}{R_{so,24}} - 0.35 \right) \tag{2.63}$$

and must be limited to 1; instead, the air humidity correction is expressed by:

$$f_{\text{w}} = \left(0.34 - 0.14 \sqrt{e_a} \right) \tag{2.64}$$

and it is smaller as the humidity increases.

The Eq. (2.62) assuming a daily average surface temperature, $T_{\mathrm{RAD},m}$ [K], equal to the daily average air temperature, $T_{a,m}$ [K], hypothesis generally true for grass well-irrigated crop. In the case of sparse vegetated areas, writing the surface average temperature as: $T^4_{\mathrm{RAD},m} = T^4_{a,m} + K_T$, the Eq. (2.62) reads:

$$R_{n,lw24} = \sigma \left[\frac{T^4_{a,\max} + T^4_{a,\min}}{2} \right] f_{\mathrm{cloud}} f_{\mathrm{w}} + K^*_T \tag{2.65}$$

where K^*_T [W m^{-2}] is an empirical correction coefficient, defined as $K^*_T = \sigma \epsilon_0 K_T$, retrievable from the analysis of *in-situ* $T_{a,m}$ and $T_{\mathrm{RAD},m}$ measurements.

2.2 Heat flow in the soil

The soil heat flux density, $G(z)$ [W m^{-2}], can be modelled, according to the law governing the heat conduction, as:

$$G(z) = -\lambda_g \frac{\partial T(z)}{\partial z} \tag{2.66}$$

where λ_g [W m^{-1} K^{-1}] is the soil thermal conductivity, $T(z)$ [K] is the soil temperature and z [m] is the distance along vertical axes. The negative sign in Eq. (2.66) indicates that $G(z)$ is in the positive direction when the temperature gradient is negative.

The value assumed by the soil heat flux in the surface soil layer ($z = 0$) is defined as G_0 and it is the same term which appears in the energy budget equation. Expressing the Eq. (2.66) at the finite differences, it is possible to derive the G_0 as:

$$G_0 = -\lambda_g \frac{T_s - T_d}{\Delta z} \tag{2.67}$$

where Δz [m] is the depth of a surface tin layer, T_s [K] is the surface soil temperature, T_d [K] is the soil temperature at the depth Δz.

The connection between $G(z)$ and the soil temperature variation in space and time can be expressed by means of continuity equation:

$$\rho_s C_s \frac{\partial T(z)}{\partial t} = \frac{\partial G(z)}{\partial z} \tag{2.68}$$

where ρ_s [kg m^{-3}] is the soil bulk density, C_s [J kg^{-1} K^{-1}] is the soil specific heat and t is the time [s]. The product $\rho_s C_s$ is defined as soil volumetric heat capacity, H_{sc} [J m^{-3} K^{-1}]. The left hand-side of Eq. (2.68) represents the heat storage in the soil, that cannot be neglected as in the atmosphere.

Combining Eqs. (2.66) and (2.68), in the hypothesis of λ_g constant with depth, is possible to obtain the well known heat equation:

$$\frac{\partial T(z)}{\partial t} = D_s \frac{\partial^2 T(z)}{\partial z^2} \tag{2.69}$$

where D_s [m^2 s^{-1}] is the soil thermal diffusivity, ratio between λ_g and H_{sc}. The Eq. (2.69) defines how the soil temperature changes in time and space. As example, the location in the soil where temperature will change faster in time is the point where the change with depth of the temperature gradient is largest (Campbell and Norman, 1998).

2.2.1 Soil thermal properties

The modelling of soil thermal properties which appear in the Eqs. (2.66)-(2.69) was the topic of a number of studies (Campbell, 1985; Johansen, 1975; McCumber and Pielke, 1981; van Wijk and de Vries, 1963).

The Johansen (1975) model allows to compute the thermal conductivity, λ_g, using the relationship:

$$\lambda_g = K_d(\lambda_* - \lambda_0) + \lambda_0 \tag{2.70}$$

where λ_* and λ_0 [W m^{-1} K^{-1}] are the thermal conductivity of saturated and air-dry soil, respectively. K_d is the dimensionless normalized thermal conductivity, known as Kersten number, for which it is possible to use the simplified equation suggested by Lu *et al.* (2007):

$$K_d = \exp\{\gamma_s[1 - S_r^{\gamma_s - \delta_s}]\} \tag{2.71}$$

where S_r is the degree of saturation (computed as a ratio of actual, θ, and saturation, θ_{sat}, soil water content), γ_s is a soil texture dependent parameter (γ_s=0.96 for soil with sand fraction, f_s, >0.4 and γ_s=0.27 for soil with f_s <0.4; see Table 2.2 for typical f_s values) and δ_s (=1.33) is a shape parameter.

Table 2.2: Soil parameters (saturation volumetric water content, θ_{sat}, sand fraction, f_s, quartz content, QC, soil bulk density, ρ_s) for thermal properties computations for the 11 soil types of the USDA textural classification (Lu *et al.*, 2009; Murray and Verhoef, 2007a).

Soil texture	θ_{sat} [m^3 m^{-3}]	f_s	QC	ρ_s [kg m^{-3}]
1. Sand	0.395	0.92	0.92	1600
2. Loamy sand	0.410	0.82	0.82	1500
3. Sandy loam	0.435	0.60	0.58	1390
4. Silt loam	0.485	0.25	0.17	1320
5. Loam	0.451	0.40	0.43	1380
6. Sandy clay loam	0.420	0.60	0.58	1350
7. Silty clay loam	0.477	0.10	0.10	1300
8. Clay loam	0.476	0.35	0.32	1290
9. Sandy clay	0.426	0.52	0.52	1250
10. Silty clay	0.492	0.10	0.06	1200
11. Clay	0.482	0.25	0.22	1100

The dry soil thermal conductivity, λ_0 [W m^{-1} K^{-1}], can be estimated by the linear equation (Lu *et al.*, 2007):

$$\lambda_0 = -0.56n + 0.51 \tag{2.72}$$

where n is the soil porosity. The use of this relationship, instead of the non-linear function retrieved by Johansen (1975), is suggested by Murray and Verhoef (2007a).

The saturated thermal conductivity, λ_* [W m^{-1} K^{-1}], is estimated using:

$$\lambda_* = \lambda_s^{(1-n)} \lambda_w^n \tag{2.73}$$

where λ_w is the thermal conductivity of the water (0.57 W m^{-1} K^{-1}) and λ_s [W m^{-1} K^{-1}] is the thermal conductivity of soil matter:

$$\lambda_s = \lambda_q^{\mathrm{QC}} \lambda_O^{(1-\mathrm{QC})} \tag{2.74}$$

where QC is the quartz content (see Table 2.2), very similar to sand fraction, λ_q is the thermal conductivity of quartz (7.7 W $m^{-1}K^{-1}$) and λ_O is the thermal conductivity of other minerals (2.0 W m^{-1} K^{-1} for QC >0.2 and 3.0 W m^{-1} K^{-1}, otherwise).

The volumetric heat capacity, H_{sc}, is defined by the standard equation suggested by van Wijk and de Vries (1963):

$$H_{sc} = H_{sc,w}\theta + (1 - \theta_{sat})H_{sc,s} \tag{2.75}$$

where $H_{sc,s}$ and $H_{sc,w}$ are the heat capacity of soil minerals (2.0×10^6 J m^{-3} K^{-1}) and water (4.2×10^6 J m^{-3} K^{-1}), respectively. While air is almost always present, its contribution to H_{sc} is negligible in practical applications. Typical value of θ_{sat} for different soil type can be found in Table 2.2.

The thermal diffusivity, D_s, can be computed for a variety of soil types using the relationship proposed by Campbell (1985):

$$D_s = A_c + B_c\theta - (A_c - D_c)\exp\left[(-C_c\theta)^{E_c}\right] \tag{2.76}$$

where A_c, B_c and D_c [m^2 s^{-1}] are functions of ρ_s, B_c is also dependent on θ, C_c is a function of the clay fraction, and E_c is a constant (=4).

Finally, the soil specific heat, C_s, can be computed following (Campbell, 1985) as:

$$C_s = 2400000\frac{\rho_s}{2.65} + 41800000\theta \tag{2.77}$$

2.2.2 Soil temperature variations

The analytical solution of the Eq. (2.69) is restricted only to very simple conditions. If the soil is assumed to be infinitely deep, the thermal properties are vertical uniform, and the surface temperature varies sinusoidally, the temperature at any depth can be computed as:

$$T(z,t) = T_{s,\text{ave}} + \Delta T\exp(-z/D)\sin[\omega(t - t_0) - z/D] \tag{2.78}$$

where $T_{s,\text{ave}}$ [K] is the average soil temperature over the temporal cycle, ΔT [K] is the amplitude of the soil surface temperature fluctuation, t_0 [s] is a phase shift that takes into account if t is expressed in local or universal time, ω_t [s^{-1}] is the daily angular frequency computed as:

$$\omega_t = \frac{2\pi}{\tau_t} \tag{2.79}$$

where τ_t [s] is the period of daily temperature fluctuations, equal to 86400 seconds. The symbol D [m] represents the so-called damping depth, defined as:

$$D = \sqrt{\frac{2D_s}{\omega_t}} \tag{2.80}$$

which determines how the surface temperature fluctuations are attenuated inside the soil with the depth, and quantifies the shift in time.

The dumping depth therefore give information on how deep the effects of surface fluctuations are relevant. As example, from Eq. (2.78) it is possible to derive how at a deep $z = 4.5D$ the amplitude is of about 0.01 of the at surface value. At this depth the soil temperature can be assumed constant during the day.

Using this finding, substituting $\Delta z = 4.5D$ in Eq. (2.67), G_0 can be approximated by the relationship:

$$G_0 = \lambda_g \frac{T_s - T_{\text{deep}}}{4.5D} \tag{2.81}$$

where T_{deep} [K] represents the soil temperature at the depth where the daily temperature fluctuations can be assumed negligible.

These conventional simplifications, thought non realistic, are accepted because carry to errors generally comparable to the range of uncertainties in G_0 observations (Campbell and Norman, 1998).

2.2.3 Relationship between R_n and G_0

In many practical application, especially using remote sensed data, G_0 cannot be directly inferred using the physically-based relationships proposed in the previous sections. However, many studies (Choudhury *et al.*, 1987; Friedl, 1995, 1996; Kustas and Daughtry, 1990) have focused the attention on empirical relationships for daytime G_0 computation, based on the analysis of ratio G_0/R_n.

For bare soil surfaces, it is generally assumed that this ratio is a function of both soil type and moisture content (Santanello and Friedl, 2003). Additionally, for vegetated or partially vegetated surface, also the amount of radiation that directly reaches the soil surface, significantly influences G_0.

Choudhury *et al.* (1987) proposed a simple relationship based on the Beer's extinction law:

$$G_0 = c_g R_{n,s} \tag{2.82}$$

where the coefficient c_g ranges between 0.2 and 0.5.

However, Kustas and Daughtry (1990) highlight how c_g is constant only for several hours around solar noon; for this reason, Friedl (1996) introduced the effect of c_g temporal variability by multiplying Eq. (2.82) by $\cos(\theta_s)$.

Another approach, developed by Kustas *et al.* (1998), is based on the computation of a dimensionless time parameter, t_n:

$$t_n = \frac{|t - t_s|}{t_s} \tag{2.83}$$

where t_s is the time of the solar noon [s]. On the basis of experimental observations, Kustas *et al.* (1998) suggest to use a c_g constant value for $t_n < 0.3$ and a linear least square regression equation between c_g and t_n, otherwise.

Similarly, Santanello and Friedl (2003) use a weighted cosine model to take into account the c_g diurnal course:

$$c_g = c_{g,\max} \cos\left[\frac{2\pi(t + C_t)}{B_t}\right] \tag{2.84}$$

where $c_{g,\max}$ is the maximum value assumed by c_g during the day, C_t [s] is the peak in time position and B_t [s] is the shape parameter of the daily c_g function.

Despite the wider applications, all these approaches not do not account for possible variation of c_g due to soil moisture conditions Friedl (1996). To overcome this limitation, Santanello and Friedl (2003) introduced a soil temperature dependence in the $c_{g,\max}$ computation, using the empirical expression:

$$c_{g,\max} = 0.0074\Delta T + 0.088 \tag{2.85}$$

This relation, valid for bare soil and sparse vegetation, assumes that the diurnal change in surface temperature allows to integrate the effect of soil type and moisture content on soil thermal properties.

When a distinction between soil and canopy radiation component is not needed, the empirical formulation developed by (Bastiaanssen, 2000) for the SEBAL (Surface Energy Balance Algorithm for Land) model is available:

$$G_0 = \left[(T_{\mathrm{RAD}} - 273.16)(0.0038 + 0.0074\alpha)(1 - 0.98\mathrm{NDVI}^4)\right] R_n \quad (2.86)$$

where the vegetation index NDVI (Normalised Difference Vegetation Index) is derived from remotely sensed red and near-infrared reflectance (see pag. 160).

More recently, Tasumi (2003) established the following equations for bare soil (assumed having a LAI ≤ 0.5) and for vegetated surface, respectively (on the basis of USDA-ARS measured data at Kimberly, Idaho):

$$G_0 = \begin{cases} \left[1.80\dfrac{T_{\mathrm{RAD}} - 273.16}{R_n} + 0.084\right] R_n & \mathrm{LAI} \leq 0.5 \\ \left[0.05 + 0.18\exp(-0.52LAI)\right] R_n & \mathrm{LAI} > 0.5 \end{cases} \quad (2.87)$$

An intermediate approach, adopted in the framework of SEBS (Surface Energy Balance System) model (Su, 2002), is the following:

$$G_0 = R_n[\Gamma_c + (1 - f_c)(\Gamma_s - \Gamma_c)] \quad (2.88)$$

in which the ratio of soil heat flux and net radiation is 0.05 (Monteith, 1973) for fully vegetated area, Γ_c, and 0.315 (Kustas and Daughtry, 1990) for bare soil, Γ_s.

2.2.4 Daily estimation

Daily estimations of soil heat flux, $G_{0,24}$ [W m^{-2}], are based on empirical formulations derived from *in-situ* observations of its diurnal course. For dense grass surface the magnitude of soil heat flux is relatively small, and it may be ignored thus (Allen *et al.*, 1998):

$$G_{0,24} \approx 0 \quad (2.89)$$

For other, non-homogeneous, surfaces an empirical expression suggested by Fuchs and Hadas (1972) is:

$$G_{0,24} = 0.35R_{n,24} - 39.35 \tag{2.90}$$

However, in many practical applications it is common to consider negligible the daily soil heat flux; especially because no information for a reliable parametrisation were available, and also because the error due to its neglecting is generally estimated to be not greater than 5%, comparable to the uncertainties associated with the retrieval of daily net radiation (Somma, 2003).

2.3 Heat and water transport in the atmosphere

The transport processes of heat and mass in atmosphere can be generally considered as turbulent phenomena, in particular in the Atmospheric Boundary Layer (ABL) which is the "interface" where all the exchange between land and the higher atmosphere happen.

The ABL is defined as the lowest layer of the atmosphere that is in direct contact with Earth's surface. Conditions and processes within the ABL will react to changes at the surface within a period of less than an hour and within a distance of less than 100 km.

The ABL can be schematically subdivided in several sub-layer, as reported in Figure 2.4. The lowest part of the ABL, generally smaller than 10% of the total boundary layer height, is referred as Surface Layer (SL). That represents the region where the fluxes do not change significantly with the height. Inside this region it is possible to identify other two sub-layers: the Roughness Sub-Layer (RS-L) and the Inertial Sub-Layer (IL). The RS-L is a region, extended from the surface to an height, z^* [m], at which the influence of the singular rough elements is mixed-up by the turbulence (Raupach and Thom, 1981). The IL represents instead the region, above the RS-L, where the flow can be considered horizontally homogeneous if the characteristics of roughness elements do not vary in the upper wind direction (Kaimal and Finnigan, 1994).

The core of the ABL is constituted by the Mixing Layer (ML), which represents the layer where active turbulence has homogenised some range of

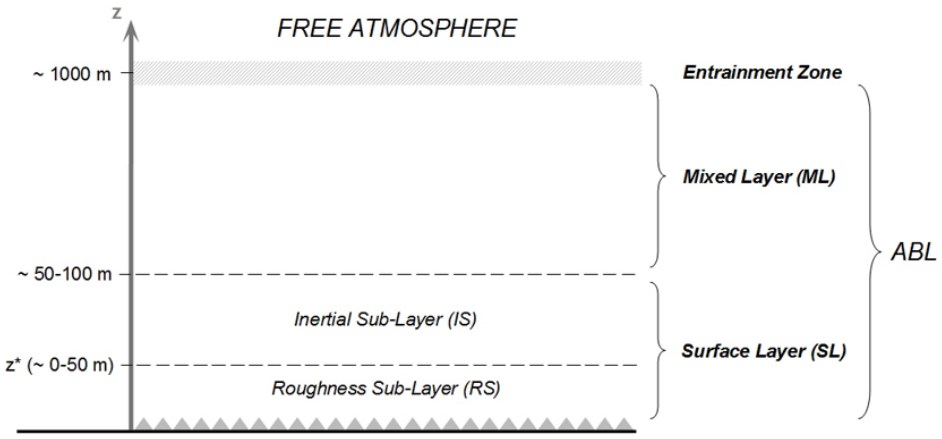

Figure 2.4: Scheme of the subdivision of the ABL in sub-layer.

depths. For this reason, ML is characterised by nearly uniform properties (e.g., potential temperature and specific humidity) throughout the layer.

At the top of ABL exists a separation zone, named entrainment zone, where a strong inversion of temperature profile causes the capping of the ABL. Above the ABL, separated by the entrainment zone, there is the free atmosphere where the wind is approximately geostrophic (parallel to the isobars). The free atmosphere is usually non-turbulent, or only intermittently turbulent. The ML assumes also the role of interface for the entrainment of the free atmosphere in the ABL.

Typical extension values of the single ABL sub-regions are indicated in Figure 2.4.

As above introduced, the ABL, with the exception of a thin layer of air very close to the surface, is essentially turbulent (Campbell and Norman, 1998). Turbulence in the atmosphere is caused by random fluctuations of wind speed and direction, temperature and gasses concentration, connected with eddy motion of the air. These eddy are substantially generated in two ways: i) mechanical turbulence, generated by friction between moving air and land surface; ii) thermal turbulence, caused by air heated/cooled at a surface and moved upward/downward due to the buoyancy.

The size of the eddies caused by these two processes are different; in fact, generally, the fluctuations from mechanical turbulence tend to be

smaller than thermal fluctuations (Campbell and Norman, 1998).

The analogies between turbulence in the atmosphere and the molecular diffusion processes, suggest for the modelling the uses of the following equations based on the well-known K-theory (Brutsaert, 1982):

$$\tau = \rho K_m \frac{\partial u}{\partial z} \tag{2.91a}$$

$$H = -\rho c_p K_H \frac{\partial \theta_a}{\partial z} \tag{2.91b}$$

$$\lambda ET = -\rho K_v \frac{\partial q}{\partial z} \tag{2.91c}$$

where τ [kg m^{-1} s^{-2}] is the shear stress, H is the sensible heat flux, λET is the latent heat flux, and the transport coefficients for turbulent diffusion replace the molecular viscosity and diffusivities (Campbell and Norman, 1998).

In Eq. 2.91 K_m, K_H and K_v [m^2 s^{-1}] are the turbulent transfer coefficients for horizontal momentum, sensible heat and water vapour respectively, ρ [kg m^{-3}] is the air density, c_p [J kg^{-1} K^{-1}] is the specific heat of air at constant pressure, λ [J kg^{-1}] is the latent heat of vaporisation, u [m s^{-1}] is the horizontal wind speed, θ_a [K] is the potential temperature, and q [kg kg^{-1}] is the specific water vapour concentration in the air, computed as the ratio between the water mass in the air and the mass of the moist air.

Commonly, the momentum flux in the surface layer is expressed using the so-called friction velocity, u_* [m s^{-1}]:

$$u_* = \sqrt{\frac{\tau}{\rho}} \tag{2.92}$$

The potential temperature, which appears in Eq. (2.91b) is related with the air temperature by the relationship:

$$\theta_a = T_a \left(\frac{100}{P_a} \right)^{0.286} \tag{2.93}$$

and then for applications closer to the land surface (where $P_a \approx 100$ kPa), it is a common practise to replace θ_a with T_a.

Unfortunately, Eqs. (2.91) are not useful for practical applications due to the impossibility to assign a values to turbulence transfer coefficients.

Experimental evidences showed that the turbulence transport coefficients must be expected to increase with height (Schwerdtfeger, 1976). Additionally, in the surface boundary layer the flux densities, τ, H and λET are assumed vertically constant. As a consequence, the increases of K with z must be balanced by the decreases in the gradients.

On the basis of these assumptions K coefficients assume the form:

$$K_m = k_v u_* (z - d_0)\phi_m \tag{2.94a}$$

$$K_H = k_v u_* (z - d_0)\phi_h \tag{2.94b}$$

$$K_v = k_v u_* (z - d_0)\phi_v \tag{2.94c}$$

where k_v is the von Karman constant (0.41), d_0 [m] is the displacement length (see sub-section 2.3.1), and ϕ_m, ϕ_h and ϕ_v are dimensionless buoyancy influences factors (equal to 1 for pure mechanic turbulence).

Assuming negligible the surface heating/cooling ($\phi_m = \phi_h = \phi_v = 1$), substituting Eqs. (2.94) into Eqs. (2.91), and integrating the obtained equations between the exchange surface and a generic height z, the resulting equations describe the wind, temperature and water vapour concentration profiles:

$$u(z) = \frac{u_*}{k_v} \ln\Big(\frac{z - d_0}{z_{0m}}\Big) \tag{2.95a}$$

$$T(z) = T_0 - \frac{H}{k_v \rho c_p u_*}\Big(\ln \frac{z - d_0}{z_{0h}}\Big) \tag{2.95b}$$

$$q(z) = q_0 - \frac{ET}{k_v \rho u_*}\Big(\ln \frac{z - d_0}{z_{0v}}\Big) \tag{2.95c}$$

where z_{0m}, z_{0h} and z_{0v} [m] are the roughness length for momentum, heat and water vapour transfer, respectively, T_0 [K] is the aerodynamic temperature and q_0 [kg kg^{-1}] is the specific water vapour concentration at the exchange height. Definitions of the introduced roughness parameters can be found in the sub-sections 2.3.1 and 2.3.2.

The effects of thermally produced turbulence on Eqs. (2.95) can be introduced taking into account the divergences of profiles in non-adiabatic conditions.

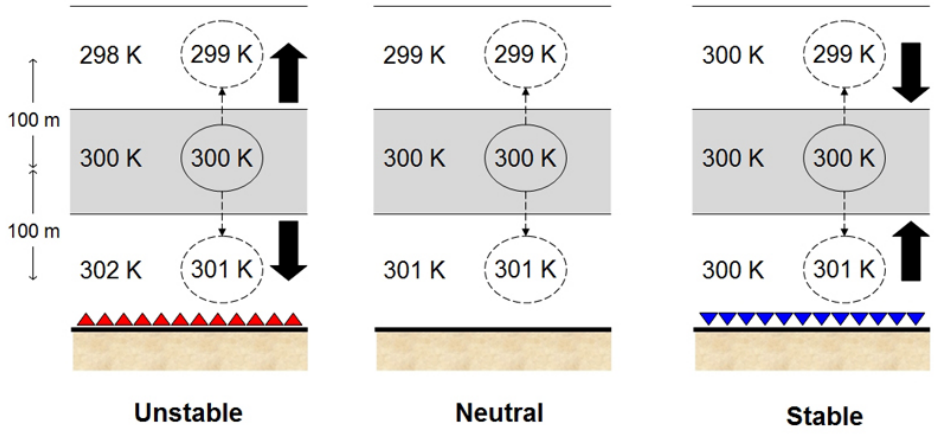

Figure 2.5: Schematic description of unstable, neutral and stable atmospheric conditions assuming adiabatic lapse rate of 1K per 100 m. On the left panel positive sensible heat flux (red arrows) causing thermal gradient greater than the reference adiabatic; on the central panel null sensible heat flux causing adiabatic gradient; on the right panel negative sensible heat flux (blue arrows) causing thermal gradient lower of the reference adiabatic (Allen *et al.*, 2002).

As expressed above, the buoyancy term can assume a role of production or destruction of the turbulence, depending on the effects of surface temperature on the atmosphere temperature. In fact, heating of the air near the surface causes an increase in turbulence and mixing; on the opposite, cooling suppress mixing and turbulence. The first condition generally happens during daytime, instead, the second one is typical of the night period (Figure 2.5).

This production/destruction of thermal turbulence is directly related to the sensible heat flux; for this reason, when H is positive (surface warmer than air) the atmosphere is said to be *unstable*, when H is negative (surface cooler than air) the atmosphere is said to be *stable* (Campbell and Norman, 1998).

Corrections of Eqs. (2.95) are realised on the basis of the Monin-Obukhov Similarity Theory (MOST), which was the starting point for the development of the ″diabatic correction″ universal functions.

The diabatic condition of the atmosphere can be expressed by means

of the Monin-Obukhov length, L [m], defined as the ratio of mechanical and thermal production of turbulence (Monteith, 1973):

$$L = -\frac{\rho c_p \theta_a u_*^3}{k_v g H} \tag{2.96}$$

When L assumes negative value ($L < 0$) the atmospheric conditions are unstable, then the actual thermal gradient is greater of the reference adiabatic one. When L assumes positive value ($L > 0$) the atmospheric conditions are stable, and the actual thermal gradient is lower of the adiabatic value. When $|L| > 100$ the effects of thermal turbulence are negligible, and the atmosphere is in adiabatic (neutral) conditions.

Since the process of momentum exchange differs from the scalar (e.g., temperature and water vapour) exchange processes (Garratt and Hicks, 1973), the diabatic correction factors are shown only for wind and temperature, assuming for water vapour and other gasses concentration the same relationships to those for temperature ($\phi_h = \phi_v$).

Although still no unanimity has been reached about the exact form of the stability correction functions, Brutsaert (1999) suggests the following formulations for the correction functions, based on the physically based approach of Kader and Yaglom (1990):

$$\phi_m = \begin{cases} \left(a_m + b_m \dfrac{\zeta}{L}\right)^{1/3} & L < 0 \\ \left(c_m + d_m \dfrac{\zeta}{L}\right) & L > 0 \end{cases} \tag{2.97a}$$

$$\phi_h = \begin{cases} \left(a_h + b_h \dfrac{\zeta}{L}\right)^{-1/3} & L < 0 \\ \left(c_h + d_h \dfrac{\zeta}{L}\right)^{-1} & L > 0 \end{cases} \tag{2.97b}$$

where ζ [m] is the height above the zero plane displacement ($\zeta = z - d_0$), and $a_{m,h}$, $b_{m,h}$, $c_{m,h}$, $d_{m,h}$ are universal constants for momentum (m) and heat (h) transport. Generally, these factors are determined by field experiments using the least square method (Marques-Filho *et al.*, 2008).

The integration of Eqs. (2.97) drives to the following profiles adiabatic correction factors, valid for both stable and unstable flows (Paulson, 1970; Webb, 1970):

$$\Psi_m = 2\ln\left(\frac{1+\mu_m}{2}\right) + \ln\left(\frac{1+\mu_m^2}{2}\right) - 2\arctan\mu_m + \frac{\pi}{2} \tag{2.98a}$$

$$\Psi_h = 2\ln\left(\frac{1+\mu_h^2}{2}\right) \tag{2.98b}$$

where the parameters μ_m and μ_h are defined as:

$$\mu_{m,h} = \begin{cases} \left(1 - 16\dfrac{\zeta}{L}\right)^{1/4} & L < 0 \\ \\ 0 & L \geq 0 \end{cases} \tag{2.99}$$

Introducing these correction factors in the profiles Eqs. (2.95), it is possible to obtain the corrected profile equations:

$$u(z) = \frac{u_*}{k_v}\left[\ln\frac{z-d_0}{z_{0m}} - \Psi_m\right] \tag{2.100a}$$

$$T(z) = T_0 - \frac{H}{k_v\rho c_p u_*}\left[\ln\frac{z-d_0}{z_{0h}} - \Psi_h\right] \tag{2.100b}$$

$$q(z) = q_0 - \frac{ET}{k_v\rho u_*}\left[\ln\frac{z-d_0}{z_{0v}} - \Psi_h\right] \tag{2.100c}$$

The expressions presented in Eqs. (2.100) are obtained considering negligible the values assumed by correction functions in correspondence of the exchange surface. In the case of neutral conditions the diabatic corrections factor are zero, returning to the Eqs. (2.95).

2.3.1 Wind profiles

In this section the analysis of wind profile is carried out assuming the simpler adiabatic conditions, considering that similar results can be obtained also for the diabatic ones.

Wind profile modelled by means of Eq. (2.95a) shows how the horizontal wind speed follows a logarithmic law, assuming a fairly constant value far from the surface, and becoming null at an elevation $z = d_0 + z_{0m}$. This equation is appropriate only in the surface layer, where u_* is constant. Additionally, as a lower boundary, the relationship is valid only for $z \geq (d_0 + z_{0m})$.

The shape of this profile is related to the efficiency of turbulent transfer; in fact, closer to the surface only small eddies are present and then the transport is less efficient compared to the higher air space where the eddies are larger.

From experimental evidences, the wind profile is equal to 0 for the bare soil near the surface. Differently, the profile over a crop is similar but shifted upward (Campbell and Norman, 1998). The term d_0 [m], named zero plane displacement, have the role to take into account this shift into Eq. (2.95a).

For a bare soil the effects related to the roughness of the surface occurs directly on the surface itself, for this reason $d_0 = 0$ and the roughness can be assumed equal to a constant typical value of $z_{0m} = 0.01$ m.

For the crop the drag of the surface occurs inside the foliage space, in correspondence of an height that have the effect to make this surface equivalent to the wind speed by means of a simple reference plane translation. A number of practical expressions for d_0 and z_{0m} calculation have been proposed on the basis of experimental observation of wind velocity ad different elevations. As example, Brutsaert (1982) suggests the following widely-adopted relationships:

$$d_0 = \frac{2}{3} h_c \tag{2.101}$$

and

$$z_{0m} = \frac{1}{8} h_c \tag{2.102}$$

These relationships allow to assess zero plane displacement and roughness length for uniform vegetated surface by knowing just the canopy height.

Adopting Eq. (2.95a) is relatively easy to obtain an estimation of wind velocity above the plant canopy. However, this equation cannot be used for wind velocity estimation in the air space inside or below the canopy crow.

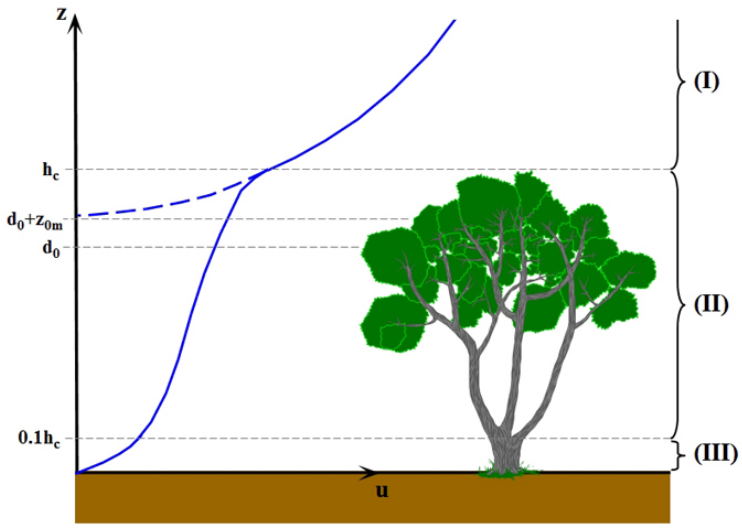

Figure 2.6: Horizontal wind speed: (**I**) just above the canopy, (**II**) within the canopy and (**III**) closer to the soil surface.

Commonly, in order to model the wind in canopy spaces, the vertical profile is divided into at least three layers (Figure 2.6) located:

(I) above the canopy;

(II) within canopy space;

(III) closer to the soil surface.

In the layer (**I**), $z \geq h_c$, the wind velocity can be still modelled using the Eq. (2.95a) with the roughness parameter derived by means of the Eqs. (2.101) and (2.102). In the layer (**II**), $0.9h_c \leq z \leq h_c$, the wind speed decreases with depth as a function of the foliage density. In the layer (**III**), corresponding to the bottom 10% of the canopy (z_s), a new logarithmic profile is developed, computed assuming $d_0 = 0$ and z_{0m} related to the characteristics of the underlying soil surface.

In most of the canopy the wind speed in the layer (**II**) is well modelled by means of an exponential decay profile (Goudriaan, 1977):

$$u(z) = u_c \exp\left[-a\left(1 - \frac{z}{h_c}\right)\right] \tag{2.103}$$

where u_c [m s^{-1}] is the wind speed at the top of the canopy, computed from Eq. (2.95a) assuming $z = h_c$, a is the extinction factor for the exponential profile.

Goudriaan (1977) suggests a simple equation for extinction coefficient computation as a function of crop structure:

$$a = 0.28\mathrm{LAI}^{2/3} h_c^{1/3} w_l^{-1/3} \tag{2.104}$$

where w_l [m] is the mean leaf size, computed by four times the leaf area divided by the perimeter.

As observed by Brutsaert (1982), the use of an exponential wind profile inside the foliage space is not always appropriate, especially in proximity of the soil surface. For this reason the logarithmic profile is suggested in the layer (**III**).

In tall tree canopies, with dense foliage in the upper space and open steam space in the lower one, a number of past studies highlighted the difficulty of specifying a unified wind profile extinction formulation (Fons, 1940; Petit *et al.*, 1976; Shaw, 1977; Uchijima and Wright, 1964).

Shaw (1977) observed that in the lower region of the canopy a hyperbolic-cosine profile may be more appropriate. On the basis of this consideration, and assuming a uniform vertical distribution of foliage, Massman (1987) suggested the following expression:

$$u(z) = u_c \left[\frac{\cosh\left(\beta_0 \dfrac{z}{h_c}\right)}{\cosh \beta_0} \right]^{1/2} \tag{2.105}$$

in which β_0 represents the extinction coefficient for hyperbolic-cosine profile, derivable using the relationship:

$$\beta_0 = \frac{4 C_d \mathrm{LAI}}{k_v^2 \alpha_*^2} \tag{2.106}$$

where C_d is the drag coefficient, typically equal to 0.2, and α_* is a dimensionless coefficient that describes the roughness of the underlying vegetative surface, having values between 1.0 and 2.0 (Raupach and Thom, 1981).

More recently, on the basis of the analysis of observed wind speed profiles acquired inside pine forests in Great Britain and the Shasta Experimental

Forest in USA, Lalic *et al.* (2003) suggest the following profile for the wind speed inside canopy space:

$$u(z) = \begin{cases} u_c \left[\dfrac{\cosh \beta_0 \left(\dfrac{z - z_d}{h_c} \right)}{\cosh \beta_0} \right]^{7/2} & z_d \leq z \leq h_c \\ C_u u_c & z_s \leq z \leq z_d \end{cases} \tag{2.107}$$

where z_d [m] is the crown bottom height, and the parameter C_u is defined as follow:

$$C_u = \left[\cosh \beta_0 \left(1 - \frac{z_d}{h_c} \right) \right]^{-7/2} \tag{2.108}$$

and it is adopted to ensure the continuity in the two wind speed sub-profiles.

The exponent 7/2 in Eq. (2.107) replaces the value 0.5 adopted by Massman (1987); this value was derived by fitting wind speed measurements in a forest in Great Britain with an empirical relationship.

2.3.2 Temperature and water vapour profiles

Due to the analogies in temperature and water vapour concentration profiles in the ABL, the analysis of the characteristics of these variables is realised jointly in this sub-section.

The shape of the two profiles can be inferred directly from the analysis of Eqs. (2.95b) and (2.95c). The relationships highlight how both temperature and specific humidity increase/decrease with z starting from a value at the source height named T_0 and q_0, respectively. The increasing or decreasing trend depends on the sign of H and λET fluxes; generally, during daytime the positive values of these fluxes causes a decrease in T and q, opposite behaviours happen during night time. However, as in the case of wind speed, this relationships are strictly applicable only for the SL.

The application of Eqs. (2.95b) and (2.95c) requires the knowledge of roughness parameter to the temperature and water vapour transfer. A common practise is to assume a correspondence between the two parameters,

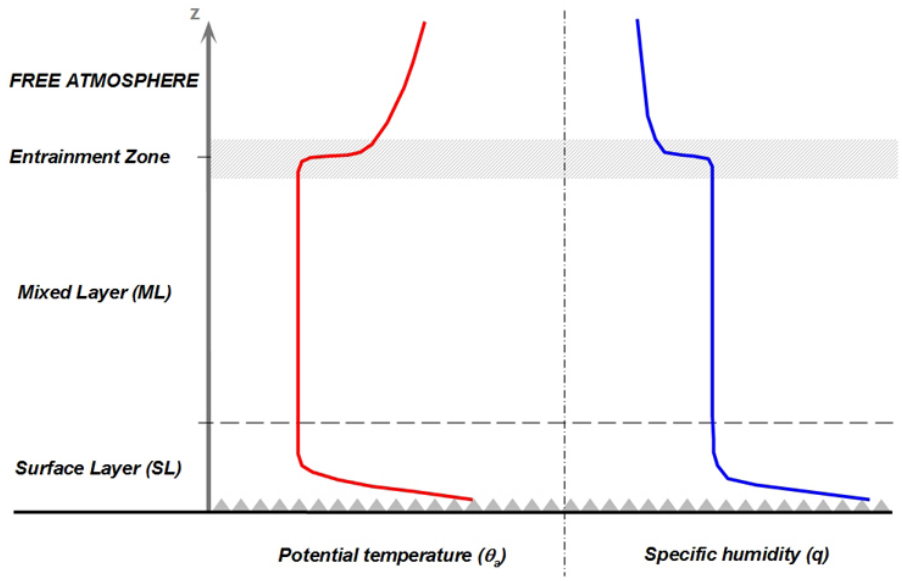

Figure 2.7: Typical shape of potential temperature (red line) and specific humidity (blue line) in the ABL during daytime.

as $z_{0h} = z_{0v}$. This approach presuppose that the drag of the surface is the same for the transport of all the scalars.

The relationship between the terms z_{0m} and z_{oh} (z_{0v}) is generally expressed as (Garratt and Hicks, 1973):

$$k_v B^{-1} = \ln\left(\frac{z_{0m}}{z_{0h}}\right) \tag{2.109}$$

where B^{-1} is the dimensionless bulk parameter, which represents the inverse of Stanton number (Owen and Thomson, 1963).

Using Raupach (1989) "localized near-field" Lagrangian theory, Massman (1999) developed a relatively complex model to calculate B^{-1}. This model explicates the dependence from properties of the canopy at both micro- and macro- scale.

For practical application, $k_v B^{-1}$ have a value ≈ 2.3 for densely vegetated areas. On the basis of this value, z_{0h} can be computed as:

$$z_{0h} = 0.1 z_{0m} \tag{2.110}$$

In order to emphasise the temperature differences of interest for buoyancy, the analysis is carried out on the above defined potential temperature. In fact, it is known that the air temperature is characterised by a decrease with z due to the reduction of atmospheric pressure. This decrease depends on the adiabatic/diabatic conditions and also on the atmospheric water content. A typical value adopted for the lapse rate is of 0.0065 K m^{-1} for neutral atmospheric conditions. Differently, the specific water content takes into account the effect of moist air mass. The qualitative analysis of θ_a and q is realised only for the unstable conditions, because of major interest for hydrological applications.

Figure 2.7 (red line) represents the typical diurnal shape of the potential temperature. In the SL θ_a decreases with the height, due to the negligible effect of pressure differences and the high contribution of the sensible heat flux. In the mixed layer, the air within the layer is characterized by an uniform value of θ_a. At the top of ML there is a strong inversion of temperature gradient in the entrainment zone.

The specific water content (blue line in Figure 2.7) shows similar trend of θ_a in both SL and ML; the main difference in the two profiles is the inversion in specific humidity that shows an opposite behaviour with a reduction in the entrainment zone.

Commonly, the inversion in potential temperature and specific humidity are represented as a discontinuous jump between the ABL and the free atmosphere, increasing in magnitude (as absolute value) when the boundary layer grows (Margulis and Entekhabi, 2004).

2.3.3 Sensible and latent heat fluxes modelling

Expliciting the Eq. (2.100a) in terms of friction velocity as:

$$u_* = \frac{k_v u}{\left[\ln\left(\frac{z_u - d_0}{z_{0m}}\right) - \Psi_m\right]} \tag{2.111}$$

it is possible to assess u_* if known the horizontal wind speed at an elevation z_u.

Introducing Eq. (2.111) in Eqs. (2.100b) and (2.100c) it is possible to

obtain the definition of sensible, H, and latent heat, λET, fluxes:

$$H = \rho c_p \left(\frac{T_0 - T_a}{r_{ah}} \right) \tag{2.112}$$

$$\lambda ET = \frac{\rho c_p}{\gamma} \left(\frac{e_0 - e_a}{r_{ah}} \right) \tag{2.113}$$

In Eq. (2.113) the specific humidity was substituted by the water vapour content: $e = \gamma \lambda / c_p q$ [kPa], were γ [kPa K^{-1}] is the psychrometric constant, and the subscripts continuing to assume the same meaning.

The term r_{ah} [s m^{-1}], defined as aerodynamic resistance for heat and water vapour transfer, can be computed as:

$$r_{ah} = \frac{\left[\ln\left(\frac{z_T - d_0}{z_{0h}} \right) - \Psi_h \right]}{k_v u_*} \tag{2.114}$$

where z_T (z_q) represents the elevation of measurement of air temperature (humidity). The introduction of this resistance term is known as the "electrical analogy", for the parallelism between the modelling of electron fluxes in circuits and energy fluxes in atmosphere.

The solution of Eqs. (2.112) and (2.113) requires, additionally to wind speed, air temperature and humidity measurements, the knowledge of the aerodynamic temperature and the water vapour content at the source height. These variables are generally not known, and difficult to measure due to the theoretical origin of their definition, especially for heterogeneous surface.

The approaches adopted for the solution of Eqs. (2.112) and (2.113) can be subdivided in two main classes: the *Big-leaf approach* and the *two-source scheme*. Moreover, two different *two-source* scheme were proposed in literature, the so called *in-series* scheme and the *in-parallel* scheme, that differ for the configuration of the resistances network adopted.

The big-leaf approach

The energy flux modelling based on the big-leaf approach starts from the theoretical background developed by Penman (1948) for surface characterised by wet surface-atmosphere interface (generally water body).

The relationship retrieved for saturated surface was extended by Penman (1956) to the case of single leaf introducing a resistance, in series with the aerodynamic resistance, which takes into account the resistance of the stomata to the flux of vapour, named stomatal resistance, r_c [s m^{-1}].

Finally, the scaling up of the model from leaf to canopy scale was realised by Monteith (1965) introducing the big-leaf concept. Substantially, adopting this hypothesis, the canopy is modelled as a single large leaf placed at the height $(d_0 + z_{0h})$ inside the crop.

On the basis of the modification of the Penman approach suggested by Monteith, the latent heat flux has the following formulation:

$$\lambda ET = \frac{\rho c_p}{\gamma}\left(\frac{e_0^* - e_a}{r_{ah} + r_c}\right) \tag{2.115}$$

where e_0^* [kPa] is the water vapour pressure at saturation at the temperature T_0, and the resistance r_c represents an equivalent resistance for a single big-leaf, computed as a combination of all leaves stomatal resistances between the saturated surface inside the leaves (under the stomata) and the source height.

The term e_0^* [kPa] can be computed by means of a linearization of the saturation water pressure curve (for small temperature differences), by means of:

$$e_0^* = e_a^* + \Delta\big(T_0 - T_a\big) \tag{2.116}$$

where e_a^* [kPa] is the air water vapour content at saturation and Δ [kPa K^{-1}] is the slope of saturation curve.

Introducing Eq. (2.116) in the (2.115), and combining the result with sensible heat definition, Eq. (2.112), and energy balance equation, Eq. (2.2), it is possible to obtain the well-known form of the Penman-Monteith (PM) equation:

$$\lambda ET = \frac{\Delta(R_n - G_0) + \rho c_p \dfrac{(e_a^* - e_a)}{r_{ah}}}{\Delta + \gamma\left(1 + \dfrac{r_c}{r_{ah}}\right)} \tag{2.117}$$

Due to the connection between stomatal resistance and crop water availability, a detailed analysis of this term is carried out in the section 2.5.

The above described approach was adopted by FAO-56 paper (Allen *et al.*, 1998) in order to define the so-called *reference evapotranspiration*. This particular value of evapotrasnpiration, denoted as ET_0, is defined as the evapotranspiration of a hypothetical grass reference crop with an assumed crop height of 0.12 m, a fixed stomatal resistance and an albedo of 0.23.

In a more recent publication (ASCE-EWRI, 2005), the fixed value of stomatal resistance was defined differently for daily and hourly applications. In particular, the daily value can be assumed equal to 70 s m^{-1}, the hourly value was fixed equal to 50 s m^{-1} for daytime and 200 s m^{-1} for nighttime computations.

The reference evapotraspiration definition allows to compute the potential (well watered-unstressed) value for every crop type, ET_p, introducing the crop coefficient (Allen *et al.*, 1998):

$$K_c = \frac{ET_p}{ET_0} \tag{2.118}$$

Values of K_c for a number of different crop types are reported in the FAO-56 paper, and are also widely discussed in literature.

In order to take into account the special features of sparse crop, the same paper proposed a more detailed approach, known as dual-crop approach, which define ET_p as:

$$ET_p = (K_{cb} + K_e)ET_0 \tag{2.119}$$

where K_{cb} is the basal crop coefficient, related to the canopy transpiration, and K_e is the coefficient for soil evaporation.

The effects of surface soil water availability on evaporation are taken into account in the dual-crop approach by means of the following relationship:

$$K_e = K_r(K_{c,\max} - K_{cb}) \tag{2.120}$$

where $K_{c,\max}$ is the maximum value of K_c, and K_r is a dimensionless evaporation reduction coefficient, ranging between 0 and 1, dependent on water availability.

In both approaches the environmental and water stress conditions are taken into account introducing multiplicative reducing factors (Allen *et al.*,

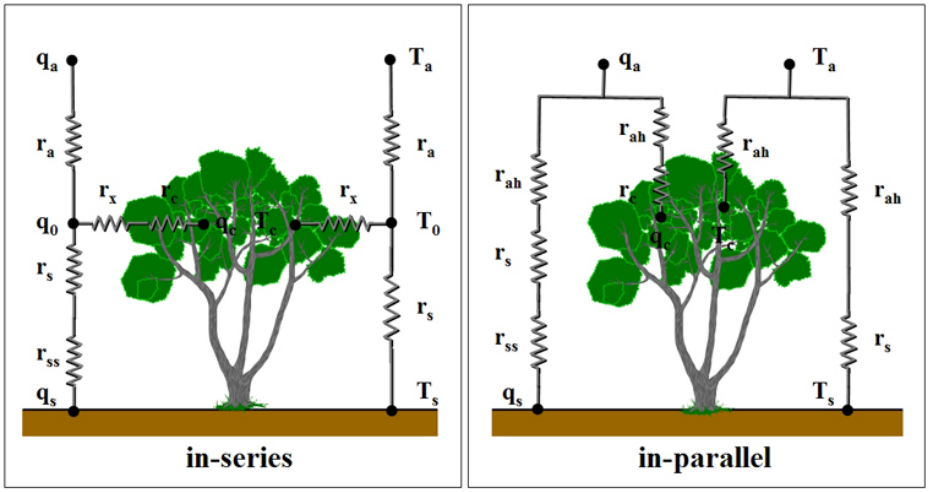

Figure 2.8: Scheme of the resistance network for the in-series (left panel) and the in-parallel (right panel) approaches.

1998), obtaining the following general relationships:

$$ET = K_s K_c ET_0 \tag{2.121a}$$

$$ET = (K_s K_{cb} + K_e) ET_0 \tag{2.121b}$$

where K_s describes the effect of soil water stress on crop transpiration.

The two-source approach

In sparsely vegetated areas the big-leaf hypothesis become unrealistic due to the interaction that occurs between the fluxes generated by the two sources (canopy and soil). Following also in this case the "electrical analogy", two different schemes were proposed in literature for the modelling of H and λET fluxes exchange for sparse crops (Figure 2.8).

In the in-parallel approach (Figure 2.8, right panel) the flux from each patch (canopy or soil) acts independently from the other. On the basis of this assumption the fluxes can be computed as:

$$H = H_s + H_c = \rho c_p \left[\frac{T_c - T_a}{r_{ah}} + \frac{T_s - T_a}{r_{ah} + r_s} \right] \tag{2.122}$$

$$\lambda ET = \lambda E_s + \lambda ET_c = \frac{\rho c_p}{\gamma}\left[\frac{e_c - e_a}{r_{ah} + r_c} + \frac{e_s - e_a}{r_{ah} + r_s + r_{ss}}\right] \tag{2.123}$$

where r_s [s m^{-1}] is the resistance to heat flow in the boundary layer above the soil surface and r_{ss} [s m^{-1}] is the soil resistance to vapour flux.

It is interesting to observe how the in-parallel scheme adopts the same resistance for canopy fluxes modelling of the big-leaf approach, only replacing the canopy temperature with the aerodynamic one. The resistance r_s aims instead to take into account the different course of the soil flux, which is partially influenced by the canopy air space.

The parallel arrangement of the resistances permits a simpler solution of the equations system and may be slightly more appropriate for very sparse vegetation where the canopy and soil less interact (Norman *et al.*, 1995).

In the in-series approach (Figure 2.8, left panel) the interactions between canopy- and soil- generated fluxes are taken into account. The formulations for H and λET fluxes computations have the forms:

$$H = H_s + H_c = \rho c_p\left[\frac{T_s - T_0}{r_s} + \frac{T_c - T_0}{r_x}\right] \tag{2.124}$$

$$\lambda ET = \lambda E_s + \lambda ET_c = \frac{\rho c_p}{\gamma}\left[\frac{e_s - e_a}{r_s + r_{ss}} + \frac{e_c - e_a}{r_x + r_c}\right] \tag{2.125}$$

where r_x [s m^{-1}] is the resistance of the canopy boundary layer, which represents the resistance of the thin air layer closer to the leaves surface (Nobel, 2005).

The term T_0 which appears in Eq. (2.124) is defined as follow:

$$T_0 = \frac{\dfrac{T_a}{r_a} + \dfrac{T_s}{r_s} + \dfrac{T_c}{r_x}}{\dfrac{1}{r_a} + \dfrac{1}{r_s} + \dfrac{1}{r_x}} \tag{2.126}$$

where the resistance r_a is computed using the Eq. (2.114) assuming $z_{0h} = z_{0m}$. This assumption causes that this temperature is defined as

the aerodynamic temperature for momentum, and it differs in theoretical definition from the aerodynamic temperature for heat introduced above.

Analogously, e_0 is defined by the following relationship:

$$e_0 = \frac{\dfrac{e_a}{r_a} + \dfrac{e_s}{r_s + r_{ss}} + \dfrac{e_c}{r_x + r_c}}{\dfrac{1}{r_a} + \dfrac{1}{r_s + r_{ss}} + \dfrac{1}{r_x + r_c}} \tag{2.127}$$

Adopting the same hypothesis of the big-leaf approach, e_s and e_c [kPa] can be computed assuming that the stomatal air space inside the leaves and the air in the soil pours are saturated, and then e_s and e_c are computable as:

$$e_s = e_a^* + \Delta\big(T_s - T_a\big) \tag{2.128a}$$

$$e_c = e_a^* + \Delta\big(T_c - T_a\big) \tag{2.128b}$$

Norman and Campbell (1983) suggest how for vegetated, semi-arid regions with low to moderate coverage, the resistance networks are indistinguishable because gradients of air temperature in the upper canopy are small. However, when the vegetation-soil system is dry, the sensible heat exchange from soil most affects the air temperature at the source height, and this effect is better captured by the in-series approach (Norman *et al.*, 1995).

Boundary layer resistances

The canopy boundary layer resistance, r_x [s m^{-1}], can be parameterised as suggested by Norman *et al.* (1995):

$$r_x = \frac{C'}{\mathrm{LAI}}\left(\frac{w_l}{u_{d_0+z_{0m}}}\right)^{1/2} \tag{2.129}$$

where C' is set equal to 90 s$^{1/2}$ m^{-1} as suggested by Grace (1981), and $u_{d_0+z_{0m}}$ [m s^{-1}] is the wind velocity at the height $(d_0 + z_{0m})$, obtained by extrapolation of extinction wind profile inside the canopy structure, as described in sub-section 2.3.1.

The resistance of the atmosphere between soil and mean source height, r_s [s m^{-1}], was modelled by Sauer *et al.* (1995) by means of a simplified semi-empirical relationship as:

$$r_s = \frac{1}{a' + b' u_s} \tag{2.130}$$

where a' [m s^{-1}] and b' are equal to 0.004 and 0.012 respectively, and u_s [m s^{-1}] is the wind velocity just above the soil surface, computable by means of extinction wind laws (Eqs. 2.103, 2.105 or 2.107) in correspondence of $z = z_s = 0.1$ m.

In the case of partial or open canopy cover, under strong convective conditions with hot, dry soil, r_s can be estimated following the modification of Eq. (2.130) proposed by Kustas and Norman (1999) based on the study of Kondo and Ishida (1997):

$$r_s = \frac{1}{c'(T_s - T_c)^{1/3} + b' u_s} \tag{2.131}$$

where the coefficient c' [m s^{-1} K$^{-1/3}$] ranges between 0.0011 and 0.0038 as function of the surface roughness. Sauer (1993) and Sauer *et al.* (1995) suggest a c' value of 0.0025 for surfaces characterised by cultivated crops.

Descriptions of the resistances to the vapour flux (r_c and r_{ss}) is reported in sub-section 2.5, due to the connections with soil water content.

2.4 Energy fluxes ratios

All the above described components of the energy balance display a typical diurnal variability, mainly related to the sinusoidal shape of the incoming solar radiation (see sub-section 2.1.1). Despite that, a number of indices retrieved as fluxes ratio showed a relative constant behaviour during daytime hours (Jackson *et al.*, 1983; Lewis, 1995). Particular interest was focused in the last years on the bowen ratio, β, and the evaporative fraction, Λ, due to its capability to take into account the available energy ($R_n - G_0$) partition and, in some case, to convert instantaneous H and λET fluxes estimations into daily values.

A number of studies (Brutsaert and Sugita, 1992; Crago, 1996; Shuttleworth *et al.*, 1989) have analysed the diurnal variation of these parameters,

in both clear and cloudy days. Especially for no-cloudy days, these parameters usually exhibit a slightly concave-up shape characterised by a minimum across the solar noon (with low standard deviation) and two maxima near sunrise and sunset (with high standard deviation).

2.4.1 Bowen ratio

The Bowen ratio, β, was originally introduced by Bowen (1926) and it is a energy partition indicator computed as a ratio between the sensible and the latent heat fluxes:

$$\beta = \frac{H}{\lambda ET} \tag{2.132}$$

Although it was defined as in Eq. (2.132), its indirect estimation (by means of temperature and humidity measurements at two elevations) was used for H and λET assessment when the available energy is known:

$$H = (R_n - G_0)\frac{\beta}{1+\beta} \tag{2.133}$$

$$\lambda ET = (R_n - G_0)\frac{1}{1+\beta} \tag{2.134}$$

The Analysis of β definition shows that it can theoretically assumes values from zero to infinite; however, typically daytime values are in the range 0–1 for well-watered areas, and up-to 10 for dry areas (Somma, 2003).

When β approaches negative values, it becomes a poor descriptor of the energy partition. Fortunately, this situation usually occurs only closer to dawn and sunset, when the fluxes are small (Brutsaert, 1982).

Despite the terms $1/(1+\beta)$ corresponds to the evaporative fraction (see definition in the sub-section 2.4.2), Crago and Brutsaert (1996) demonstrated the scarce stability of β during the day, and a clear daily cycle due to changes in energy partitioning related to the closure of stomata in early afternoon. As a consequence, daily evapotranspiration can be assessed only by means of an integration of a sequence of measurements/estimations, but not from a single instantaneous midday value.

2.4.2 Evaporative fraction

The evaporative fraction, Λ, is defined as the ratio between latent heat flux and available energy:

$$\Lambda = \frac{\lambda ET}{R_n - G_0} \tag{2.135}$$

Usually the evaporative fraction scaled between 0 and 1, exceeding the unity only during night time or cloudy-day. Additionally, the main characteristic of Λ is its constancy during daytime, making it an useful tool to describe surface energy partition at daily scale.

The daytime integration is based on the hypothesis that Λ removes available energy diurnal cycle, and isolates the surface control on turbulent flux partition which vary approximately at daily-time scale (Gentine *et al.*, 2007).

The diurnal behaviour of Λ depends on environmental factors such as air temperature, soil water content and leaf area index, whereas it is found to be almost independent of wind speed even if wind is an important forcing factor driving turbulent exchange at the surface (Gentine *et al.*, 2007).

Typically, Λ daily trend shows a concave-up shape, which is partially related to the phase difference between soil heat flux and net radiation, observed by many authors (Fuchs and Hadas, 1972; Idso *et al.*, 1975; Santanello and Friedl, 2003).

The diurnal shape of Λ could causes the underestimation of daily evapotranspiration when the instantaneous value is used as time integration parameter (Crago, 1996). However, the systematic underestimations of Λ, due to the concave-up shape, are generally smaller than those for β, this because the use of the more stable available energy in the computation of Λ instead of the sensible heat flux adopted for the retrieval of β (Crago and Brutsaert, 1996).

On the basis of these considerations, Kustas *et al.* (1994), among others, used Λ to extrapolate daily evapotranspiration from instantaneous remote sensing flux estimates under cloud-free conditions, and estimated at most 10% underestimation due to the night evaporation not accounted by this method. These results suggest a relative constant daytime behaviour, generally known as ″self preservation″.

2.5 Connection between water flow in the soil and evapotranspiration

In the hydrological cycle the soil water content plays a fundamental role, due to his key involvement in energy and water mass exchange processes in the land-atmosphere system.

The term soil water content (or soil moisture) refers to the water that occupies the spaces between the soil particles. The actual value of the soil water content is mainly influenced by:

- the soil texture, as percentage of clay, sand and silt, which determines the soil water-holding capacity. Also variations in organic matter, porosity and soil structure affect the water content distribution. Generally, soil characterized by fine structure (clay and loam) have higher water-holding capacity of sandy soil, according to the higher porosity;
- the topography, and in particular the slope of the surface. The soil moisture at the top of an hill is generally lower than the values in the lower part; additionally, the slopes facing the south (in the north hemisphere) tend to be drier than the slopes facing the north due to the higher incoming radiation;
- the vegetation coverage and the land use. The vegetation density affects directly the available precipitation (and then infiltration and stream flow), moreover, water uptake from crop causes a reduction in water content in the soil interested by roots;
- the precipitation (and irrigation) previous history, and in particular the eventual phase shift between the wet season and the crops growing season.

The water content of the soil is commonly expressed in terms of mass or volume; in the case of mass-based approach it is defined as, m [kg kg^{-1}]:

$$m = \frac{m_w}{m_s} \tag{2.136}$$

where m_w [kg] is the mass of water and m_s [kg] is the total mass of soil.

The volumetric soil water content, θ [m^3 m^{-3}], can be instead defined as:

$$\theta = \frac{\rho_s}{\rho_w} m \tag{2.137}$$

where ρ_w [kg m^{-3}] is the water density (approximately equal to 1000 kg m^{-3}). Typical values of ρ_s can be found in Table 2.2.

Generally the volumetric water content is more useful for the in-field studies. For this reason in this thesis the term water content refers always to the volumetric one.

Theoretically, volumetric water content ranges between 0 (completely dry soil) to a maximum value equal to the soil porosity (all the pores are filled with water). However, for agricultural purposes some other typical values are of interest (Cavazza and Patruno, 2005):

- the practical saturated soil water content, θ_{sat}, corresponding to a water potential of 0, generally lower than the porosity due to the air trapped in the soil in practical saturation processes;
- the field capacity, θ_{fc}, which represents the water content held in the soil after the excess water has drained away, computed in correspondence of a suction pressure of -33 J kg^{-1};
- the wilting point water content, θ_{wl}, which is the value that occurs when the soil becomes too dry, and the plants are not longer able to extract the water, defined as the value at -1500 J kg^{-1} of suction pressure.

2.5.1 Modelling of soil water content dynamic

The in-time dynamic of soil water content can be analysed by means of the water budget equation, which represents the balance between hydrological inputs and losses (as briefly introduced in Figure 1.1). Water balance can refer to various soil depth, depending on the aim of the analysis.

An approach, based on the force-restore scheme, is the one proposed by Noilhan and Planton (1989) for the modelling of the soil moisture in the root zone. Following Deardorff (1977) the model considers the surface soil water content, θ_1 [m^3 m^{-3}], representative of a thin surface layer (which

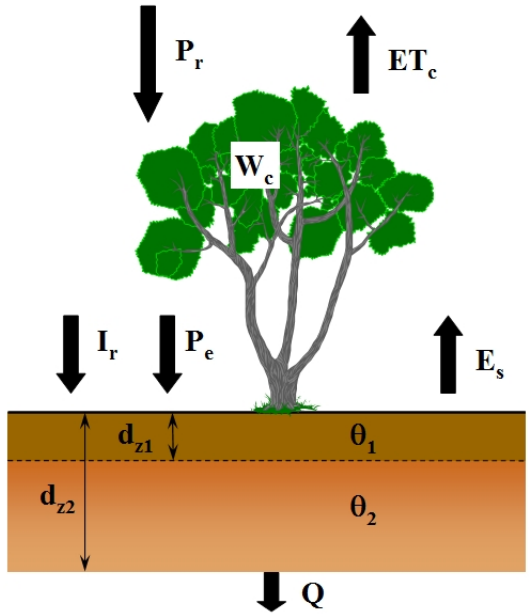

Figure 2.9: Scheme of the force-restore water balance.

interacts directly with the atmosphere) and the mean root zone water content, θ_2 [m^3 m^{-3}].

This approach divides the soil into two reservoirs (see Figure 2.9), of depth d_{z1} and d_{z2} [m] respectively, expressing the balances as:

$$\frac{\partial \theta_1}{\partial t} = \frac{C_1}{d_{z1}}(P_e + I_r - E_s) - \frac{C_2}{\tau_t}(\theta_1 - \theta_{eq}) \tag{2.138a}$$

$$\frac{\partial \theta_2}{\partial t} = \frac{1}{d_{z2}}(P_e + I_r - E_s - ET_c - Q) \tag{2.138b}$$

where P_e [mm s^{-1}] is the precipitation rate infiltrating into the soil, I_r [mm s^{-1}] is the irrigation rate, E_s and ET_c [mm s^{-1}] are the soil evaporation and canopy evapotranspiration, respectively, and Q [mm s^{-1}] is the subsurface drainage to soil layers beneath the rooting zone.

The first term on the right side of Eq. (2.138a) represents the influences of surface fluxes where the contribution of the root uptake is negligible, and the second term characterises the diffusivity of water in the soil.

Table 2.3: Coefficients for soil hydraulic parametrisation of the force-restore water balance scheme for the 11 soil types of the USDA textural classification. Values of b_* are the slopes of retention curve given by Clapp and Hornberger (1978), other coefficients are estimated by Noilhan and Planton (1989).

Soil texture	b_*	p_*	a_*	$C_{1,sat}$	$C_{2,ref}$
1. Sand	4.05	4	0.387	3.9	0.082
2. Loamy sand	4.38	4	0.404	3.7	0.098
3. Sandy loam	4.90	4	0.219	1.8	0.132
4. Silt loam	5.30	6	0.105	0.8	0.153
5. Loam	5.39	6	0.148	0.8	0.191
6. Sandy clay loam	7.12	6	0.135	0.8	0.213
7. Silty clay loam	7.75	8	0.127	0.4	0.385
8. Clay loam	8.52	10	0.084	0.6	0.227
9. Sandy clay	10.40	8	0.139	0.3	0.421
10. Silty clay	10.40	10	0.075	0.3	0.375
11. Clay	11.40	12	0.083	0.3	0.342

The term θ_{eq} [m^3 m^{-3}] is the water content when gravity balances the capillary forces, computable following the polynomial function suggested by Clapp and Hornberger (1978):

$$\frac{\theta_{eq}}{\theta_{sat}} = \left(\frac{\theta_2}{\theta_{sat}}\right) - a_*\left(\frac{\theta_2}{\theta_{sat}}\right)^{p_*}\left[1 - \left(\frac{\theta_2}{\theta_{sat}}\right)^{8p_*}\right] \tag{2.139}$$

where the two parameters a_* and p_* are defined for all the 11 USDA soil types (see Table 2.3).

The coefficient C_1 describes the relative depth of soil influenced by the surface external hydrological forces, calculated starting from the Darcy's law, assuming constant hydraulic proprieties and sinusoidal variation of the surface water flux, as (Noilhan and Planton, 1989):

$$C_1 = C_{1,sat}\left(\frac{\theta_{sat}}{\theta_1}\right)^{0.5b_*+1} \tag{2.140}$$

where the coefficient $C_{1,sat}$ is calculated starting from the values of hydraulic parameters at saturation and b_* is the slope of the retention curve on a logarithmic graph (Clapp and Hornberger, 1978). Values assumed by both coefficients for different soil types are reported in Table 2.3.

The parameter C_2 characterises the velocity at which the water profile is restored to its equilibrium. Following the force-restore approach (Noilhan and Planton, 1989), this parameter is related to the soils texture properties and soil water content by the semi-empirical relationships:

$$C_2 = C_{2,ref}\left(\frac{\theta_2}{\theta_{sat} - \theta_2 + 0.001}\right) \tag{2.141}$$

where, also in this case, the values assumed by coefficient $C_{2,ref}$ are reported in Table 2.3.

The drainage can be computed as a function of the soil saturated hydraulic conductivity, K_{sat} [m s^{-1}], the saturated water content and the slope of retention curve, according to the following equation (Clapp and Hornberger, 1978):

$$Q = K_{sat}\left(\frac{\theta_2}{\theta_{sat}}\right)^{2b_*+3} \tag{2.142}$$

The partition of the total precipitation between intercepted and effective components can be estimated on the basis of the following equation for canopy water storage, W_c [mm]:

$$\frac{\partial W_c}{\partial t} = P_r - E_{wc} \tag{2.143}$$

were P_r [mm s^{-1}] is the total rainfall and E_{wc} [mm s^{-1}] is the wet canopy evaporation, computed using the Eq. (2.117) setting $r_c = 0$.

This approach assumes that the irrigation is not intercepted by foliage, and the canopy have a maximum water holding capacity, $W_{c,max} = 0.2\text{LAI}$ (Crow *et al.*, 2008).

When W_c is below the threshold $W_{c,max}$, then P_e is equal to zero. In contrast, when W_c exceeds the value of $W_{c,max}$, then $P_e = P_r - E_{wc}$. Surface runoff is produced when Eqs. (2.138a) or (2.138b) estimate a soil water content value exceeding θ_{sat}.

Equations (2.138) highlight how the evapotranspiration terms directly influence soil water content dynamic both in the surface layer and the root zone. The next sub-sections (2.5.2 and 2.5.3) report how to introduce the effects of soil water dynamic within the energy fluxes modelling.

2.5.2 Evaporation from soil surface

Commonly, experimental observations highlight how the process of evaporation from the soil surface proceeds differently when the soil is wet and when it become drier. In the first stage a constant high rate occurs, followed in the second stage by a falling rate. Generally, the first stage is significant only when the atmospheric water demand is low.

In the past, a number of relationships were proposed to take into account the effects of the surface water content on the evaporation, by means of the resistance r_{ss} introduced in sub-section 2.3.3.

Camillo and Gurney (1986) suggest the following empirical relationship for r_{ss} modelling:

$$r_{ss} = a_{ss}(\theta_{sat} - \theta_1) - b_{ss} \tag{2.144}$$

where the parameters a_{ss} [s m^{-1}] and b_{ss} [s m^{-1}] were derived empirically by different authors by means of liner regression analysis of observed evaporation values. As examples, Cayrol *et al.* (2000) suggest value of 7000 and 1520 s m^{-1}, respectively, instead Saito *et al.* (2006) suggest values of 4140 and 805 s m^{-1}.

Another widely-adopted formulation, proposed by Sellers *et al.* (1992), is the following:

$$r_{ss} = \exp\left(A_{ss} - B_{ss}\frac{\theta_1}{\theta_{sat}}\right) \tag{2.145}$$

where the empirical parameters A_{ss} and B_{ss} are set equal to 8.2 and 4.3, respectively (Kustas *et al.*, 1998).

2.5.3 Transpiration water control

The interactions between water flow in the soil and plant transpiration are quite complex, due to the mutual effect of roots on the water re-distributions, and of water availability on plants uptake.

Generally, detailed modelling of how water moves from soil to roots, through the xylem, to the leaves and then it evaporates in the stomatal cavities of the leafs is not-useful in practical hydrological applications. Due to the analogies between water flow in the plant and electric circuits, Ohm's law is used to describe the water flow in the soil-plant-system.

Adopting this analogy, the idea of introducing the control acted by water availability on plant transpiration is then realised by means of the stomatal resistance, described in sub-section 2.3.3. The reduction of transpiration rate due to the limited water availability is known as *water stress*.

A widely-adopted approach for water control modelling is the following, firstly introduced by Jarvis (1976):

$$r_c = r_{c,\min} F_1 F_2^{-1} F_3^{-1} F_4^{-1} \tag{2.146}$$

where $r_{c,\min}$ [s m^{-1}] is the resistance value in absence of stress conditions, and the multiplicative coefficients F_1, F_2, F_3 and F_4 take into account the effects of photosynthetic activity, soil moisture, atmospheric water pressure deficit and air temperature on stomatal closure, respectively.

The minimum stomatal resistance can be computed adopting the formula suggested by Allen *et al.* (1989):

$$r_{c,\min} = \frac{r_l}{0.5\mathrm{LAI}_c} \tag{2.147}$$

where r_l [s m^{-1}] represents the single leaf stomatal resistance, and the coefficient 0.5 is used to take into account the leaf area that actively contribute to the transpiration process (Allen *et al.*, 1998).

As briefly introduced above, the Eq. (2.146) allows to take into account the stress effects related to different state variables (solar radiation, air temperature, atmospheric water pressure), not only to the soil moisture deficit.

If the soil water content is the only limiting factor, the coefficients F_1, F_3 and F_4 can be set equal to 1, and the stress conditions are computable by means of the parameter F_2, defined as (Thompson *et al.*, 1981):

$$F_2 = \begin{cases} 1 & \theta_2 > \theta_{cr} \\ \dfrac{\theta_2 - \theta_{wl}}{\theta_{cr} - \theta_{wl}} & \theta_{wl} \leq \theta_2 \leq \theta_{cr} \\ 0 & \theta_2 < \theta_{wl} \end{cases} \tag{2.148}$$

where θ_{cr} is the critical water content at which plant stress starts, parameterized as $0.75\theta_{sat}$.

If the other stress factors are not negligible, then it can be computed following the relationships proposed by Dickinson (1984) and Sellers (1986).

In particular, the coefficient F_1 can be modelled as (Dickinson, 1984):

$$F_1 = \frac{1+f}{f+\dfrac{r_{c,\min}}{r_{c,\max}}} \tag{2.149}$$

where:

$$f = 1.1\frac{R_s}{R_{sl}\mathrm{LAI}} \tag{2.150}$$

in which $r_{c,\max}$ is the maximum stomatal resistance typically set to 5000 s m^{-1} (Crow *et al.*, 2008), R_{sl} is a minimum solar radiation for the beginning of photosynthetic activity (30 W m^{-2} for a forest and 100 W m^{-2} for a crop).

The F_3 factor, which takes into account the atmospheric water pressure deficit, can be computed as (Sellers, 1986):

$$F_3 = 1 - 0.025(e_a^* - e_a) \tag{2.151}$$

Finally, the F_4 factor takes into account the effect of air temperature, and can be estimated as (Dickinson, 1984):

$$F_4 = 1 - 0.0016(298 - T_a)^2 \tag{2.152}$$

Detailed analyses on daily shape of the stomatal resistance, realised by means of *in-situ* measurements, highlight a diurnal behaviour also on the unstressed single leaf value (Fernàndez *et al.*, 1997). For this reason the value r_l in Eq. (2.147) can be fixed different during daytime and nighttime (for hourly applications), to partially take into account this behaviour (ASCE-EWRI, 2005).

Part II

Materials and Methods

Chapter 3

Micro-meteorological measurements

The observation of meteorological variables in a specific environment is fundamental to understand the connections between land-atmosphere system status and external forces, and it is known as micro-meteorology. Generally, the meteorological conditions of a site are well defined if known the main variables (e.g., air temperature and humidity, rainfall, solar radiation, wind velocity). However, the analysis of energy and water balance requires to observe how these factors combines to define the principal variables involved in the balance.

Following the format adopted in the previous chapter, a distinction between measurements of turbulent drive fluxes, radiative fluxes, and heat diffusion in the soil will be carried out.

3.1 Turbulent heat and water transfer

The intensity of the turbulence in the ABL is generally be quantified by means of the Turbulent Kinetic Energy (TKE). Assuming:

- horizontal homogeneity;
- stationary flow;
- negligible transport and pressure correlation terms;

- a coordinate system aligned with the mean horizontal wind direction (x);

the TKE budget equation reads (Stull, 1988):

$$\epsilon = -\overline{u'w'}\frac{\partial \overline{u}}{\partial z} + \frac{g}{\overline{\overline{T}}}\overline{w'T'} \tag{3.1}$$

where ϵ [m^2 s^{-3}] is the dissipation rate and the first and second terms on the right-hand side represent the mechanical TKE production, generated by wind shear, and the thermal production/destruction generated by the sensible heat flow, respectively.

The mechanical shear term is expressed by the product of the vertical gradient of the mean horizontal wind speed, $\frac{\partial \overline{u}}{\partial z}$ [s^{-1}], and of the covariance of horizontal (u' [m s^{-1}]) and vertical (w' [m s^{-1}]) wind speed fluctuations, $-\overline{u'w'}$ [m^2 s^{-2}].

The buoyancy term is defined by the product of $\frac{g}{\overline{\overline{T}}}$, where g is the standard gravitational acceleration (equal to 9.81 m s^{-2}) and $\overline{T}$ [K] is the average air (potential) temperature, and of the covariance between vertical wind speed fluctuations and air temperature fluctuation (T' [K]), $\overline{w'T'}$ [m s^{-1} K].

Analogously, it is possible to derive the budget equation for all the scalar variables in a turbulent medium. As example, on the basis of the same assumptions of Eq. (3.1), the budget equation for the air temperature can be expressed as (Stull, 1988):

$$\epsilon_T = -\overline{w'T'}\frac{\partial \overline{T}}{\partial z} \tag{3.2}$$

where ϵ_T [K^2 s^{-1}] represents the dissipation rate for the (potential) temperature, and $\frac{\partial \overline{T}}{\partial z}$ [K m^{-1}] is the vertical gradient of air temperature.

Instead, the budget equation for the air water vapour concentration reads (Stull, 1988):

$$\epsilon_q = -\overline{w'q'}\frac{\partial \overline{q}}{\partial z} \tag{3.3}$$

in which ϵ_q [m s^{-2}] represents the dissipation rate for specific water vapour concentration, $-\overline{w'q'}$ [m s^{-1} kg kg^{-1}] is the covariance of vertical wind

speed and water vapour (q' [kg kg^{-1}]) turbulent fluctuations, and $\frac{\partial \overline{q}}{\partial z}$ [kg kg^{-1} m^{-1}] is the vertical gradient of specific water vapour concentration.

The budget Eqs. (3.1) and (3.2) ca be also expressed in a non-dimensional form, introducing the dimensionless groups f_ϵ and f_T, as following:

$$f_\epsilon = \phi_m - \frac{\zeta}{L} \tag{3.4}$$

and

$$f_T = \frac{3}{k_v^{2/3}} - \frac{\phi_h}{f_\epsilon^{1/3}} \tag{3.5}$$

where $\phi_m = k_v \zeta / u_* \frac{\partial \overline{u}}{\partial z}$ and $\phi_h = k_v \zeta / T_* \frac{\partial \overline{T}}{\partial z}$ are the dimensionless factors introduced in sub-section 2.3 (Eqs. (2.97)). The term T_* [K] is the temperature scale (defined in the sub-section 3.1.2 via Eq. (3.19)).

The Eqs. (3.1)-(3.3) and the Eqs. (3.4) and (3.5) are the basis for eddy correlation and scintillometry energy fluxes measurements techniques, described in the following sub-sections.

3.1.1 Eddy correlation technique

As introduced in the section 2.3 the environmental variables involved in the sensible and latent heat fluxes are fundamentally the wind velocity, the air temperature and the water vapour concentration.

The main difference between wind and the other variables is that wind is a vector quantity, which requires 3 components for his definition. For convenience, the coordinate system is oriented with the x axis point the mean wind direction, the y axis orthogonally to the x one, on the same horizontal plane, and the z axis oriented vertically. The wind velocity components are then named u, v and w, where u is the component in the x direction, v in the y direction and w in the z direction.

As previously introduced, turbulent flow in the atmosphere consists of a number of eddies (of different size); focusing the attention on the eddies in a defined point of the ABL, the processes can be schematically represented as in Figure 3.1. This figure highlights how the turbulent transfer of a

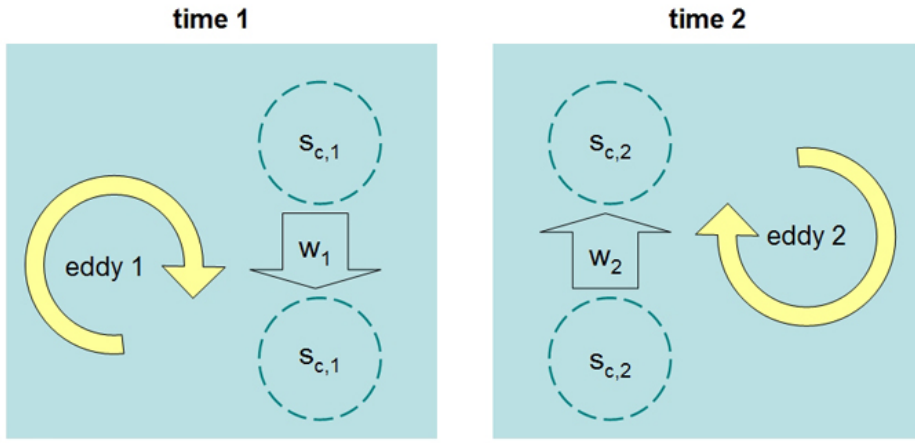

Figure 3.1: Schematic representation of transport process of any scalar by means of eddies. At one location, at time 1, eddy 1 moves air parcel down at the speed w_1. Then, at time 2, eddy 2 moves another parcel up at the speed w_2. Each parcel has a concentration of any scalar, s_c, at time 1 and 2 (redraw from Burba and Anderson, 2005).

scalar is related to the variation of wind speed and of the scalar itself at the same point in time.

For this reason, the observation of these 5 scalar quantities (3 wind components, air temperature and humidity) allows to infer the heat and water vapour fluxes in the ABL. In fact, the generic flux, on the basis of eddy correlation (EC) technique, can be computed as a covariance between instantaneous deviation in vertical wind speed (w') from the mean value ($\overline{w}$) and instantaneous deviation of the generic scalar ($s_c{}'$), from its mean value ($\overline{s_c}$), multiplied by mean air density.

This energy fluxes definition is based on the assumptions that: i) all the eddy (including the smaller and the bigger ones) are taken into account in turbulent fluctuation computation, ii) the Raynolds decomposition is applicable, iii) the air density fluctuations are negligible (Burba and Anderson, 2005).

The first assumption influences directly the measurements sampling frequency, that must be higher than 10 Hz, and the in-time averaging window which must be wide enough to observe the larger eddies. The application of Reynolds decomposition requires, instead, the removing of

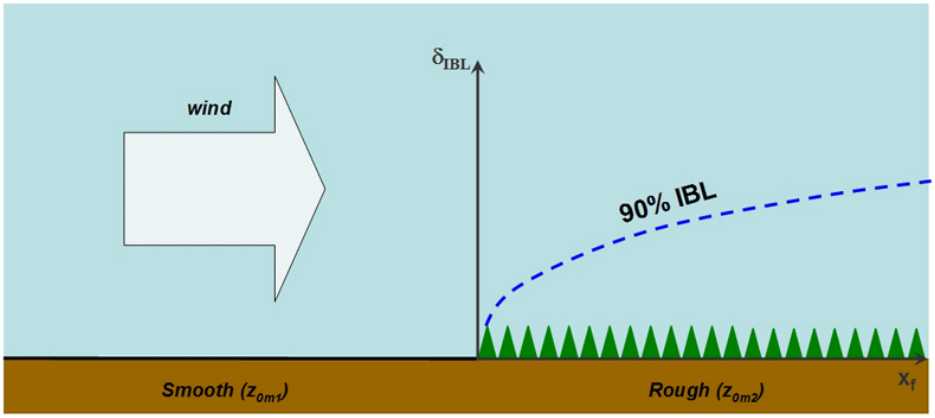

Figure 3.2: Scheme of the Internal Boundary Layer (IBL) development from smooth to rough surface: the IBL grows downstream depending on the magnitude of the modification.

low frequency trend, and that limits the amplitude of the average window.

Additionally, others two fundamental hypotheses of EC technique are the absence of advection (steady state conditions) and the negligibility of fluxes divergence/convergence. Both of these hypotheses are well verified for horizontal homogeneous terrains. Advection, in fact, is significantly only when spatial gradient in wind velocity exists. In steady state condition ($u = cost.$), when two adjacent surfaces are characterised by different roughness length, the wind vertical profile, in the passage from a surface to another, requires a development of a new Internal Boundary Layer (IBL), in equilibrium with the new surface condition (Figure 3.2).

As reported by Kaimal and Finnigan (1994), a relationship developed to model the IBL growth, as a function of the roughness length of the two surfaces and the upwind distance, is the one proposed by Elliott (1958):

$$\frac{\delta_{\mathrm{IBL}}}{z_{0m2}} = 0.75 + 0.03 \ln\left(\frac{z_{0m1}}{z_{0m2}}\right)\left(\frac{x_f}{z_{0m2}}\right)^{0.8} \tag{3.6}$$

where δ_{IBL} [m] is the IBL elevation at the upwind distance x_f [m], z_{0m1} and z_{0m2} are the roughness length for momentum transfer of the two surfaces (see Figure 3.2).

To ensure that the surface in upwind distance is homogeneous enough to establish a full developed IBL, a number of simple criteria on minimum fetch distance were proposed, as the one suggested by Gash (1986):

$$x_{f90} = \frac{\zeta\left[\ln\left(\frac{\zeta}{z_{0m}}\right) - 1 + \frac{\zeta}{z_{0m}}\right]}{k_v^2 \ln\big(0.90\big)} \tag{3.7}$$

in which x_{f90} [m] is the upwind distance (under neutral stability conditions) required to obtain the adjustment of 90% of the IBL.

For moderate rough surfaces (as typical agricultural field) and classical EC installation height, Eq. (3.7) drives to the well-known practical expression: $x_{f90} = 100\zeta$ (Leclerc and Thurtell, 1990; Paço *et al.*, 2006).

On the basis of these preliminary considerations and assuming all the described hypotheses, the momentum, sensible heat and latent heat fluxes can be measured by means of the following relationships:

$$u_* = \sqrt{-\sigma_{uw}} \tag{3.8a}$$

$$H = \rho c_p \sigma_{wT} \tag{3.8b}$$

$$\lambda ET = \lambda \rho \sigma_{wq} \tag{3.8c}$$

where σ_{uw} [m^2 s^{-2}] is the covariance between horizontal and vertical wind velocities, σ_{wT} [m s^{-1} K] is the covariance between vertical wind speed and temperature and σ_{wq} [m s^{-1}] is the covariance between vertical wind speed and water vapour concentration.

In order to compute the covariances in Eqs. (3.8), the following corrections to the raw data are applied:

- linear de-trending;
- coordinate system rotation;
- correction for spectral loss;

The **linear de-trending** aims to remove the low frequency trends in the data, as required by the steady state hypothesis. Commonly, the data de-trending is realised by using linear departures from a short term

(running) mean (Moncrieff *et al.*, 2004), computed recursively as (taking as example the u wind component):

$$\overline{u}_i = \left[1 - \exp(-\Delta t_u/\tau_u)\right] u_i + \left[\exp(-\Delta t_u/\tau_u)\right] \overline{u}_{i-1} \tag{3.9}$$

where Δt_u is the sampling interval and τ_u is the time constant.

The **coordinate rotation** transforms are applied to the average wind components obtained from the running means in order to generate a null vertical and lateral mean wind speeds (Finnigan *et al.*, 2003). A first rotation of the z axis is realized in order to remove the v component equal to 0, a second rotation around the y axis aims to remove the w component of wind velocity, finally, a third and last rotation of the new x axis make equal to 0 the covariance between v and w. The results of these rotations are the average rotated wind velocity components:

$$\langle \overline{u} \rangle = \overline{u} \cos\theta_r \cos\phi_r + \overline{v} \sin\theta_r \cos\phi_r + \overline{w} \sin\phi_r \tag{3.10a}$$

$$\begin{aligned} \langle \overline{v} \rangle = {} & \overline{v} \cos\theta_r \cos\psi_r - \overline{u} \sin\theta_r \cos\psi_r \\ & + \overline{w} \cos\phi_r \sin\psi_r - \overline{u} \sin\phi_r \sin\psi_r \end{aligned} \tag{3.10b}$$

$$\begin{aligned} \langle \overline{w} \rangle = {} & \overline{w} \cos\phi_r \cos\psi_r - \overline{u} \cos\theta_r \sin\phi_r \cos\psi_r \\ & - \overline{v} \sin\theta_r \sin\phi_r \cos\psi_r + \overline{u} \sin\theta_r \sin\psi_r \\ & - \overline{v} \cos\theta_r \sin\psi_r \end{aligned} \tag{3.10c}$$

where the rotations θ_r and ϕ_r are defined as:

$$\theta_r = \arctan \frac{\overline{v}}{\overline{u}} \tag{3.11a}$$

$$\phi_r = \arctan \frac{\overline{w}}{\overline{u} \cos\theta + \overline{v} \sin\theta} \tag{3.11b}$$

and the rotation ψ_r is defined as halftime the arctangent of the ratio between vw covariance and its square difference before the final rotation.

Analogously, is possible to define the rotated variances of the wind speed components and the rotated covariances, not reported for concision.

The correction for **spectral loss** attempts to correct the measured data from the influences of the measurement system itself, and from the imperfect responding of the sampling system (Moncrieff *et al.*, 1997).

Additionally, in order to compute the latent heat flux using the Eq. (3.8c), the Webb-Pearman-Leuning correction is performed on the water vapour for the density effects (Webb *et al.*, 1980).

The computation of sensible heat flux by means of Eq. (3.8b) requires high frequency measurements of air temperature (such the ones performed by a platinum resistance wire). These measurements can be, in alternative, replaced by a temperature retrieved from anemometer data, called sonic temperature, T_{son} [K], defined as (Moncrieff *et al.*, 1997):

$$T_{son} = \frac{c_s^2}{403} = T_a\left(1 + 0.32\frac{e_a}{P_a}\right) \tag{3.12}$$

where c_s [m s^{-1}] is the speed of sound in air.

According to Stull (1988) T_{son} is close to the potential temperature, and then T_{son} is an adequate surrogate of T_a in most conditions. However, when vapour pressures are high, Webb-Pearman-Leuning corrections should be applied (Moncrieff *et al.*, 1997). At high wind speeds there are additional errors owing to wind speed and momentum stress, which need to be considered (Liu and Peters, 2001; Schotanus *et al.*, 1983).

On the basis of these corrections H can be computed directly from three-dimensional wind velocity measurements as:

$$H = \rho c_p(\sigma_{wT_{son}} - 0.000321\sigma_{wq}\overline{T}_{son}) \tag{3.13}$$

Finally, in order to remove the lower quality data, a despiking procedure can be applied to the average fluxes data, as the one suggested by Vickers and Mahrt (1997).

3.1.2 Scintillometry technique

While the eddy correlation technique is a sort of ‟direct″ measurements of the turbulence, a number of more indirect micro-meteorological techniques were developed to observe ABL turbulent fluxes.

An interesting alternative, which had in the last decade a strong *renaissance* (de Bruin, 2002), is the scintillometry, mainly due to the capability to observe source areas bigger than EC system, and then more useful for remotely sensed data validation.

The scintillometry technique is based on the detection of the light intensity fluctuations caused by fluctuations of the refractive index of air. These fluctuations, known as *scintillations*, are indicators of the ‟turbulent

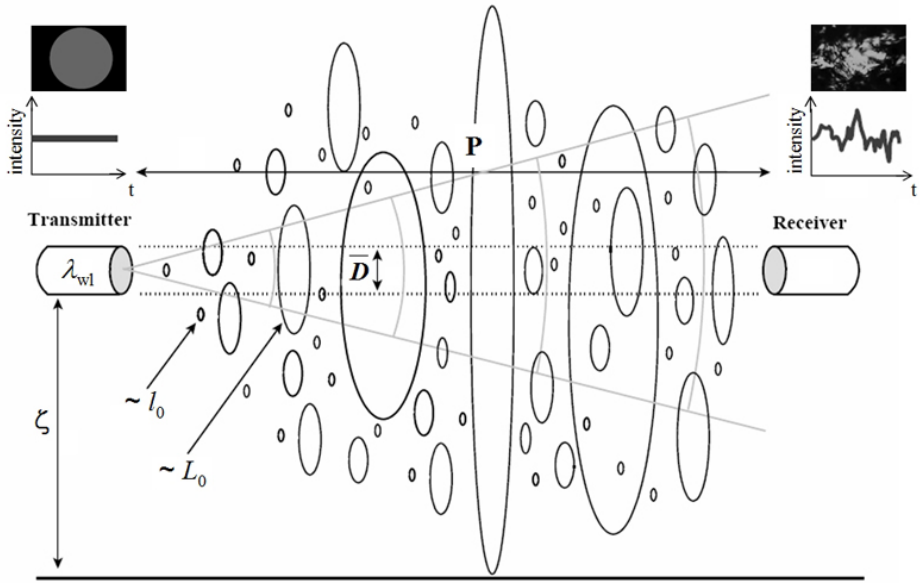

Figure 3.3: Schematic drawing of an electromagnetic radiation transfer in the scintillometer path. The energy emitted by the transmitter (constant intensity at the wavelength λ_{wl}) is scattered by eddies in the atmosphere and then acquired by the receiver at the distance P (fluctuations of the beam intensity) (redraw from Meijninger, 2003).

strength″of the atmosphere, and then, of the ability of the atmosphere to transport sensible heat and water vapour.

Generally, a scintillometer is constituted by a transmitter and a receiver: the transmitter is an electromagnetic radiation emitter, with an aperture diameter, $\overline{D}$ [m], the receiver measures the intensity fluctuations in the signal, caused by diffractive scattering by turbulent eddies in the propagation path, P [m] (see Figure 3.3).

The dissipation process of turbulent kinetic energy can be represented by means of the energy spectrum. Similarly, it is possible to define the three-dimensional spectrum of refractive index fluctuations, ϕ_n, schematically depicted in Figure 3.4 as a function of the wave number ($K = 2\pi/\lambda_{wl}$).

From this scheme it is possible to distinguish three regions of the spectrum:

- the *production* region, including the eddies greater than the outer

scale, L_0 ($\approx 10^1$ m), where the energy is introduced in the turbulent spectrum. In this region the turbulence is not isotropic and not homogeneous;

- the *inertial range*, the part of the spectrum included between the outer scale and the inner scale, l_0 ($\approx 10^{-3}$ m). This part of the spectrum is not dependent on the energy input and on the dissipation, then only energy transfer is relevant (energy cascade);

- the *dissipation* region, the part of the spectrum, characterized by eddies smaller than l_0, where the viscous dissipation become significant.

Modelling of ϕ_n in the inertial range and in the dissipation region was realized by Tatarskii (1961) and Hill and Clifford (1978), respectively, by means of the following formulations:

$$\phi_n = 0.033 C_n^2 K^{-11/3} \qquad 2\pi/L_0 < K < 2\pi/l_0 \tag{3.14a}$$

$$\phi_n = 0.033 C_n^2 K^{-11/3} f_B(K l_0) \qquad K > 2\pi/l_0 \tag{3.14b}$$

where C_n^2 [$\mathrm{m}^{-2/3}$] is the structure parameter of the refractive index of air, and the function $f_B(K l_0)$ [m^{-4}] is used to model the so-called *Hill bump* in the dissipation range.

The Eqs. (3.14a) and (3.14b) highlight how the fluctuations of the refractive index of air are a function of only C_n^2 in the inertial range, and of both C_n^2 and l_0 in the dissipation region.

According to the wave propagation theory in a random media, the interactions between turbulent eddies and electromagnetic wave are different in function of the relationship between eddies size and the first Fresnel zone ($F = \sqrt{\lambda_{\mathrm{wl}} P}$, [m]) . Statistical solution of this equation allows to find a connection between scintillometer measured signal and C_n^2 and l_0 variables.

Depending on the wavelength of the emitted electromagnetic radiation and the typical path distance, the scintillometers differ in the theoretical assumptions adopted to resolve the wave propagation theory.

In Table 3.1 the main characteristics of scintillometers are reported for: SAS (Small Aperture Scintillometer), LAS (Large Aperture Scintillometer),

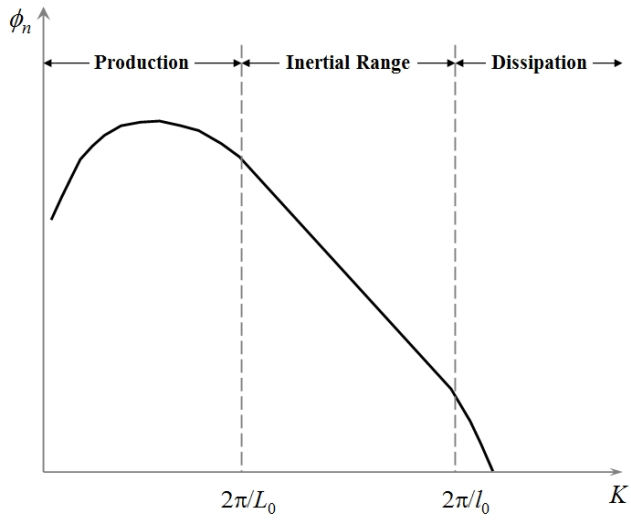

Figure 3.4: Schematic representation of the three-dimensional spectrum of refractive index fluctuations.

XLAS (eXtra Large Aperture Scintillometer) and RWS (Radio Wave Scintillometer).

The analyses of this chapter refer always to the SAS. For this type of scintillometer, as reported in Table 3.1, the most effective eddy have the same dimension of the inner scale, then the signal fluctuations are related to both C_n^2 and l_0. For this reason, the emitted radiation of a SAS is generally a laser coherent source, split in two beams of orthogonal polarisations. The variance of the single beam, named B_{11} and B_{22} [$\mathrm{m}^{-11/3}$], respectively, and the covariance of the two amplitudes, B_{12} [$\mathrm{m}^{-11/3}$], can be expressed as:

$$B_{12} = 0.124 C_n^2 K^{7/6} P^{11/6} f_B\left(\frac{l_0}{F}, \frac{d}{F}, \frac{\overline{D}}{F}\right) \tag{3.15}$$

where the function f_B describes the decrease of B_{12} in the dissipation range with increasing of l_0, $\overline{D}$ and d (separation between the two laser beams, $\approx$ 2.7 mm).

In order to retrieve the single channel variances (B_{11} or B_{22}) using the Eq. (3.15), the term d must be set equal to zero.

Due to the dependence of refractive index of air in the dissipation range

Table 3.1: Overview of different scintillometer types: the Small Aperture Scintillometer (SAS), the Large Aperture Scintillometer (LAS), the eXtra Large Aperture Scintillometer (XLAS) and the Radio Wave Scintillometer (RWS) (redraw from Meijninger, 2003).

Type	λ_{wl} [nm]	P [km]	$\overline{D}$ [m]	F [m]	Most effective eddy
SAS	670	0.02–0.25	0.002	≈ 0.01	$\approx F$
LAS	930	0.25–5	0.15	≈ 0.05	$\approx \overline{D}$
XLAS	930	1–10	0.32	≈ 0.08	$\approx \overline{D}$
RWS	11000	1–10	0.60	≈ 5	$\approx F$

to C_n^2 and l_0, the simultaneous measurements of the fluctuations of two different beams allow the determination of the terms C_n^2 and l_0 using the set of Eqs. (3.15). In particular, the estimation of l_0 and C_n^2 from the raw SAS observations is performed following the approach introduced by Thiermann (1992): the correlation coefficient $R_{12} = B_{12}/(B_{11}B_{22})^{1/2}$ is a function of normalized l_0 only (fixed d and D), then the inner scale is directly computed from the simultaneous measurements of the fluctuations of two different beams. When l_0 is known, B_{11} (or B_{22}) allows the determination of C_n^2 using Eq. (3.15).

Following Hill *et al.* (1980), the C_n^2 can be related to three terms: structure parameters of the temperature, C_T^2 [K^2 m$^{-2/3}$], humidity, C_q^2 [m$^{-2/3}$], and covariance term, C_{Tq} [K m$^{-2/3}$], using the relationship:

$$C_n^2 = \left(\frac{A_T^2}{T_a^2}\right)C_T^2 + \left(\frac{A_T A_q}{T_a q_a}\right)C_{Tq}^2 + \left(\frac{A_q^2}{q_a^2}\right)C_q^2 \tag{3.16}$$

where A_T and A_q are two parameters that take into account the relative contribution of temperature and humidity to the observed C_n^2 value.

Generally, for the adopted wavelength, the term that contain C_T^2 is prevalent to the others, then the temperature structure parameter can be derived from C_n^2 simply by:

$$C_T^2 = C_n^2\left(\frac{T_a^2}{P_a c_\lambda}\right)^2\left(1 + \frac{0.03}{\beta}\right)^{-2} \tag{3.17}$$

where c_λ is the refractive index coefficient for air at 670 nm, equal to 7.89 $\times$ 10^{-5} K hPa^{-1}.

In the Eq. (3.17) the humidity correction term, proposed by Wesely (1976), can be assumed equal to 1 when the Bowen ratio is not far away from the unity.

The inner scale can be used to assess the dissipation rate of TKE (introduced in Eq. (3.1)), by means of the relationship proposed by Frehlich (1992):

$$\epsilon = \nu^3 \left(\frac{7.4}{l_0} \right)^4 \tag{3.18}$$

where ν [m^2 s^{-1}] is the air kinematic viscosity, and the constant 7.4 was derived by Hill (1997).

Using the MOST it is possible to connect ϵ and C_T^2 with u_* and temperature scale, T_* [K]:

$$T_* = -\frac{H}{\rho c_p u_*} \tag{3.19}$$

respectively, by means of the dimensionless analysis.

In particular, using the turbulence theory it is possible to define the following non-dimensional groups:

$$\frac{k_v \zeta \epsilon}{u_*^3} = f_\epsilon \left(\frac{\zeta}{L} \right) \tag{3.20}$$

$$\frac{C_T^2 \zeta^{2/3}}{T_*^2} = f_T \left(\frac{\zeta}{L} \right) \tag{3.21}$$

where the universal functions f_ϵ and f_T, determined experimentally, differ for stable and unstable conditions. Unfortunately, nowadays there is no unanimity between their final mathematical forms found by different authors (see as example the review of Savage, 2008).

One of the wider used approach, adopted also by the Scintec AG acquisition and processing software (Scintec, 2006), is the one proposed by Thiermann and Grassl (1992). These authors suggest the following

formulations:

$$f_\epsilon\left(\frac{\zeta}{L}\right) = \left(1 - 3\frac{\zeta}{L}\right)^{-1} - \frac{\zeta}{L} \tag{3.22a}$$

$$f_T\left(\frac{\zeta}{L}\right) = 4\beta_1\left[1 - 7\frac{\zeta}{L} + 75\left(\frac{\zeta}{L}\right)^2\right]^{-1/3} \tag{3.22b}$$

when $L < 0$, and

$$f_\epsilon\left(\frac{\zeta}{L}\right) = \left[1 + 4\frac{\zeta}{L} + 16\left(\frac{\zeta}{L}\right)^2\right]^{-1/2} \tag{3.23a}$$

$$f_T\left(\frac{\zeta}{L}\right) = 4\beta_1\left[1 + 7\frac{\zeta}{L} + 20\left(\frac{\zeta}{L}\right)^2\right]^{1/3} \tag{3.23b}$$

valid when $L > 0$. The parameter β_1 is Obukhov-Corrsin constant, equal to 0.86.

Once computed the variables T_* and u_* it is possible to derive the sensible heat flux as:

$$H = -\rho c_p T_* u_* \tag{3.24}$$

The solution of the system of Eqs. (3.24) and (3.22)-(3.23), requires an iterative procedure that drives to the correct estimation of sensible heat flux for both stable and unstable conditions.

Unfortunately, the SAS does not allow to infer directly the latent heat flux, due to the negligible effect of the air humidity fluctuations on the beams in the red wavelength. For this reason, additional measurements of net radiation and soil heat flux are required for latent heat flux estimation as residual term of the energy balance Eq. (2.2).

As reported in many papers (e.g., Foken, 2006), the use of similarity theory is limited by the validity only in the inertial sub-layer (constant flux layer) above the roughness sub-layer (see sub-section 2.3 for the sub-layers definition).

Generally, for small dense canopies the thickness of RS-L is negligible if compared to the IS height; however, in the case of tall vegetation a number of different criteria have been proposed to determine the z^* height (see the

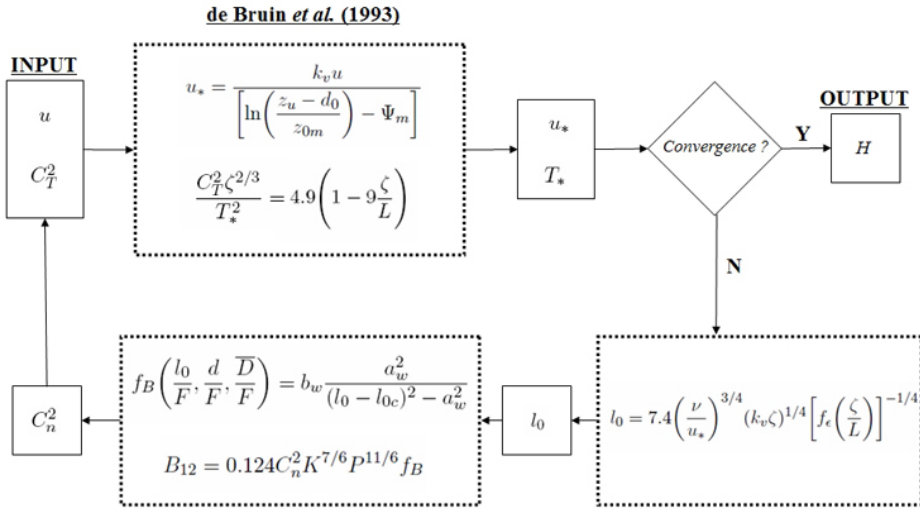

Figure 3.5: Flow-chart describing the iterative procedure for SAS sensible heat flux estimation.

extensive review of de Ridder (2010)). As example, Garratt (1978) and Garratt (1980) suggested the following formulations:

$$z^* = 3s_{\text{row}} \tag{3.25a}$$

$$z^* = 4.5h_c \tag{3.25b}$$

where the roughness sub-layer height is scaled using the horizontal inhomogeneity (expressed by means of row spacing or canopy height).

When the instrument height is lower than z^*, an alternative approach can be adopted, following the flow-chart described in Figure 3.5. The description of this methodology is focused on the daytime (unstable) conditions, due to the preponderant contribute to the evapotranspiration fluxes.

As described in Figure 3.5 a first-guess estimation of u_* and T_* is obtained on the basis the approach proposed by de Bruin *et al.* (1993). This approach adopts the following formulation for T_* computation (when $L < 0$):

$$f_T\left(\frac{\zeta}{L}\right) = 4.9\left(1 - 9\frac{\zeta}{L}\right) \tag{3.26}$$

derived from the expression suggested by Wyngaard *et al.* (1971).

The friction velocity can be assessed using an additional standard wind speed measurements above the canopy, by means of the MOST vertical wind profile definition (see Eq. (2.111)).

The first guess estimation of the friction velocity allow to retrieve l_0, by means of a combination of the Eqs. (3.18) and (3.20):

$$l_0 = 7.4\left(\frac{\nu}{u_*}\right)^{3/4}(k_v\zeta)^{1/4}\left[f_\epsilon\left(\frac{\zeta}{L}\right)\right]^{-1/4} \tag{3.27}$$

This new value of l_0 is used to retrieve a new estimation of C_n^2 on the basis of an empirical fitting law of the f_B function (see Eq. (3.15)):

$$f_B\left(\frac{l_0}{F}, \frac{d}{F}, \frac{\overline{D}}{F}\right) = b_w \frac{a_w^2}{(l_0 - l_{0c})^2 - a_w^2} \tag{3.28}$$

where a_w [m^2], b_w [m^{-4}] and l_{0c} [m] are fitting parameters, function of the installation configuration (e.g., path length). The use of a simple empirical fit is suggested only by computational convenience and implies no theoretical foundation.

The new value of C_n^2 derived from single beam amplitude (B_{11} or B_{22}) allows to restart the described procedure, continuing with an iterative procedure since the convergence in L (and then H) is reached.

The use of this approach introduces an independent estimation of u_* starting from a simple measurements of horizontal wind speed, allowing to disregard the link between l_0 and R_{12}. Additionally, the locally-fitted law of f_B allows to take into account the dependence of SAS B_{11} (B_{22}) signal from both l_0 and C_n^2 in the dissipation range of the spectrum, differently from LAS for which C_n^2 can be derived directly from B_{11} (B_{22}) without the knowledge of l_0.

3.1.3 Source area and footprint function detection

As a consequence of the turbulent nature of the micro-meteorological measurement of scalar fluxes in the atmosphere, a fundamental issue is the definition of the relationship between the measurements realized at a certain location and the area which generate these fluxes.

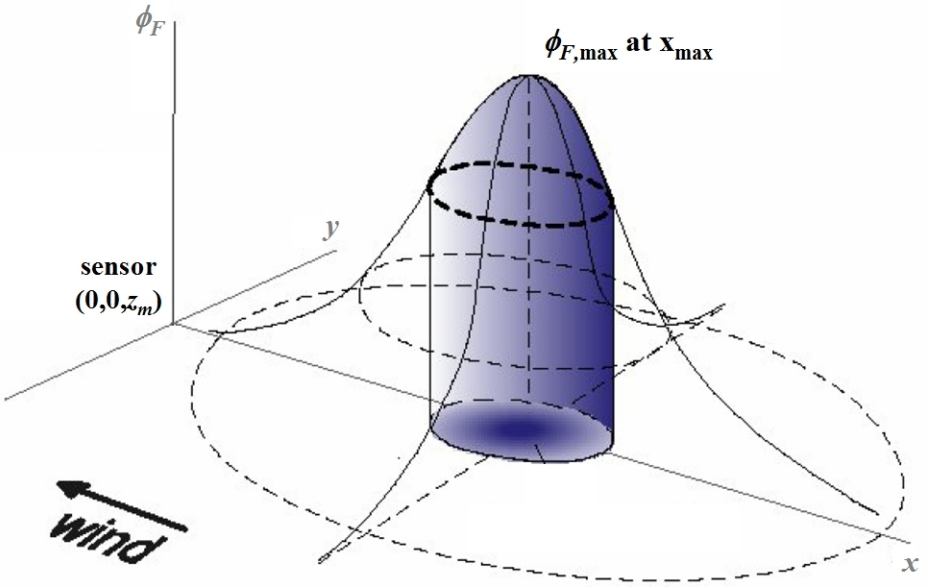

Figure 3.6: Schematic representation of the footprint function. The source weight is small for small separation distances. It rises to a maximum with increasing distance and then falls off again to all sides as the separation is further increased (redraw from Schmid, 1994).

In the last fifteen years, boundary-layer meteorologists have introduced the concept of *footprint* function to describe the source area of turbulent fluxes (Kormann and Meixner, 2001).

In literature two different approaches were suggested to estimate the footprint:

- the formulations based on the solution of advection-diffusion equation;
- the modelling based on the Lagrangian approach.

For practical applications the attention was generally focused on analytical solution of the two-dimensional advection-diffusion equation, despite these approaches are valid only under the hypotheses of horizontal homogeneity and stationarity, and neglecting the in-canopy flow characteristics (Göckede *et al.*, 2005).

On the basis of these assumptions, the vertical turbulent flux, $F_l(0, 0, z_m)$, measured at an height $z = z_m > 0$ in correspondence of the origin of the

coordinate system is related to the surface flux upwind of the measurement point, $F_l(x, y, 0)$, by (Schuepp *et al.*, 1990):

$$F_l(0, 0, z_m) = \int_{-\infty}^{\infty} \int_{0}^{\infty} F_l(x, y, 0)\phi_F(x, y, z_m)\mathrm{d}x\mathrm{d}y \tag{3.29}$$

where ϕ_F [m^{-2}] is the footprint function. This function describes the flux portion seen at $(0, 0, z)$ which is caused by a unit point source at the location $(x, y, 0)$. On the basis of this definition, ϕ_F has the role of weighting function of the surface originated fluxes; for this reason the integration of ϕ_F returns a unitary value. Definition of the adopted coordinate system is reported in Figure 3.6, with the schematic representation of ϕ_F function.

Footprint function for eddy correlation systems

Following the footprint generic definition, the approach proposed by Kormann and Meixner (2001) is now discussed. This methodology assumes:

1. stationary conditions;
2. horizontally homogeneous turbulent flow;
3. homogeneous and isotropic terrain at $z = 0$;
4. power-law for the vertical profile of horizontal wind speed and eddy diffusivity;
5. analytical approximation of vertical profiles with power-law functions.

The footprint, per unit point source, is described as a gradient diffusion process:

$$\phi_F(x, y, z) = -K(z)\frac{\partial \gamma_c}{\partial z} \tag{3.30}$$

where $K(z)$ [$\mathrm{m}^2\ \mathrm{s}^{-1}$] is the eddy diffusivity profile and γ_c [$\mathrm{s}\ \mathrm{m}^{-3}$] is the downwind ($x > 0$) concentration distribution of a unit point source.

Equation (3.30) can be integrated over the crosswind direction (y), obtaining the crosswind integrated flux footprint (or vertical flux per unit point source), $f_F(x, z)$ [m^{-1}].

The footprint function can be expressed as:

$$\phi_F(x, y, z) = D_y f_F(x, z) \tag{3.31}$$

where D_y [m^{-1}] is the crosswind distribution function.

Assuming a Gaussian distribution across the crosswind direction, D_y can be expressed by (Pasquill, 1974):

$$D_y = \frac{1}{\sqrt{2\pi}\sigma_y} \exp\left(-\frac{y^2}{2\sigma_y^2}\right) \tag{3.32}$$

where the dispersion σ_y [m] is commonly assumed to depend on atmospheric stability and downwind distance as (Pasquill, 1974; Schmid, 1994) $\sigma_y = \sigma_v x/u$, with σ_v [m s^{-1}] being the constant crosswind fluctuation.

Assuming a power-law for the vertical profiles of horizontal wind speed and eddy diffusivity:

$$u(z) = u_z z_z^m \tag{3.33a}$$
$$K(z) = k_z z_z^n \tag{3.33b}$$

the $f_F(x, z)$ function can be expressed, using the continuity equation (see Kormann and Meixner (2001) for more details), as:

$$f_F(x, z) = \frac{1}{\gamma(\mu)} \frac{\xi_z^\mu}{x^{1+\mu}} \exp(-\xi_z/x) \tag{3.34}$$

where $\gamma(\cdot)$ is the Gamma function of argument $(\cdot)$, μ is a constant defined as $\mu = (1 + m_z)/h$, with the shape factor $h = 2 + m_z - n_z$, and ξ_z [m] is the flux length scale defined as:

$$\xi_z = \frac{u z^h}{h^2 k} \tag{3.35}$$

The Eq. (3.34) include the well-known footprint model of Schuepp *et al.* (1990) when the exponents of power-law are assumed $m_z = 0$ and $n_z = 0$, respectively.

The wind velocity and eddy diffusivity power-law constants (u_z, m_z, k_z and n_z) are determined by means of MOST following the analytical approach suggested by Huang (1979).

In particular, the exponents m_z and n_z can be expressed by:

$$m_z = \begin{cases} \dfrac{u_*}{k_v u}\left(1 + 5\dfrac{\zeta}{L}\right) & L > 0 \\ \dfrac{u_*}{k_v u}\left(1 - 16\dfrac{\zeta}{L}\right)^{-1/4} & L < 0 \end{cases} \tag{3.36}$$

and

$$n_z = \begin{cases} \dfrac{1}{1 + 5\dfrac{\zeta}{L}} & L > 0 \\ \dfrac{1 - 24\dfrac{\zeta}{L}}{1 - 16\dfrac{\zeta}{L}} & L < 0 \end{cases} \tag{3.37}$$

Instead, the constants u_z [s^{-1}] and k_z [$\mathrm{m\ s}^{-1}$] can be determined by the inversion of Eqs. (3.33), with $u(z)$ computed using the Eq. (2.111), and $K(z)$ following the relationships:

$$K(z) = \begin{cases} \dfrac{k_v u_*}{\dfrac{\zeta}{L}} \dfrac{1}{1 + 5\dfrac{\zeta}{L}} & L > 0 \\ \dfrac{k_v u_*}{\dfrac{\zeta}{L}} \dfrac{1}{\left(1 - 16\dfrac{\zeta}{L}\right)^{-1/2}} & L < 0 \end{cases} \tag{3.38}$$

with ζ computed for $z = z_m$.

Finally, the the maximum values of the footprint function, $\phi_{F,\max}$ [m^{-2}], and its spatial location, $x_{\max}$ [m], are reported:

$$\phi_{F,\max} = \frac{(1+\mu)^{1+\mu}}{\Gamma(\mu)\xi_z} \exp(-1-\mu) \tag{3.39}$$

and

$$x_{\max} = \frac{\xi_z}{1+\mu} \tag{3.40}$$

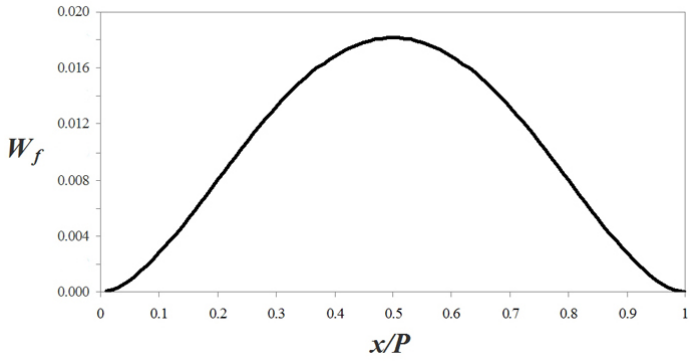

Figure 3.7: Normalized path weighting function for scintillometer footprint computation.

Even though its simplifications, this analytical approach allows to detect the main characteristics of the source area for measurements collected in one point.

Footprint function for scintillometer systems

The peculiarities of a scintillometer measurements requires a footprint model that takes into account the differences from point source techniques as the EC one. The adopted approach considers a spatial integration of single point footprints (computed as described in the previous sub-section for EC systems) by means of the weighting function suggested by Göckede *et al.* (2005):

$$W_f(x) = x^{11/6}(P-x)^{11/6}\Big[\sum_{x=0}^{P}\big(x^{11/6}(P-x)^{11/6}\big)\Big]^{-1} \tag{3.41}$$

This technique requires a discretization of the path length in a finite number of elements, then one footprint is computed for each single segment. The final foortprint is obtained by averaging the single footprint and assuming for each one the corresponding weighting factor computed by means of Eq. (3.41).

This approach allows to consider that the centre part of the path has the highest influence on the scintillometer measurements (Figure 3.7).

Finally, the addition of all individual normalised source areas along the scintillometer path yield to the source area for a linear measurement.

It is interesting to highlight how both the total size and the shape of the source area for scintillometer measurements are highly dependent on the relationship between wind direction and path orientation, as already demonstrated by Meijninger *et al.* (2002).

3.2 Other energy fluxes measurement

As reported in the previous sub-section, scintillometry technique allows to ˜measure″only the sensible heat flux, requiring additionally measurements of net radiation and soil heat flux for latent heat flux retrieval. Also for the eddy correlation technique the availability of additional information on energy budget terms permits to evaluate the quality of the turbulence measurements and the reliability of balance closure (see sub-section 3.3).

Moreover, net radiation measurements are essential for many applications, e.g., albedo retrieval (Betts and Ball, 1997). Analogously, soil heat flux measurements are fundamental, for example, in thermal inertia applications for soil water content assessment (Murray and Verhoef, 2007a,b).

3.2.1 Net radiation measurements

Net radiation measurements can be directly performed by using a *net-radiometer*, or separately measuring its components using *pyranometer*, for short-wave radiation, and *pyrgeometer*, for long-wave radiation (Figure 3.8).

The *net-radiometer* (Figure 3.8, left panel) is used to measure the net radiative flux in the wavelength range 0.3 to 40 μm. The net radiation flux is computed as the difference between the radiative power received from (or emitted to) the upper hemisphere and the radiative power received from (or emitted to) the lower hemisphere, where both refer to the same horizontal plane.

The operation principle of the instrument is based on the measurement of the difference between the case temperature and the temperature of two horizontal sensor planes, one looking upwards and one looking downwards.

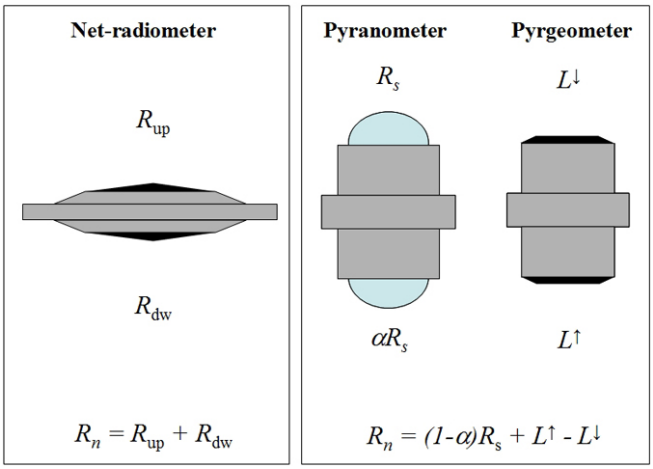

Figure 3.8: Schematic representation of instruments for net radiation measurements and main measured variables. On the left panel a net-radiometer, on the right panel a pyranometer and a pyrgeometer.

The case temperature is sensed separately by means of Pt-100 resistance thermometer or similar.

Despite this instrument provides a simple way to measure R_n, its operational principle do not allow to infer separately on the net radiation short-wave and long-wave components.

When detailed information of radiative balance are required, the joint use of a pyranometer and pyrgeometer represents an adequate tool (Figure 3.8, right panel). The coupled use of these two instruments is commonly known as 4-component net radiometer.

Pyranometer easily provides short-wave radiation measurements adopting calibration to international standards or solar cells. In particular, the instrument generates a electrical signal, converted in radiation by means of a calibration constant. Generally this instrument is a blackened thermopile devices equally sensitive across the solar spectrum (0.3–2.5 μm). Some silicon photodetector sensors are sensitive in a limited part of the spectrum only (0.4–1.1 μm), but are calibrated to give accurate readings in a wide range of light conditions.

Ideally, solar radiation measurement requires that the sensor response varies with the cosine of the angle of incidence. For this reason the

pyranometer should have a so-called "cosine response" that is close to the ideal cosine characteristic. Generally the instrument is covered by a glass or quartz dome, which improves directional response and provides both a protection function (from convection) and a filtering of radiation outside the measurement range.

Incoming and outgoing radiations are measured placing the instrument facing -up or -down, respectively. Instruments which provide contemporary upward and downward measurements are named albedometers, due to the capability to infer the albedo as a ratio between downward and upward observations.

Similar to pyranometer, the *pyrgeometer* measures the long-wave components of the net radiation (4–40 μm) by means of a thermistor and a resistance temperature detector built-in for case temperature compensating. In fact, the measured signal represents the energy exchange (in the thermal infrared) between the case of the instrument and the surface that it is facing. In order to obtain a measurements of energy flux a correction for case temperature is needed.

The filtering of solar radiation is generally realized by means of a silicon dome with a solar blind filter coating.

If a double pyrgeometer (one facing up and one facing down) is used for net log-wave radiation computation, the correction of the upward and downward fluxes are not needed, because the two correction terms nullify each other.

The joint use of pyrgeometer and suitable surface temperature measurement allow the estimation of surface emissivity, by inversion of the StefanBoltzmann law.

3.2.2 Soil heat flux measurements

Commonly, soil heat flux measurements are carried out by means of flux plate; this sensor is constituted by a flat plate sensitive to the flow in the direction perpendicular to the sensor surface (Figure 3.9). A thermopile (i.e., a number of thermocouples connected in series) is used, generating a voltage that is proportional to the temperature difference between the joints. This temperature difference is proportional to heat flux, depending only on the thickness and the thermal conductivity of the sensor and surrounding medium. Generally, the thermopile is embedded in a filling

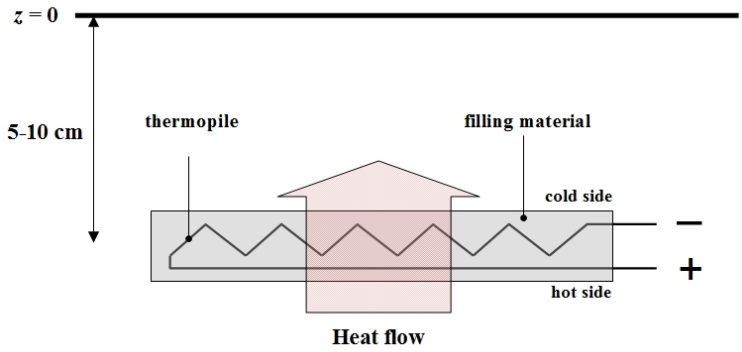

Figure 3.9: Schematic representation of soil heat flux plate (redraw from Hukseflux, 2000).

material (usually a plastic).

In practical applications of measuring soil heat flux, conventional heat flux sensors are not very reliable, this because the soil thermal parameters changes with soil water content. For this reason, the more recent instruments are based on the *self-calibration* procedure.

Adopting this approach the sensor generates a known heat flux, and the output signal is registered. If the output deviates from the predicted value the thermal properties of the sensor and the surrounding medium (soil) is different, and the conversion factor is re-calibrated.

Another (additive) correction to the measured data is related to the energy stored in the layer above the heat flux plate. This correction is required because plates are installed at a depth of about 5–10 cm whereas surface fluxes (at $z = 0$) are required for practical applications.

The storage term can be computed if the change in soil temperature and the volumetric soil heat capacity are known, this requires the knowledge of the surface soil water content, as expressed by Eq. (2.75). These measurements are generally provided by ancillary instruments conveniently located (see as example Campbell-Inc. (2007) for more details).

3.3 Energy balance closure check

One method to independently evaluates scalar fluxes estimated from eddy covariance is energy balance closure. An imbalance between the fluxes measured by eddy correlation system, $H + \lambda ET$, and an independent measurement of the remaining available energy, $R_n - G_0$, *may* indicate inaccurate observation of turbulent fluxes (Wilson *et al.*, 2002).

The emphasis on the word *may* is reported because, as introduced in Chapter 2, the commonly adopted from of the surface energy budget, Eq. (2.2), neglects the contributes of some terms that appear in the complete formulation, Eq. (2.1). As a consequence, the imbalance of simplified energy budget can be ascribed to these two different causes (instruments inaccuracy and/or not negligible terms).

As observed by Wilson *et al.* (2002) the FLUXNET dataset shows frequently (but not always) an underestimations of about 10–30%$of H + \lambda ET$ with respect to the available energy. In literature several reasons of this incongruity have been discussed, as summarized by Culf *et al.* (2004) and Foken *et al.* (2006):

- the main source of uncertainties on energy balance closure is related to the measurement errors of the eddy covariance technique, which cause a systematic underestimation of the turbulent fluxes. However, in the recent years the improvements in sensors and in the correction methods have made the acquired data more reliable than in the past (Moncrieff, 2004);

- the effective negligibility of storage terms is another aspect that influences the balance closure, especially at local scale where their contribute can be significant (Foken and Wichura, 1996);

- the unclosure of the energy balance was also connected with the heterogeneity of the land surface (Panin *et al.*, 1998). The authors assumed that the heterogeneities generate eddies at larger time scales than eddies measured with the eddy-covariance method; additionally, advection and organized turbulence structures cause similar problems (Finnigan *et al.*, 2003; Kanda *et al.*, 2004);

- energy imbalance can be also considered as a scale problem, related

to the differences in source area sizes of the different measurement techniques. Energy balance is based on the hypothesis that the source area is the same for all the measured fluxes; actually, each flux is a spatial average of a different source area. In fact, net radiation and soil heat flux source areas are time-invariant, differently from latent and sensible heat fluxes; moreover, G_0 source area (≈ 1 m^2) is several order of magnitude smaller than H and λET ones ($\approx 1 \times 10^4$ m^2), and similar consideration can be made for R_n measurements ($\approx 1 \times 10^2$ m^2).

Despite these considerations, traditionally, energy balance closure check has been accepted as an important test of eddy covariance data (Anderson *et al.*, 1984; Mahrt, 1998). Additionally, due to the use of EC measurements as a "ground truth" for energy balance models validation, in practical applications energy balance closure is enforced.

In the past years a number of studies (Anandakumar, 1999; Ezzahar *et al.*, 2009; Savage, 2008) have focused the attention on the estimation of the uncertainties in H observations using different methodologies (e.g., eddy correlation, scintillometry, Bowen ratio, surface renewal).

As example, Foken (2008) found that λET and H errors are in the ranges of about 10–20% and 5–15%, corresponding to 20–50 W m^{-2} and 15–30 W m^{-2}, respectively.

The same author, found that the most accurate measurement is the net radiation, with an error of about 6% and that the ground heat flux have an higher percentage error, but with the lower value in terms of energy ($\approx$ 15 W m^{-2} for canopies full cover). The resulting, total, probable error of $R_n - G_0$ is of about 10% for homogeneous sites.

As introduced above, all models of surface energy and mass exchange are based on the conservation principles; therefore, the use of surface flux data to validate land surface models requires that conservation of energy has to be satisfied, and the measured energy budget must be closed using some method (Prueger *et al.*, 2005; Twine *et al.*, 2000).

A simple approach to check and enforce the closure is the one proposed by Prueger *et al.* (2005), adopted for the SMACEX experimental campaign. Following this approach, energy balance closure was computed from the 30-min averaged components and summed into daytime flux totals, defining daytime periods by using the criteria: $R_n > 100$ W m^{-2}. The closure ratio

(CR) was computed by means of the following relationship:

$$CR = \frac{H + \lambda ET}{R_n - G_0} \tag{3.42}$$

and the offset between the average value of this ratio and the unitary value was evaluated. The balance closure is considered satisfactory when $CR > 0.85$ (Meyers and Hollinger, 2004; Prueger *et al.*, 2005; Wilson *et al.*, 2002).

Moreover, Prueger *et al.* (2005) on the same dataset found that the greater scatter in the data is in the λET measurements, suggesting that when energy balance closure is problematic it tends to be concentrated in λET. For this reason, the closure approach suggested by the authors is to compute the latent heat flux as a residual terms of the energy budget assuming unbiased the measurements realized for the other fluxes.

This methodologies, known as *residual closure*, draw up the eddy correlation measurements to the scintillometer one, which adopts necessarily the same assumption for λET determination. This method of closure is generally very appealing because the measurements of λET are ignored and unneeded (Stannard *et al.*, 1994).

Another approach is to assume that β is correctly measured by EC system, so the values of H and λET can be adjusted to balance the available energy (Twine *et al.*, 2000); in literature this methods is refereed as the *Bowen ratio closure*.

Following this approach the SEB equation can be rearranged as:

$$R_n - G_0 = (H_{\text{mis}} + \Delta H) + (\lambda ET_{\text{mis}} + \Delta \lambda ET) \tag{3.43}$$

where the sub-script "mis" represents the EC measured value, ΔH and $\Delta \lambda ET$ are the closure errors for H and λET, respectively.

Equation (3.43) assumes that errors in the measured available energy are absent or negligible.

The two correction terms can be computed, preserving the measured value of Bowen ratio, as:

$$\Delta \lambda ET = \frac{(R_n - G_0) - \left[(1 - \beta)\lambda ET_{\text{mis}}\right]}{1 + \beta} \tag{3.44a}$$

$$\Delta H = \beta(\lambda ET_{\text{mis}} + \Delta \lambda ET) - H_{\text{mis}} \tag{3.44b}$$

So, the corrected values of the fluxes can be computed as:

$$\lambda ET = \lambda ET_{\text{mis}} + \Delta\lambda ET \tag{3.45a}$$

$$H = H_{\text{mis}} + \Delta H \tag{3.45b}$$

This approach have the advantage to take into account the measured values of latent heat flux, spreading the error between the two most uncertain data, proportionally to the magnitude. Despite that, due to the well-known instability of β when it approaches negative values (see subsection 2.4.1), the application of this methodology can become problematic during nighttime, sunset and sunrise.

Chapter 4

SEB remote sensing-based approaches

Spatially distributed assessment of evapotranspiration was recognised as one of the main topic in hydrological science in the last 30 years, due to the significant spatial variability of this quantity in both natural and agricultural landscape.

Despite the numerous approaches developed to estimate evapotranspiration, it is widely recognized that the up-scaling of point-scale observation is inapplicable, and a realistic parametrisation of spatially distributed model is complex and extremely time-consuming.

The limitations in the application of hydrological and meteorological approaches for evapotranspiration retrieval were partially addressed by the increase in remotely sensed data availability. The attraction of using remote sensing to monitor land surface temperature (using thermal infrared spectral bands) and reflectivity (in visible and near infrared regions) is explained by the ability of this tool to: i) return spatially distributed information on vegetation coverage and spectral characteristics (e.g., albedo) over large heterogeneous regions; ii) observe surface temperature which is closely related to surface energy fluxes partition, due to the impact of land surface temperature in all the four main energy balance variables (see Chapter 2).

The integration of remotely sensed data and land surface modelling for evapotranspiration assessments can be realized in three different ways

(Kalma *et al.*, 2008):

- the first class of approaches calculates the latent heat flux (at the remote observation overpass time) as the residual term of the energy balance equation, using the remotely-sensed radiometric temperature as a direct input of the SEB models. Daytime integration is realised using self preservation parameters (see sub-section 2.4);

- the second type of approaches uses a combination of water stress indices and meteorological-based ET_p estimation to obtain time-continuous evapotranspiration maps. Water stress indices can be obtained by means of empirical approaches or SEB residual models;

- the third approaches are developed to compute all the components of the surface energy budget (in the simplified form of Eq. (2.2)) using continuous Land Surface Models (LSMs) which include Soil-Vegetation-Atmosphere Transfer (SVAT) schemes. In this context, remotely-sensed data can be used to retrieve models input parameters and as additional observations for data assimilation.

The next sub-sections briefly describe the approaches investigated in this thesis, following the above introduced subdivision and referring to the fluxes theoretical modelling drawn in the Chapter 2.

4.1 Residual SEB approaches

The so-called residual approaches base the estimation of evapotranspiration on the assumption of the reliability of energy budget equation, computing the latent heat flux as a residual term.

In fact, all the remaining energy budget terms in Eq. (2.2) depend on the land surface temperature, so the observation of this variable allows to adopt the latent heat flux as an unknown in the energy budget modelling.

Of particular interest is the connection between remotely-observed radiometric temperature and the aerodynamic temperature which appears in Eq. (2.112) for sensible heat flux modelling. The replacing of T_0 with T_{RAD} is generally accepted for dense canopies but this drives to high errors for sparse canopies (Troufleau *et al.*, 1997). To resolve the non-uniqueness

of the T_0 *vs.* T_{RAD} relationship, a number of approaches were recently developed.

The SEB models developed in the last two decades can be classified, depending on the adopted scheme (see sub-section 2.3.3), in *one-source*, or big-leaf, models (Monteith, 1965), *two-source* models (Shuttleworth and Wallace, 1985) or *multi-layer* models, which are essentially an extension of the two-source approach.

Table 4.1 reports a synthetic review of the main residual models developed to combine remotely-sensed data and SEB schemes.

In the next sub-sections the descriptions of the TSEB (Two Source Energy Balance) model (Kustas and Norman, 1999; Norman *et al.*, 1995) and ALEXI (Atmosphere-Land Exchange Inverse) approach (Anderson *et al.*, 1997) are reported, with particular attention to the adopted hypotheses for the numerical solutions of the two-source budget equations.

4.1.1 The TSEB model

The TSEB model, originally developed by Norman *et al.* (1995) and subsequently adapted by Kustas and Norman (1999) for strongly sparse vegetation, aims to accommodate the difference between aerodynamic temperature and remotely-observed radiometric temperature by means of the separation of canopy and soil contributions.

In fact, the soil and vegetation temperatures contribute to the radiometric temperature proportionally to the fraction of the radiometer field of view occupied by each component. Instead, the contribution of these temperatures to the aerodynamic one is proportionally to the resistances to turbulent transport, and then there is no obvious relationship between radiometric and aerodynamic temperatures.

The TSEB model bases its estimation on the following relationship for the partition of canopy and soil temperature (Becker and Li, 1990):

$$T_{\mathrm{RAD}} = \left[f_c T_c^4 + (1 - f_c) T_s^4 \right]^{1/4} \tag{4.1}$$

where the effects of the sensor view angle on radiometric temperature and fraction coverage were removed for near-nadir acquisitions.

A schematic description of the TSEB model is reported in Figure 4.1. This flow chart highlights the connections among the main inputs, state

Table 4.1: Summarize of remote sensing approaches for estimating evapotranspiration using residual energy balance scheme.

Scheme	Acronym	Source	Main hypothesis
One-source	–	Stewart *et al.* (1994)	• empirical adjustment of aerodynamic resistance.
One-source	SEBAL	Bastiaanssen *et al.* (1998a)	• image-based calibration of aerodynamic difference.
One-source	SEBS	Su (2002)	• aerodynamic difference modelled using boundary conditions derived from routinely meteorological data.
One-source	–	Boegh *et al.* (2002)	• use of the decoupling coefficient (Jarvis and McNaughton, 1986) to assess stomatal control.
One-source	METRIC	Allen *et al.* (2007)	• modification of SEBAL approach based on boundary condition derived from standardized PM equation.
Two-source	TSEB	Norman *et al.* (1995)	• separation of canopy and soil contribution on the observed radiometric temperature (single and dual angle).
Two-source	–	Chehbouni *et al.* (2001)	• using dual angle observations of surface radiometric temperature.
Two-source	ALEXI	Anderson *et al.* (1997)	• time-integrated approach based on two-times observations of radiometric temperature during the morning.
Two-source	DTD	Norman *et al.* (2000)	• use of time rate change in both radiometric temperature and near-surface air temperature.

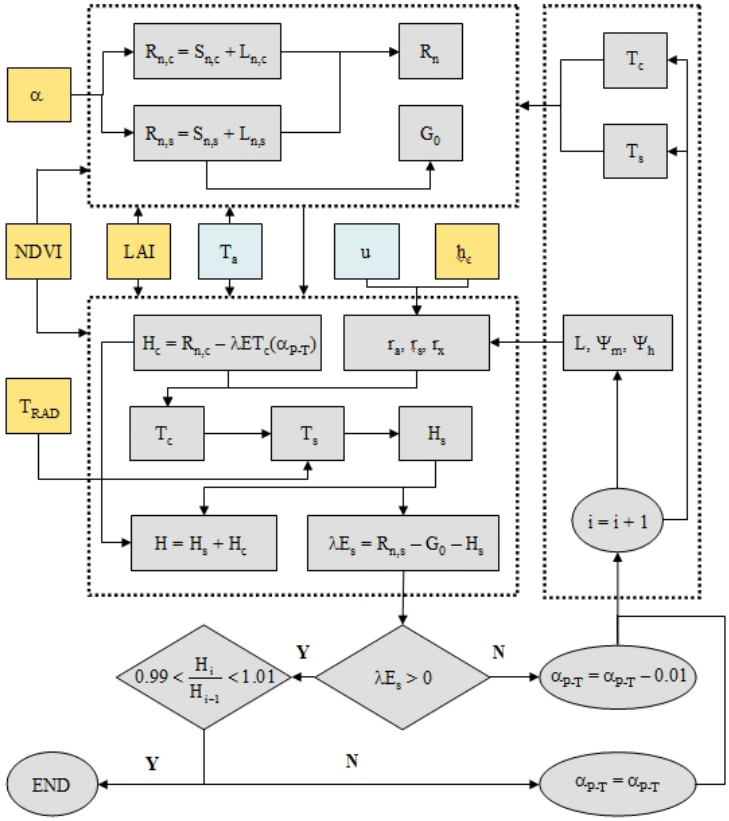

Figure 4.1: Flow chart of the TSEB model. Orange boxes highlight remotely sensed variables and blue boxes highlight the meteorological ancillary data.

variables and outputs of the model, summarizing the adopted procedure later on described in this sub-section.

The modelling of net radiation is carried out, separately for canopy and soil layers, by means of the Eqs. (2.48).

The short-wave components can be derived from Eqs. (2.49), assuming clear sky conditions at the sensors time-overpass and so a solar radiation computable using Eq. (2.24).

Differently, the long-wave components computation by means of Eqs. (2.54) requires the knowledge of canopy and soil temperature. For this

reason, a first guess estimation of $L_{n,s}$ and $L_{n,c}$ can be obtained assuming $T_c = T_a$, then T_s by means of Eq. (4.1) inversion.

The soil heat flux is computed adopting the approach suggested by Norman *et al.* (1995) in the original TSEB formulation (Eq. (2.82)), but taking into account c_g daily variability as introduced by (Santanello and Friedl, 2003) via Eq. (2.84).

The parameters in the latest equation were assumed equal to: $c_{g,\max} = 0.2$ according to the variability explored by the studies of Choudhury (1987), Friedl (1996) and Kustas and Daughtry (1990), $C_t = 3600$ s following Cellier *et al.* (1996), and $B_t = 74000$.

In order to solve the system of Eqs. (2.124), (2.126) and (4.1) for sensible heat fluxes modelling another equation is required. As initial hypothesis, a reasonable estimation of T_c is obtained by partitioning the net radiation in canopy layer into sensible and latent heat fluxes using the Priestley-Taylor approximation (Priestley and Taylor, 1972). This assumption allows to compute the sensible heat flux in canopy layer as:

$$H_c = \left[1 - \alpha_{\text{P-T}} f_g \frac{\Delta}{\Delta + \gamma}\right] R_{n,c} \tag{4.2}$$

where f_g is the fraction of LAI that is green (assumed to be unity when no information is available), and $\alpha_{\text{P-T}}$ is the Priestley-Taylor coefficient equal to 1.26 for potential (unstressed) conditions.

The numerical solution adopted to assess T_c and T_s is the one reported in the in the Appendix A of Norman *et al.* (1995), based on the linearization of Eq. (4.1).

The linear approximation of vegetation temperature, $T_{c,\text{lin}}$, is represented by the following equation:

$$T_{c,\text{lin}} = \frac{\dfrac{T_a}{r_a} + \dfrac{T_{\text{RAD}}}{r_s(1-f_c)} + \dfrac{H_c r_x}{\rho c_p}\left(\dfrac{1}{r_a} + \dfrac{1}{r_s} + \dfrac{1}{r_x}\right)}{\dfrac{1}{r_a} + \dfrac{1}{r_s} + \dfrac{f_c}{r_s(1-f_c)}} \tag{4.3}$$

where the resistances r_a, r_s and r_x are computed by means of Eqs. (2.114), (2.131) and (2.129), respectively.

As reported in sub-section 2.3.3, the resistance r_a is analogous to r_{ah} assuming $z_{0h} = z_{0m}$.

Considering valid the following approximation:

$$(T_{c,\text{lin}} + \delta T_c)^4 = T_{c,\text{lin}}^4 + 4T_{c,\text{lin}}^3 \Delta T_c \tag{4.4}$$

which is realistic when $T_{c,\text{lin}} \gg \Delta T_c$, a relationship for ΔT_c computation is derived:

$$\Delta T_c = \frac{T_{\text{RAD}}^4 - f_c T_{c,\text{lin}}^4 - (1 - f_c) T_D^4}{4(1 - f_c) T_D^3 \left(1 + \dfrac{r_s}{r_a}\right) + 4 f_c T_{c,\text{lin}}^3} \tag{4.5}$$

where

$$T_D = T_{c,\text{lin}} \left(1 + \frac{r_s}{r_a}\right) - \frac{H_c r_x}{\rho c_p} \left(1 + \frac{r_s}{r_x} + \frac{r_s}{r_a}\right) - T_a \frac{r_s}{r_a} \tag{4.6}$$

Finally, the correct value of T_c is given by:

$$T_c = T_{c,\text{lin}} + \Delta T_c \tag{4.7}$$

The soil temperature can be obtained from Eq. (4.1), therefore aerodynamic temperature and soil heat sensible flux can be retrieved applying Eqs. (2.126) and (2.124), respectively.

At this point, the soil evaporation can be computed as a residual term of the soil energy balance equation (2.3a), as:

$$\lambda E_s = R_{n,s} - G_0 - H_s \tag{4.8}$$

If λE_s is positive, then a correct partition of energy fluxes in soil and canopy layers is reached. If λE_s is negative, the energy assigned to the transpiration process is too high, so a smaller value of $\alpha_{\text{P-T}}$ is used since λE_s becomes zero, and H_s is equal to:

$$H_s = R_{n,s} - G_0 \tag{4.9}$$

An analytical solution of this second hypothesis can be obtained, starting from a linear approximation of aerodynamic temperature, $T_{0,\text{lin}}$:

$$T_{0,\text{lin}} = \frac{\dfrac{T_a}{r_a} + \dfrac{T_{\text{RAD}}}{f_c r_x} - \dfrac{(1 - f_c)}{f_c r_x} \left(\dfrac{(R_{n,s} - G_0) r_s}{\rho c_p}\right) + \dfrac{(R_{n,s} - G_0)}{\rho c_p}}{\dfrac{1}{r_a} + \dfrac{1}{r_x} + \dfrac{(1 - f_c)}{f_c r_x}} \tag{4.10}$$

Using the same approximation given by Eq. (4.4) but for T_0:

$$\Delta T_0 = \frac{T_{\mathrm{RAD}}^4 - (1-f_c)\left(\frac{(R_{n,s}-G_0)r_s}{\rho c_p} + T_{0,\mathrm{lin}}\right)^4 - f_c T_E^4}{4f_c T_E^3\left(1+\frac{r_x}{r_a}\right) + 4(1-f_c)\left(\frac{(R_{n,s}-G_0)r_s}{\rho c_p}\right)^3} \tag{4.11}$$

where

$$T_E = T_{0,\mathrm{lin}}\left(1+\frac{r_x}{r_a}\right) - \frac{(R_{n,s}-G_0)r_x}{\rho c_p} - \frac{T_a r_x}{r_a} \tag{4.12}$$

and

$$T_0 = T_{0,\mathrm{lin}} + \Delta T_0 \tag{4.13}$$

Finally, the soil surface temperature can be calculated as:

$$T_s = T_0 + \frac{(R_{n,s}-G_0)r_s}{\rho c_p} \tag{4.14}$$

and the canopy temperature can be derived from Eq. (4.1). The canopy sensible heat flux, calculated using Eq. (2.124), allows to obtain λET_c as a residual term of Eq. (2.3b).

This solution corresponds to a computation of canopy transpiration using the Priestley-Taylor approximation with $\alpha_{\text{P-T}} < 1.26$.

If the difference between T_{RAD} and T_a is very large, this second solution can drive to negative value of λET_c. In this case transpiration and soil evaporation may be both equal to zero, and the balance closure is addressed assuming $H_c = R_{n,s}$ and G_0 as a residual term of Eq. (2.3a).

During the iterative procedure adopted to solve the energy balance equation with the correct value of $\alpha_{\text{P-T}}$, the stability functions (see Eqs. (2.98) in sub-section 2.3) are computed as a function of $H = H_c + H_s$, in order to correct the resistance values for diabatic conditions. Additionally, the new value of T_s and T_c obtained from the sensible heat fluxes computation are used to replace the first guess values used in net radiation computation.

Scene-based internal calibrated air temperature

Unlike the internally calibrated remote sensing based model (Allen *et al.*, 2007; Bastiaanssen *et al.*, 1998a; Roerink *et al.*, 2000; Su, 2002), the TSEB approach uses the remotely observed surface temperature as a direct input. As a consequence, the TSEB scheme has greater sensitivity to uncertainties in T_{RAD} retrieving procedure (Choi *et al.*, 2009).

One of the main problem of using surface temperature derived by remote sensing, is related to the uncertainties in its estimation, especially when it is used jointly to *in-situ* air temperature measurements. In many cases, in fact, the magnitude of the uncertainties is often comparable with the aerodynamic difference ($T_0 - T_a$) values (Norman *et al.*, 2000).

Numerous factors need to be quantified in order to assess the accuracy of surface temperature retrieval (Goetz *et al.*, 1995), including sensor radiometric calibration, correction for atmospheric attenuation of the at-sensor signal, correction for surface emissivity, characterization of spatial variability in ground cover (Hatfield *et al.*, 1984), and the combined effects of viewing geometry, background, and fractional vegetative cover (e.g., Friedl and Davis, 1994; Kimes *et al.*, 1980; Norman *et al.*, 1990).

Additionally, the use of measured air temperature requires the presence of weather station in proximity of the study area, and an instrument elevation (above the ground) greater than the maximum canopy height. Especially the latest issues, can become problematic for applications in areas characterized by tall vegetation.

An improvement in TSEB model performances can be obtained, as suggested by Norman *et al.* (2006), introducing the internal-scene calibration (IC) approach adopted by SEBAL (Surface Energy Balance Algorithm for Land) model (Bastiaanssen *et al.*, 1998a,b), in order to derive an estimation of the air temperature. Assuming the presence in the scene of a well irrigated full covered vegetation area, the air temperature, $T_{a,\mathrm{IC}}$, can be assessed using the relationship:

$$T_{a,\mathrm{IC}} = T_0 - \frac{r_a}{\rho c_p}\left[R_{n,c}\left(1 - 1.26\frac{\Delta}{\Delta+\gamma}\right)\right] \tag{4.15}$$

where T_0 can be assumed equal to the observed radiometric temperature, due to the absence of soil layer.

The air temperature obtained by Eq. (4.15), on the hypothesis of uniform atmospheric forcing, can be used as upper boundary condition for the whole scene.

4.1.2 The ALEXI approach

The ALEXI (Anderson *et al.*, 1997) is an operational two-source model able to evaluate the surface energy balance given measurements of the time rate of change in surface radiometric temperature during the morning hours.

The need of two-times morning remotely sensed T_{RAD} observations restrict the applicability to geostationary satellite. Currently, the regional ALEXI model is being applied on a daily basis at 10-km resolution over the continental U.S. using measurements of morning rise of surface temperature from GOES-E and -W (Anderson *et al.*, 2007a,b). Additionally, similar projects are in development for Europe and Africa continents, thanks to the high observation frequency of the new MSG/SEVIRI system (Anderson *et al.*, 2011; Li *et al.*, 2009).

The two-source surface layer model adopted in ALEXI is analogous to the TSEB model described in the previous section. In this case, due to the not-negligible effect of the sensor field of view, the radiometric temperature of partially vegetated surfaces can be expressed as:

$$T_{\mathrm{RAD}}(\vartheta) = \left[f_c(\vartheta) T_c^4 + \Big(1 - f_c(\vartheta)\Big) T_s^4 \right]^{1/4} \tag{4.16}$$

where $f_c(\vartheta)$ is the fraction of the sensor field of view occupied by vegetation when viewed at a zenith angle ϑ [rad].

For a canopy with a random distribution of leaves (see sub-section 2.1.4 for the extensions to clumped vegetation), $f_c(\vartheta)$ ca be expressed as:

$$f_c(\vartheta) = 1 - \exp\left(\frac{-0.5\mathrm{LAI}}{\cos\vartheta} \right) \tag{4.17}$$

Assuming in the ALEXI the air temperature as additional unknown, the system of equation described in sub-section 4.1.1 become unresolvable. The ALEXI takes advantage from the temporal information, using it to eliminate the need of ground measurements of air temperature.

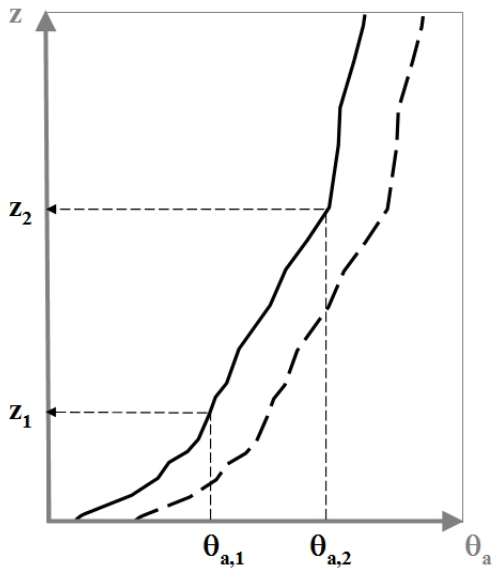

Figure 4.2: Scheme of the procedure used to diagnose ABL growth during the time interval from t_1 to t_2. Dashed line represents the observed morning sounding. Continuous line represents the shifted sounding (redraw from Anderson *et al.*, 1997).

In order to internally computes an above canopy air temperature at a nominal blending height consistent with the observed surface temperature (Anderson *et al.*, 2008), in the ALEXI model the evolution of air temperature is evaluated according to the independent balance of the energy budgets at the surface (at two times t_1 and t_2) and the ABL growth.

The development of ABL and its energy conservation is described by means of a simple slab-model of the mixing layer (McNaughton and Spriggs, 1986). The slab-model assumes that the air within the layer is at an uniform potential temperature (see section 2.3).

The subscript "i" is used hereafter to indicates the quantities at the specific time t_i (with $i = 1, 2$).

Assuming that the height of boundary layer at time t_i can be approximated by the value z_i at which an adiabatic curve at the current mixed layer potential temperature, $\theta_{a,i}$, intersects an early morning temperature profile (see Figure 4.2), similarly to Tennekes (1973).

On the basis of this assumption, the height of ABL during the convective phase is uniquely defined by the current surface air temperature and the morning sounding. Neglecting the effects of subsidence and horizontal advection, McNaughton and Spriggs (1986) suggest the following simplified conservation equation of ABL over the time:

$$\rho c_p(z_2\theta_{a,2} - z_1\theta_{a,1}) = \int_{t_1}^{t_2} H(t)\mathrm{d}t + \rho c_p \int_{z_1}^{z_2} \theta_a(z)\mathrm{d}z \tag{4.18}$$

where $\theta_a(z)$ is the potential temperature profile in the mixing layer at the time t_1, obtained, for example, from an early morning sounding.

Following this scheme, the growth of the mixed layer, from height z_1 to z_2, is determined by the amount of energy supplied to the mixed layer from the surface during the time interval $t_2 - t_1$ as sensible heat flux and by the resistance to ABL growth.

Despite the extreme simplification, the errors related to these ones are generally negligible in the practical applications, during morning and under clear-sky conditions (Wetzel *et al.*, 1984).

In order to solve Eq. (4.18), a linear sensible heat behaviour increasing with time is assumed, valid in the morning hours from just after the sunrise until just before the noon. This assumption allows to express the sensible heat flux at the time t_i as follow:

$$H_i = \frac{2\rho c_p t_i}{(t_2^2 - t_1^2)}\left[z_2T_{a,2} - z_1T_{a,1} - \int_{z_1}^{z_2} \theta_a(z)\mathrm{d}z\right] \tag{4.19}$$

where the potential temperature in the mixed layer is assumed equal to the air temperature of the surface.

The application of Eq. (4.19) requires that the temperatures of the morning sounding are consistent with the air temperature derived from the surface energy balance model component. However, in the practical applications, local atmospheric soundings are unavailable; additionally, systematic bias in the observed radiometric temperature will translated into a bias in the estimates of θ_a.

To overcome these problems, the time-change in temperature is adopted instead of absolute measured values assuming that the height of ABL at time t_1 is a small fixed value ($z_1 \approx 50$ m). As a consequence, the observed

early morning sounding is shifted in order to obtain a value of $\theta_{a,1}$ for $z = z_1$, and the integration in Eq. (4.19) is realized over this shifted profile (see Figure 4.2).

Starting from a first guess estimation of $T_{a,1}$ and $T_{a,2}$, the use of Eq. (4.19) allows a fist guess estimation of H_1 and H_2. These fluxes can be used as input for the assessment of new values for $T_{a,1}$ and $T_{a,2}$ in according to the surface energy budget at the two times:

$$T_{a,i} = T_{\mathrm{RAD},i}(\vartheta) - \frac{H_i r_{a,i}}{\rho c_p} - f_c(\vartheta)\frac{H_{c,i} r_{x,i}}{\rho c_p} - \left[1 - f_c(\vartheta)\right]\frac{H_{s,i} r_{s,i}}{\rho c_p} \quad (4.20)$$

In the Eq. (4.20) a first-pass estimation of $H_{c,i}$ is obtained from Eq. (4.2), with the Priestley-Taylor coefficient equal to 1.26, and $H_{s,i} = H_i - H_{c,i}$.

The previous first guess estimations of $T_{a,i}$ are replaced with these new values, and the morning sounding is shifted according to the new $T_{a,1}$ value. The hypothesis of canopy potential transpiration is replaced using an iterative approach following the same consideration described in the TSEB sub-section (4.1.1).

On the basis of this description, it is clear how the main difference in the TSEB and ALEXI required data is the absence of *in-situ* air temperature measurements for the ALEXI, replaced by the early morning sounding. All the ancillary meteorological data, including radio sounding, can be obtained by global circulation model products, for example the ones provided by ECMWF (European Centre for Medium-range Weather Forecast).

The choice of the time integration limits in Eq. (4.19) directly affects the accuracy of the model estimates of surface fluxes. Obviously, the choice of t_1 and t_2 is bounded by the assumption of the sensible heat flux linearity. This limits the choice of t_2 at least one hour before local noon, and of t_1 at least one hour after the sunrise. Additionally, the two observations should be placed far enough in time so that a strong temperature change is detected.

On these bases, the authors suggest to use radiometric surface temperature measurements acquired at 1.5 and 5.5 hours past sunrise, yielding a time interval between the two observation of $t_2 - t_1 = 4$ h .

4.1.3 Daytime integration

All the remote sensing-based approaches provide instantaneous estimations corresponding to the sensors overpass time. However, generally the practical applications require integrated values of evapotranspiration over the day.

The most common approach adopted the self-preservation of evaporative fraction (Brutsaert and Sugita, 1992; Crago, 1996) and the negligibility of the daily soil heat flux compared to the daily net radiation. On these bases, the daily evapotranspration, ET_{24}, can be derived as following:

$$ET_{24} = 86400\Lambda\frac{R_{n,24}}{\lambda} \tag{4.21}$$

For instantaneous value computed around the 5.5 h past sunrise, Anderson *et al.* (1997) found differences of about 10% between estimated and measured energy fluxes. For this reason, these authors suggest to adopt a value of evaporative fraction equal to $\Lambda' = 1.1\Lambda$.

Another approach for the daily evapotranspiration assessment is based on the dependence of evapotranspiration flux on incoming solar radiation, Jackson *et al.* (1983), assuming the following relationship:

$$ET_{24} = 86400\left(\frac{R_{s,24}}{R_s}\right)ET \tag{4.22}$$

The last method uses the ratio between instantaneous and daily reference evapotranspiration as integration parameter:

$$ET_{24} = \left(\frac{ET}{ET_0}\right)ET_{0,24} \tag{4.23}$$

where the ratio between instantaneous actual and reference evapotranspiration represents the adjusted crop coefficient (K_cK_s) introduced by Allen *et al.* (1998).

4.2 Water stress index approaches

High temporal and spatial resolutions ET assessment using the residual approach requires the availability of adequate remotely sensed observations, especially as regards as surface radiometric temperature maps.

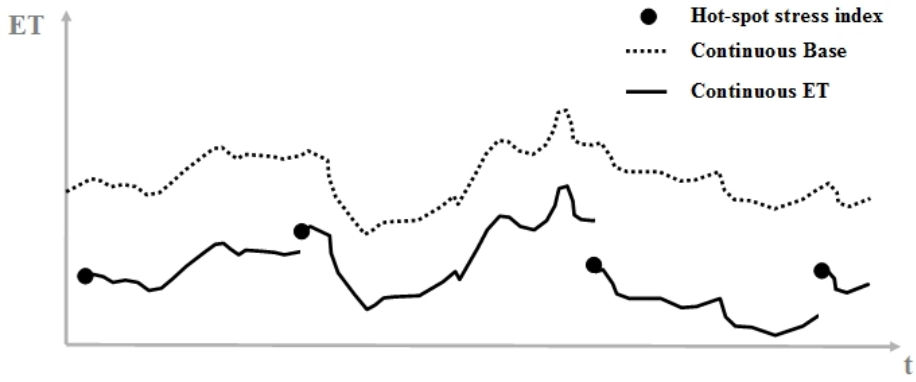

Figure 4.3: General scheme of the ET estimations based on water stress index approaches. Continuous estimations of base variable is corrected by means of hot-spot stress index in order to obtain continuous ET assessments.

In the case of operational high resolution thermal data (e.g., Landsat, ASTER) the poor temporal resolution ($\approx$ 15 days) allows only "hot-spot" estimations of ET. On the contrary, daily available thermal data (e.g., MSG, MODIS) are charachterized by moderate/low spatial resolution, not adequate for field scale applications in fragmented areas.

Additionally, the theoretical acquisition frequency of operational satellites is reduced by cloud coverage, which limits also direct daily application of residual approaches using moderate/low spatial resolution data.

For all these reasons, continuous daily ET estimations can be obtained only combining stress index, derived from hot-spot ET estimates, with a continuous estimation of a "base" variable (Figure 4.3).

In the next sub-sections three methodologies are described, different for the adopted base variable, focusing the attentions on the ancillary data required for their application.

4.2.1 The Dis-ALEXI technique

The high temporal resolution of geostationary data, adopted for the application of ALEXI model, generally allows almost daily ET estimations. In fact, cloud coverage affects the estimates, for each pixel, only for few days. The filling of these gaps is generally obtained using continuous

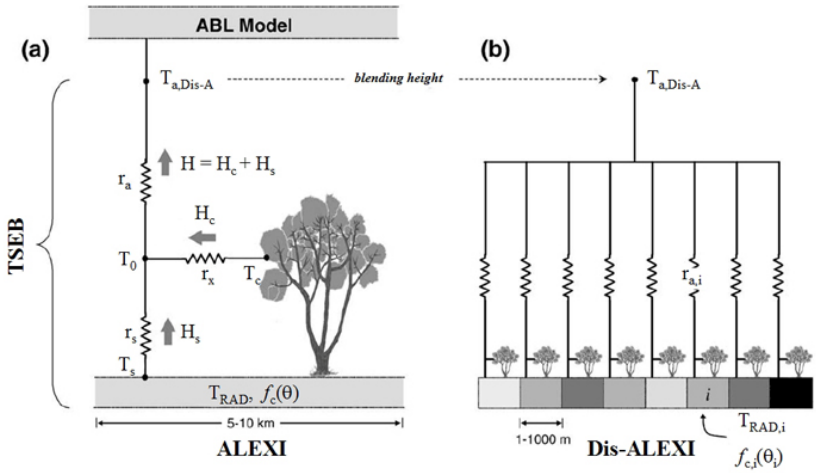

Figure 4.4: Diagram representing the ALEXI (a) and Dis-ALEXI (b) modelling schemes, highlighting sensible heat fluxes (H) resistances network. Dis-ALEXI uses the air temperature predicted by ALEXI near the blending height ($T_{a,\text{Dis-A}}$) to disaggregate low-resolution ALEXI fluxes, given high-resolution surface radiometric temperature.

estimations of daily net radiation (as described in sub-section 2.1.5) and applying Eq. (4.21) with Λ, for the cloudy pixels, assumed equal to the value of the previous day.

Starting from ALEXI ET estimations, the Dis-ALEXI technique, (developed by Norman *et al.* (2003)), spatially disaggregate these coarse-resolution regional maps ($\approx$ 5-10 km) to finer resolution flux estimates for local application. Dis-ALEXI uses the air temperature diagnosed by ALEXI ($T_{a,\text{Dis-A}}$), instead of local observed air temperature (Figure 4.4), to evaluate energy fluxes at local scale using a single high/moderate-resolution thermal image.

Adopting this approach, the continuous variable is the estimate of ET at coarse resolution available from ALEXI daily application, and the hot-spot stress index is derived from ET estimates obtained when at high resolution images are available (Figure 4.5). The ratio between high and low resolution maps allows to obtain a proxy variable, useful for the coarse-resolution ET maps disaggregation when high resolution thermal maps are not available.

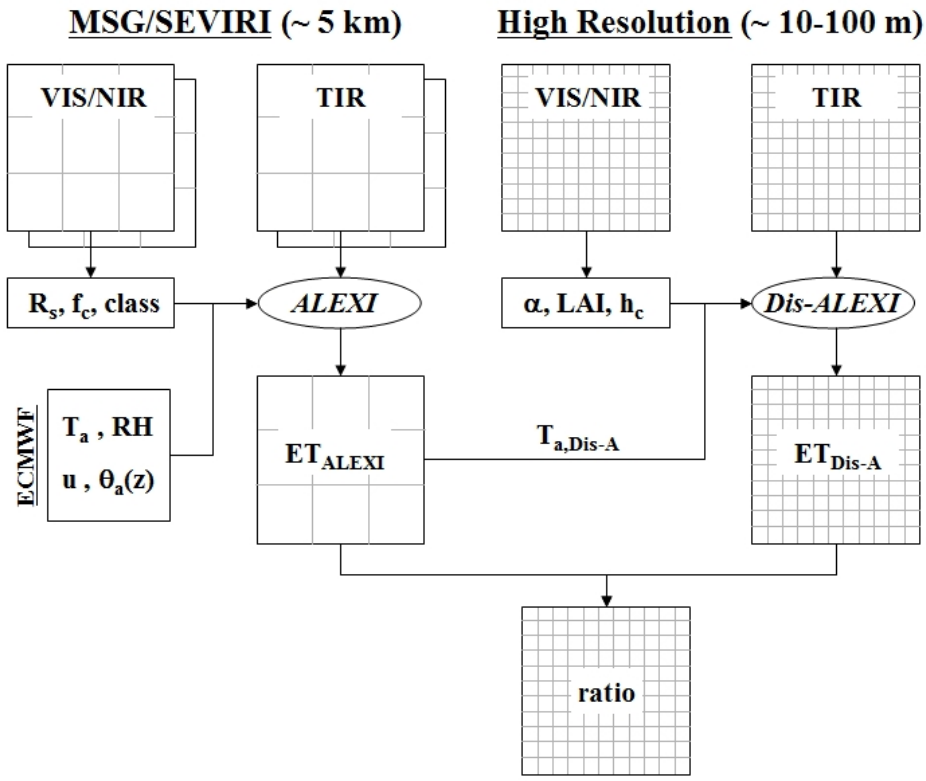

Figure 4.5: Schematic representation of the time-integration of ALEXI/Dis-ALEXI approach. MSG/SEVIRI data allow continuous daily ET estimates (ET_{ALEXI}) used as base variable. The ratio between ALEXI and Dis-ALEXI maps represents the hot-spot stress index.

This approach assumes that the spatial distribution of the stress factors (e.g., water availability) within the low resolution pixel is the same between two high resolution acquisition, but the average stress of the low resolution pixel is variable in time.

4.2.2 The remote sensing physically-based method

This approach (named PM-based) is based on a continuous daily estimations of ET_p (base variable) by means of a direct applications of the PM relationship (Eq. (2.117)) and hot-spot stress index represented by K_s coefficient retrieved as ratio between ET, derived from residual approach, and ET_p itself (Figure 4.6).

The ET_p estimations based on the PM approach can be expressed by means of the following functional relationship:

$$ET_p = f(T_a, u, RH, R_s, \alpha, \mathrm{LAI}, h_c, r_{c,\min}) \tag{4.24}$$

where the 4 variables (T_a, u, RH, R_s) represent the required meteorological data, obtainable from weather station measures, α, LAI and h_c are the remote sensing-derived variables and $r_{c,\min}$, computed using Eq. (2.147), substitutes the stomatal resistance in Eq. (2.117) for unstressed condition ($r_c = r_{c,\min}$).

The application of PM formulation when high resolution images are not available is possible due to the low temporal variability of the remotely observed surface parameters (α, LAI and h_c), considered constant between two consecutive high resolution acquisitions.

The hot-spot high spatial resolution observations of ET allow the assessment of a stress coefficient as:

$$K_s = \frac{ET}{ET_p} \tag{4.25}$$

assumed constant between two acquisitions of high resolution image, and used for ET assessment in absence of thermal data by inverting the Eq. (4.25).

This approach allows to directly take into account the effective crop characteristics in a spatial distributed way, replacing the assumption of tabled crop coefficients, still requiring detailed measurements of meteorological variables for the PM relationship applicability. However, the

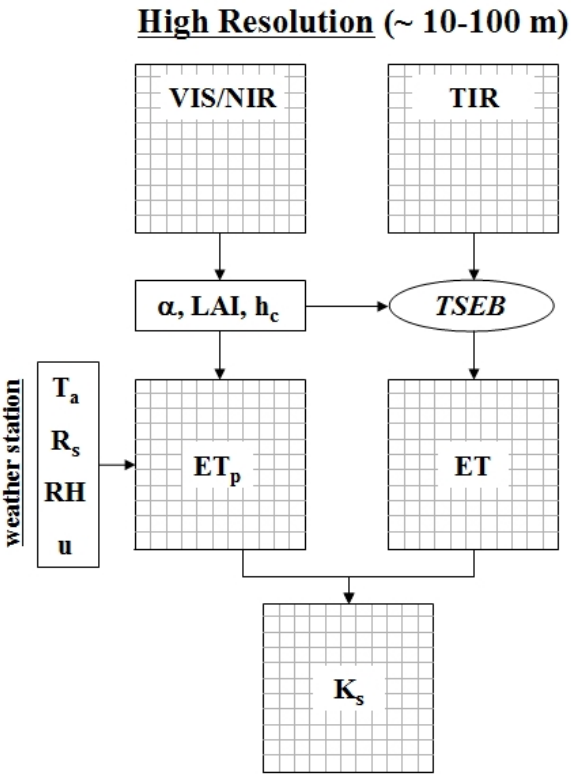

Figure 4.6: Schematic representation of the time-integration approach based on phisically-based ET_p estimations. PM formulations is used for ET_p assessment (base variables) and the stress parameter K_s (ratio between ET and ET_p) is the hot-spot stress index.

use of constant stress condition between two high resolution images do not allow to take into account the reduction of water availability due to the evapotranspiration process or the increase in water availability due to rainfall/irrigation.

4.2.3 The remote sensing simplified approach

The applicability of the previous described approach can be limited by the availability of local weather station observation, especially for ET estimations in wide areas.

For this reason, a number of approaches were developed in order to assess reference evapotranspiration and crop coefficient using remotely-sensed data, minimising the need of ancillary meteorological data.

A simple approach is based on the possibility to assess, in a reliable manner, ET_0 using an empirical-corrected version of the Priestley and Taylor (1972) formulation, and on the relationship between the crop coefficient and the remote sensing-derived vegetation index (e.g., NDVI), as reported in Figure 4.7.

The methodology (named RS-based) suggest to assess ET_0 [mm d^{-1}] using the Priestley and Taylor (1972) expression:

$$ET_0 = 86400 \frac{1.26}{\lambda} \frac{\Delta}{\Delta + \gamma} R_n \tag{4.26}$$

However, in warmer and dryer conditions, the classical PT formulation appears to lead to an underestimation of the effective values. For this reason a correction additional term is proposed, Δ_{corr} [mm d^{-1}], to take into account this discrepancy (de Bruin, 1987):

$$\Delta_{\text{corr}} = -0.61 \frac{R_s}{R_{so}} + 1.22 \left(\frac{R_s}{R_{so}} \right)^2 \tag{4.27}$$

in which R_s is derived from MSG data (as reported in sub-section 2.1.1) and R_{so} can be assessed using Eq. (2.58) with $\tau_{sw} = \tau_{swo}$.

The total net radiation can be computed separately for the short-wave and long-wave radiations; the first one assuming the albedo equal to 0.23 and using the 30-minutes incoming solar radiation maps produced by the LSA SAF from the MSG data (see sub-section 2.1.1). The long-wave

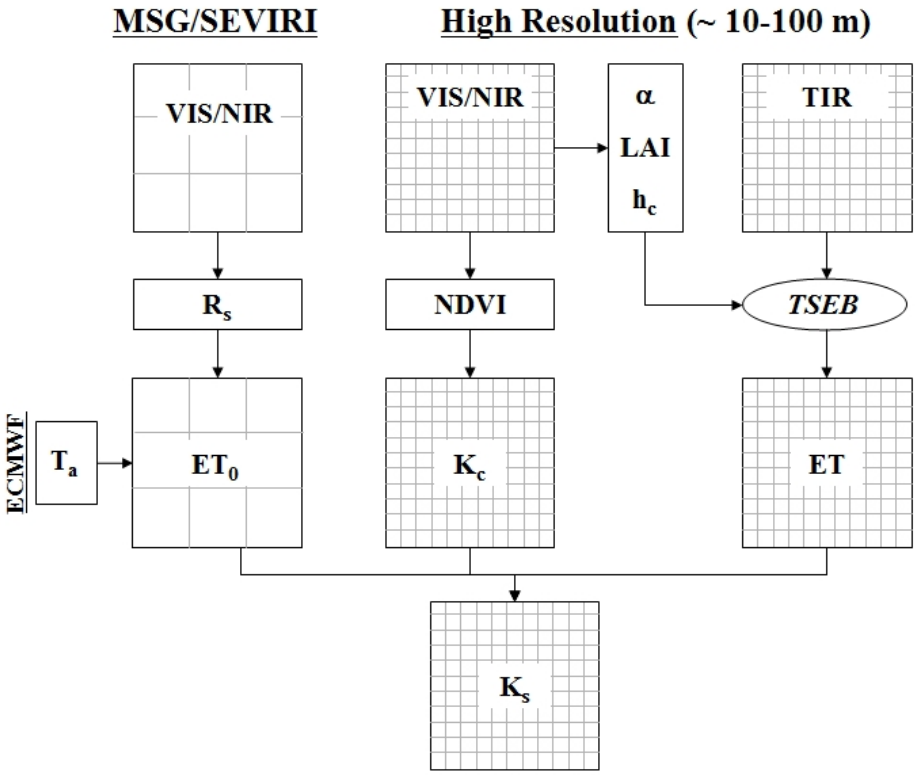

Figure 4.7: Schematic representation of the time-integration approach based on simplified ET_p estimations. Low resolution MSG data are used for ET_0 assessment and $K_c - \text{NDVI}$ relationship is adopted for high resolution ET_p assessment (base variables). The stress parameter K_s (ratio between ET and ET_p) represents the hot-spot stress index.

component, in the case of well-watered crop, can be reasonably assessed using a simple empirical relationship proposed by W. Slob (H.A.R. de Bruin personal communication):

$$L_n = 110\frac{R_s}{R_a} \tag{4.28}$$

where the extra-terrestrial solar radiation is computed using Eq. (2.5), and the empirical coefficient assumes the same value suggested by de Bruin (1987) for the Netherlands.

The only ancillary data required by this methodology for ET_0 computation is the average daily air temperature, used for the computation of Δ and γ in Eq. (4.26). This variable can be derived, for not-monitored area, from ECMWF global circulation model products.

The potential evapotranspiration is assessed from the reference value by means of the inversion of Eq. (2.118), adopting a crop coefficient derived by the NDVI by means of the following empirical relationship proposed by D'Urso and Menenti (1995):

$$K_c = 1.25\text{NDVI} + 0.2 \tag{4.29}$$

High spatial resolution maps of NDVI can be retrieved by hot-spot remotely observations, assuming a tiny temporal variability of this one and then a constant value between two successive acquisitions.

This simplified approach, and analogous ones, was applied in a variety of meteorological conditions and crop types, see for example Calera *et al.* (2004), Er-Raki *et al.* (2007), Gonzàlez-Dugo and Mateos (2008), Heilman *et al.* (1982), Neale *et al.* (1989).

The greater advantage of this approach is the simplification in ET_0 estimation, which allows potential evapotranspiration assessment also in area characterized by the absence of weather station.

4.3 Land Surface Models

Land Surface Models (LSMs) are a wide category of models developed to estimate heat and mass transfer at the land surface. LSMs generally contain physical, or empirical, descriptions of the transfer processes in

the SPA continuum, and under proper initial conditions, they provide continuous simulations when driven by weather data (Kalma *et al.*, 2008).

One of the main limitation of LSMs applicability is the requirements of a number of input parameters related to vegetation and soil characteristics, which are not readily available for landscapes or regions. For this reason, as discussed by Overgaard *et al.* (2006), energy-based LSMs are of particular interest because their strong link to remotely sensed variables.

The two LSMs adopted in this thesis are both based on the numerical solution of the hydrological balance based on the force-restore scheme. As described in sub-section 2.5.1, this approach models separately the water content dynamic in the surface layer and in the root zone by means of two reservoirs scheme.

Starting from a defined initial conditions for θ_1 and θ_2, at $t = 0$, the Eqs. (2.138a) and (2.138b) can be expressed, using the finite differences method, as:

$$\theta_{1,i+1} = \theta_{1,i} + \Delta t \left[\frac{C_1}{d_{z1}} \Big(P_{e,i+1} + I_{r,i+1} - E_s(\theta_{1,i}) \Big) - \frac{C_2}{\tau_t} (\theta_{1,i} - \theta_{eq}) \right] \tag{4.30a}$$

$$\theta_{2,i+1} = \theta_{2,i} + \Delta t \left[\frac{1}{d_{z2}} \Big(P_{e,i+1} + I_{r,i+1} - E_s(\theta_{1,i}) + ET_c(\theta_{2,i}) + Q \Big) \right] \tag{4.30b}$$

where the sub-script "i" represents the integration time step, fixed equal to $\Delta t = 3600$ s. The explicit dependence of E_s and ET_c from θ_1 and θ_2, respectively, is adopted on the basis of the slow dynamic of soil water contents.

The availability of meteorological variables at hourly scale allows the solution of Eqs. (4.30a) and (4.30a) once defined the connections between evapotranspiration process and soil water content. In the next sub-section two approaches are described to model E_s and ET_c.

4.3.1 The dual-crop coefficient approach

A simple way to model the soil evaporation and the canopy transpiration processes is the dual-crop coefficient approach (named 2-CC), introduced by the FAO-56 paper (Allen *et al.*, 1998) and described in sub-section 2.3.3.

Adopting this approach soil evaporation can be expressed as:

$$E_s = K_e ET_0 \tag{4.31}$$

where the coefficient for soil evaporation is modelled using the approach introduced by Eq. (2.120).

The maximum value of K_c in Eq. (2.120) is assumed equal to a fixed value of 1.2, instead the reduction coefficient, K_r, is computed as a function of θ_1:

$$K_r = \begin{cases} 1 & \theta_1 > \theta_{cr} \\ \dfrac{\theta_1 - \theta_{wl}}{\theta_{cr} - \theta_{wl}} & \theta_{wl} \leq \theta_1 \leq \theta_{cr} \\ 0 & \theta_1 < \theta_{wl} \end{cases} \tag{4.32}$$

Analogously, the crop transpiration can be simply modelled as:

$$ET_c = K_s ET_p \tag{4.33}$$

where the potential evapotranspiration can be modelled in a physically-based way as described in sub-section 4.2.2.

The stress coefficient, considering the water availability the only environmental reducing factor, can be expressed as:

$$K_s = \begin{cases} 1 & \theta_2 > \theta_{cr} \\ \dfrac{\theta_2 - \theta_{wl}}{\theta_{cr} - \theta_{wl}} & \theta_{wl} \leq \theta_2 \leq \theta_{cr} \\ 0 & \theta_2 < \theta_{wl} \end{cases} \tag{4.34}$$

The values obtained from the Eqs. (4.31)–(4.34) allow the solution of the hydrological balance for each time step.

4.3.2 The SVAT approach

The approaches based on the detailed modelling of mass and energy exchange in the SPA are generally known as Soil-Vegetation-Atmosphere Transfer (SVAT) models.

A more detailed modelling of the evapotranspiration process can be obtained on the basis of the complete solution of the two-source energy budget Eqs. (2.3a) and (2.3b). In fact, the additional modelling of λE_s and λET_c, by means of Eq. (2.125), allows to resolve the energy balance also in absence of surface temperature measurements.

In particular, assuming:

- the in-series modelling of sensible and latent heat fluxes, Eqs. (2.124) and (2.125),respectively;
- the net radiation partitioning modelled as described in sub-section 2.1.4;
- the soil heat flux defined by means of Eq. (2.81);

the solution of two-source surface energy budget can be obtained from the following system of equations:

$$\begin{bmatrix} a_{11} & a_{12} & a_{13} & a_{14} \\ a_{21} & a_{22} & a_{23} & a_{24} \\ a_{31} & a_{32} & a_{33} & a_{34} \\ a_{41} & a_{42} & a_{43} & a_{44} \end{bmatrix} \times \begin{bmatrix} T_0 \\ T_c \\ T_s \\ e_0 \end{bmatrix} = \begin{bmatrix} b_1 \\ b_2 \\ b_3 \\ b_4 \end{bmatrix} \tag{4.35}$$

where the four unknowns T_0, T_c, T_s and e_0 allow the estimation of all the fluxes in Eqs. (2.3a) and (2.3a), including the latent heat one.

The parameters a_{11}–a_{44} are defined as follow:

$$a_{11} = \frac{1}{r_a} + \frac{1}{r_s} + \frac{1}{r_x} \tag{4.36a}$$

$$a_{12} = -\frac{1}{r_x} \tag{4.36b}$$

$$a_{13} = -\frac{1}{r_s} \tag{4.36c}$$

$$a_{14} = 0 \tag{4.36d}$$

$$a_{21} = 0 \tag{4.36e}$$

$$a_{22} = -\frac{\Delta}{r_x + r_c} \tag{4.36f}$$

$$a_{23} = -\frac{\Delta}{r_s + r_{ss}} \tag{4.36g}$$

$$a_{24} = \frac{1}{r_a} + \frac{1}{r_s + r_{ss}} + \frac{1}{r_x + r_c} \tag{4.36h}$$

$$a_{31} = -\frac{\rho c_p}{r_x} \tag{4.36i}$$

$$a_{32} = \frac{\rho c_p}{r_x} + \left[\frac{\rho c_p}{\gamma\Delta}\frac{1}{r_x + r_c}\right] \tag{4.36j}$$

$$a_{33} = 0 \tag{4.36k}$$

$$a_{34} = -\frac{\rho c_p}{\gamma(r_x + r_c)} \tag{4.36l}$$

$$a_{41} = -\frac{\rho c_p}{r_s} \tag{4.36m}$$

$$a_{42} = 0 \tag{4.36n}$$

$$a_{43} = \frac{\rho c_p}{r_s} + \left[\frac{\rho c_p}{\gamma\Delta}\frac{1}{r_s + r_{ss}}\right] + \frac{\lambda_g}{4.5D} \tag{4.36o}$$

$$a_{44} = -\frac{\rho c_p}{\gamma(r_s + r_{ss})} \tag{4.36p}$$

instead, the known terms b_1–b_4 are:

$$b_1 = \frac{T_a}{r_a} \tag{4.37a}$$

$$b_2 = \frac{e_a}{r_a} + \left[(e_a^* - \Delta T_a)\left(\frac{1}{r_x + r_c}\frac{1}{r_s + r_{ss}}\right)\right] \tag{4.37b}$$

$$b_3 = R_{n,c} - \left(\frac{\rho c_p}{\gamma}\frac{e_a^*}{r_x + r_c}\right) + \left(\frac{T_a \Delta \rho c_p}{\gamma}\frac{1}{r_x + r_c}\right) \tag{4.37c}$$

$$b_4 = R_{n,s} + \frac{\lambda_g}{4.5D}T_{\text{deep}} - \left(\frac{\rho c_p}{\gamma}\frac{e_a^*}{r_s + r_{ss}}\right) + \left(\frac{T_a \Delta \rho c_p}{\gamma}\frac{1}{r_s + r_{ss}}\right) \tag{4.37d}$$

The dependence of known coefficients b_3 and b_4 from the unknowns T_c and T_s (by means of the terms $R_{n,c}$ and $R_{n,s}$, see Eqs. (2.54) and (2.55)) is addressed by the iterative solution of the system of Eqs. (4.35). The iterative approach allows also to take into account the effects of stability conditions on resistance, analogously to the approach described for the TSEB.

The functional connection between E_s–ET_c and hydrological balance is obtained, in this case, by the dependence of the resistance r_c and r_{ss} on θ_1 and θ_2, expressed by Eqs. (2.145) and (2.146).

4.4 Data Assimilation in LSMs

The basic objective of data assimilation technique is to merge different information sources, with the purpose to provide the best estimate of the current state of an environmental system.

In the past, meteorologists and oceanographers have successfully managed this challenge, developing numerous data assimilation techniques (see Bennett and Ho, 1992; Courtier *et al.*, 1993). Data assimilation has been recently applied also in hydrological problems (McLaughlin, 1995), within three data assimilation frameworks (McLaughlin, 2002):

- *interpolation*, adopted to characterize the state of the system in a time-invariant condition;
- *smoothing*, adopted to characterize the time-dependent state of the system over a fixed data interval when a set of observations are available;
- *filtering*, adopted to characterize the state of the system over a growing data interval when new observation are continuously available.

In the context of continuous modelling of soil water content and evapotranspiration is obvious to refer to the filtering problem, which can be solved with variational method or sequential assimilation. In the first case, the whole set of available observations is used to update model state and parameters. The second approach, involves the correction of state variables (e.g., soil moisture) whenever new observation are available.

In practise, due to the indefinitely increasing of observations, the variational schemes generally adopt fixed lag windows (Meirink and Bergamaschi, 2008) sometimes computationally inefficient. For this reason, the sequential scheme are usually widely used.

Remotely sensed land surface temperature have been assimilated into various point-scale scheme for land surface modelling (Kalma *et al.*, 2008) by comparing simulated and observed temperatures and adjusting either state variable (e.g., Caparrini *et al.*, 2003; Olioso *et al.*, 2002) or model parameters (e.g., Boulet *et al.*, 1999; Braden and Blanke, 1993; Couralt *et al.*, 2005).

Significant progresses in the recent years in estimation surface fluxes from thermal imagery sequences considerably improve the case studies on the assimilation of ET or soil moisture maps derived from satellite, as described by van der Hurk *et al.* (1997) and Pan *et al.* (2008).

Sequential assimilation algorithms typically divide the estimation process into two steps (McLaughlin, 2002): 1) the propagation of the system state between two following measurement times (also known as prediction), and 2) the update of the state to account the new information (correction). This approach is schematically described in Figure 4.8. Due to the stochastic framework of the data assimilation, both propagation and updating provide estimation of the probability density of the state.

Close form solution of the propagating of state density function and successive updating is available, on the basis of Bayes theorem, only in the simple linear Gaussian case. The solution of this problem is the widely used Kalman filter (Kalman, 1960), which is the base for almost all the practical filtering applications.

4.4.1 Kalman filtering problem

The theory on the optimal filtering of linear dynamic system with additive Gaussian noise was initially developed by Kalman (1960). Following his approach, the temporal evolution of the state of the system (in our case the soil water content) can be functionally described as:

$$\theta_{t+1} = f(\theta_t, j_t, \psi, t) + \varpi_t \tag{4.38}$$

where θ_{t+1} and θ_t are the state of the system at the time $t+1$ and t, respectively, j_t is the vector of forcing data (external inputs), ψ is the

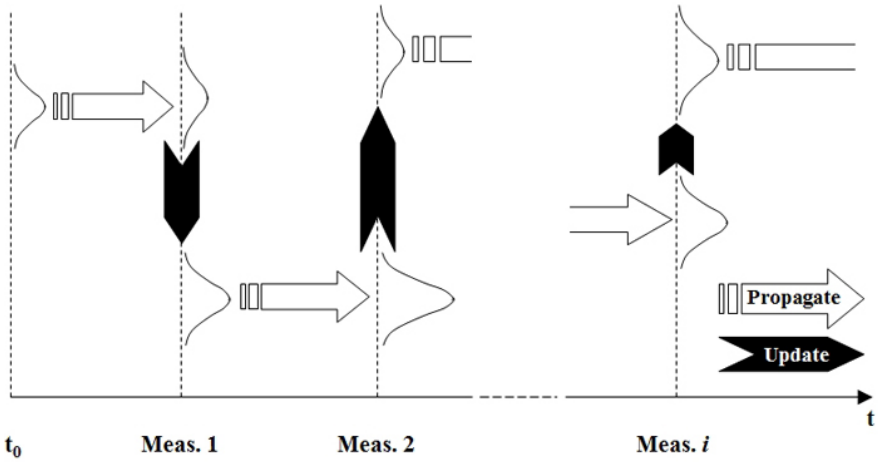

Figure 4.8: Sequential data assimilation filtering. The probability density of the state is propagated forward to the next observation time and then updated by means of the new measurements (redraw from McLaughlin, 2002).

vector of the model parameters and ϖ_t is the additive model uncertainty.

Since the system states are not necessarily observable, it is useful to define a vector, $\overline{y}_t$, of the observable outputs (e.g., surface temperature, energy fluxes) that depend on the states:

$$\overline{y}_t = g(\psi, t) \tag{4.39}$$

The vector $\overline{y}$ (also known as prediction vector) is generally associated to the observation vector, $\hat{y}$, which represent the remotely observed values of the outputs.

If the Eqs. (4.38) and (4.39) are linear, with independent, Gaussian and additive errors, the state estimation with minimum errors can be obtained as:

$$\theta^{+}_{t+1} = \theta^{-}_{t+1} + \Xi_{t+1}(\hat{y}_{t+1} - \overline{y}_{t+1}) \tag{4.40}$$

in which the super-scripts "+" and "-" identify the update and propagate state of the system, respectively.

The term Ξ_{t+1} represents the *Kalman gain matrix*, defined as:

$$\Xi = \Sigma^{\theta y}\left[\Sigma^{yy} + \Sigma^{y}\right]^{-1} \tag{4.41}$$

where $\Sigma^{\theta y}$ is the forecast cross covariance of the state and the prediction, Σ^{yy} is the forecast error covariance matrix of the prediction and Σ^{y} is the covariance of the remote observation.

In the Eq. (4.41) the sub-script "t" was skipped just for simplicity from all the terms.

4.4.2 The ensemble Kalman filter

Despite its interesting features (e.g., optimality, analytical solution) the hypotheses adopted for the derivation of the Kalman filter preclude the applicability in strongly non-linear model or system characterized by non-Gaussian errors.

For this reason, Evensen (1994) have introduced the so-called Ensemble Kalman Filter (EnKF), which bases the computation of the error covariance matrices by means of Monte Carlo method (Liu and Chen, 1995).

Ensemble filtering provides an alternative that addresses many of the difficulties posed by high-dimensional non-linear filtering problem (Evensen, 1994; Miller *et al.*, 1994; Reichle *et al.*, 2002). More recently, smother methods were also introduced (e.g., Cohn *et al.*, 1994; Evensen and van Leeuwen, 2000), but these ones are not considered in this work.

In the EnKF framework, the covariance matrices are computed by means of an appropriate ensemble of the model states. Because an ensemble of finite size, n_r, only provides an approximation of the true error covariance matrix, the ensemble size in the Monte Carlo sampling should be opportunely chosen.

The use of Monte Carlo procedure allows to compute the covariances in Eq. (4.41) by means of a numerical solution. The Eq. (4.41) can be applied to update both the system state and the model parametrisation, as described in the following sub-sections.

State update filtering

The flow chart in Figure 4.9 schematically represents the EnKF procedure adopted to update the system state.

After defining the sample size, the forcing data are perturbed by adding a noise, η_t^i, with covariance Σ^j to the i-th (of n_r) replicate:

$$j_t^i = j_t + \eta_t^i \qquad \eta_t^i \sim N(0, \Sigma^j) \tag{4.42}$$

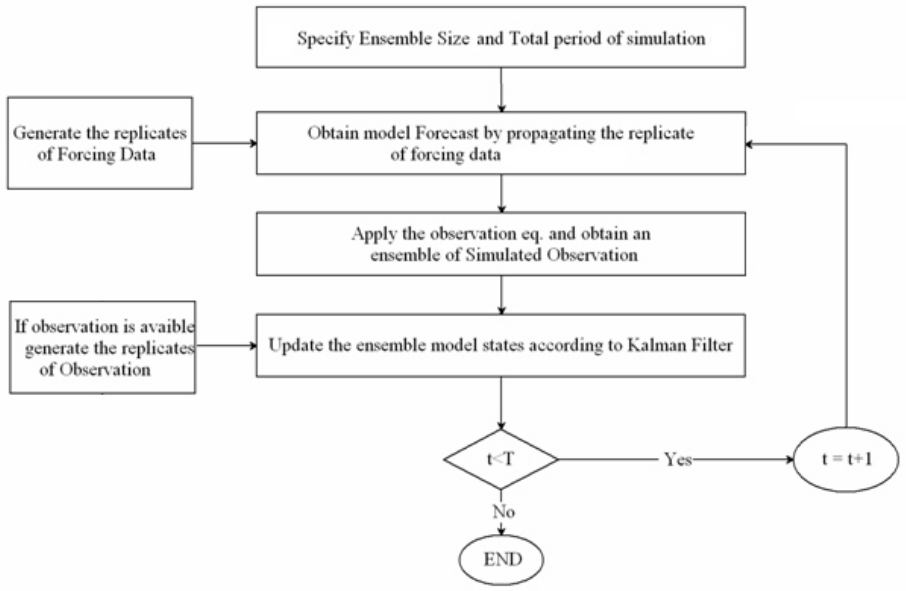

Figure 4.9: State update flowchart using the ensemble Kalman filter (adapted from Moradkhani *et al.*, 2005).

The n_r model forecasts are obtained by propagating the forcing data using the model equation:

$$\theta_{t+1}^{i} = f(\theta_t^i, j_t^i, \psi, t) + \varpi_t^i \qquad i = 1, ..., n_r \tag{4.43}$$

where the model parameter vector are time-invariant and defined *a priori*.

When the observation are available, the i-th trajectory of the observation replicates are generated by adding the noise ς_t^i with covariance Σ^y, as defined in Eq. (4.41).

The replicates of the state are then updated by means of the ensemble version of the Kalman filtering:

$$\theta_{t+1}^{i+} = \theta_{t+1}^{i-} + \Xi_{t+1}^{\theta}(\hat{y}_{t+1}^i - \overline{y}_{t+1}^i) \tag{4.44}$$

where Ξ^{θ} is computed by means of Eq. (4.41). The main advantage of this approach is that the estimation of the *a priori* error covariance is not needed, although it can be numerically computed from the ensemble replicates.

Dual state-parameter filtering

Although models are generally defined by means of parameters that are physically defined and time-invariant, one of the main source of uncertainties in a model prediction is its parametrization. Models parameter can be estimated in a batch-processing using historical data or by means of their physical meaning. Because there is no guarantee that model parametrization is correctly realised and its behaviour does not change over the time, model adjustment through the time may be required (Moradkhani *et al.*, 2005).

An alternative way for model parameters estimation problem is the dual state approach, designed as two sub-sequential filters as described in Figure 4.10.

Following this approach, the time-dependent model parameter, ψ_t, are updated similarly to the system state according to the standard Kalman filter equation. In order to extend the applicability of this approach to parameter estimation, we need to treat the parameters similarly to the state variables with the difference that parameter evolution should be set up artificially (Gordon *et al.*, 1993).

Following the approach suggested by West (1993a,b), known as kernel smoothing, the parameters samples are artificially propagated as:

$$\psi_{t+1}^{i-} = \alpha_p \psi_t^{i+} + (1-\alpha_p)\overline{\psi_t^{+}} + h_p \upsilon_t^i \qquad \upsilon_t^i \sim N(0, \Sigma^{\psi}) \tag{4.45}$$

where $\overline{\psi_t^{+}}$ is the samples average, α_p is the shrinkage factor (0,1), and h_p is the smoothing or variance reduction parameter. The last two are related by: $\alpha_p^2 + h_p^2 = 1$.

The propagated parameter samples are updated, before to update the system state, by means of the following filtering equation:

$$\psi_{t+1}^{i+} = \psi_{t+1}^{i-} + \Xi_{t+1}^{\psi}(\hat{y}_{t+1}^i - \overline{y}_{t+1}^i) \tag{4.46}$$

The Kalman filter for the case of parameters vector update is defined, analogously to Eq. (4.41), as:

$$\Xi^{\psi} = \Sigma^{\psi y}\left[\Sigma^{yy} + \Sigma^{y}\right]^{-1} \tag{4.47}$$

where $\Sigma^{\psi y}$ is the cross covariance of the parameter ensemble and prediction ensemble.

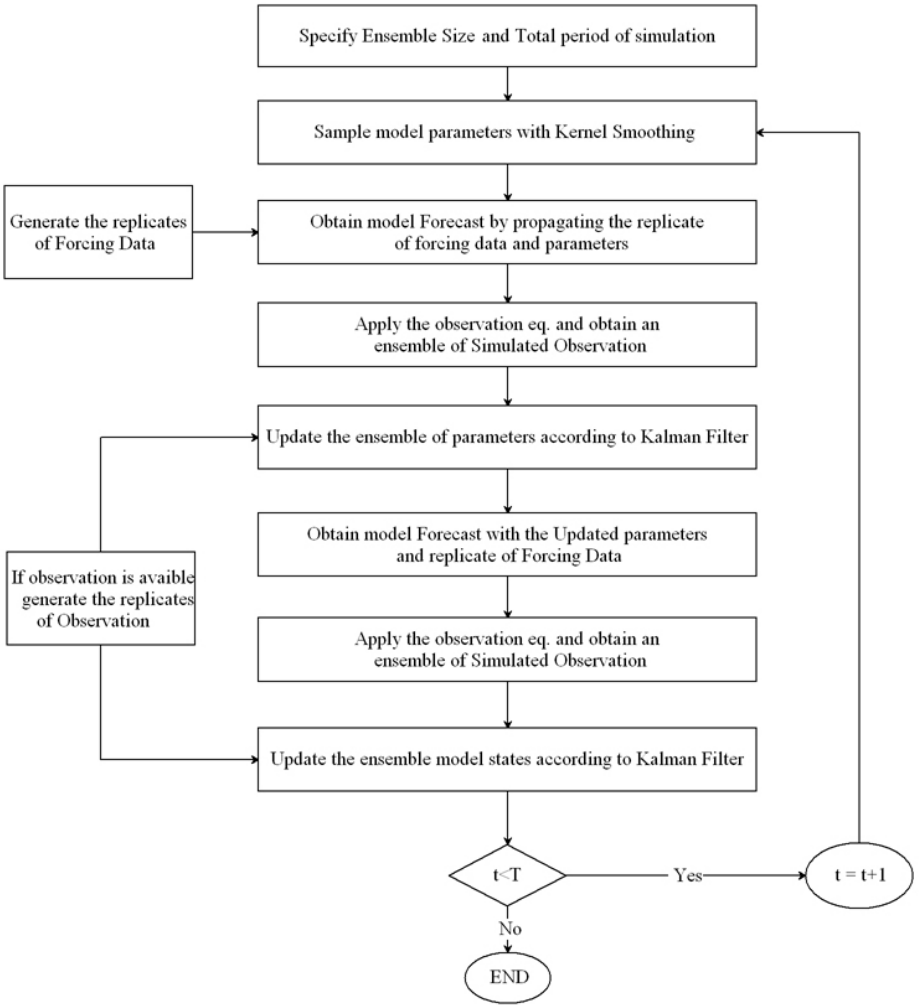

Figure 4.10: Dual state-parameter estimation flowchart using the ensemble Kalman filter by kernel smoothing of parameters (redraw from Moradkhani *et al.*, 2005).

Equality constrain

Due to the update of system state, the EnKF causes the water budget imbalance. For this reason, the final step in data filtering is the application of a water balance constraint filter, as suggested by Pan *et al.* (2008). This constraint works as a post-processor that redistributes the budget imbalance term back into various balance terms according to their uncertainty levels.

In particular, we adopts a simplified version of this approach which assigns the imbalance term only to soil evaporation and canopy transpiration, proportionally to the fluxes magnitudes.

Chapter 5

Study area and materials

In this chapter the description of the test site monitored during the 2007–2009 period by means of micro-meteorological installations, including two eddy-covariance and a scintillometer systems is reported. During the 2008 the same area was interested by a set of remote sensing airborne acquisitions, in order to retrieve high resolution maps of some variables of hydrological interest. Contextually, MSG products, processed by LSA SAF system, were acquired and used for coarse spatial resolution variables retrieval. This dataset was used for the analysis of micro-meteorological measurements reliability, following the criticisms highlighted in Chapter 3, and for the application and validation of the approaches described in Chapter 4.

5.1 Test site description

The study site is located in southern Italy, Sicily, in a highly fragmented agricultural landscape, mainly dominated by orchards and vineyards with strongly clumped vegetation cover, set in a typical Mediterranean climate.

In detail, the experiment site is located in south-west coast of Sicily about 5 km south-east of the town of Castelvetrano (TP) (37°38'35" N latitude and 12°50'50" E longitude). The crops grown in this region are mainly olive trees, grapes and citrus trees. The landscape around the study

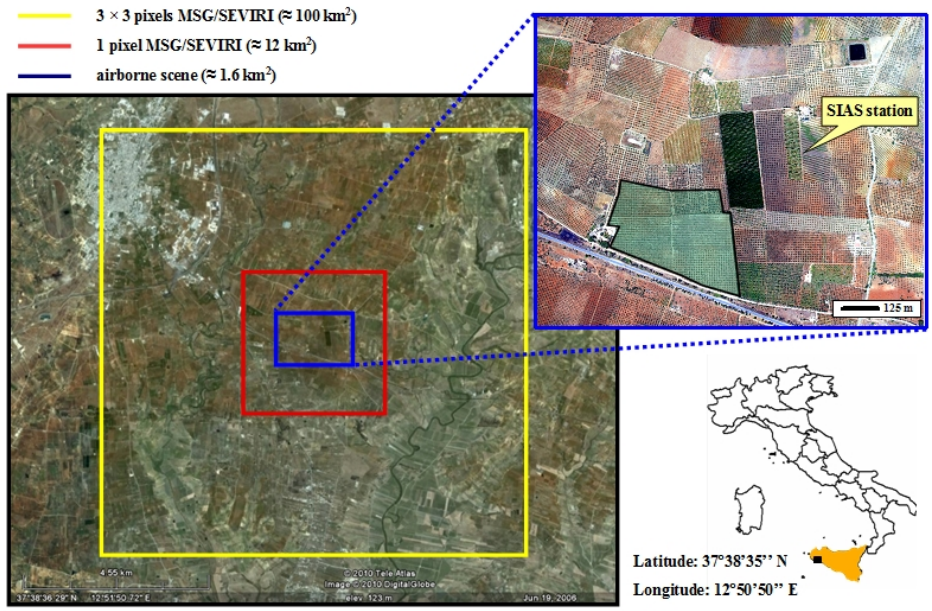

Figure 5.1: Geographical localization of the study area. The blue box demarcates the area interested by airborne acquisitions, highlighted on the right. Red and yellow boxes demarcate an area one and three-times the average MSG pixel ($\approx$ 3.2 km side length), respectively. Both the boxes are centered on the airborne acquisition area. The green filled area in the right-side images highlights the field interested by micro-meteorological installations.

site is generally flat and highly fragmented, with a mean field size of few hectares, alternating different crop types and fallow fields with bare soil (Figure 5.1).

The area interested by airborne remote sensing acquisitions encompasses a surface of approximately 160 ha (1.6 km^2) in area. In the eastern side of this area is located a meteorological installation of the SIAS (*Servizio Informativo Agrometeorologico Siciliano*), which provides measurements of the main meteorological variables (e.g., incoming solar radiation, air temperature, pressure and humidity, wind velocity and rainfall).

From a climatic standpoint, the area is characterized by a typical Mediterranean climate with moderate rainfall during the autumn and winter periods and very high air temperature, with little precipitation

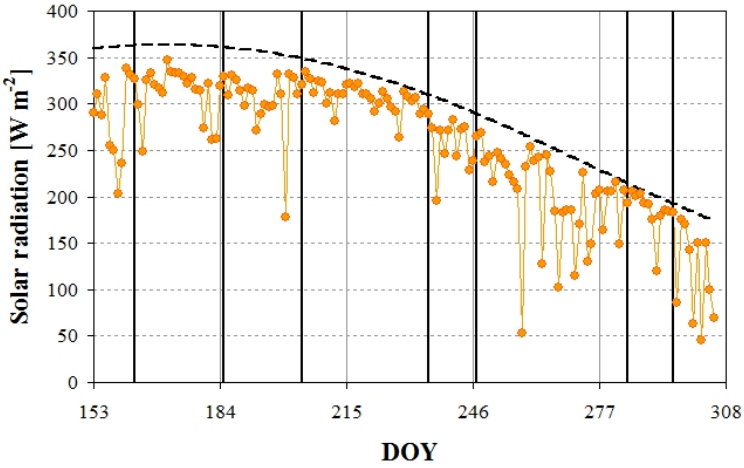

Figure 5.2: Daily average solar radiation observed by SIAS station from June to October 2008. Orange line with circles represents R_s, dotted black line R_{so}. Black vertical bars highlight the airborne overpasses.

during the summer months. The phase shift between the crop phenological (growth) cycle and the rainfall events generally results in a high evaporative demand during the Summer period, especially in absence of precipitation during the Spring. The average annual rainfall ranges, in the last 5 years, from 450 to 650 mm; on the contrary, atmospheric evaporative requirement (computed using the FAO-56 formulation) generally exceeds the annual rainfall, and ranges, in the same period, between 1000 and 1200 mm.

Figures 5.2–5.6 show the daily values of the main meteorological variables in the period June–October 2008.

The observed solar radiation values (Figure 5.2) highlight an almost constant value of about 350 w m^{-2} in the first two observed months (June and July), and a decrease close to linearity in the remaining period, to a value of about 150 w m^{-2} in the last days of October. The upper envelope of R_s values with the R_{so} ones confirms the good response of the station on the basis of the integrity analysis suggested by Allen *et al.* (1998).

Air temperature data (Figure 5.3) analysis shows how the dataset can be subdivided in two main periods: a first one, June-August, with an higher average value ($\approx$ 298 K) and strong variability; a second one, September-October, with lower average value ($\approx$ 292 K) and smaller variability.

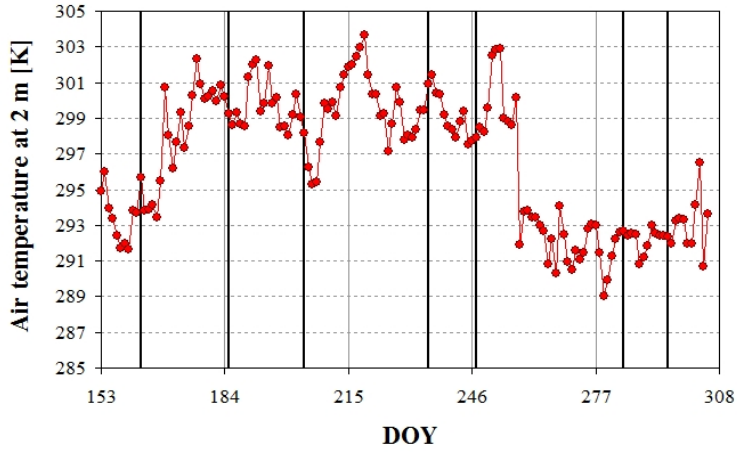

Figure 5.3: Daily average air temperature observed by SIAS station from June to October 2008. Black vertical bars highlight the airborne overpasses.

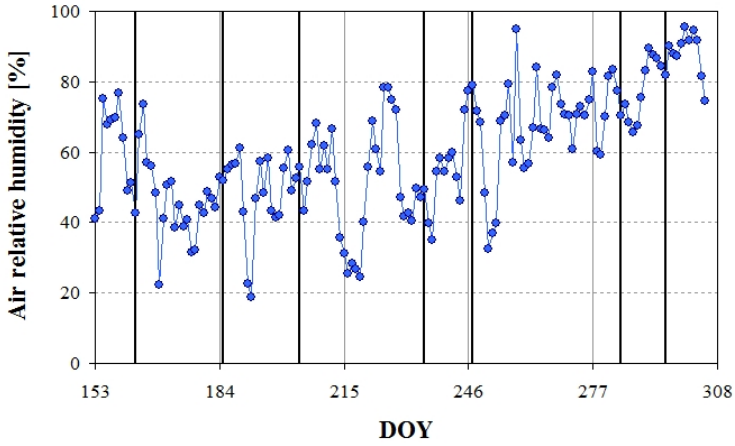

Figure 5.4: Daily average air relative humidity observed by SIAS station from June to October 2008. Black vertical bars highlight the airborne overpasses.

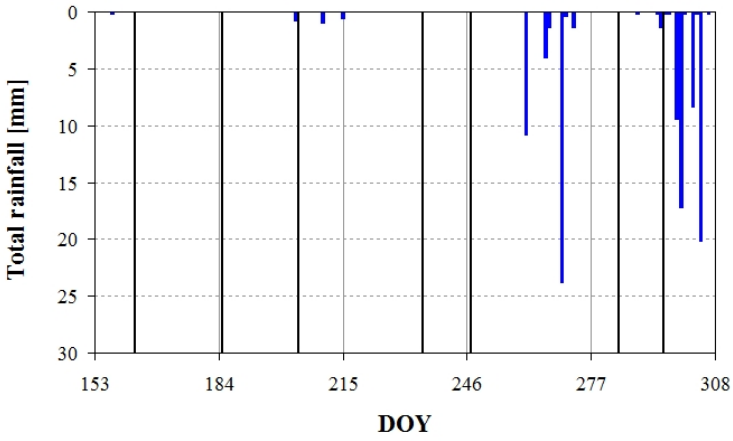

Figure 5.5: Daily total rainfall observed by SIAS station from June to October 2008. Black vertical bars highlight the airborne overpasses.

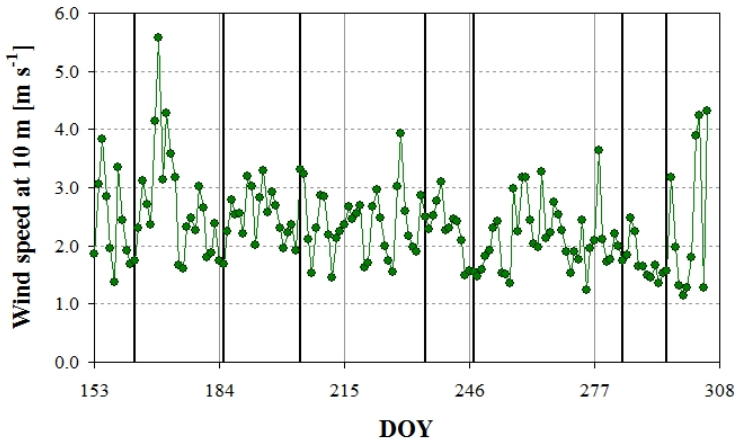

Figure 5.6: Daily average horizontal wind speed observed by SIAS station from June to October 2008. Black vertical bars highlight the airborne overpasses.

Opposite behaviour can be found in air relative humidity data (Figure 5.4), where a first low humidity period is followed by a second moist period.

Both these behaviours can be explained by the analysis of rainfall plot (Figure 5.3), which presents two significant rainfall periods in the middle-end of September, with a total rainfall of about 40 mm, and at the end of October (60 mm).

Finally, the analysis of horizontal wind speed data (Figure 5.6) do not show particular trend in the data, with an average value of about 2.5 m s^{-1}, with extremes of about 1 and 5.5 m s^{-1}.

The southern part of the area is mainly characterized by olive orchards, and in particular an olive (*Nocellara del Belice*) field of about 13 ha in size (demarcated by green-filled area in Figure 5.1) located within the "*Consiglio*" farm. This orchard was the object of micro-meteorological measurements by means of the experimental stations.

The orchard olive trees have been planted on regular grid with a plants density of about 250 trees/ha. The mean olive canopy height is about 3.3 m with a mean fractional canopy cover of approximately 0.35. The soil can be classified as silty clay loam, according to the USDA classification, with average content of clay, silt and sand of 24, 16 and 60% respectively.

In order to analyze the in-field homogeneity, the entire olive orchard was subdivided into 7 sub-plots (Figure 5.7). The main average sub-plots characteristics are reported in Table 5.1.

The small standard deviation (± 0.04) of the field fraction cover confirms a quite good homogeneity, allowing to consider the field suitable for micro-meteorological installations.

In Figure 5.7 the locations of the micro-meteorological installations, as detailed in the next sub-section, are also reported.

5.2 Experimental installations

As introduced in the previous sub-section, the experimental olive orchard was monitored by means of three micro-meteorological installations.

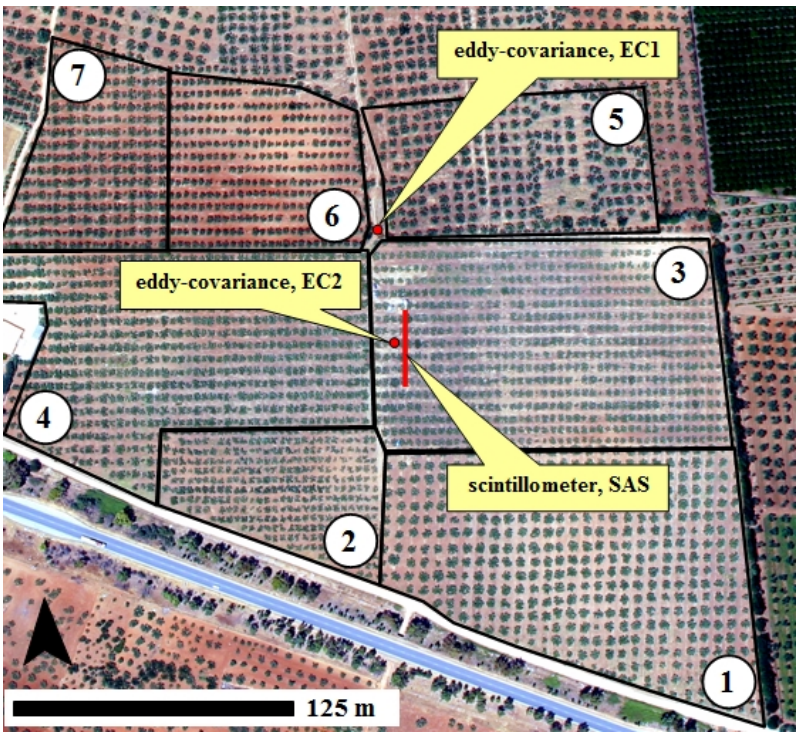

Figure 5.7: Orthophoto of the test field, and its partition in sub-plots with localization of the eddy covariance (EC1 and EC2) and small aperture scintillometer (SAS) installations.

Table 5.1: Main characteristics of the sub-plots which constitute the olive orchard under study.

Sub-plot	Surface [ha]	Plants spacing [m × m]	f_c	Irrigation
1	3.15	8 × 8	0.32	trickle
2	0.95	6 × 6	0.39	sprinkler
3	3.00	5 × 8	0.30	trickle
4	2.71	8 × 5	0.36	sprinkler
5	1.46	8 × 8	0.41	aspersion
6	1.31	5 × 8	0.32	sprinkler
7	1.11	5 × 8	0.35	sprinkler

Figure 5.8: Eddy-covariance installation EC1.

5.2.1 Eddy-covariance system, EC1

The eddy-covariance system EC1 is located, as reported in Figure 5.7, in the northern part of the experimental field and it is part of the CarboItaly project, ˝the Italian network of eddy covariance installations for agricultural and forest sink˝ (Papale, 2006).

The installation was set-up in the spring of the 2006 and it still provides continuous measurements of water vapour, carbon dioxide and other energy balance component fluxes. It is propriety of the SIAS and is managed by the research group of Prof. Motisi (*Dipartimento di Colture Arboree, Università degli Studi di Palermo*) and by the CNR-IBIMET (Bologna).

The EC1 system (Figure 5.8) consists of a NR-Lite-L net radiometer (*Kipp & Zonen*), placed at an elevation of 8.5 m, for field representative (canopy and soil) measurements of: i) incoming beam and diffuse solar radiation plus long-wave irradiance from the sky, ii) outgoing reflected solar radiation plus terrestrial emitted long-wave component. The soil heat flux was measured using three flux plates (HFP01, *Hukseflux*) located in

Figure 5.9: Detail of CSAT3-3D sonic anemometer and LI7500 open-path gas analyzer the of the EC1 system.

the exposed bare soil at a measurements depth of about 5 cm. Both net radiation and soil heat flux measurements were stored at 30-minute time interval.

The high frequency measurements were carried out by means of a CSAT3-3D sonic anemometer (*Campbell Scientific Inc.*) and a LI7500 open-path gas analyzer (*Li-cor Biosciences Inc.*), that measured the concentration of H_2O and CO_2, installed at an elevation of 8 m above the ground (Figure 5.9); sample frequency for the raw data for both instruments was 10 Hz.

All the data were recorded using a CR3000 datalogger (*Campbell Scientific Inc.*) equipped with a PCMCIA memory card, without the need of external portable computer for data storage. The half-hourly values were successively derived in the post-processing phase.

The post-processing phase follows the CarboEurope IP standard protocol. In summary, the de-trending technique, reported in (Moncrieff *et al.*, 2004), was applied, sonic anemometer data were transformed using a coordinate rotation (Finnigan *et al.*, 2003) and the correction for spectral

Table 5.2: Main characteristics of SLS20 double beam small aperture scintillometer.

Parameter	Symbol	Unit	Value
Wavelength	λ_{wl}	nm	670
Diameter	$\overline{D}$	mm	2.5
Separation between two beams	d	mm	2.7
Path length	P	m	95
Fresnel zone	F	mm	8.0

loss was performed (Moncrieff *et al.*, 1997).

High frequency anemometer data were corrected for sonic temperature and sensible heat flux (Liu and Peters, 2001; Schotanus *et al.*, 1983) and vapour pressure data were corrected by means of Webb-Pearman-Leuning procedure (Moncrieff *et al.*, 1997).

Finally, the data were adjusted by means of a de-spiking procedure as described by Vickers and Mahrt (1997).

5.2.2 Scintillometer system, SAS

The scintillometer installation was located in the middle of the olive experimental site (see Figure 5.7) and acquired data during three separate periods: July–September 2007, August–October 2008 and May–August 2009.

The instruments used in this experiment were composed by the Optical Energy Balance Measurement System (OEBMS1) developed by *Scintec AG*. In detail, the system included a SLS20 double beam small aperture scintillometer (Figure 5.10), characterized by an aperture size of 2.5 mm, a beam displacement of 2.7 mm, a beam divergence of 5 mrad, and an operational beam wavelength of 670 nm. These and others main SAS characteristics are reported in Table 5.2.

Both transmitter and receiver were installed on two tubular scaffolding iron-frameworks, with a path distance of about 95 m, along the north-south direction almost perpendicularly to the dominant wind direction. The instrument height was set-up at 5.8 m for the 2007, and 7.1 m for the 2008 and 2009.

Net radiation was measured using a two component pyrradiometer (*Schenk GmbH*, model 8111), installed at an elevation of 7.5 m a.g.l., as the

Figure 5.10: Scintillometer installation SAS.

difference between the radiation received from the upper sensor hemisphere and the radiation received from the lower sensor hemisphere, where both refer to the same horizontal plane (Figure 5.11).

Soil heat flux was computed using three soil heat plates (HFP01SC, *Hukseflux*), placed respectively: one in correspondence of canopy foliage projection, in order not to be exposed to direct solar radiation; one in an always directly exposed bare soil; and the last in an intermediate position. Data from the three soil plates have been finally averaged to retrieve a field scale representative value.

All the OEBMS1 data were acquired every 2 minutes, with scintillometer raw data coming from an average of 20 acquisitions, using a signal processing unit interface with all the sensors and a connection with a PC.

The SAS raw data were directly post-processed by the acquisition software, which returns as output: sensible heat flux, friction velocity,

Figure 5.11: Pyrradiometer (*Schenk GmbH*, model 8111) of the OEBMS1 system installed on the SAS transmitter iron-frameworks at an elevation of 8 m a.g.l. (upper panel). In the lower panel a detail of the pyrradiometer (on the right side) and of the solar radiometer (on the left side).

scale temperature and Monin-Obukhov length for both stable and unstable conditions.

As described in sub-section 2.3, the latent heat flux is computed directly by the acquisition software as a residual of the energy balance equation, on the basis of the other components measurements, and also in this case both for stable and unstable sensible heat flux cases.

The choice of the proper stability condition, and the relative MOST derived fluxes, was done with auxiliary air temperature gradient measurements realized by two aspirated temperature sensors PT-1000 (Figure 5.12), placed above the ground at about 4 and 5.5 m.

In addition, in the post-processing phase, the 2-minutes time step fluxes

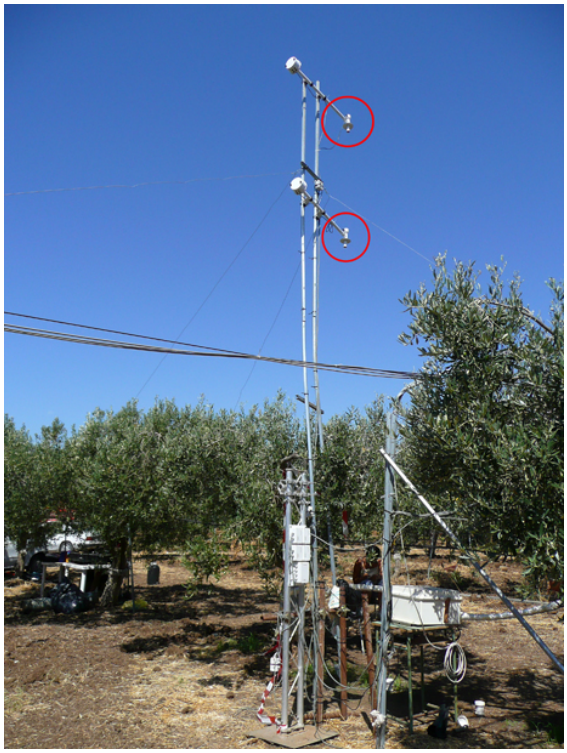

Figure 5.12: Detail of the two aspirated temperature sensors PT-1000 of the OEBMS1 system. The two sensors, placed at an elevation above the ground of about 4 and 5.5 m, allow to detect the proper stability conditions.

were averaged to a 30-minute and 1 hour time interval, to allow the direct comparison with the eddy-covariance outputs ad models estimations.

5.2.3 Eddy-covariance system, EC2

The eddy-covariance system EC2 was installed in the 2009 in the middle of the SAS path, as highlighted in Figure 5.7, with the aim to minimize the discrepancies in the two technique source areas.

The EC2 system (Figure 5.13) is constituted by a CNR-1 four component net radiometer (*Kipp & Zonen*), placed at an elevation of 8.5 m. This instrument, in the 4SCM configuration, allows to measure separately two short-wave radiation signals (incoming and outgoing) and two far infrared signals (emitted and incident) and, for calculation purpose (see sub-section 3.2.1), case temperature by means of one PT-100 signal. The two solar radiation measurements were performed by face -down -up CM3 sensors, and the far infrared radiation by means of two analogous CG3 sensors.

The soil heat flux was measured using two flux plates (HFP01, *Hukseflux*) located in the exposed and shadowed bare soil, respectively, at a measurements depth of about 10 cm. Both net radiation and soil heat flux measurements were stored at 30-minute time interval.

The high frequency measurements were carried out, similarly to the EC1 system, by means of a CSAT3-3D sonic anemometer (*Campbell Scientific Inc.*) and a LI7500 open-path gas analyzer (*Li-cor Biosciences Inc.*), that measured the concentrations of H_2O and CO_2, installed at an elevation of 7 m above the ground (Figure 5.13); sample frequency for the raw data for both instruments was 20 Hz. The EC2 high frequency instruments were placed at the same height of the SAS laser path, in order to minimize, also in this case, the discrepancies between the two measurements.

Additionally measures are canopy and soil surface radiometric temperature realized using two IRTS-P precision infrared sensors (*Apogee Instruments Inc.*), placed at an elevation above the ground of 4 and 1.5 m, respectively.

Moreover, standard low-frequency (30-minutes) meteorological measurements as air temperature, pressure and humidity, wind speed and direction, were realized. Photosynthetically Active Radiation (PAR, incoming radiation in the range 0.35–0.75 μm) was measured, separately for total and diffuse components, by means of two SKP 215 quantum sensor

Figure 5.13: Eddy-covariance installation EC2.

(*Skye Instruments Ltd.*), one of which was equipped with a shadow-band to obscure the solar disk from the sensor.

Finally, vegetation growth were continuously monitored by means of SKR 1800 two channel light sensor (*Skye Instruments Ltd.*), for the measurements of reflectances in red (0.66 μm) and near-infrared (0.73 μm) bands, used for vegetation indices assessment (e.g., NDVI).

All the data (low and high frequency) were recorded using a CR5000 datalogger (*Campbell Scientific Inc.*) equipped with a PCMCIA memory card.

The high frequency data were pre-processed adopting the procedure implemented by Manca (2003), substantially analogous to the one described for the EC1 raw data.

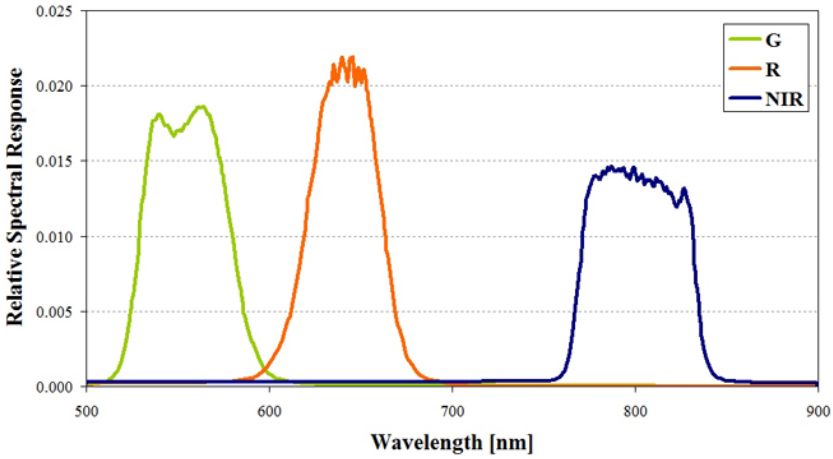

Figure 5.14: *Duncantech MS4100* relative spectral responses for green (G), red (R) and near-infrared (NIR) bands.

5.3 Acquisition and processing of remotely sensed data

The remotely-sensed dataset used to apply the previous described approaches is constituted by 7 high resolution airborne images, acquired between June and October 2008 as part of the DIFA (*DIgitalizzazione della Filiera Agroalimentare*) project, and LSA SAF products derived from MSG images acquired in 2007 and 2008.

5.3.1 Airborne - high resolution images

The airborne remote sensing data were collected by Terrasystem s.r.l. using a SKY ARROW 650 TC/TCNS aircraft, at a height of nearly 1000 m a.g.l.. The platform had on board a multispectral camera *Duncantech MS4100* with 3 spectral bands at green (G, 530-570 nm), red (R, 650-690 nm) and near-infrared (NIR, 767-832 nm) wavelengths, and a *Flir SC500/A40M* thermal camera for radiometric temperature estimation. The *Duncantech* sensor relative spectral responses are reported in Figure 5.14. The nominal pixel resolution was approximately 0.6 m for VIS/NIR acquisitions, and 1.7 m for the thermal-IR data.

Table 5.3: Scheduling of the airborne remotely-sensed images.

n. flight	Date	DOY	Time [local*]
1	11/06/2008	163	13:30
2	03/07/2008	185	11:00
3	22/07/2008	204	11:30
4	22/08/2008	235	12:00
5	03/09/2008	247	11:30
6	10/10/2008	284	11:00
7	21/10/2008	295	11:30

*local time = UTC + 2

In Figures 5.2–5.6 the scheduling of the acquisitions (vertical black lines), along with the temporal trend of the main meteorological variables observed by SIAS weather station are overimposed. A summary of the acquisition days and time are also reported in Table 5.3.

Of particular interest are the two moderate rainfall events (of about 10 and 25 mm) that occurred between the 5^{th} and the 6^{th} remote sensing acquisitions on DOY 258 and 267 (see Figure 5.5). These events made the last two acquisitions different from the previous overpasses in terms of water availability and, consequently, potential water stress conditions. Additionally, the analysis of Figures 5.3, 5.4 and 5.2 highlights how the air temperature and humidity and the solar radiation were completely different for these last two acquisitions.

Measurement campaigns for airborne data calibration

To produce reliable surface reflectance and radiometric surface temperature maps, removing effects of atmospheric absorption and scattering, the aircraft imagery was semi-empirically calibrated using *in-situ* radiometric observations. Additionally, retrievals of vegetation properties such as LAI and canopy height were improved using ground-truth data.

The ground measurement campaigns were conducted during each of the 7 acquisition days, starting 2 hours before the acquisition and finishing 2 hours after the aircraft overpass.

Specifically, spectroradiometric measurements were collected with an ASD Inc. FieldSpec HandHeld spectroradiometer over a number of natural

and artificial surfaces with different radiometric characteristics, surface temperature was measured using non-contact thermal-IR radiometers, LAI was measured for different crops using a LAI2000 optical instrument (*Li-cor Biosciences Inc.*), together with canopy height measurements. A linear interpolation (in time) of both spectroradiometric and surface temperature measurements was used for all the ground targets, in order to extrapolate the values at the same time of aircraft overpass.

Retrieval of variables of hydrological interest

In order to obtain the spatial distribution of the variables of interest for hydrological applications, the acquired snapshots were combined into a set of mosaics to overlap the entire study area. The obtained G, R and NIR maps of the 7 date were geo-referenced, radiometrically calibrated, and the atmospheric influence was removed by means of the empirical line method (Slater *et al.*, 1996) using the spectroradiometric information collected by *in-situ* measurements.

Similar corrections were applied to the thermal images to obtain ground-emitted radiance, $R^{\uparrow}$ [W m^{-2} μm^{-1} sr^{-1}], starting from the at-sensor data, R_{sens} [W m^{-2} μm^{-1} sr^{-1}].

Details on the pre-processing phase are reported in the Appendix A, with particular regard on the empirical radiometric calibrations of the multispectral and thermal images.

The multispectral images were used to derive the Normalized Difference Vegetation Index, NDVI, as (Rouse *et al.*, 1973):

$$\text{NDVI} = \frac{r_{\text{NIR}} - r_{\text{R}}}{r_{\text{NIR}} + r_{\text{R}}} \tag{5.1}$$

This index assumes value between -1 and +1, and it is useful to distinguish water body (NDVI <0) and land surface (NDVI >0). Additionally, NDVI can be used to discriminate full covered area and bare soil pixels; for this purpose limit values of $\text{NDVI}_{\text{max}} = 0.85$ and $\text{NDVI}_{\text{min}} = 0.15$ were assumed.

These limits can also be used for nadiral fraction cover retrieval by means of the relationship proposed by Choudhury *et al.* (1994):

$$f_c = 1 - \left(\frac{\text{NDVI}_{\text{max}} - \text{NDVI}}{\text{NDVI}_{\text{max}} - \text{NDVI}_{\text{min}}} \right)^{0.9} \tag{5.2}$$

where the exponent 0.9 is equal to the one suggested by Richter and Timmermans (2009).

This relationship was validated by means of a comparison with plot-scale average fraction coverage derived from an orthophoto (0.4 m resolution) acquired in correspondence of the first flight using a Canon EOS 20D digital camera. The average fraction coverage was derived, for each sub-plots demarcated in Figure 5.7, by means of a fixed threshold to distinguish between vegetate and non-vegetated areas. The results obtained for the sub-plots using Eq. (5.2) are the same reported in Table 5.1.

The surface albedo was retrieved using Eq. (2.38), with the weighting factors calibrated by means of a weighted linear combination of the observed reflectances (Price, 1990). For this purpose, "*true*" albedos were derived by means of spectral integration of signatures on different targets. Artificial reflectances for bands G, R and NIR were retrieved from the same data using the relative spectral response functions. Minimization of the difference between "*true*" albedos and simulated ones led to the following relationship:

$$\alpha = 0.312 r_{\mathrm{G}} + 0.277 r_{\mathrm{R}} + 0.411 r_{\mathrm{NIR}} \tag{5.3}$$

A comparison of the "*true*" albedo *vs.* simulated one is reported in Figure 5.15 in order to highlight the high performance of Eq. (5.3).

Leaf area index maps were derived using the following formula, introduced by Clevers (1989):

$$\mathrm{LAI} = -\frac{1}{0.75} \ln\left(1 - \frac{\mathrm{NDVI}}{0.95}\right) \tag{5.4}$$

where the parameters 0.75 and 0.95 were locally calibrated using the in-situ measurements of LAI at plant scale. The lower limit of validity of Eq. (5.4) was fixed equal to $\mathrm{NDVI} > 0.15$, assuming the LAI null for the lower values.

The results of calibration procedure for the first images are reported in Figure 5.16, where the measured LAI is compared with the modelled one derived from the NDVI maps. Due to the negligible variability of LAI for the olive trees (observed in the *in-situ* measurements), the calibration parameters were taken constant during the whole study period.

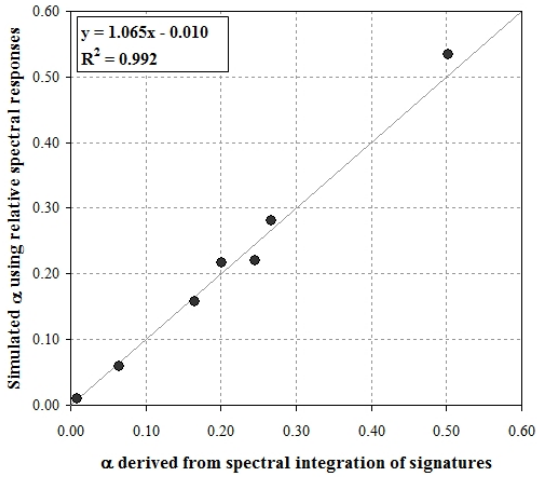

Figure 5.15: Analysis of weighted linear combination approach for albedo retrieval. Reference values were derived from spectral integration of signature on different targets, modelled values were obtained from simulated remotely sensed data using *Duncantech MS4100* camera relative spectral response functions.

Finally, the canopy heights were retrieved by means of local calibrated LAI-based polynomial empirical relationship, as suggested by Anderson *et al.* (2004). The result of the calibration procedure is reported in Figure 5.17.

Radiometric surface temperature maps, primary input of the TSEB model, were retrieved from ground-emitted radiance (see Appendix A) by means of Plank's law, as:

$$T_{\mathrm{RAD}} = \frac{c_2}{\lambda_{\mathrm{wl}}} \left[\ln \left(\frac{c_1 \epsilon_0}{\pi R^{\uparrow} \lambda_{\mathrm{wl}}^5} + 1 \right) \right]^{-1} \tag{5.5}$$

where c_1 and c_2 are two constants from Plank's law, λ_{wl} is the middle wavelength of the *Flir* camera spectral response (≈ 10.5 μm) and ϵ_0 was estimated using the relationship proposed by Sobrino *et al.* (2007) for the CIMEL 312-1 band 1 (see sub-section 2.1.3). In this equation the dependencies of $R^{\uparrow}$ and ϵ_0 from wavelength are removed just to simplify the notation.

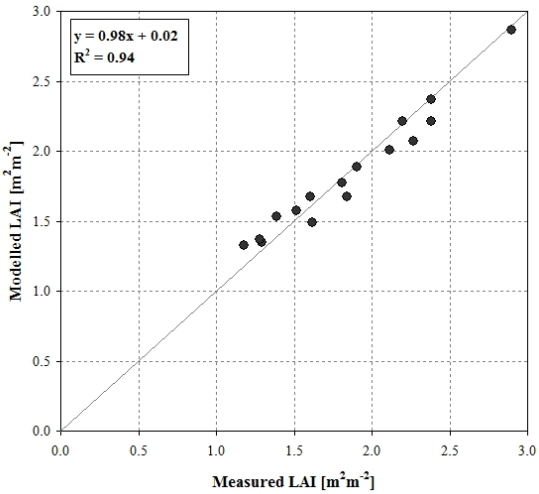

Figure 5.16: Analysis of LAI images calibration procedure. The measured values were derived, at plant scale, by means of Li-cor measurements and modelled values were obtained by means of calibrated Clevers model.

The surface temperature and biophysical parameters obtained maps were aggregated and co-registered to a common resolution of 12 m, to avoid spatial discrepancies between the multi-spectral and thermal datasets, following the suggestion of Anderson *et al.* (2004).

The aggregation procedure was essentially performed by means of the following simple expression, which refers to the NDVI:

$$\langle \mathrm{NDVI} \rangle = \sum_i f_i \mathrm{NDVI}_i \tag{5.6}$$

where the subscript "i" indicates the high resolution pixel inside the lower resolution one, and f_i is a weighting factor which takes into account the fraction of low-resolution pixel occupied by a high resolution one.

In the case of surface albedo, in order to determine separately the albedo of canopy and soil inside the 12 m resolution pixel, the average expressed by Eq. (5.6) is extended only to the vegetated pixels (NDVI > 0.85) and bare soil pixels (NDVI < 0.15), respectively.

The up-scaling of radiometric temperature was performed, instead, by

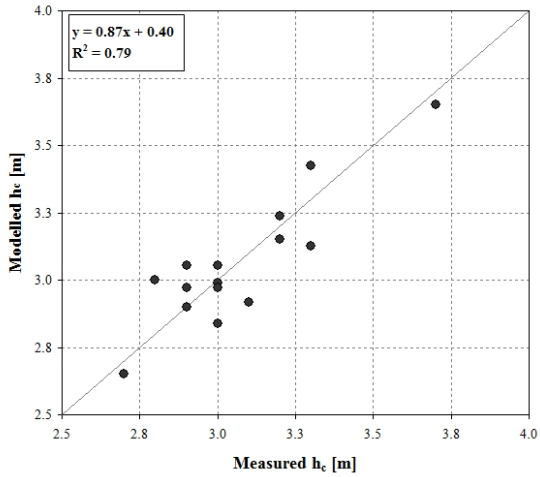

Figure 5.17: Analysis of h_c images calibration procedure. The measured values were measured for the same plant adopted for LAI calibration and modelled values were obtained by means of locally-calibrated empirical relationship.

means of the following relationship:

$$\langle T_{\mathrm{RAD}} \rangle = \frac{\left[\sum_i f_i \epsilon_{0,i} \left(T_{\mathrm{RAD},i}\right)^4\right]^{0.25}}{\langle \epsilon_0 \rangle} \tag{5.7}$$

The resolution of 12 m was also selected in order to obtain a pixel dimension just greater than the average rows space, minimizing the presence of bare soil (or full covered) pixels inside sparse vegetated fields. In fact, at higher resolutions (in the order of 10^0 m), these areas are constituted by an alternation of full vegetated and bare soil pixels, not well schematized using the two-source in-series resistance network.

5.3.2 MSG satellite - low resolution images

The adopted low resolution maps were obtained, as previously introduced, by LSA SAF system (Figure 5.18, `http://landsaf.meteo.pt/`) for the period 2007–2008. The products used in this thesis are the radiometric temperature (named LST), fraction coverage (named FVC) downwelling short-wave (named DSSF) and long-wave (named DSLF) radiations.

Figure 5.18: Homepage of the LSA SAF system (`http://landsaf.meteo.pt/`).

The entire dataset consist of 717 daily FVC images (743 MB), 34,006 half-hour DSSF images (1.3 GB), 34,098 half-hour DSLF images (14.5 GB) and 67,967 15-minutes LST images (18.2 GB). All the data were in *bzip2* format, and the de-compressed files were codified following the *HDF5* standard. The raw data include 4 specific geographical regions (Europe, north and south Africa and south America).

Automatic Quality Control is performed on all products, and LSA SAF provides quality information on a pixel basis. Quality control data contain the error estimate and it defines the confidence level of the different products on the basis of theoretical model assumptions and considering the statistical uncertainties of the observations and model parameters.

Additionally, a post-processing of the data was required in order to remove some gap in the original dataset, as described below, and the obtained filled hourly maps were used to extract the ALEXI inputs at the time t_1 and t_2 by means of in-time linear interpolation.

FVC product

Fraction coverage maps are generated daily at the full MSG/SEVIRI instrument spatial resolution, using the three sensor short-wave channels. The product is based on an optimised spectral mixture analysis to take into account the sub-pixel heterogeneity of vegetation (Garcìa-Haro *et al.*, 2005). A Bayesian model is used to compute the relative likelihood of membership in each soil/vegetation single-model and unmixing is performed using standardised signatures in order to reduce the influence of external factors. FVC is finally estimated using a linear-weighted combination single-model estimate (for more details see LSASAF, 2008).

In order to remove missing pixels from the dataset, a simple procedure was applied: the missing data were replaced with the value of the same

pixel in the previous day, under the hypothesis of negligible variation of the fraction coverage in 1 day.

DSSF product

The DSSF product is generated following the procedure described in sub-section 2.1.1, based on the methodology adopted by Mètèo-France in the framework of OSI SAF (Brisson *et al.*, 1999). The system provides 30-minutes based solar radiation estimations for all the cloudy coverage conditions.

From this dataset, hourly estimations were realized on the basis of pixel-by-pixel estimation of clear sky solar radiation. In particular, when a hour is missing, it is replaced with the average of the previous and following half hour data; in the case of sparse missing window, larger than half-hour, the filling data are obtained by multiplying the correspondent clear sky radiation by a cloud factor computed by means of the ratio of MSG and clear sky solar radiation in the previous hour. Finally, in the case of missing data for the whole day and domain (due to malfunctioning of the sensor), in absence of information on the cloudy condition, the solar radiation was assumed equal to the clear sky one.

DSLF product

The DSLF product is derived by combining satellite and numerical weather prediction data. In particular, the adopted algorithm consists of an hybrid method based on two different bulk parameterisation schemes (Josey *et al.*, 2003; Prata, 1996) using as input ECMWF forecasts of 2 m temperature, 2 m dew point temperature and total column water vapour as well as cloud products from NWC SAF (see LSASAF, 2010, for more details).

Also in this case, the DSLF maps were aggregated at hourly scale, in order to minimize the missing data, and the missing data were replaced by means of the procedure described in sub-section 2.1.3.

LST product

Radiometric surface temperature retrieval is based on the generalised split-window algorithm (Wan and Dozier, 1996). This algorithm performs

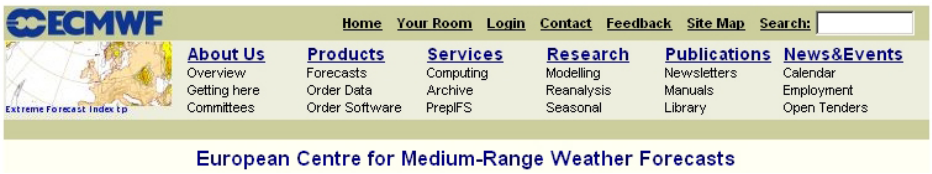

Figure 5.19: Homepage of the ECMWF system (`http://www.ecmwf.int/`).

corrections for atmospheric effects based on the differential absorption in two thermal-IR bands. A look-up table of optimal coefficients is previously determined at individual classes of satellite viewing angles, and covering different ranges of water vapour and near-surface air temperature (see LSASAF, 2009). The surface emissivity is retrieved using the approach suggested by Caselles *et al.* (1997), based on the FVC maps, also retrieved by the LSA SAF.

The identification of cloudy pixels is based on the cloud mask generated by the NWC SAF software: also in this case the missing data were filled analogously to the DSSF case. Initially, the hourly LST maps were set equal to the correspondent one of the raw MSG dataset. The missing pixels were then substituted by the average of the previous and following 15 minutes data. The remains missing data were filled in the same way, using the 30 minutes across images. This procedure allows removing the missing data related only to the malfunctioning of the system.

5.3.3 Other ancillary meteorological data

In addition to the meteorological observation acquired by SIAS weather station, meteorological variable fields required by ALEXI models were obtained from the ECMWF (European Centre for Medium-range Weather Forecast) interim re-analysis retrieved data (Figure 5.19, `http://www.ecmwf.int/`).

This ECMWF dataset stores data since the 1989 at the temporal resolution of 6 hours (0, 6, 12, 18 UTC), in 38 pressure levels (from 1000 to 1 hPa) and with a spatial resolution of 1.5°× 1.5°on the Europe domain.

The products acquired from the ECMWF dataset include vertical profiles of air temperature, pressure and humidity, and wind velocity components. All the data are available in two different standard formats:

the GRIB (GRIdded Binary) or the NetCDF (Network Common Data Form).

Of particular interest for the ALEXI applications are the potential temperature profiles at the early morning, obtained from the air temperature and pressure fields at the 6 UTC, assuming this observation time as the closer one to the average sunrise time in the study area.

Part III

Applications and Results

Chapter 6

Analysis of surface fluxes measurements

The energy fluxes observed by micro-meteorological installations described in the section 5.2 were used as reference to evaluate the remote-sensing based models performance.

In order to adopt these measures as a reliable reference, their accuracy should be quantified; in particular, the uncertainties related to assuming the observations representative of the field-scale fluxes were analyzed both at hourly and daily time scale. Additionally, reliability of the surface energy budget closure was analyzed, testing different approaches to force the balance closure of the eddy covariance observations.

To enlarge the investigation to a more consistent dataset, the analyses were performed for the triennium 2007-2009. The derived remarks were used to obtain the most reliable dataset for the 2008, assuming it as the reference for all the subsequent models validation.

6.1 Comparison between EC and SAS H fluxes

As highlighted by the theoretical background on turbulent transfer, the observation of turbulent fluxes in the lower atmosphere represents, at the present, the complexest issue in the measurements of surface energy budget terms.

Actually, despite the already numerous applications of EC, the reliability

of its measurements in areas characterized by sparse tall canopies can lead to inaccurate observations of the field-average fluxes (Vogt *et al.*, 2004), mainly because the relatively small footprint of a single EC system may not well represent the complex spatial variability of surface fluxes in these systems.

On the contrary, the scintillometer technique had in the last few decades a strong "renaissance"(de Bruin, 2002) especially due to the larger source area, comparable with typical extension of agricultural fields. Despite that, the indirect approach at the base of scintillometry requires detailed analyses of the reliability of the assumed hypotheses, especially in areas characterised by significant interactions between soil and vegetation transfer processes.

Additionally, the scintillometer provides only sensible heat flux measurements; as a consequence, latent heat flux can be obtained only as residual term of the surface energy budget equation if the available energy at-surface is accurately known. This limitation requires accurate analysis of the effective reliability of theoretical balance closure, obtainable only by analyzing EC latent heat flux direct observations.

6.1.1 Source areas and footprints evaluation

Before to proceed with the analysis of turbulent fluxes observations, a preliminary analysis of the study area was focused on the wind field characteristics in order to detect the source area extension for each experimental installation.

First of all, an analysis of the wind direction was performed using the hourly data observed by SIAS station in the period 2007-2009. The data were subdivided in 18 classes, 20°wide, and the occurrence frequency function was derived for both the whole dataset and the dayhours data only.

The radar-plots in Figure 6.1 show the results obtained from the frequency analysis. By observing the graph obtained from the entire dataset (left panel) it is clear the presence of 3 predominant directions: the SE sector (around 140°), the NW sector (around 320°) and the N-NE sector (between 0°and 40°). The analysis of the only dayhours data, more interesting for hydrological applications, highlights how the two opposite directions NW and SE are prevailing, with the higher frequency

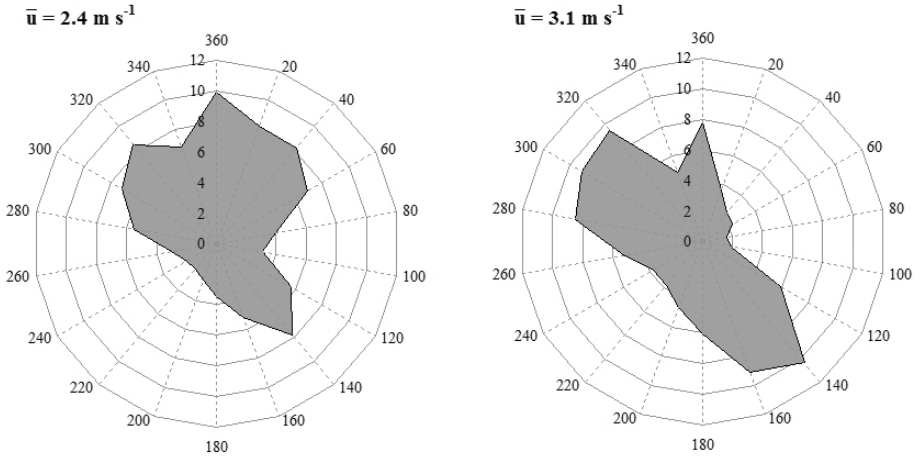

Figure 6.1: Frequency analysis of the 10-m wind direction during the study period 2007-2009. The left panel reports the results relative to the whole day; the right panel reports the results limited to the dayhours. The value $\overline{u}$ represents the average wind speed retrieved from the corresponding dataset.

in correspondence of the direction 140°(about 10%).

On the basis of this analysis, Figure 6.2 reports the footprints, retrieved by means of the Kormann and Meixner (2001) model, for the EC1 (left panel), SAS (centre panel) and EC2 (right panel) installations relative to the predominant daytime condition. In particular, these conditions were assumed equal to an average wind speed of 3.1 m s^{-1} originates from 140°in unstable conditions defined by $u_* = 0.4$ m s^{-1} and $L = -50$ m.

These plots highlight how all the three source areas, relative to the 90% of the observed fluxes, are within the study field in the average daytime conditions for predominant wind direction.

Additionally, the theoretical circle with radius equal to the maximum extension of the plotted footprints enclose the source areas for all the direction in the average meteorological conditions. These areas result almost always within the study field, with the exception of the infrequently 200-180°directions for the SAS and EC2 installations.

This analysis allows to affirm how the observed fluxes can be considered, on average representative of the olive orchard during the study period. Moreover, it is evident that the source area of the installation EC2, located

Figure 6.2: Footprints for the installations: a) EC1, b) SAS and c) EC2, calculated using the model of Kormann and Meixner (2001) for the daytime predominant wind direction (140°). The three areas encompass the 90% of the observed fluxes in the unstable conditions defined by $u_* = 0.4$ m s^{-1} and $L = -50$ m.

in the middle of the SAS path, is partially overlapped with the SAS one, suggesting a possible increase in the fluxes matching between these tow installations compared to the EC1 one.

6.1.2 Analysis of stand alone-SAS observations

In order to analyze the capability of stand alone-SAS installation to provide reliable observations of turbulence characteristics, the approach proposed by Thiermann and Grassl (1992) (described in sub-section 3.1.2) was tested. In particular, the SAS measures were compared with the EC1 system ones in terms of H and u_* derived variables.

The plots in the Figures 6.3 and 6.4 show the comparisons for the years 2007 and 2008, respectively, both in terms of sensible heat flux (left panels) and friction velocity (right panels).

The analysis of H highlights an underestimation for the SAS, more relevant in the 2007 (linear regression slope equal to 0.77) than in the 2008 (linear regression slope equal to 0.83). On the contrary, the determination coefficient is higher in the 2007 (R^2=0.83) compared to the 2008 (R^2=0.71), highlighting an improvement in the agreement of the H estimations with the increase of SAS elevation but with a detriment in the data correlation.

An explanation of these results can be found by observing the similar behaviour of the u_* data (Figures 6.3 and 6.4, right panels), which highlights the clear underestimation of SAS friction velocity in 2007, but with a relatively high R^2 (≈ 0.65). The change in instrument height made in

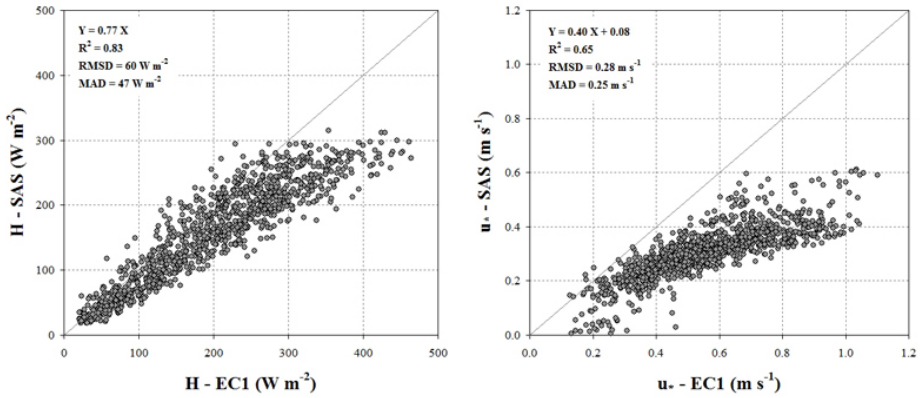

Figure 6.3: Scatterplots comparing the EC1 and SAS sensible heat flux (left panel) and friction velocity (right panel) measurements during 2007.

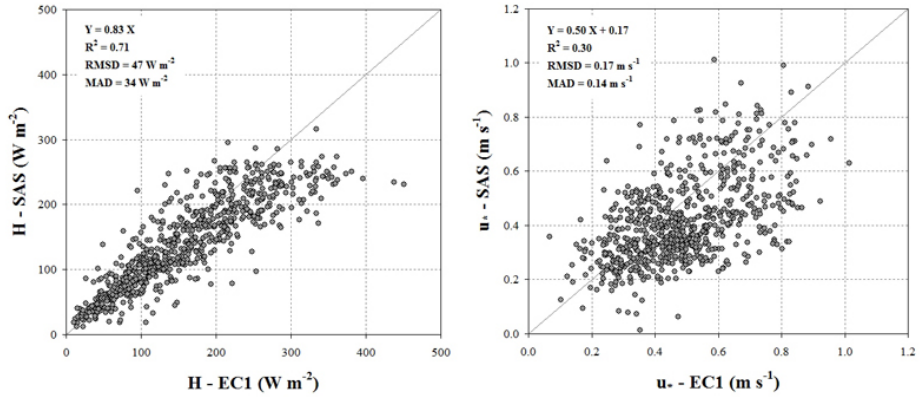

Figure 6.4: Scatterplots comparing the EC1 and SAS sensible heat flux (left panel) and friction velocity (right panel) measurements during 2008.

Table 6.1: Summary of the statistics of the SAS retrieved variables compared with the observations made by EC1 system.

Variable	Year	Scale	slope	R^2	MAD	RMSD
H	2007	$z - d_0$	0.77	0.83	47	60
		z	1.08	0.79	40	53
	2008	$z - d_0$	0.83	0.71	34	47
		z	0.99	0.76	30	42
u_*	2007	$z - d_0$	0.40	0.65	0.25	0.28
		z	0.56	0.65	0.24	0.27
	2008	$z - d_0$	0.50	0.30	0.14	0.17
		z	0.56	0.33	0.14	0.17

the 2008 improves the agreement in the estimation of EC1 and SAS (increase of Root Mean Square Difference, RMSD, and Mean Absolute Difference, MAD), but at disadvantage of the correlation between the two measurements, emphasized by the drastic reduction of R^2.

These results, obtained scaling the fluxes with $(z - d_0)$, should be affected by the considerable thickness of the roughness sub-layer in this sparse tall crops system. Hypothesising the measurements realized within the RS-L, the fluxes computation should be modified scaling the MOST with z. This modification allows an improvement in the agreement between SAS and EC1 H fluxes, obtaining regression slopes (forced to pass through the origin) close to 1. Despite that, the analysis of u_* shows up no-improvement in the agreement (as summarized in Table 6.1). These results suggest that the better performances of the z-scaled H fluxes are not supported by a better performance in terms of u_* and T_* assessments, and so this should not be considered as an optimal result.

As a consequence of these suboptimal performances of the stand alone installation, the successive analyses were focused on the friction velocity assessment in this sparse tall crops system. The choice to focus the attentions on this topic is supported by the finding of de Bruin (2002) and Hartogensis *et al.* (2002), which have attributed the H underestimation to the errors in u_* assessment.

Moreover, de Bruin (2002) highlights how the same underestimations were present also in the l_0 assessed in stable conditions. Additional analyses

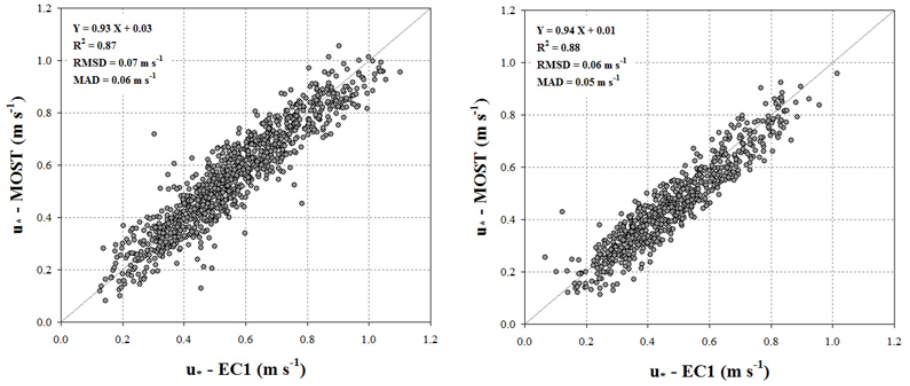

Figure 6.5: Scatterplots comparing the MOST-derived and the EC1-observed friction velocity in the 2007 (left panel) and 2008 (right panel).

made by Hartogensis (2006) suggest how the errors in u_* seems to be independent of MOST scaling and related to the assessment of l_0 from the two beams covariance.

6.1.3 Diagnosis of friction velocity characteristics

On the basis of the results reported in the previous sub-section, the attention was pointed out on the behaviour of u_* for this sparse tall crops system. For this reason, the observations realized by EC1 system were analyzed in details and compared with the theoretical one obtained using the MOST-based relationship.

The observation of the scatterplot between the EC1 measured wind speed and friction velocity shows a strong linear relationship between these two variables, characterized by a slope parameter that increases with canopy height.

Assuming a zero-plane displacement height and a roughness length for momentum transfer equal to the classical fraction of canopy height, as reported in the Eqs. (2.101) and (2.102) (see sub-section 2.3.1), the application of Eq. (2.111) returns the results reported in Figure 6.5.

These plots show the scatterplots between MOST-derived and EC1-observed friction velocity at half-hourly time scale, for 2007 (Figure 6.5, left panel) and 2008 (Figure 6.5, right panel), respectively.

It is clear how the observed friction velocity are quite well reproduced by the theoretical one obtained from the classic MOST approach in spite of the simple parametrization of the roughness parameters. However, even if the adopted roughness parameters seems to be unrealistic for this sparse crops, the analysis of different parametrizations for d_0 and z_{0m} suggests how this solution represents the best fitting of the observed u_* values.

Another consideration can be made on the weight of stability correction factor, which only slightly influences the values modelled via Eq. (2.111), mainly due to the measurements height relatively close to the surface which made small the corrections also for large H fluxes.

These considerations drive to two principle findings: i) the roughness parameters for this complex crop seems to be well represented by the classical values proposed in literature (e.g., Brutsaert, 1982); ii) the friction velocity can be moderately well modelled using the classical MOST formulation and the corrections to take into account the non-neutral conditions (see sub-section 2.3) are generally small.

6.1.4 Evaluation of SAS alternative approach

On the basis of the finding summarized in the previous sub-sections, the applicability of the alternative methodology was encouraged. As a consequence, this approach was tested for the three study periods, including the previously unanalyzed measures made by EC2 installation in the 2009.

The scatterplots of Figures 6.6 and 6.7 show the comparison of the EC1 sensible heat flux (left panels) and friction velocity (right panels) with the SAS ones after the application of the proposed alternative procedure. These results highlight the improvements in the agreement both in terms of H and u_*, with a slope of the regression lines very close to the best fit.

Moreover, the indices of agreement MAD and RMSD for H are of about 35 and 45 W m^{-2}, respectively, generally lower than the ones retrieved with the classical MOST approach, especially for 2007, and comparable to the uncertainties found by other authors for the SAS technique (Ezzahar *et al.*, 2009; Savage, 2008). The improvements in u_* assessment are more evident, confirming the reliability of the adopted relationship.

Additionally, the plots of Figure 6.8 reports the same comparisons relative to the observations of H (left panel) and u_* (right panel) realized by EC2 and SAS systems in the 2009. The better results obtained in

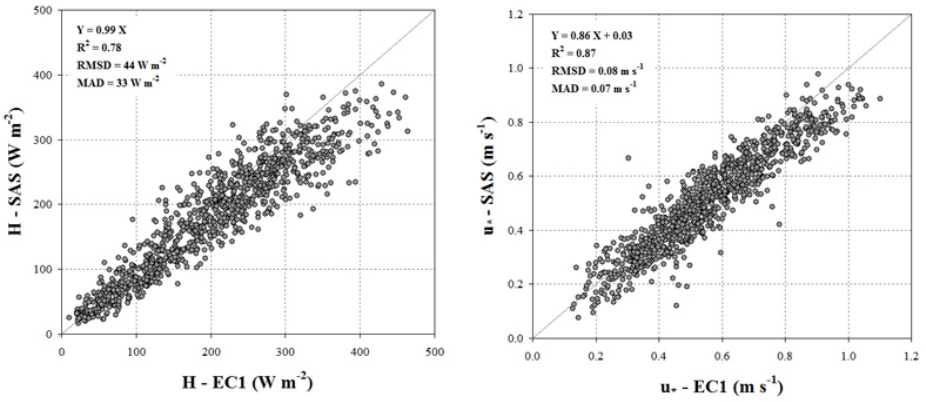

Figure 6.6: Scatterplots comparing the EC1 and SAS sensible heat flux (left panel) and friction velocity (right panel) measurements collected during 2007, applying the alternative approach to SAS data.

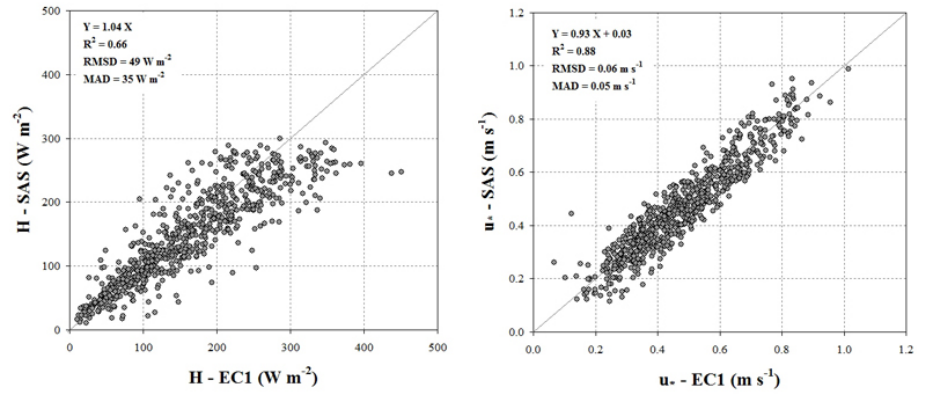

Figure 6.7: Scatterplots comparing the EC1 and SAS sensible heat flux (left panel) and friction velocity (right panel) measurements collected during 2008, applying the alternative approach to SAS data.

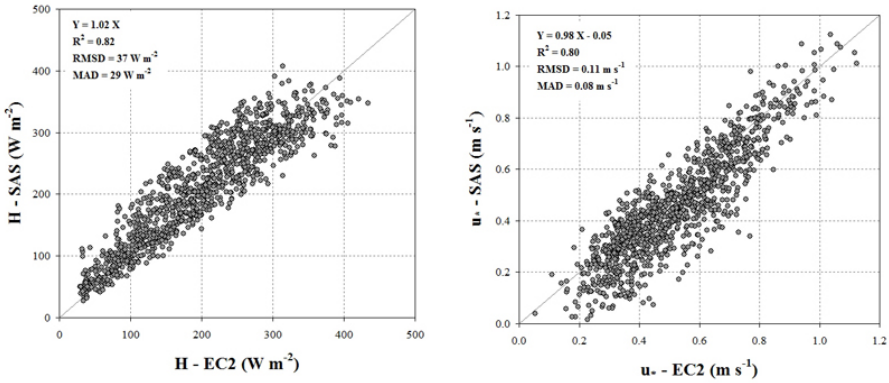

Figure 6.8: Scatterplots comparing the EC1 and SAS sensible heat flux (left panel) and friction velocity (right panel) measurements collected during 2009, applying the alternative approach to SAS data.

this case are probably due to the best matching of the source areas of these two installations, showing an increase in H measures agreements demonstrated by the reduction of MAD and RMSD to values of 29 and 37 W m^{-2}, respectively.

These results allow to affirm the reliability of the assumptions adopted in the proposed approach; moreover, the improvements in the agreement between the two techniques with the simple addition of a wind speed measurements seems to endorse the applicability of the alternative approach in this study area.

Furthermore, despite the parameterization of displacement and roughness lengths seems to be problematic for sparse tall crops, in this study case the EC-observed values are well reproduced adopting the "classical" formulation proposed by Brutsaert (1982).

6.2 Uncertainties in available energy assessment

Generally, the measurement of available energy, or separately of the net radiation and soil heat flux, is considered easier and more reliable if compared with the turbulent fluxes. Despite that, the limited influencing area of the measurements technique, especially for G_0 observations, could

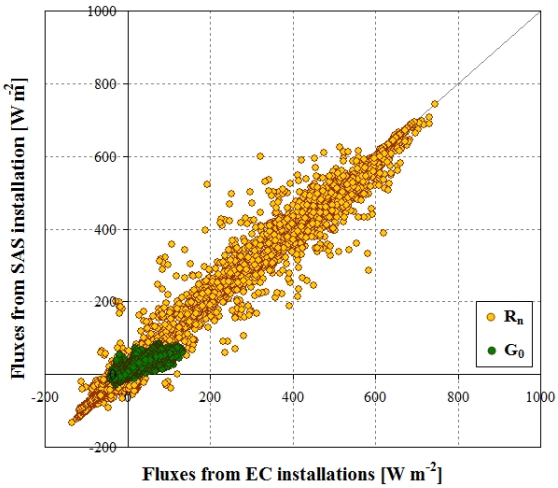

Figure 6.9: Scatterplot between hourly net radiation (orange dots) and soil heat flux (green dots) observed by ECs (EC1 in 2007 and 2008, EC2 in 2009) and SAS during the study period.

cause remarkable differences with field scale averaged fluxes.

For this reason, the observations realised by the ECs and SAS independent systems were compared at hourly scale to quantify the uncertainties associated to the values obtained averaging all the available observations.

The plot in Fig. 6.9 shows the scatterplots between ECs and SAS hourly net radiation (orange dots) and soil heat flux (green dots). The analysis of this plot highlights the good agreement among the two fluxes measured by the three installations (EC1 and SAS in 2007 and 2008, EC2 and SAS in 2009) despite the differences in instruments location.

In particular, the only remarkable difference can be observed for the higher G_0 values, where the values measured by EC installations showed a little overestimation, mainly due to the location of EC1 heat plates only in correspondence of exposed bare soil.

Table 6.2 summarises the statistical indices adopted to evaluate the agreement between the fluxes observed with the different installations. In particular, the dimensional indices MAD and RMSD and the relative index RE (Relative Error) were used.

The values assumed by MAD and RMSD for the R_n suggest uncer-

Table 6.2: Statistics derived by the comparison between ECs and SAS 30-min observed available energy.

Flux	Data	Mean [W m^2]	MAD [W m^2]	RMSD [W m^2]	RE [%]
R_n	All	124	18	34	14.5
G_0		9	12	19	133.3
R_n	Day	320	24	37	7.5
G_0		30	14	22	46.7

tainties in the order of 20-35 W m^{-2}, which only slightly increase if the daytime observations only were analysed. Also the magnitude of RE is only partially influenced by avoiding the nighttime values from the analysis, obtaining RE values of 14.5% and 7.5% in the cases of all data and daytime data, respectively.

In the case of G_0 MAD and RMSD assume values between 10 and 20 W m^{-2}, only slightly influenced by the dataset adopted. The analysis of RE highlights higher value of this index compared to the value assumed for R_n. The greater relative error obtained considering the complete dataset is mainly due to the reduced value of the average G_0, this despite the relative large amount of exposed bare soil.

This analysis confirms how the uncertainties, quantified in terms of MAD and RMSD, in the fluxes that constitute the available energy is generally smaller than the one observed for the sensible heat flux. Nevertheless, the values assumed by RE show how the high spatial variability of G_0 is not well represented by the local measurements realized with the flux plates, and how the efficacy of these measurements is guaranteed only by the small magnitude of this flux.

6.3 Surface energy balance closure

The problems related to the effective theoretical energy balance closure was previously introduced in the sub-section 3.3. Here, the reliability of the closure for the two EC installations is evaluated, analysing also the better method to force the closure.

Additionally, the latent heat flux derived from ECs observations are

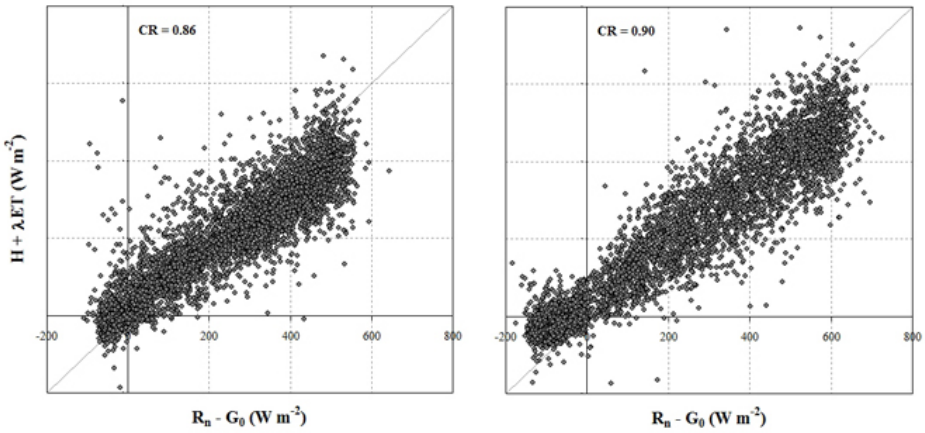

Figure 6.10: Scatterplot between hourly available energy and turbulent fluxes measured by: left panel, EC1 system in both 2007 and 2008; right panel, EC2 system in 2009.

compared with the one retrieved with the residual approach from SAS observations, in order to quantify the uncertainties associated to the observation adopted in the next models validation phase.

6.3.1 Balance closure for EC systems

As preliminary analysis, the surface energy balance closure was checked for both EC1 and EC2 systems by means of the scatterplots between available energy and turbulent fluxes. The scatterplots, were used to compute the CR index, previously defined by Eq. 3.42 in sub-section 3.3, on the whole EC1 and EC2 datasets.

The plots in Figure 6.10 report the results relative to the EC1 system, including both 2007 and 2008 data, and the EC2 system for 2009. The plots reports also the value assumed by CR index, equal to 0.86 for the EC1 and 0.90 for the EC2. These values are slightly greater than the admissible value of 0.85 adopted by numerous authors (Meyers and Hollinger, 2004; Prueger *et al.*, 2005; Wilson *et al.*, 2002).

Despite a satisfactory degree of closure was obtained for both EC systems, the aim to use these data to validate models based on an implicit closure of the budget suggests to force the closure of the energy balance to

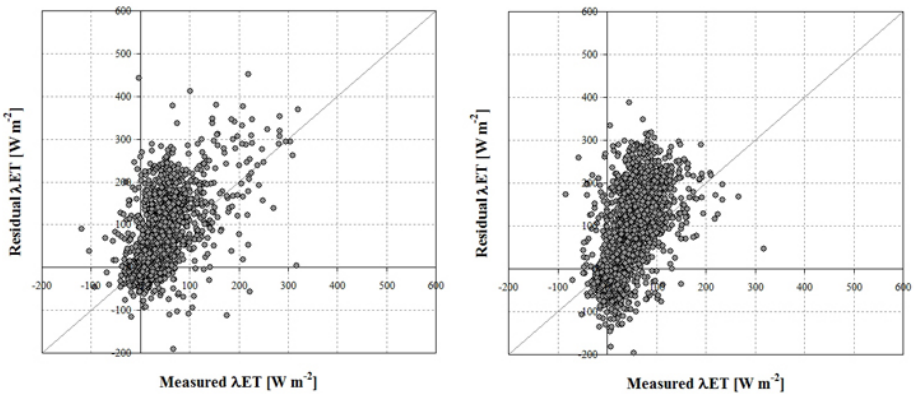

Figure 6.11: Scatterplots between hourly measured and residual latent heat fluxes from EC1 measures in 2007 (left panel) and 2008 (right panel).

set uniform the following comparisons.

For these reasons, the *residual* approach was applied to the EC1 data, and the obtained λET fluxes were compared with the observed ones. The plots of Figure 6.11 report these comparisons, which highlight high discrepancies and modest correlations between the residual and the observed latent heat fluxes. This analysis suggests how the balance unclosure for the EC1 system is strongly related to the high underestimation of the *real* λET flux by the measured one.

These considerations are partially confirmed by the comparison of the EC1 H fluxes with the SAS ones, reported in the sub-section 6.1, which shows always a high correlation, also in the case of the stand alone-SAS retrieved fluxes.

The analysis of the observations collected by EC2 system confirms the previouly reported considerations, showing a definitely better agreement between the residual and the observed λET fluxes, as reported in Figure 6.12 (left panel).

It is interesting to highlight how in this latter case both the correlation and the agreement between the observed fluxes and the ones retrieved with the *Bowen ratio closure* method (see sub-section 3.3 for the definition) are high (Figure 6.12, right panel). Additionally, also the correlation between *residual* and *Bowen* λET fluxes is quite high (not reported) and very close

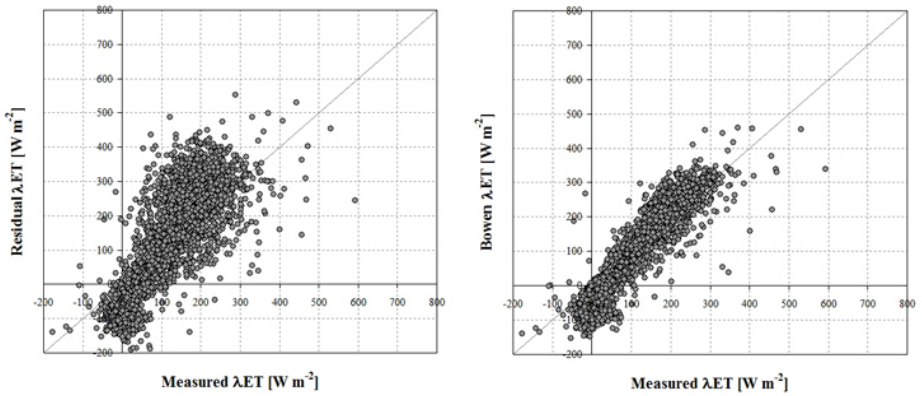

Figure 6.12: Scatterplots report the comparison between the hourly measured latent heat flux and the residual (left panel) and bowen (right panel) ones for the EC2 measures in 2009.

to the best fit line.

It is important to notice how, due to the well known instability of β when it approaches negative values (see sub-section 2.4.1), the *Bowen ratio closure* method was used only when $\beta > 0$, adopting the *residual closure* in the other cases.

These considerations suggest that the *Bowen ratio closure* method seems to be the better method to force the closure only when the quality of the observed λET fluxes is high, and the discrepancies with the residual ones are small, i.e., the case of EC2 observations. In the case of small correlation between the observed and the residual values, the analysis of the data suggests to skip the observed values, and to assume the *residual closure* as the reference method. This last consideration is confirmed by the good agreement between *residual* and *Bowen* λET fluxes when the λET observed data are reliable.

On the basis of this analysis, the λET fluxes for the EC1 system were derived adopting the *residual closure* approach, instead, the budget closure of the fluxes observed by EC2 system was forced adopting the *Bowen ratio closure* method.

Table 6.3: Summary of hourly surface energy fluxes statistics derived from ECs and SAS observations collected during daytime.

Flux	Data	Mean [W m^2]	MAD [W m^2]	RMSD [W m^2]	RE [%]
R_n	All	124	18	34	14.5
G_0		9	12	19	133.3
H		69	18	38	26.1
λET		46	38	53	82.6
R_n	Day	320	24	37	7.5
G_0		30	14	22	46.7
H		170	28	44	16.5
λET		120	42	56	35.0

6.3.2 Retrieval of reference hourly fluxes dataset for 2008

Focusing the attentions on the measurements collected during the June-October 2008, due to the availability of high resolution remotely sensed-data only in this period, the analyses reported in the previous sub-section were used to derive the most reliable dataset relative to the monitored olive orchard.

In particular, the data measured by the two installations EC1 and SAS were independently averaged at hourly scale, and a unique field-scale reference dataset was constituted by means of a combination of the independent two.

The obtained dataset is reported in Figure 6.13, including approximately the 94% and the 77% of useful data for the available energy and turbulent fluxes, respectively.

Due to the availability of two independent measurements dataset of each surface energy budget flux, the average dataset was associated to an estimation of the measures uncertainties, as summarized in Table 6.3 for both the all-day and the *sole* daytime.

The data reported in Table 6.3 highlight how the main uncertainties in terms of absolute indices (MAD and RMSD) is associated to the turbulent fluxes, even if the indices for H are very similar to the one for R_n. The analysis in terms of relative errors confirms the greater uncertainties for λET, highlighting how the higher magnitude of the R_n fluxes reduce sensibly the RE value compared to the H one.

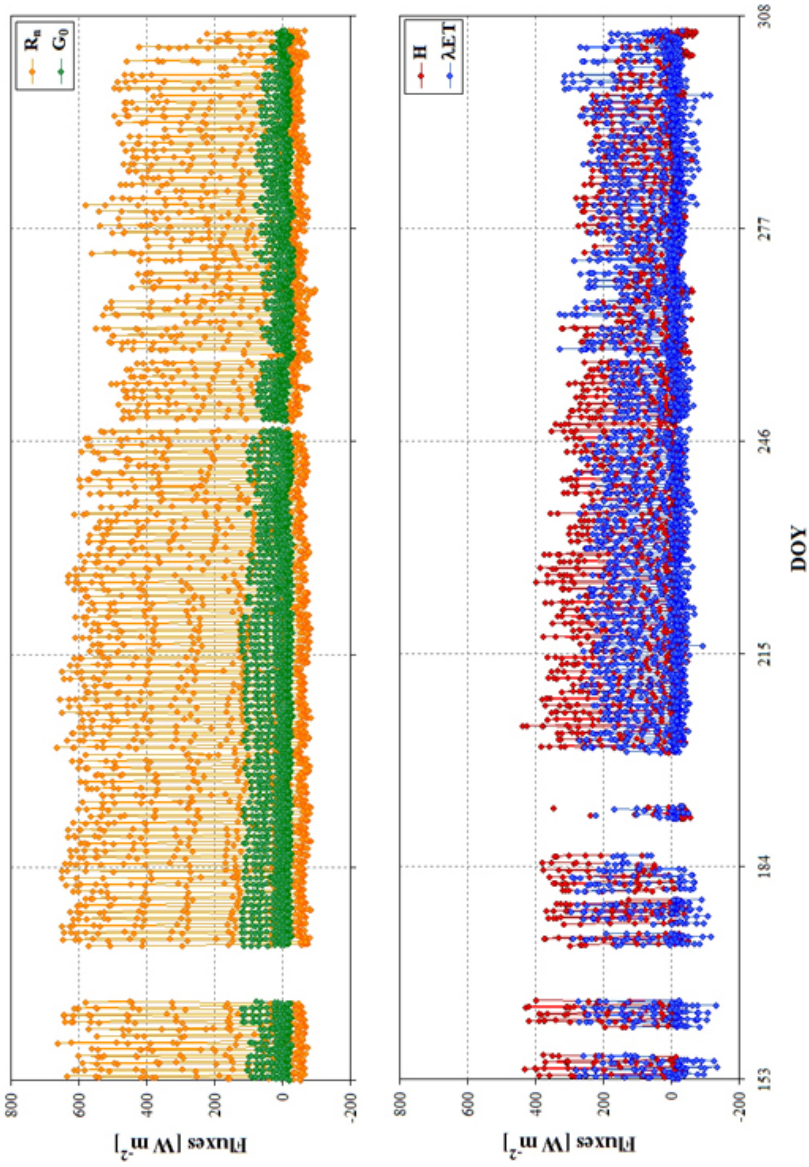

Figure 6.13: Hourly surface energy fluxes measured by EC1 and SAS systems in the period June-October 2008. Upper panel reports the net radiation (orange dots) and the soil heat flux (green dots). Lower panel reports sensible heat flux (red dots) and latent heat flux (blue dots).

6.4 Daily fluxes estimation

Analogously to the analysis carried on in the previous sub-section on the hourly data, the most reliable dataset at daily scale was retrieved with particular regards to the net radiation and the actual evapotranspiration.

Additionally, analyses on the self preservation of some fluxes ratios and on the reliability of daily net radiation modelling were performed in this section.

6.4.1 Analysis of daily net radiation

The modelling of daily net radiation, as reported in the sub-section 2.1.5, is widely performed by means of the well known formulation proposed in the FAO-56 paper.

As previously highlighted, in this formulation, the scheme adopted for the long-wave modelling is realistic only in the case of well watered grass surface. In this case, in fact, the daily average surface temperature can be considered well described by the average air temperature, allowing the computation of $R_{n,lw24}$ by means of the simple Eq. (2.62).

The availability in the EC2 installation of a 4-component net radiometer allows to validate the applicability of this relationship in the study case of a sparse tall crop. The graph of Figure 6.14 reports the comparison between the observed daily long-wave net radiation on the FAO-56 modelled one.

This scatterplot clearly highlights the underestimation of the FAO-56 approach, quantifiable in about the 42%. This underestimation can be connected with the underestimation of daily average surface temperature, also reported by the scatterplot in Figure 6.15.

As highlighted by Figure 6.15, during the study an almost constant bias between air and surface temperature occurred, quantifiable in about 5 K. This value can be used to derive the constant K_T^* in Eq. (2.65), which in this case assumes the value of 30.2 W m^{-2}.

This approach, despite its empirically calibration with respect of *in-situ* observations, is useful to quantify the bias between the values retrieved with classical FAO-56 formulation and the effective $R_{n,lw24}$.

Figure (6.16) reports the comparison between the observed $R_{n,lw24}$ (left panel) and $R_{n,24}$ (right panel) and the modelled ones taking into account the K_T^* correction.

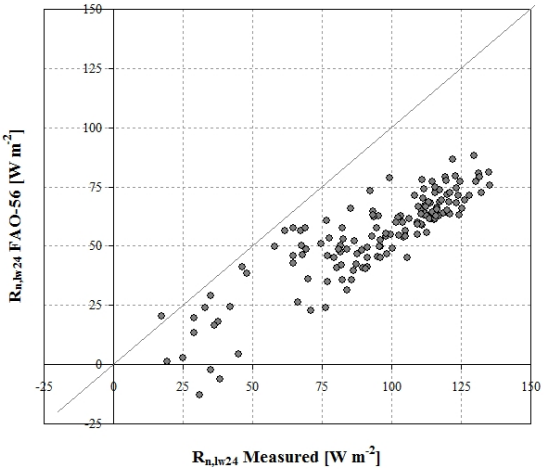

Figure 6.14: Scatterplot between measured and FAO-56 modelled net long-wave radiation at daily scale in 2009.

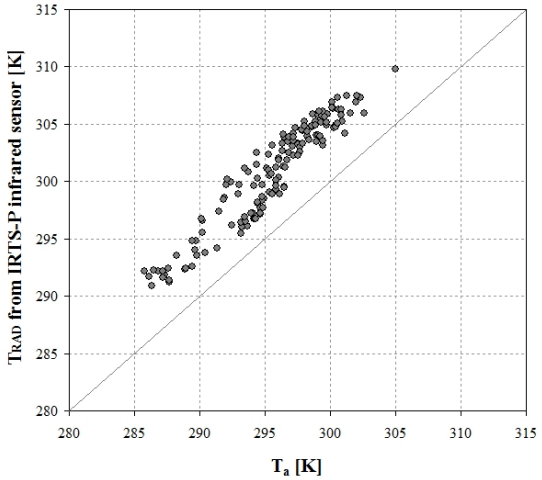

Figure 6.15: Scatterplot between daily average air temperature and surface temperature measured during 2009. The surface temperature was derived from half-hourly measures collected by IRTS-P precision infrared sensors, corrected by surface emissivity as reported in sub-section 2.1.3.

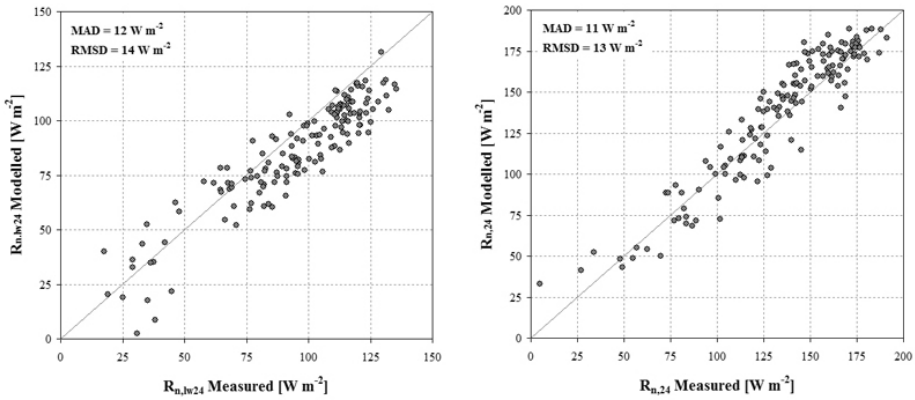

Figure 6.16: Scatterplots between measured daily long-wave (left panel) and total net radiation (right panel) and the same ones taking into account the K_T^* correction factor.

The good performances of the new modelling approach are confirmed by the small values assumed by MAD and RMSD for both long-wave component and global $R_{n,24}$, with values in the order of 10-15 W m^{-2}.

6.4.2 Self conservation and daily ET extrapolation

The daily observations of net radiation and actual evapotranspiration allow to validate some assumption adopted by residual remote sensing-based approaches in the ET_{24} extrapolation from instantaneous fluxes.

In particular, the relationships described in sub-section 4.1.3 were tested adopting as reference the daily ET retrieved by temporal integration of the hourly λET fluxes reported in the previous sub-section 6.3.2.

In order to simulate the remotely sensed instantaneous Λ, the values observed between the 9 and the 12 UTC were used. Similarly, also the instantaneous R_s and ET_0, required by Eqs. (4.22) and (4.23), respectively, were derived by averaging the values in the same temporal window.

The plot in Figure 6.17 reports the results relative to the application of the Eq. (4.21) with the modified Λ' (equal to 1.1Λ) as suggested by Anderson *et al.* (1997).

This graph shows the satisfactory performance of the tested formulation, which returns indices of agreement in the order of 0.3 mm d^{-1}. These

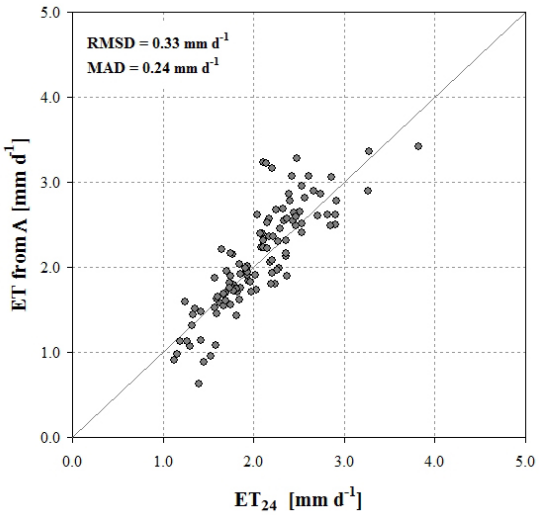

Figure 6.17: Scatterplot between daily evapotranspiration derived from hourly measures and extrapolated by means of daytime evaporative fraction. The data are relative to the observation realized by EC1 and SAS systems in 2008.

results, according to the finding of Brutsaert and Sugita (1992), Gonzàlez-Dugo *et al.* (2009) and Gurney and Hsu (1990), highlight how the neglecting of $G_{0,24}$ and the underestimation of daily Λ from morning hours values can be quantified in 10% in this dataset of observations.

On the basis of this finding, the Eq. (4.21) with the modified evaporative fraction was chosen for the daily integration of the instantaneous remotely sensed fluxes obtained by the models applied in the next Chapter.

6.4.3 Analysis of daily evapotranspiration

The hourly fluxes reported in the sub-section 6.3.2, and in particular the λET observations, were used to derive daily actual evapotranspiration for the study field in the period June-October 2008. This variable is the common one adopted in the practical applications of crop water stress detection.

The Figure 6.18 shows the temporal trend of the actual evapotranspiration (blue dots) obtained as average of the available hourly fluxes.

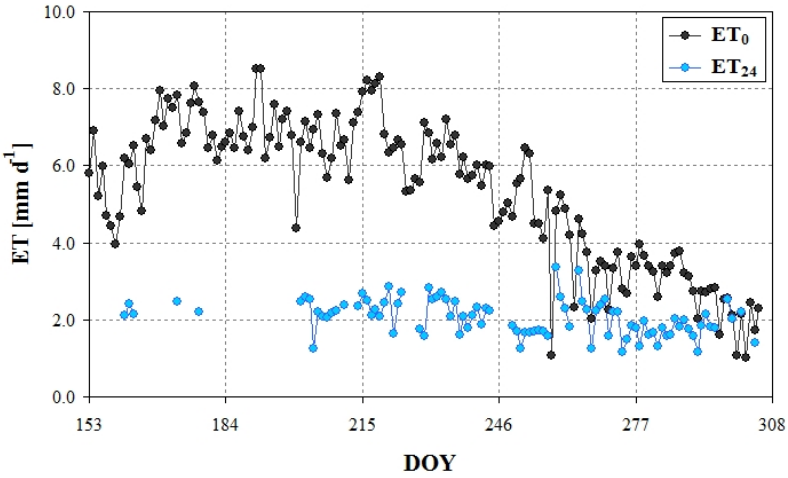

Figure 6.18: Daily actual (blue dots) and reference (grey dots) evapotranspiration observed in the period June-October 2008. The actual values were obtained by a combination of EC1 and SAS hourly measures, instead, the reference values were derived from hourly SIAS weather station observations by means of FAO-56 formulation (see sub-section 2.3.3).

Table 6.4: Statistics derived by the comparison between ECs and SAS observed daily evapotranspiration.

Variable	Mean [mm d^{-1}]	MAD [mm d^{-1}]	RMSD [mm d^{-1}]	RE [%]
ET_{24}	2.06	0.40	0.49	19.5

In the study period, constituted by 153 days, there were 92 useful data, corresponding to the 60% of the whole period.

Table 6.4 reports some statistics derived from EC1 and SAS observed values; the average evapotranspiration results equal to about 2 mm d^{-1} and the correspondent uncertainties can be quantified in the order of 0.4 mm d^{-1} (by means of RMSD and MAD indices).

It is interesting to notice how the relative high RE, equal to 19.5%, is not so far from the uncertainties suggested by Allen *et al.* (1998) for standard ET_0 estimations, equal to the 10-15%; this result, considering the significant major complexity in the actual ET measurements, can be

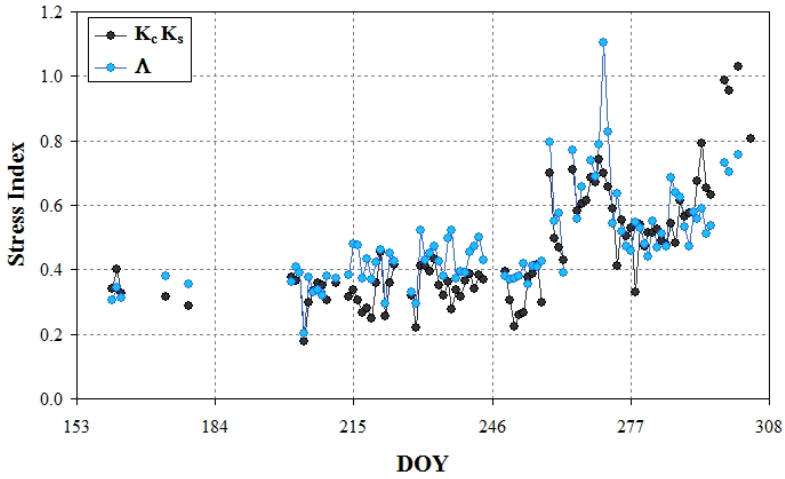

Figure 6.19: Daily stress index (grey dots) and evaporative fraction (blue dots) observed in the period June-October 2008. The stress index represents the product between crop coefficient (K_c) and stress coefficient (K_s) as defined in sub-section 2.3.3. The evaporative fraction was derived as average of the hourly values observed between the 9 and 12 UTC.

considered satisfactory. Moreover, the results reported in literature for similar studies (Shuttleworth, 2008; Wilson *et al.*, 2001) highlighting results in the order of 0.4–0.5 mm d^{-1} also for crops characterized by simpler structures (e.g., full covered grass field).

The ET_{24} data reported in Figure 6.18 highlights a slightly constant trend, with values ranging between 1.5 and 3 mm d^{-1} during all the observed period. The analysis of the ET_0 values (grey dots in Figure 6.18) shows instead a decreasing trend in September-October (approximately between DOY 246 and 308), suggesting a reduction in water stress during this period.

This consideration is confirmed by the analysis of the ration between ET_{24} and ET_0, reported in Figure 6.19, which corresponds to the product K_cK_s as defined by Eq. (2.121a) in sub-section 2.3.3. In fact, this plot highlights an increase of this index from values of about 0.3 to values equal to 0.55.

It is interesting to analyze also the temporal trend of daytime Λ (blue

dots in Figure 6.19), defined as described in the previous sub-section, which shows the same behaviour of the product $K_c K_s$.

Finally, also the magnitude of Λ and $K_c K_s$ seems to be very similar, but this last instance should be just a coincidence and it is not supported by physical justification. However, the similarity in temporal shape supports the use of Λ as proxy variable to quantify the water stress (as introduced in sub-section 4.2.1).

Chapter 7

Application of residual SEB models

This chapter is dedicated to the analysis of the results obtained by applying the residual SEB models by means of the airborne high resolution images acquired in 2008. In particular, the TSEB model was analyzed, focusing on some critical point related to high resolution applications. Moreover, the applicability of ALEXI/Dis-ALEXI procedure was investigated.

7.1 Validation of TSEB at local scale

In this section the results relative to the application of TSEB model (described in sub-section 4.1.1) at local scale are reported. In particular, the data retrieved by airborne overpasses were used as main inputs of the model, in order to analyze the model's performance at field scale using high resolution detailed information. Moreover, two sensible features of the model were investigated in details: the first, strongly related to the sparse configuration of olive trees, was the effects of different in-canopy wind profiles on heat fluxes assessment; the second was the possibility to minimize the errors related to the imperfect surface temperature data calibration by means of scene-based approaches or time-differencing schemes.

In order to validate the TSEB model results, the observations made by EC1 and SAS, processed as described in Chapter 6, were used as reference

Table 7.1: Fluxes observed by EC1 and SAS installations during the airborne overpasses. All the fluxes are in [W m^{-2}].

n.	Date	DOY	Time [local*]	R_n [W m^{-2}]	G_0 [W m^{-2}]	H [W m^{-2}]	λET [W m^{-2}]
1	11/06/2008	163	13:30	601	111	403	87
2	03/07/2008	185	11:00	460	56	246	158
3	22/07/2008	204	11:30	521	44	332	145
4	22/08/2008	235	12:00	480	54	227	199
5	03/09/2008	247	11:30	461	41	247	173
6	10/10/2008	284	11:00	335	41	146	148
7	21/10/2008	295	11:30	390	29	200	161

*local time = UTC + 2

ground truth characterized by the uncertainties summarized in Table 6.3 (sub-section 6.3.2).

The fluxes observed at the airborne overpass times, each obtained as a temporal average of the values in a window of 2 hours centred on the overpass time itself, are reported in Table 7.1.

With the intent to clarify the application of TSEB model in the study area, Table 7.2 briefly summarizes the main lumped parameter adopted in the simulations.

More details on the physical meaning of each parameter can be found in Chapter 2 where the theoretical background is described. The choice related to the r_s resistance parametrization and in-canopy wind profile models are deeply discussed in sub-section 7.1.2.

7.1.1 Analysis of olive field uniformity

Before to proceed with the comparison between EC-SAS observed fluxes and the modelled ones, an analysis of the effective homogeneity of the olive field was performed; this topic is crucial to assess whether the micro-meteorological installations provide flux measurements representative of the field-average fluxes obtainable by averaging the spatially distribute TSEB outputs on the field extension.

In fact, as reported in sub-section 6.3.2, fluxes from the SAS and EC systems were averaged and taken as reference values characterizing the entire olive orchard.

Table 7.2: Main parameters used in the TSEB model simulations.

Variable	Parameter	Description	Value
R_n	κ	Extinction coefficient for solar radiation	0.60
	κ_L	Extinction coefficient in the long-wave	0.95
	ϵ_c	Emissivity of canopy layer	0.98
	ϵ_s	Emissivity of soil layer	0.97
G_0	$c_{g,\max}$	Maximum value assumed by c_g during the day	0.20
	B_t	Shape parameter of the daily c_g function	3600
	C_t	Position on the daily c_g peak	74000
r_a	d_0	Zero-plane displacement length	$2/3h_c$
	z_{0m}	Roughness length for momentum transfer	$1/8h_c$
r_x	C'	Coefficient for leaf boundary-layer resistance	90
	w_l	Mean leaf size	0.04
r_s	b'	Coefficient for wind speed	0.012
	c'	Coefficient for convective velocity	0.0025
u_s	z_s	Height above the soil where is minimal the effect of soil surface roughness	0.10
	C_d	Drag coefficient	0.20
	α_*	Roughness of the underlying surface	1.5
	z_d	Crown bottom height	$1/3h_c$

To endorse the hypothesis of uniformity in this field, with particular regards to the 7 airborne acquisitions, spatial variability in remotely-observed NDVI and T_{RAD} was assessed for each of the sub-plots reported in Figure 5.7 in the section 5.1. In particular, the 7 sub-plots reported in Figure 5.7 were partially joined in 5 sub-areas uniform in terms of irrigation system.

The results of this analysis, reported in Tables 7.3 and 7.4, demonstrated that the deviation of single sub-area mean values from the global mean (reported in the column "All") is always lower than the standard deviation for both NDVI and T_{RAD}. Moreover, the single sub-plot standard deviation is always comparable with the global one, confirming a substantial uniformity on the spatial distribution of vegetation in the whole plot.

The only observed exception is for radiometric temperature in sub-plot O5 for the 3$^{\mathrm{rd}}$ acquisition (DOY 204). This behaviour can be explained by

Table 7.3: NDVI mean and standard deviation (in brackets) for the olive sub-fields and the whole field, computed for the 7 airborne acquisition dates.

DOY	O1	O3	O2+O4	O5	O6+O7	All
163	0.43 (0.06)	0.41 (0.05)	0.43 (0.05)	0.41 (0.05)	0.38 (0.06)	0.41 (0.05)
185	0.40 (0.05)	0.39 (0.05)	0.40 (0.05)	0.41 (0.05)	0.37 (0.05)	0.39 (0.05)
204	0.39 (0.05)	0.39 (0.05)	0.40 (0.05)	0.40 (0.05)	0.36 (0.05)	0.39 (0.05)
235	0.41 (0.05)	0.39 (0.04)	0.41 (0.05)	0.40 (0.04)	0.37 (0.05)	0.40 (0.04)
247	0.46 (0.06)	0.41 (0.05)	0.45 (0.05)	0.43 (0.05)	0.38 (0.05)	0.43 (0.05)
284	0.50 (0.04)	0.46 (0.05)	0.53 (0.05)	0.51 (0.04)	0.48 (0.05)	0.50 (0.04)
295	0.51 (0.04)	0.47 (0.05)	0.54 (0.04)	0.54 (0.04)	0.51 (0.05)	0.51 (0.04)

a break in the irrigation system a few days before the airborne overpass, which caused a local increasing in surface soil moisture and, consequently, a reduction of soil surface temperature.

Fortunately, the mean wind direction during the 3rd acquisition precludes the possibility that the instrument source areas include this sub-plot (see also frequency distribution of wind direction during daytime reported in Figure 6.1). For this acquisition, TSEB results from sub-plot O5 have been removed from spatial averages.

On the basis of this analysis of spatial variability, the fluxes maps retrieved by the TSEB model were spatially averaged over the whole field (with the above mentioned exception), and the mean values were compared with the fluxes reported in Table 7.1.

7.1.2 Impact of in-canopy wind profile modelling

In this study case the absence of *in-situ* in-canopy wind profile measurements, due to the difficulty to characterize it in such sparse tall system, suggests to evaluate the performance of the three different models by means of the impact on heat fluxes assessment.

Table 7.4: T_{RAD} mean and standard deviation (in brackets) for the olive sub-fields and the whole field, computed for the 7 airborne acquisition dates.

DOY	O1	O3	O2+O4	O5	O6+O7	All
163	319.94 (2.71)	317.68 (2.02)	318.94 (3.00)	317.90 (1.99)	319.43 (2.02)	318.78 (2.35)
185	317.69 (2.73)	316.56 (2.11)	315.57 (2.58)	315.71 (2.00)	317.55 (2.10)	316.62 (2.30)
204	316.39 (2.03)	315.43 (2.18)	315.35 (2.24)	312.06 (3.67)	316.68 (1.84)	315.18 (2.39)
235	314.57 (2.87)	317.40 (1.67)	316.67 (1.91)	318.06 (1.75)	318.16 (1.73)	316.97 (1.99)
247	314.08 (2.34)	315.26 (2.00)	313.26 (2.68)	315.52 (2.30)	314.55 (1.92)	314.53 (2.25)
284	300.95 (0.97)	301.46 (0.96)	300.98 (1.15)	302.55 (1.25)	302.34 (1.27)	301.66 (1.12)
295	301.95 (1.93)	302.57 (1.43)	300.75 (1.83)	302.18 (2.07)	301.40 (1.78)	301.77 (1.81)

Sensitivity analysis

A preliminary qualitative analysis of the three wind profile formulations has been performed to highlight the general behaviours of each one. Figure 7.1 reports in-canopy wind profiles obtained using the Goudriaan, Eq. 2.103, Massman, Eq. (2.105), and Lalic, Eq. (2.107), models, generated using mean field properties retrieved for the olive trees of the study site.

For comparison purposes, elevation a.g.l. was normalized by canopy height, whereas wind speed was normalized with respect to the speed just above the canopy. In this way, both variables range between 0 and 1.

These comparisons show that the Goudriaan and Massman approaches return very similar values in the upper canopy layer, with divergent results in the lower profiles characterized by higher wind speeds from the Massman relationship. The Lalic model, instead, is characterized by a larger extinction in the upper layer and very low wind speeds in the lower portion of in-canopy airspace.

Additionally, it is interesting to highlight how the greater differences among the three models can be observed in the lower portion of the profiles, which is the more interesting for the assessment of sensible heat flux generated by the soil surface.

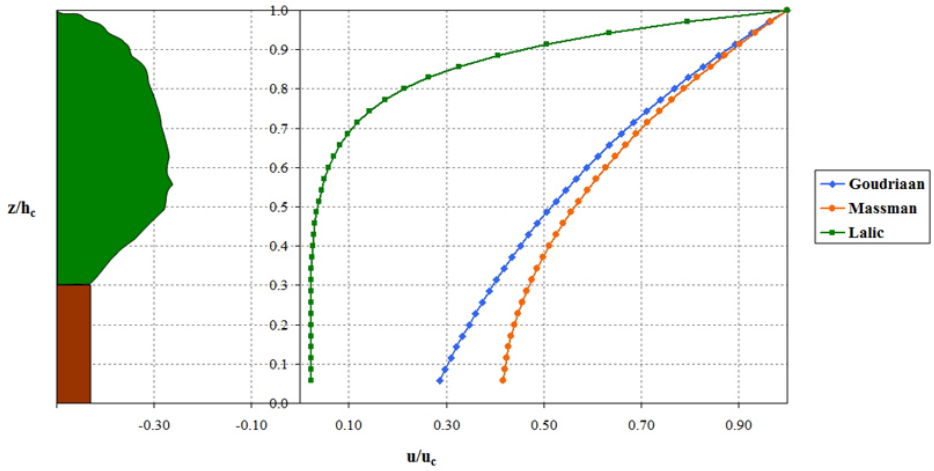

Figure 7.1: Example of normalized in-canopy wind profiles retrieved using Goudriaan (blue rhombus), Massman (orange circles) and Lalic (green squares) schemes.

It should be stressed, however, that these considerations are strongly related to the values assigned in the analysis of canopy structure, then can not be considered as a general finding, but only specific result for this (or similar) case study.

To better understand the effects upon in-canopy wind profile models of primary biophysical variables, a sensitivity analysis was carried out. In particular, we focused the attention on the effect on above-soil wind speed (u_s) at an height $z_s = 0.1$ m, which, as defined in sub-section 2.3.3, represents the variables of interest for TSEB model application.

Figure 6 shows the variability in u_s/u_c changing the values of LAI and h_c, chosen inside the typical range of variability for Mediterranean agricultural crops. Looking at Figure 7.2 we see that the Massman (left panel) and Lalic (centre panel) models show low sensitivity to the assumed h_c, whereas the Goudriaan (right panel) model shows wind speed reduction, increasing the non-linearly with canopy height. Moreover, the Goudriaan approach shows an almost linear dependence on LAI over this range, while the Massman and Lalic formulations show saturation in the extinction effect for higher values of LAI.

At all values of LAI and h_c, the Lalic model generates the lowest

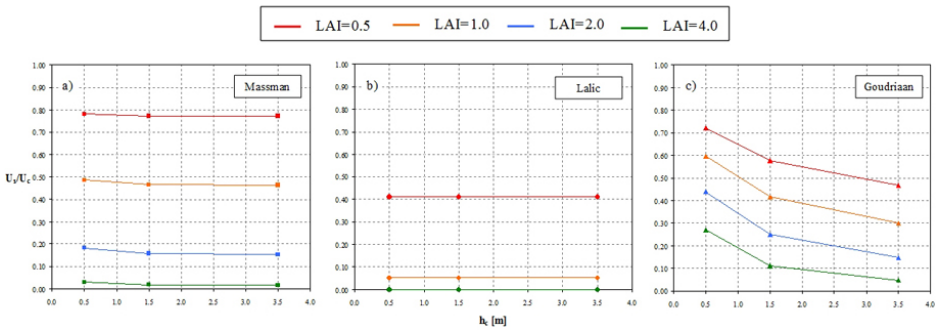

Figure 7.2: Sensitivity of u_s/u_c to the three selected in-canopy wind profiles to variations in LAI and h_c. Panel (a) shows the results for Massman model (square dotted lines); panel (b) shows the results for Lalic model (circle dotted lines); panel (c) shows the results for Goudriaan model (triangle dotted lines).

values of u_s (as seen in Figure 7.1). In contrast, the Goudriaan approach returns low values of u_s only under conditions of high LAI and h_c, while the Massman model requires only high LAI for significant wind speed reduction. The net effect is that the Lalic model typically produces higher values of r_s, tending to reduce the influence of soil fluxes on the in-canopy microclimate. This has the effect of reducing sensible heat flux estimates from the TSEB model under sparse canopy conditions where $R_{n,s}$ is relatively large.

Models comparison on olive field

The previously reported sensitivity analysis suggests how the olive crop represents an optimal condition to test the performance of the different in-canopy wind speed profiles. The fluxes modelled by TSEB at high spatial resolution were aggregated at field scale and in Figure 7.3 are compared *vs.* the measured fluxes.

Both modelled net radiation and soil heat flux show good agreement with measured fluxes. For sensible heat, both the Goudriaan and Massman models provide reasonable estimates while the Lalic model underestimates H by 90 W m^{-2} on average. This results in an overestimation of latent heating by the Lalic model, whereas the Massman and Goudriaan approaches both return reliable results for λET.

Statistical comparisons between modelled and measured fluxes are

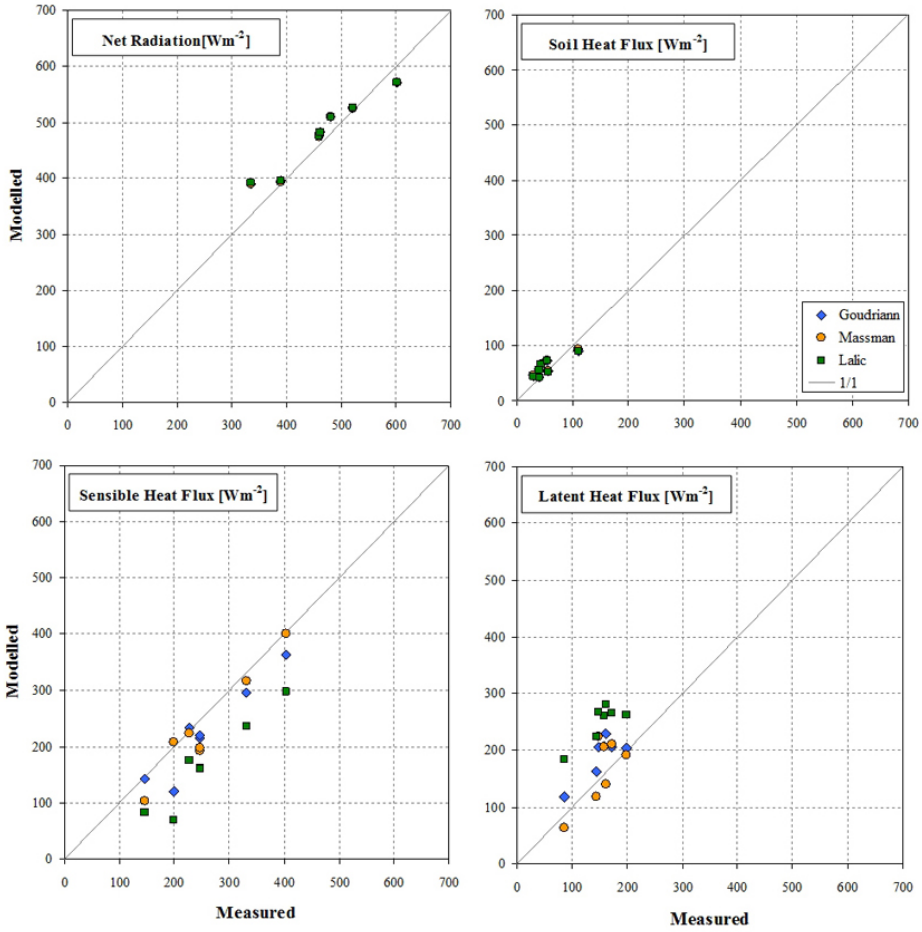

Figure 7.3: Scatterplots of measured *vs.* TSEB modelled net radiation (upper left panel), soil heat flux (upper right panel), sensible heat flux (lower left panel) and latent heat flux (lower right panel) using the three different in-canopy wind profile models.

Table 7.5: RMSD and MAD statistics [W m^{-2}] computed using TSEB modelled and EC-SAS measured values collected during the 7 acquisition dates in correspondence of the olive field.

Model	Index	R_n	G_0	H	λET
Goudriaan	MAD	23	15	32	37
	RMSD	28	17	40	43
Massman	MAD	23	14	25	34
	RMSD	28	16	32	40
Lalic	MAD	23	15	89	96
	RMSD	29	17	92	98

shown in Table 7.5. In terms of RMSD and MAD, the Massman approach yields the lowest errors in sensible and latent heat fluxes. The Goudriaan approach, used in the standard implementation of the TSEB, also returns reasonable estimates in H and λET, comparable with the measurement uncertainties (see Table 6.3 in sub-section 6.3.2). In contrast, the Lalic in-canopy wind profile model yields unacceptable high errors with respect to measured fluxes.

The statistics in Table 7.5 also suggest that the TSEB yields reasonable estimates of net radiation and soil heat flux, and that model-measurement agreement for flux components is not very sensitive to the choice of in-canopy wind profile law.

Figure 7.4 finally shows in detail a histogram of the mean observed sensible heat flux for each remote sensing acquisition date, along with modelled values obtained using the 3 in-canopy wind profile formulations. This plot shows that in these cases the Massman and Goudriaan approaches yield values very close to the measurements. In contrast, the Lalic approach yields relatively poor flux estimates.

The analysis of standard deviation values (vertical bars in Figure 7.4), representing the within-field spatial variability, highlights a significant heterogeneity in the H flux (standard deviation in the order of 70 W m^{-2}) due to the sparse configuration of the threes in the field.

It should be noted that results from the Massman model are strongly related to the choice of the α_* parameters in Eq. (2.105), which can change considerably for different land uses, and for the same field during the year. This provides additional complexity in spatially distributed applications of

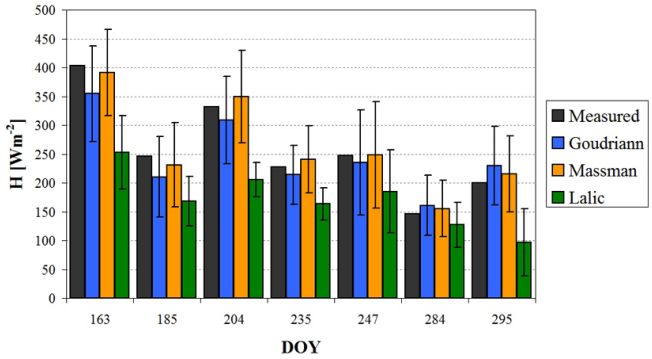

Figure 7.4: Bar plot comparing measured and modelled sensible heat fluxes using different in-canopy wind profiles for the 7 acquisition dates. The modelled values correspond to the mean olive field values and the vertical lines represent the standard deviation error bars.

TSEB, because of the introduction of an additional parameter not easily retrievable from remote sensing data.

7.1.3 Scene-based estimation of air temperature

The previously discussed applications were realized using as input the air temperature measured by SIAS weather station located within the study area (see Figure 5.1). In this section, adopting these results as a reference, the methodology to assess T_a directly from the information embedded in the scene (introduced in sub-section 4.1.1) will be discussed.

This approach aims to reduce the model uncertainties related to possible imperfection in air-surface temperature difference computation. In this case, due to the availability of *in-situ* measurements for images correction, the calibrated surface temperature allows to directly compare both the modelled fluxes and air temperature.

Due to sparse clouds cover during the 6^{th} acquisition (DOY 284), which precludes the application of ALEXI/Dis-ALEXI approach (reported in the next sub-sections), for homogeneity the following analyses were focused on the remaining 6 acquisitions only.

TSEB sensitivity to temperature biases

In order to test how TSEB approach behaves in the face of uncalibrated or biased T_{RAD} data, a sensitivity analysis was conducted, perturbing the calibrated surface temperature fields by known amounts and assessing the impact on derived air temperatures and surface fluxes.

Particularly, in this analysis "synthetic" radiometric temperature maps were derived from the 6 calibrated data by adding ± 1 and ± 3 K and using models outputs obtained with the actual thermal observations as a reference. The advantage of this approach is to quantify the errors considering different scenarios (in terms of wind speed, solar radiation, air temperature, etc.) representative of the real conditions.

Plots in Figure 7.5 show the behaviour of scene-averaged TSEB surface fluxes differences (expressed as percentage) over the image as a function of surface temperature induced errors (ΔT_{RAD}). For each graph the box in the upper-right corner highlights the average slope of the 6 lines, corresponding to the errors related to a unitary error in surface temperature. These values indicate the sensitivity of the modelled fluxes to the uncertainties in the radiometric temperature calibration procedure.

Figure 7.5 (upper -left and -right panels) demonstrates weak sensitivity of the net radiation and soil heat flux, with mean error of -1.5% K^{-1} and -1.6% K^{-1}, corresponding to about -7 and -1 W m^{-2} K^{-1}, respectively. In contrast, the sensitivity of H and λET is quite relevant, as highlighted by the plots in Figure 7.5 lower -left and -right panels. The average slopes are of about 10% K^{-1} and -20% K^{-1}, respectively, corresponding to 26 and -32 W m^{-2} K^{-1}.

Moreover, it is clear how the errors in H and λET are also significantly different for each acquisition, mainly due to the combined effects of wind speed (and then the aerodynamic resistances) and surface temperature magnitude on the assessed fluxes.

For this reason, in Table 7.6 the results obtained for each energy flux are summarized, reporting the average slope of the errors lines and also the minimum and maximum values.

From the analysis of these data it is evident how the sensitivity of R_n and G_0 is not only small, but also the range of variability is slightly significant. Conversely, the range of variability of errors in H and λET is consistent and equal to 7% K^{-1} and 8.5% K^{-1}, respectively.

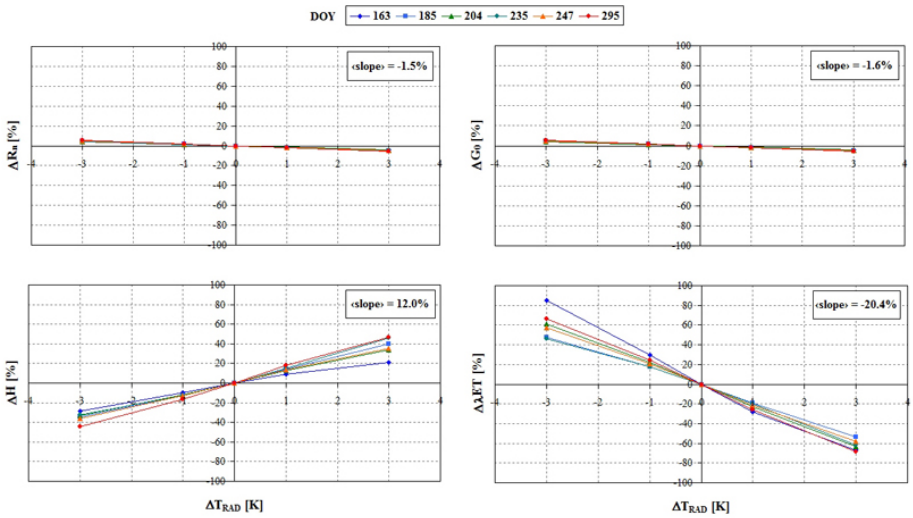

Figure 7.5: Sensitivity of scene-averaged TSEB modelled surface fluxes from the additive errors in surface radiometric temperature. Upper left panel shows the results for R_n; upper right panel shows the results for G_0; lower left panel shows the results for H and lower right panel shows the results for λET. Coloured lines represent the results in correspondence of the airborne acquisitions.

Moreover, it is possible to observe in Figure 7.5 how the relationships between errors in H and λET and ΔT_{RAD} is slightly non-linear, reducing their slope with the increase of the surface temperature error. Even though that evidence, to simplify the analysis, the average slopes were considered to obtain a simpler indicator of the sensitivity.

Finally, it is important to emphasize that the average error in latent heat flux estimation results as a composition of the errors in the other balance components, due to the residual approach adopted by the TSEB model.

Analysis of internal-calibrated TSEB performance

Afterwards the quantification of model sensitivity to errors in temperature, the internal calibration procedure was introduced to TSEB model, naming this version TSEB-IC (see sub–section 4.1.1).

Table 7.6: Summary of the results obtained from the sensitivity analysis of TSEB model, reporting the percentage errors (minimum, mean and maximum values) in surface fluxes related to additive errors introduced in surface temperature.

⟨slope⟩ [%]	R_n	G_0	H	λET
Min	-1.4	-1.4	8.2	-16.8
Mean	-1.5	-1.6	12.0	-20.4
Max	-1.8	-1.8	15.2	-25.3

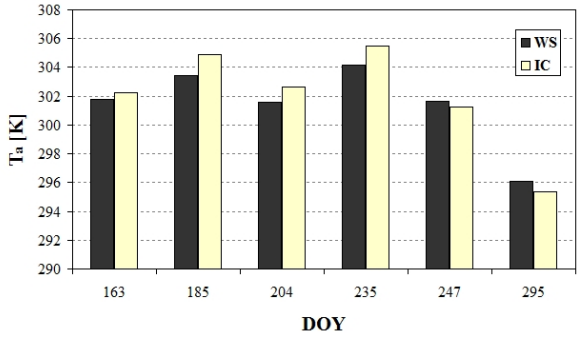

Figure 7.6: Comparison between air temperature measured by weather station (WS) and modelled ones by scene-based approach (IC) in correspondence of the airborne acquisitions.

For the TSEB-IC applications, the nominal scene air temperatures were computed for a pixel in an irrigated citrus grove located in the middle of the test site (dense vegetated area with rectangular shape in Figure 5.1). This area fulfils the two main hypotheses that dictated the choice of the boundary condition: an almost full covered area (to minimize the contribution of the soil layer) and the absence of limitation in water availability.

The application of TSEB model and Eq. (4.15) for the 6 selected dates allows to assess both surface energy fluxes and air temperature at the reference height ($T_{a,\mathrm{IC}}$). In particular, Figure 7.6 reports the values of air temperature obtained from TSEB-IC applications together with the ones measured by weather station (WS).

The analysis of Figure 7.6 highlights the satisfactory matching between

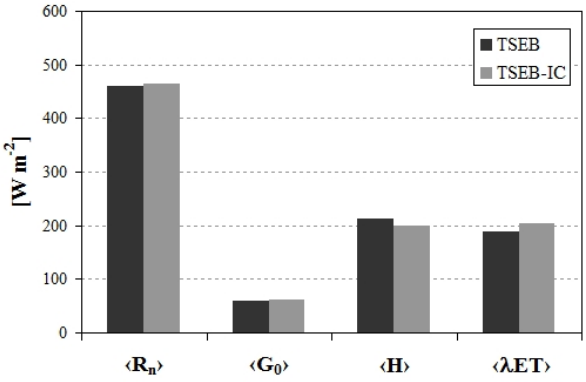

Figure 7.7: Bar-plot comparing the average (in time and space) fluxes modelled by TSEB and TSEB-IC approaches.

observed and modelled T_a, with differences lower than 1 K. These differences, under the evidences of sensitivity analysis, correspond to differences in modelled energy fluxes comparable with the uncertainties observed for the TSEB model in the previously reported validation phase.

It is important to stress that this might not be the case if the surface temperature maps had not been well calibrated. In the case of uncalibrated T_{RAD} maps, the TSEB-IC is specifically designed such that the derived values of $T_{a,\mathrm{IC}}$ would adjust to absorb the bias and to preserve the fluxes.

To better quantify the differences induced by the air temperature internal calibration procedure, the scene-averaged fluxes retrieved by TSEB-IC were compared with the fluxes computed by TSEB. Figure 7.7 reports the mean surface energy fluxes from both modelling approach, computed over all acquisition dates.

For R_n and G_0, the differences are practically negligible, whereas H and λET computed without local air temperature show biases of only 10% compared to TSEB ones. These behaviours are justified by the non systematic differences between IC and WS air temperatures, which causes a sort of compensation effects in the temporal average.

To evaluate how modelling discrepancies vary with date, Figure 7.8 displays bar-plots representing the differences between classical TSEB and TSEB-IC for all the main surface energy fluxes. In these plots, as horizontal dashed lines, are also shown the uncertainties in fluxes measurements (as

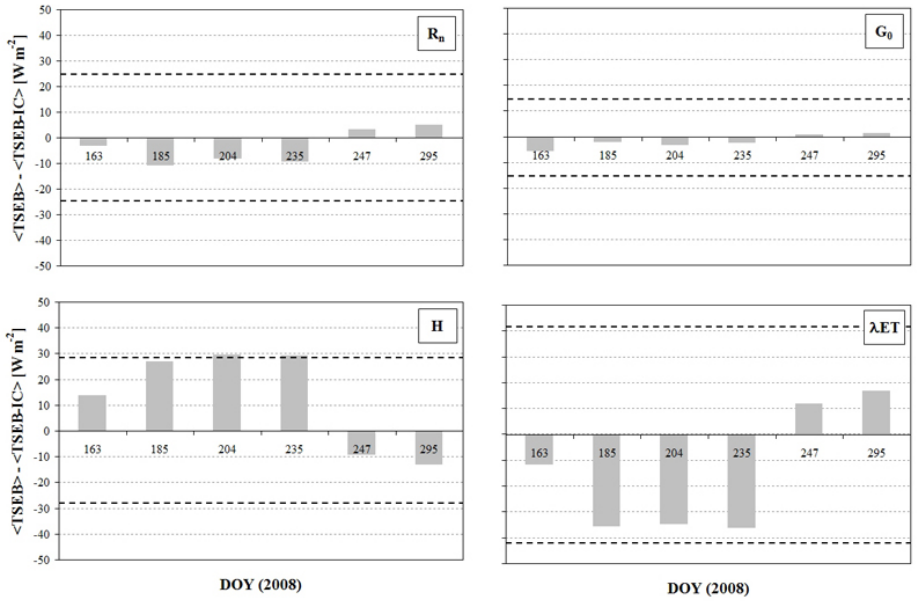

Figure 7.8: Bar-plots representing the differences between scene-averaged fluxes modelled by TSEB and TSEB-IC approaches. Upper left panel shows the net radiation, upper right panel shows the soil heat flux, lower left panel shows the sensible heat flux and the lower right panel shows the latent heat flux. Horizontal dashed lines represent ±MAD values derived from micro-meteorological measures.

±MAD values) assumed as limits of admissibility.

In many cases, the inter-model flux differences are smaller than the observational uncertainties. In particular, the differences in terms of R_n and G_0 are negligible in comparison, with values lower than 10 W m^{-2}, due to the weak sensitivity of TSEB available energy to errors in air temperature values. Differences in H and λET fluxes are more substantial, approaching the observational MAD especially for the DOY 185 and 204, where Figure 7.6 shows the largest overestimation in air temperature. This result may have been due to the ET reference field values less than the potential ones, perhaps due to small degree of moisture stress.

Nevertheless, even for these dates the differences are only slightly larger than the observational uncertainty. Additionally, in average the differences

are lower than the MAD values, allowing to affirm that these differences can be considered acceptable in both cases. Inter-model differences were smaller for the last two acquisitions (DOY 247 and 295), when the wind speeds were lower and the sensible heat fluxes were smaller. The small differences for the first acquisition (DOY 163) are due to the good agreement between air temperatures used in the two approaches (Figure 7.6).

7.2 Application of ALEXI/Dis-ALEXI procedure

The ALEXI model, due to its characteristics, was developed to assess surface energy fluxes partition at continental scale. However, it can be used also as a boundary condition for local-scale applications by means of the previously introduced Dis-ALEXI procedure (see sub-section 4.2.1).

The base of this sub-section are the ALEXI applications in the Italian domain based on the full-resolution MSG products. In particular, the main inputs of the ALEXI model were the maps reported as example in Figure 7.9. More details on the MSG-derived inputs can be found in the sub-section 5.3.2; moreover, a detailed analysis of the ALEXI model performance on the Italian domain are reported in Cammalleri *et al.* (2011).

In this section the results at local scale are analyzed in correspondence of the olive study field. In particular, the indirect validation of the ALEXI outputs and the use of ALEXI-derived H fluxes for the assessment of air temperature in the study case, similarly to the previously discussed TSEB internal-calibrated case, are deeply discussed.

7.2.1 Investigation of ALEXI fluxes at local scale

The application of ALEXI model at local scale was realized in 2008 extracting the data used in Italian domain on the pixels centred on the study site. As example, Figure 7.10 reports the temporal behaviour of incoming solar radiation (DSSF product) at the time t_2 of ALEXI application, together with the values observed by SIAS weather station located in the study area.

Ii is clear a general agreement of the two R_s trends, and also the analysis of the scatterplot between the two quantity (not reported here) shows a satisfactory agreement.

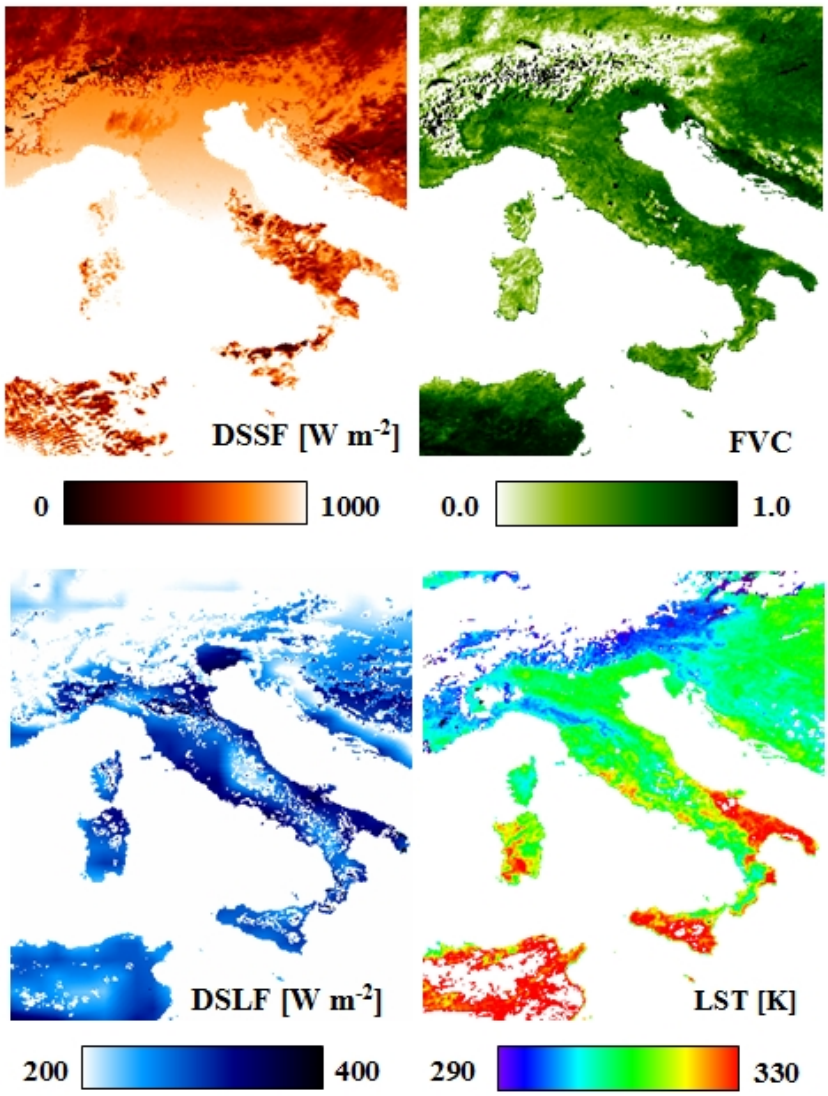

Figure 7.9: Example of the ALEXI inputs derived from Meteosat satellite data acquired on 1 July 2008. See sub-section 5.3.2 for acronym definitions.

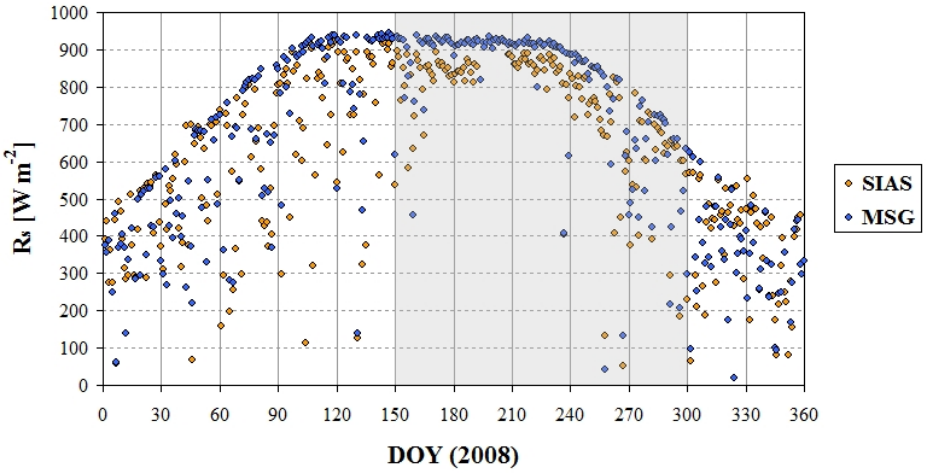

Figure 7.10: Measured (orange dots, from SIAS weather station) and remotely-derived (blue dots, from MSG data) incoming solar radiation in the study site for the 2008. The data correspond to the time t_2 of application of the ALEXI. The grey-filled area highlights the study period (June-October).

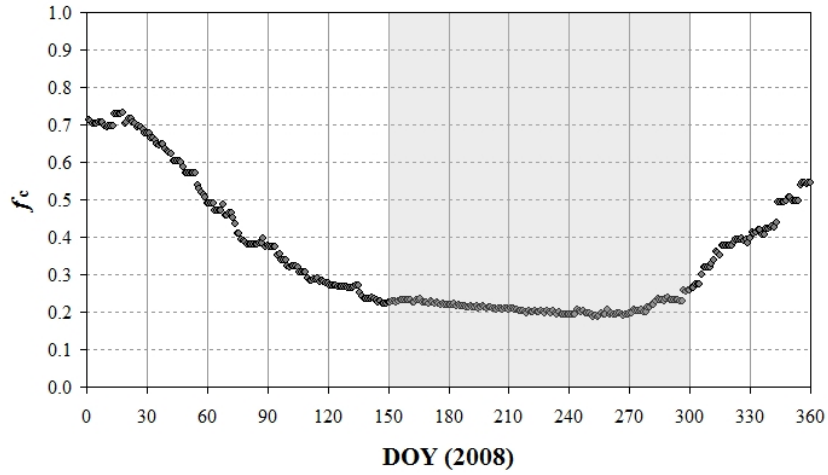

Figure 7.11: Remotely-derived fraction coverage in the study site at daily scale for the 2008. The grey-filled area highlights the study period (June-October).

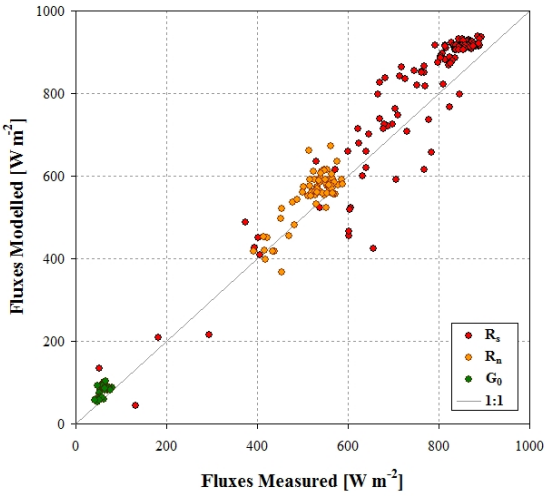

Figure 7.12: Scatterplot of observed *vs.* ALEXI-derived available energy at the time t_2 for the study period (June-October). The red dots represent the incoming solar radiation, the orange dots the net radiation and the gree dots the soil heat flux.

Similarly, Figure 7.11 reports the temporal trend of the fraction cover (FVC product) derived at daily scale from the LSA SAF. This variable shows a concave-up shape, with an almost constant value during the study period (highlighted by the grey-filled box) approximately equal to 0.2.

Some preliminary analyses of the ALEXI data were performed by a brute comparison between the locally observed fluxes and the modelled one. In particular, Figure 7.12 shows the scatterplot relative to the incoming solar radiation (ALEXI model input) and the two components of available energy (R_n and G_0) relative to the study period (June-October 2008).

These comparisons show a fair agreement between the measured data and the remotely-derived ones, through the evident differences in source areas. In fact, despite the ranges of variability of the data are relatively small, these are scattered close to the 1:1 line, and this seems to suggest a significant correlation between the remotely-derived and *in-situ* measured values.

Unfortunately, similar behaviour can not be found in the turbulent fluxes, which show, as expected, a significant dispersion that made complex

the analysis of the agreement with the *in-situ* measured fluxes.

This behaviour is partially explained by the higher spatial variability of the turbulent fluxes due to the heterogeneity of the landscape in the study area. This problem, widely known in literature (Famiglietti and Wood, 1995; Hall *et al.*, 1992; Norman *et al.*, 2003), made complex the direct validation of the ALEXI model outputs, suggesting to use an indirect approach, as the Dis-ALEXI.

On the basis of the above reported considerations, the ALEXI H fluxes retrieved in correspondence of the airborne acquisitions were preliminary compared with the scene-averaged fluxes assessed by TSEB model. As previously reported, the presence of sparse clouds during the 6^{th} acquisition does not allow the application of ALEXI in this date; moreover, the airborne overpass times do not coincide with the ALEXI application times (t_1 and t_2); for this reason a linear interpolation was realized to obtain the ALEXI fluxes at the time of the overpasses.

Figure 7.13 reports the comparison between TSEB scene-averaged H fluxes and the ALEXI ones retrieved as described in the paragraph above. Despite the differences in source areas (100 km^2 for the ALEXI and 1.6 km^2 for the TSEB) the comparison is surprising good, showing a small dispersion of the data around the 1:1 line.

This results represents a promising starting step for the application of Dis-ALEXI procedure, which is analyzed and discussed in the next sub-section.

7.2.2 Validation of ALEXI using Dis-ALEXI approach

As described in the sub-section 4.2.1, the general idea of the Dis-ALEXI approach is to use the air temperature diagnosed by ALEXI instead of a locally observed air temperature, along with high resolution temperature fields typically acquired by aircraft or polar orbiting satellites. This approach implicitly implies two basic hypotheses:

1. the local application of TSEB is realized exactly in correspondence of the ALEXI t_2 time;

2. the errors in high-resolution T_{RAD} maps are the same of the ones in low-resolution (MSG) products.

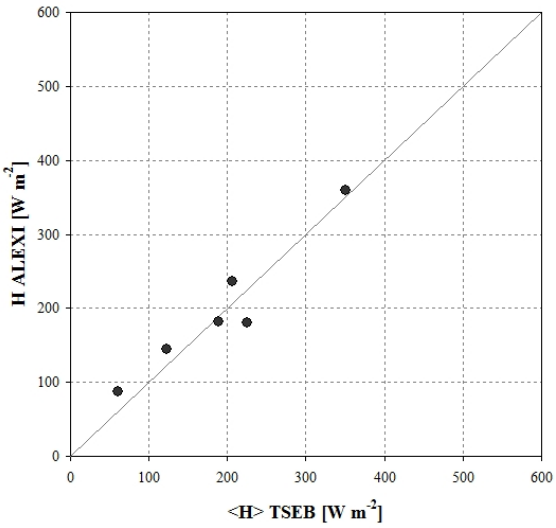

Figure 7.13: Scatterplot comparing the scene-averaged H fluxes, derived from TSEB model applied using airborne images, and H fluxes at the airborne overpasses time derived from ALEXI modelled values in the pixel centred on study area.

It is easy to understand how both these hypotheses are difficult to be respected in the practical applications: the first one due to the limitation in overpass time of high resolution sensors, depending on the polar sun-synchronous orbit or airborne flight time; the second one due to the impossibility to correctly quantify the errors in radiometric temperature calibration.

To ensure that Dis-ALEXI H fields reaggregate to values generated by ALEXI, the air temperature (named $T_{a,\text{Dis-A}}$) is iteratively modified until the average of Dis-ALEXI fluxes matches ALEXI at each ALEXI pixel (Anderson *et al.*, 2008). This allows to use the same T_{RAD} field for of the TSEB and TSEB-IC applications. The ALEXI sensible heat flux used to normalize the area-averaged Dis-ALEXI H field via $T_{a,\text{Dis-A}}$ adjustment was derived at the airborne overpass time by means of temporal linear interpolation between the two ALEXI H fluxes at the times t_1 and t_2.

The plot in Figure 7.14 reports the air temperature values derived applying the Dis-ALEXI procedure (Dis-A) compared with the one observed

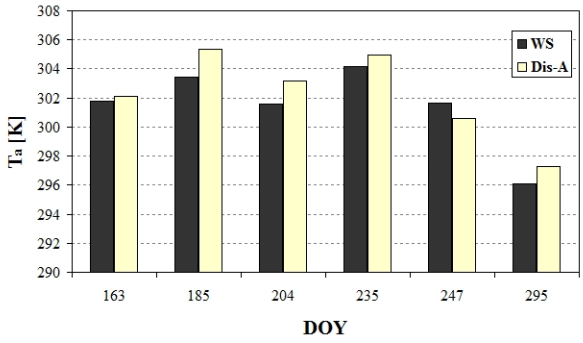

Figure 7.14: Comparison between air temperatures measured by weather station (WS) and modelled ones by Dis-ALEXI (Dis-A) in correspondence of the airborne acquisitions.

by SIAS weather station.

As evident by the analysis of the data reported in this figure, the Dis-ALEXI procedure was applied only for 6 acquisitions, this because (as previously refereed) the date of the 6^{th} acquisition was characterised by sparse clouds during the day, which precludes the application of ALEXI.

The results reported in Figure 7.14 highlight the good agreement between the modelled data and the *in-situ* observations, with differences in the order of 1 K in average. These results are aligned with the ones obtained by applying the internal-calibrated approach (see sub-section 7.1.3) despite the above mentioned differences in the extension of the areas covered by a single MSG full-resolution pixel and the airborne scene.

Analogously to the case of TSEB-IC model, also in this case the Dis-ALEXI performances were analyzed by comparing the scene- and time-averaged fluxes with the classical TSEB one. The results, represented by means of a bar plot in Figure 7.15, show the practically negligible differences between the two models outputs, lower than 10 W m^{-2}.

In order to evaluate how the errors are distributed across the different acquisitions, in Figure 7.16 are reported the bar-plots (one for each surface energy flux) representing the differences between the TSEB and Dis-ALEXI scene-averaged fluxes for the different airborne acquisition dates. Also in this case, two dashed lines are reported on the plots representing the $\pm$MAD of the corresponding measurements.

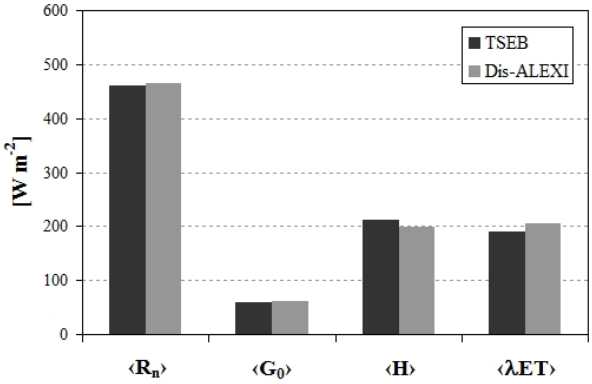

Figure 7.15: Bar-plot comparing the average (in time and space) fluxes modelled by TSEB and Dis-ALEXI approaches.

The analysis of this data highlights how the results are similarly to the one obtained for the TSEB-IC model. Indeed, the differences between the TSEB and Dis-ALEXI models are practically always lower than the corresponding MAD value. In particular, the differences in terms of R_n and G_0 result practically negligible, due to the very small sensitivity of TSEB to errors in temperature values (see sensitivity analysis, Figure 7.6).

More substantial are the differences in H and λET fluxes, with magnitudes comparable with the MAD of the observations, especially for the DOY 185 and 204. The discrepancies on these two dates are probably due to the differences between H ALEXI and scene-averaged TSEB fluxes. However, also in the case of these fluxes, the differences can be considered acceptable because lower in average of the MAD values of the measurements.

These results confirm how the ALEXI/Dis-ALEXI approach, despite it was developed for the disaggregation of ALEXI fluxes at basin or regional scale, seems to provide realistic upper boundary condition also in such small area applications.

7.3 Validations and comparisons at daily scale

Afterwards the detailed analysis of instantaneous energy fluxes estimation, and the considerations on in-canopy wind speed profiles, the capability

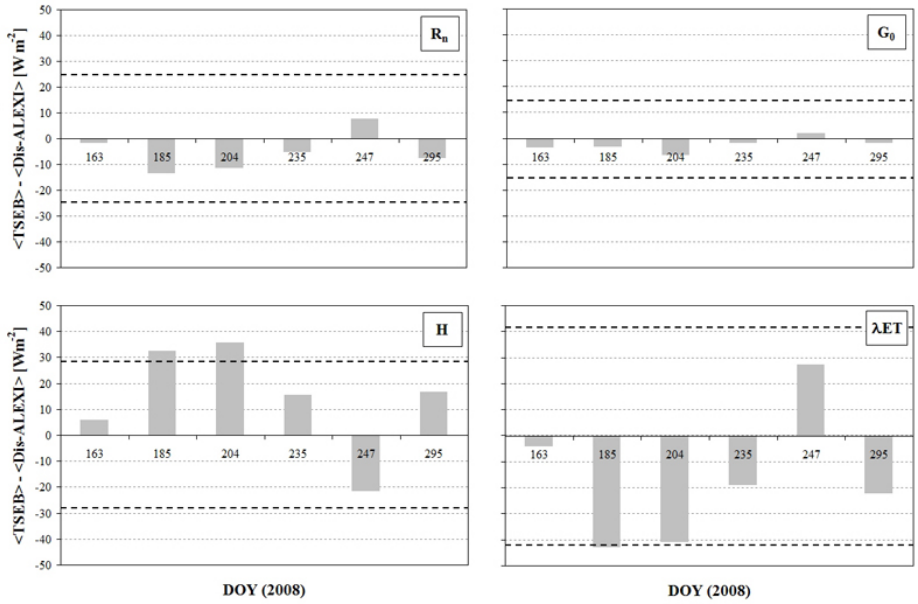

Figure 7.16: Bar-plots representing the differences between scene-averaged fluxes modelled by TSEB and Dis-ALEXI approaches. Upper left panel shows the net radiation, upper right panel shows the soil heat flux, lower left panel shows the sensible heat flux and the lower right panel shows the latent heat flux. Horizontal dashed lines represent ±MAD values derived from micro-meteorological measures.

of the TSEB modelling framework to provide robust estimates of daily evapotranspiration, with and without local observations of air temperature, was also tested.

This is a crucial issue, because in practical hydrological applications the required final product is generally represented by ET_{24} maps. Furthermore, because the TSEB computes λET as a residual, daily ET represents a sort of summary of the models uncertainties in all flux components.

Additionally, as preliminary shown on the micro-meteorological measurements, the pertinence of some assumptions on daily net radiation estimation (see sub-section 6.4.1) and self preservation of evaporative fraction (see sub-section 6.4.2) have to be confirmed.

As first test, the fluxes derived from classical TSEB model (adopting

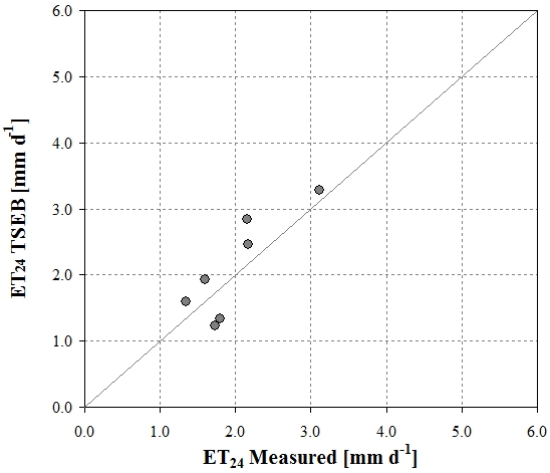

Figure 7.17: Scatterplot comparing the measured and TSEB-derived daily evapotranspiration in correspondence of the olive groove.

in this phase always the Massman in-canopy wind speed formulation, sub-section 7.1.2) were integrated at daily scale using the formulations described in sub-section 4.1.3. In particular, the best results were obtained adopting the Eq. (4.21) with the correction to Λ suggested by Anderson *et al.* (1997).

These results, reported in Figure 7.17, are similar to the ones obtained by analyzing the daily evapotranspiration measured by EC1 and SAS micrometeorological stations, confirming the finding reported in sub-section 6.4.2.

It is important to stress that the daily long-wave net radiation adopted to derive $R_{n,24}$, to be introduced in Eq. (4.21), was assessed by means of the theoretical relationship proposed in sub-section 2.1.5 (see Eq. (2.65)) after the introduction of the empirically assessed coefficient K_T^*. This solution suggests the requirements of further studies on this coefficient to generalize the procedure for a variety of canopy coverage.

On the other hand, the estimations obtained with the other methodologies were not so far from this optimal results, suggesting the possibility to obtain reliable results also with scale parameters derivable in a simpler way.

The obtained results showed a satisfactory agreement with the observed

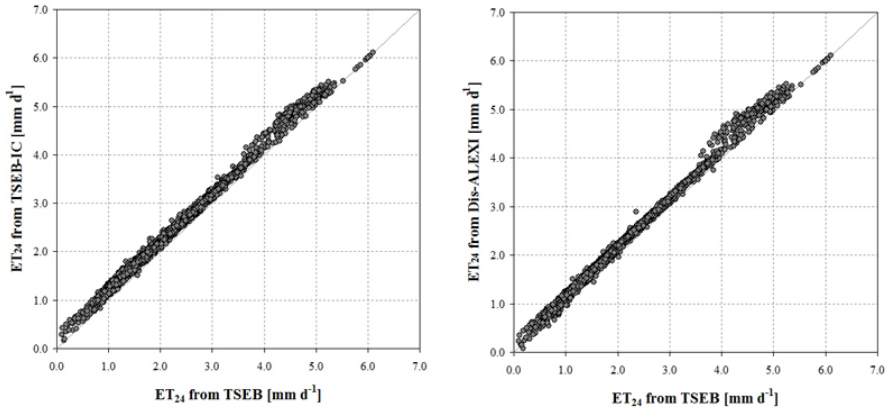

Figure 7.18: Scatterplots comparing the six acquisitions-average daily evapotranspiration derived from: left panel, TSEB and TSEB-IC; right panel TSEB and Dis-ALEXI.

values, characterized by average deviation from the observations quantified by RMSD and MAD of 0.42 and 0.39 mm d^{-1}, respectively. These values are comparable with the measurement uncertainties, generally assumed equal to 0.5 mm d^{-1} (see Table 6.4).

On the basis of these results, the analysis of the ET_{24} maps obtained by means of TSEB-IC and Dis-ALEXI was performed, focusing the attentions on both the agreement with the TSEB ones and the accord in terms of spatial distribution of ET_{24} within the airborne scenes.

The two scatterplots reported in Figure 7.18 show the comparison between the 6-scenes average TSEB ET_{24} values and the corresponding ones retrieved by TSEB-IC (left panel) and Dis-ALEXI (right panel).

These plots highlight the small dispersion of the data across the 1:1 line, with an overestimation of about 0.2 mm d^{-1} on average in both TSEB-IC and Dis-ALEXI approaches.

The analysis of ET_{24} spatial patterns was realized by mapping the ET_{24} averaged over each of the 6 acquisitions as reported in Figure 7.19.

These maps demonstrate the good agreement in the spatial patterns among the three models across the whole scene. The only remarkable difference can be found in the dry areas in the north-west part of the scene, where TSEB returns lower values compared with the other two approaches.

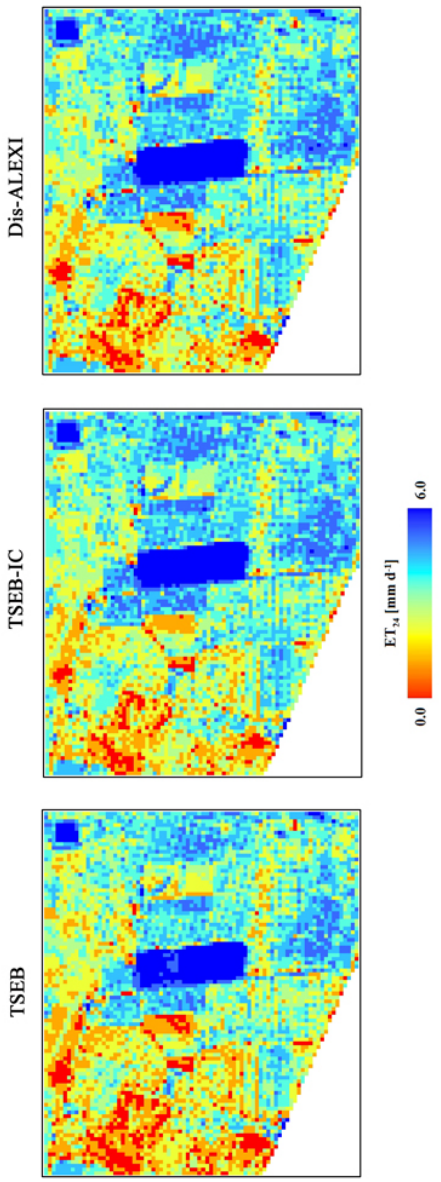

Figure 7.19: Maps representing the 6 acquisitions-average daily evapotranspiration derived from TSEB (left panel), TSEB-IC (centre panel) and Dis-ALEXI (right panel).

The good correspondence of spatial patterns observable in Figure 7.19, and the small additive bias, suggests that the errors related to the differences in air temperature are uniformly distributed across the scene. This is not surprising given that the air temperature is assumed constant within the scene by all the three models.

Chapter 8

Continuous daily ET estimations

In this chapter the estimations of evapotranspiration in the olive study field are analyzed. The tested models include remote sensing-based residual approaches and schemes based on the coupling of energy and hydrological balances. The 5 applied models were previously described in the subsections 4.2 and 4.3.

The simulations cover a time interval of 153 days (from 1 June to 31 October of the 2008) and adopt the airborne images to derive all the parameters required to define the surface characteristics.

All the applied models allow to assess the outputs in a spatially distributed way at the spatial resolution of 12 m; then, the retrieved results were averaged in correspondence of the olive field and compared with the observed values.

Model's performances were tested both in terms of evapotranspiration and stress indices at daily scale, and hourly surface fluxes. Overall accuracy of the models was assessed using the previously introduced MAD, RMSD and RE and two different efficiency indices: the efficiency index of Nash and Sutcliffe, E, and the Willmott's index of agreement, IA, (see Appendix B for more details).

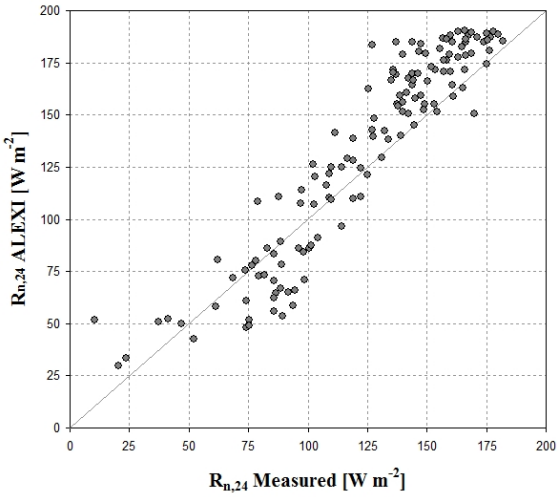

Figure 8.1: Scatterplot comparing the daily net radiation locally-measured and modelled by ALEXI. The data refer to June–October 2008 study period.

8.1 Application of ALEXI/Dis-ALEXI at daily scale

The ALEXI/Dis-ALEXI application, previously discussed in sub-section 7.2.2, allows us to assess the daily evapotranspiration, at high spatial resolution, in correspondence of the airborne overpasses.

However, as described in sub-section 4.1.2, the ALEXI procedure provides continuous low resolution estimation of ET_{24} by means of continuous assessment of $R_{n,24}$ and assessment of Λ in cloud-free days (see sub-section 4.1.2 for details).

On the basis of these low resolution modelled fluxes the high resolution ET_{24} assessment is obtained by means of the simple downscaling procedure reported in sub-section 4.2.1.

As first evaluation of the performance of this procedure, the continuous estimations of $R_{n,24}$ were compared with the locally observed values by means of a scatterplot analysis, as reported in Figure 8.1.

These estimations, despite the significant differences between pixel resolution (3.5 km) and instrument footprint ($\sim$ 20 m), showed a substantial agreement between modelled and measured values, with an average error

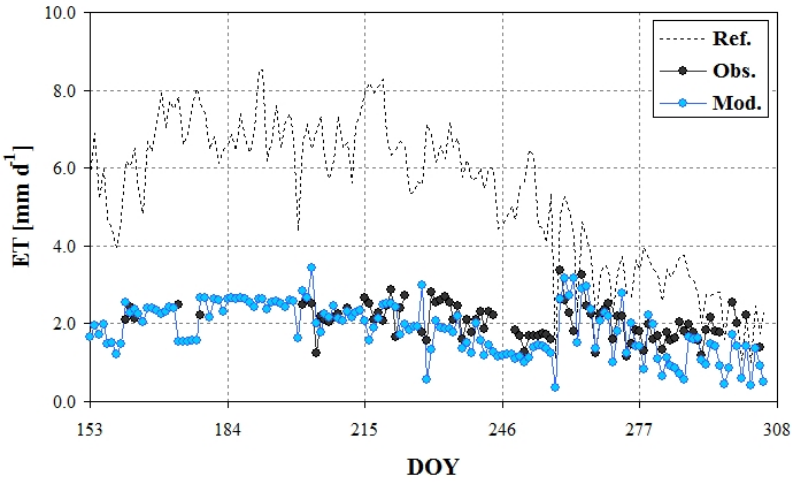

Figure 8.2: Temporal trend of daily evapotranspiration modelled by ALEXI/Dis-ALEXI procedure. The Obs. values correspond to the observations made by EC1/SAS systems; Mod. values are the ones modelled by ALEXI/Dis-ALEXI procedure; and Ref. values are the ET_0 derived applying the FAO-56 formulation on the locally observed weather data.

quantified by a MAD of 15 W m^{-2} (equivalent to about 0.5 mm d^{-1}). Moreover, the scatterplot analysis shows a slightly bias between observed and modelled values, with an overestimation of the higher values and an underestimation of the lower ones; however, this bias is comparable with the data dispersion.

These data were joined with the low resolution ET_{24} estimations, which cover directly the 51% of the simulation period (78 days), in order to obtain continuous estimation of daily ET at low resolution.

Finally, adding the information obtained by means of airborne overpasses, high-resolution maps of daily ET were obtained for the whole study period. Figure 8.2 reports the olive field-averaged ET_{24} values obtained taking into account the fluxes downscaling performed by Dis-ALEXI technique.

These results show a moderate agreement with the observed values, with a slight underestimation in the second part of the study period (after the DOY 230). This behaviour can be partially explained by the irrigation

supplies which occur in the second part of the simulation period. Instead, it is interesting to notice how the models is able to catch the increase of ET_{24} in the days after the rainfall events in the DOY 258 and 267 due to the use of a low resolution actual evapotranspiration as proxy variable; the latter accounts for the variability in water availability at large scale, as the one caused by a rainfall event.

The indices of agreement MAD and RMSD assume values slightly greater than the measurements uncertainties, equal to 0.51 and 0.60 mm d^{-1}, respectively. These values are generally comparable with the accuracy associated to large scale ET assessment, confirming an almost acceptable performance of the model. Moreover, the relative error (24.5%) is only slightly higher than the measurements uncertainties.

8.2 Use of hot-spot TSEB estimations for daily ET monitoring

The outputs of TSEB, similarly to the Dis-ALEXI ones, were used to rescale a continuous variable, represented in this case by the potential evapotranspiration (see sub-sections 4.2.2 and 4.2.3).

The procedures adopted for the ET_p assessment were represented by two different schemes: the former based on the direct application of Penman-Monteith formulation (PM-based approach, sub-section 4.2.2); the latter one is based on a remote estimation of both ET_0 and K_c (named RS-based approach, sub-section 4.2.3).

As deeply discussed in Chapter 4, the remote estimation of ET_0 was realized mainly by means of MSG observation of incoming solar radiation. As first step, these estimations were compared with the one retrieved applying the FAO-56 standard formulation by means of locally observed weather data. The latter method was assumed as the reference one for the assessment of ET_0 in absence of local measurements of this variable.

This comparison is reported in the scatterplot of Figure 8.3, corresponding to the values simulated for the years 2007 and 2008.

The results obtained by applying the Eq. (4.26), despite the numerous simplifications, showed a good agreement with the locally derived values, with MAD and RMSD equal to 0.49 and 0.62 mm d^{-1}, respectively. These values, considering an average ET_0 of about 3.5 mm d^{-1}, correspond to

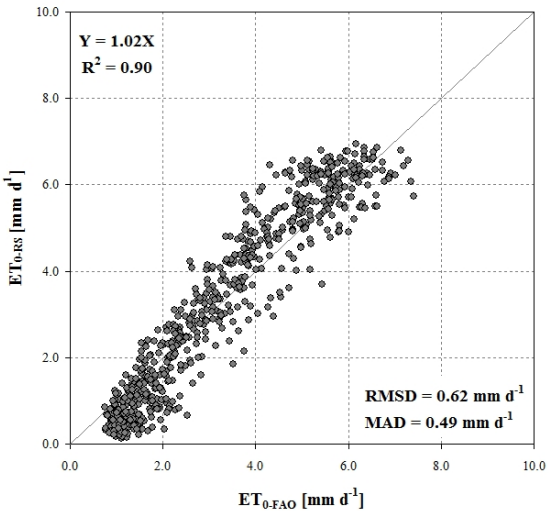

Figure 8.3: Scatterplot comparing the reference evapotranspiration derived from FAO-56 formulation ($ET_{0\text{-FAO}}$) and modelled using remotely-sensed data ($ET_{0\text{-RS}}$).

a relative error of about 14–18%, only slightly higher than the accuracy assumed by FAO-56 formulation.

Moreover, also the analysis of linear regression line returns a significant high determination coefficient ($R^2 = 0.90$) and a slope close to the unity.

These continuous remote estimations of ET_0, together with the K_c modelled at high resolution by means of Eq. (4.29), allow to obtain continuous estimation of daily ET_p during the study period.

Analogously, the application of PM formulation at hourly basis, as described by the functional relationship in Eq. (4.24), allows the direct assessment of high spatial resolution of ET_p for the whole airborne scene.

The temporal trend of these two estimations of ET_p, averaged in correspondence of the olive field, was plotted in the Figure 8.4 together with the one of FAO-56 standard procedure (assumed again as the reference).

The comparison reported in Figure 8.4 shows a general agreement among the three ET_p is observable, with a quite good correspondence between the FAO-56 one and the PM-based. The RS-based approach returns values that agrees well in the main trend but which misses some small scale dynamic due to the invariance of K_c between two airborne

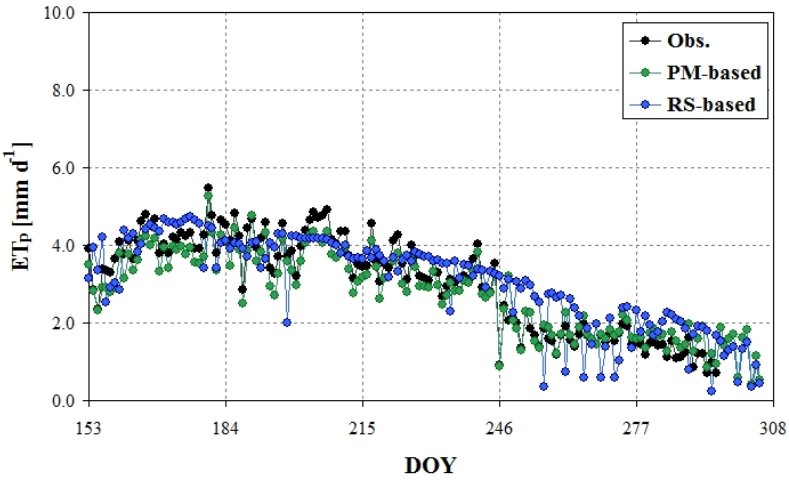

Figure 8.4: Temporal trend of potential evapotranspiration modelled by RS-based (blue dots) and PM-based (green dots) approaches. The Obs. values correspond to the ET_p derived applying the FAO-56 standard formulation on the locally observed weather data.

acquisitions.

It is important to notice how the application of FAO-56 approach was possible only because of the detailed knowledge of study area, which permits to correct the standard tabled K_c values to take into account the effective crop characteristics (e.g., fraction cover, canopy height).

In this context, the extremely good performance of the PM-based approach confirms its capability to obtain reliable ET_p also in absence of *in-situ* information on crop characteristics. Moreover, considering the reduced amount of information required by the RS-based approach (all derived from remote observation), also the latter estimations become interesting in the framework of the applicability in absence of local weather station.

Both these estimations of ET_p were used to derive continuous daily actual evapotranspiration by means of a stress coefficient computed on the base of hot-spot ET_{24} maps obtained by means of TSEB model.

The plot in Figure 8.5 shows the results relative to the use of RS-based ET_p as continuous proxy variable. The red rhombus in the same

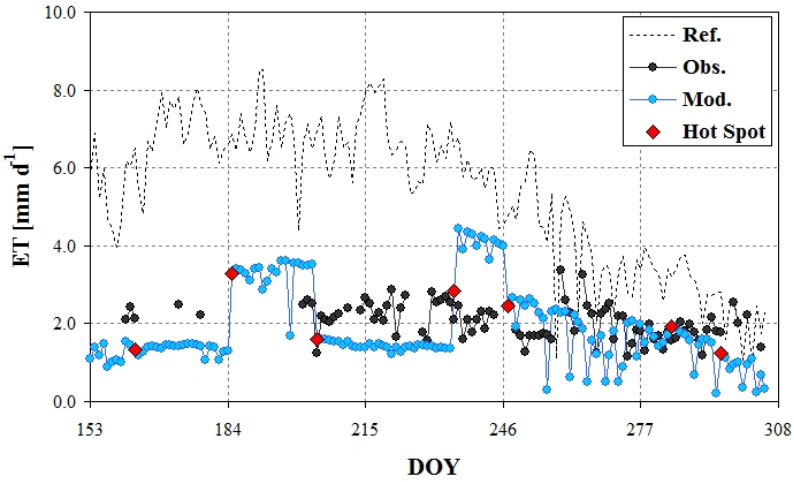

Figure 8.5: Temporal trend of daily evapotranspiration modelled by RS-based approach. The Obs. values correspond to the observations made by EC1/SAS systems; Mod. values are the ones modelled by means of remotely sensed ET_p and hot-spot TSEB estimations (red rhombus); and Ref. values are the ET_0 derived applying the FAO-56 formulation on the locally observed weather data.

figure highlight the estimations realized by TSEB in correspondence of the airborne overpasses, used for the assessment of K_s values, which are constant between two acquisitions.

The results reported in Figure 8.5 showed how in many cases the estimations retrieved by RS-based approach are unsatisfactory, with clear biases especially in the first period (until DOY 246). This behaviour is mainly due to the direct influences of single hot-spot bias on the assessment of ET in a long period (approximately 2 weeks) between two successive airborne acquisitions.

In fact, the errors in TSEB hot-spot estimations, previously considered globally acceptable (see sub-section 7.3), becomes the cause of systematic biases in long term assessments. This behaviour is clearly evidenced by the jumps in modelled ET_{24} values between two following airborne acquisitions.

The previously reported consideration of smaller errors in the estimations performed in the last acquisitions (characterized by lower water stress) is again confirmed by the better performance in the last days of the

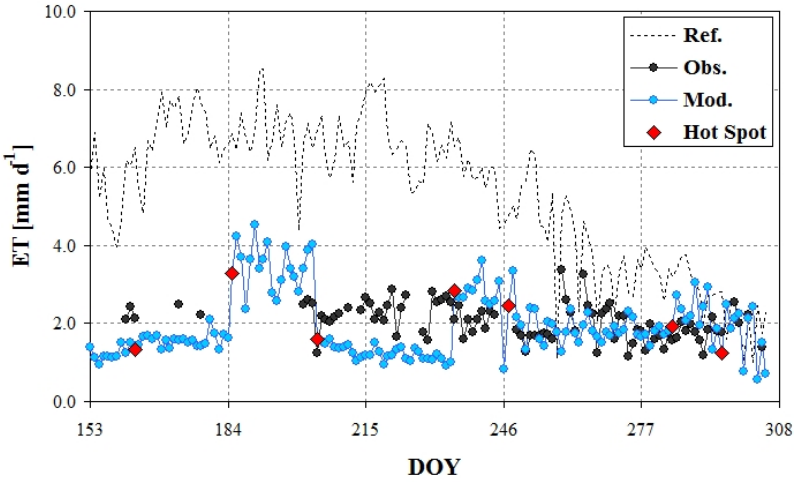

Figure 8.6: Temporal trend of daily evapotranspiration modelled by PM-based approach. The Obs. values correspond to the observations made by EC1/SAS systems; Mod. values are the ones modelled by means of Penman-Monteith ET_p and hot-spot TSEB estimations (red rhombus); and Ref. values are the ET_0 derived applying the FAO-56 formulation on the locally observed weather data.

simulation period.

The indices of agreement assume in this case values approximately equal to 1 mm d^{-1} (MAD = 0.91 and RMSD = 1.09), two times the measurements accuracy, confirming the poor performance of the RS-based approach. Also the RE value, close to 45%, suggests the poor performance of the RS-based model.

Similar considerations can be expressed for the PM-based model, which results are reported in Figure 8.6. Despite that, in this case the agreement with the observed values seems slightly better, showing however the same characteristic jumps in correspondence of the TSEB hot-spot estimations.

The analysis of MAD and RMSD indices, which are equal to 0.72 and 0.86 mm d^{-1}, respectively, highlights the improvement in model performance compared with the RS-based case. Also the relative error (RE = 33%) become closer to the one for the ALEXI/Dis-ALEXI, still remaining unsatisfactory. An explanation of this better performance can be found in the better agreement in the day-by-day comparison of ET_p

values with the effective atmospheric requirement; this behaviour limits the systematic biases which is dragged to the days comprised between two successive airborne acquisitions.

However, despite the improvements in PM-model performance, the statistical indices suggest how the obtained outputs are characterized by an unsatisfactory degree of accuracy for detailed field-scale applications.

Finally, it is interesting to notice how both the PM- and RS- based models were not able to catch the ET_{24} increase few days after the rainfall events; this can be explained by the absence of information related to these events neither in the adopted hot-spot images (acquired few days before/after the events) nor in the continuous proxy variables (potential evapotranspiration values, which is independent from effective soil water availability).

8.3 Application of land surface models

Differently from the previously analyzed approaches, the models analyzed in this sub-section introduce the direct modelling of latent heat flux to overcome the requiring of daily surface temperature observations. In these cases, adopting an hydrological scheme based on the force restore approach (see sub-section 4.3), is possible to obtain continuous estimation of both actual evapotranspiration and soil water content.

Two different models were applied, the first based on a scheme similar to the one proposed by FAO-56, called dual crop coefficient (2-CC) and developed for daily estimations; the second one is based on the coupled solution of energy and hydrological balance at hourly scale by means of a SVAT scheme.

The inputs involved in these two models include the precipitation and the irrigation at daily and hourly scale, respectively, further highlighting the increase in required information compared to the previously reported approaches.

Additionally, the introduction of an hydrological scheme, even if simple, requires the definition of soil hydraulic characteristics and root zone extension. The soil parameters assumed for the simulations are summarized in Table 8.1. These values were obtained from *in-situ* charachterization of the study site (Minacapilli *et al.*, 2009) or directly from the tabled values

Table 8.1: Soil parameters adopted in the force-restore scheme for 2-CC and SVAT simulations.

Parameter	Description	Value	Source*
θ_{sat}	Saturated soil water content	0.42	a
θ_{wl}	Residual soil water content	0.11	a
K_{sat}	Saturated hydraulic conductivity	1.27×10^{-6}	a
d_{z1}	Soil surface layer thickness	0.1	a
d_{z2}	Root zone layer thickness	0.9	a
b_*	Slope of the retention curve on a log graph	10.4	b
a_*	Parameter for θ_{eq} computation	0.075	b
p_*	Parameter for θ_{eq} computation	10.0	b
$C_{1,sat}$	Value assumed by C_1 at saturation	0.375	b
$C_{2,ref}$	Parameter for C_2 computation	0.3	b

* Source are as follow: (a) Minacapilli *et al.* (2009); (b) Noilhan and Planton (1989)

as suggested by Noilhan and Planton (1989).

The initial soil water content conditions, for both the applied models, were fixed equal to 0.30 m^3 m^{-3} for the root zone layer and 0.10 m^3 m^{-3} for the surface layer; these values were derived from *in-situ* measurements acquired few days after the simulations beginning.

8.3.1 Analysis of dual crop coefficient model

The dual crop coefficient (2-CC) approach, as described in sub-section 4.3.1, models the potential crop transpiration by means of a direct application of the PM formulation at hourly scale analogously to the approach previously reported in sub-section 8.2. These estimations, aggregated at daily scale, were used jointly with stress coefficients K_s and K_r to derive actual evapotranspiration at daily scale.

Thanks to the application of the dual crop coefficient the estimation of evaporation and transpiration, separately, was allowed. These two values were introduced in the hydrological balance Eqs. (4.30) to model water content in surface layer and root zone.

Analogously to the previous reported cases, the model outputs were compared with the observations made by micro-meteorological installations at daily scale. This comparison, reported in Figure 8.7, shows the good agreement between the modelled and observed values across the whole

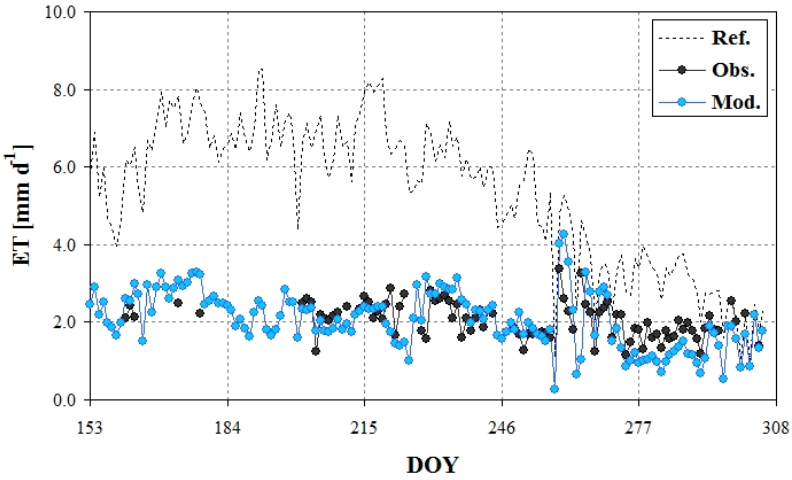

Figure 8.7: Temporal trend of daily evapotranspiration modelled by 2-CC approach. The Obs. values correspond to the observations made by EC1/SAS systems; Mod. values are the ones modelled by means of dual crop coefficient scheme and force restore approach; and Ref. values are the ET_0 derived applying the FAO-56 formulation on the locally observed weather data.

simulation period.

In fact, the temporal trend of the observed ET_{24} is well reproduced by the 2-CC model both in the drier and wetter periods. In particular, the increase of evapotranspiration after the rainfalls that occurs in the DOY 258 and 267 is also caught by the models due to the increase in soil evaporation component.

Even if the observed daily ET flux showed only a slight variability during the study period, is possible to observe how the 2-CC model, differently from the ones analyzed in the previous section, is able to reasonably catch the short term fluctuations in the observed ET_{24}.

As introduced by the qualitative analysis, the indices of agreement MAD and RMSD show the good capability of the 2-CC to model the daily evapotranspiration, with values equal to 0.48 and 0.61 mm d^{-1}, respectively. These values are slightly higher of the uncertainties in observed data, but can be considered not far from the acceptability. Moreover, a RE value of 23.2% suggests how the performance of the model are very close to the

measurements uncertainties (20%).

Despite the approximations in the modelling of water stress (by means of simple multiplicative coefficients) which seem to be unrealistic especially for sparse tall crops, the obtained agreement with the observed values seems to endorse the applicability of this method in such system with the above reported degree of accuracy.

8.3.2 Analysis of SVAT model

The SVAT model simulation was performed in the previously introduced study period by means of hourly meteorological inputs. In order to made comparable the results with the ones obtained with 2-CC approach, a zero flux was assumed at the bottom of soil profile ($Q = 0$). This hypothesis is justified by the presence of a layer with low permeability located at a depth of 1.2 m, just few cm below the assumed root zone depth.

Due to the temporal scale adopted by the model, the comparison between simulated and observed values was performed both in terms of hourly energy fluxes and daily actual evapotranspiration.

Validation at hourly scale

The analysis of hourly energy fluxes was simply realized by comparing both the agreement in terms of diurnal shape and value-by-value correspondence. Figure 8.8 reports the modelled fluxes for a period of 20 days (from DOY 200 to DOY 220) with the corresponding measured values. In the upper panel the data relative to the available energy are reported, instead, the lower panel reports the values corespondent to the turbulent fluxes.

As observable from these plots the model outputs well agree with the observations, with a general agreement between simulated and measured fluxes in the daily shape of all the variables.

A detailed analysis of the temporal trends shows a good agreement in the day-time values and a slight underestimation in the night-time simulated fluxes, especially for net radiation and sensible heat flux. Consequently the simulated values of latent heat fluxes show the overestimation at the night time (Figure 8.8, lower panel).

In order to quantify the model performance, the modelled fluxes were plotted against the observed one by means of scatterplots, as shown in

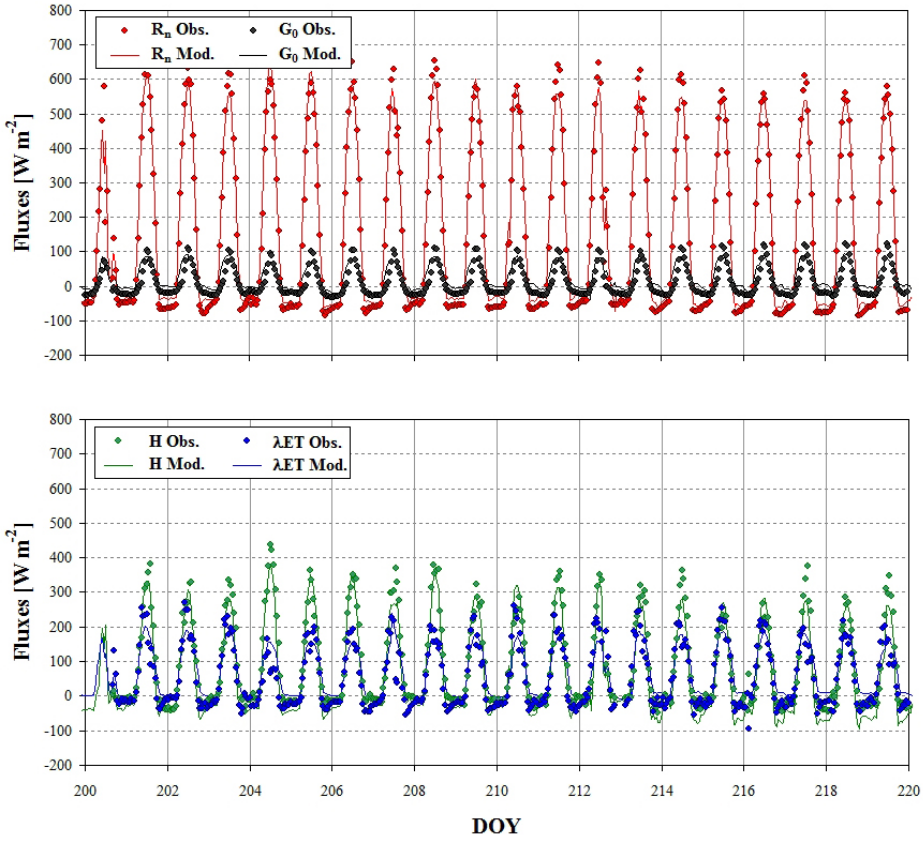

Figure 8.8: Temporal trend of hourly fluxes modelled by SVAT approach in a subset of 20 days in the simulation time. Upper panel shows the observed (dots) and modelled (continuous line) net radiation (in red) and soil heat flux (in black). Lower panel shows the observed (dots) and modelled (continuous line) sensible (in green) and latent (in blue) heat fluxes.

Table 8.2: Summary of hourly energy fluxes statistics derived from the comparison of SVAT modelled values and EC/SAS observed ones.

Flux	MAD [W m^2]	RMSD [W m^2]	E	IA
R_n	28	41	0.97	0.99
G_0	16	20	0.67	0.91
H	34	47	0.87	0.95
λET	34	44	0.82	0.93

Figure 8.9.

The analysis of the scatterplots in Figure 8.9 confirms how the data are moderately little dispersed around the 1:1 line, showing no significant bias in the modelled fluxes.

Table 8.2 summarizes the values of the statistical indices for all the terms of the surface energy balance, at an hourly scale. The statistical metrics indicate that the mean errors for the modelled fluxes are of the same order of magnitude of the uncertainties associated with the measurements, with the higher values of MAD and RMSD for H and λET equal for both to about 35 and 45 W m^{-2}, respectively.

The analysis of agreement index IA shows a good model performance for all the surface fluxes, with values always higher than 0.9. Similarly, the analysis of the E index shows values close to 1 (perfect match) for R_n, and quite high values also for H and λET, confirming a general good accuracy of the modelled values. The value of E index obtained for G_0 (0.67) is also significantly high, but suggests the possibility to improve the performance by means of a more physically-based scheme. However, considering the small impact of G_0 value on the daily ET estimation, the accuracy in G_0 assessment can be considered acceptable, since the mean errors (MAD and RMSD) are low.

The obtained accuracy is generally comparable with the ones reported in similar studies (Boulet *et al.*, 2000; Falge *et al.*, 2005; Schelde *et al.*, 1997; van der Keur *et al.*, 2001) carried out under different climatic conditions and crop types.

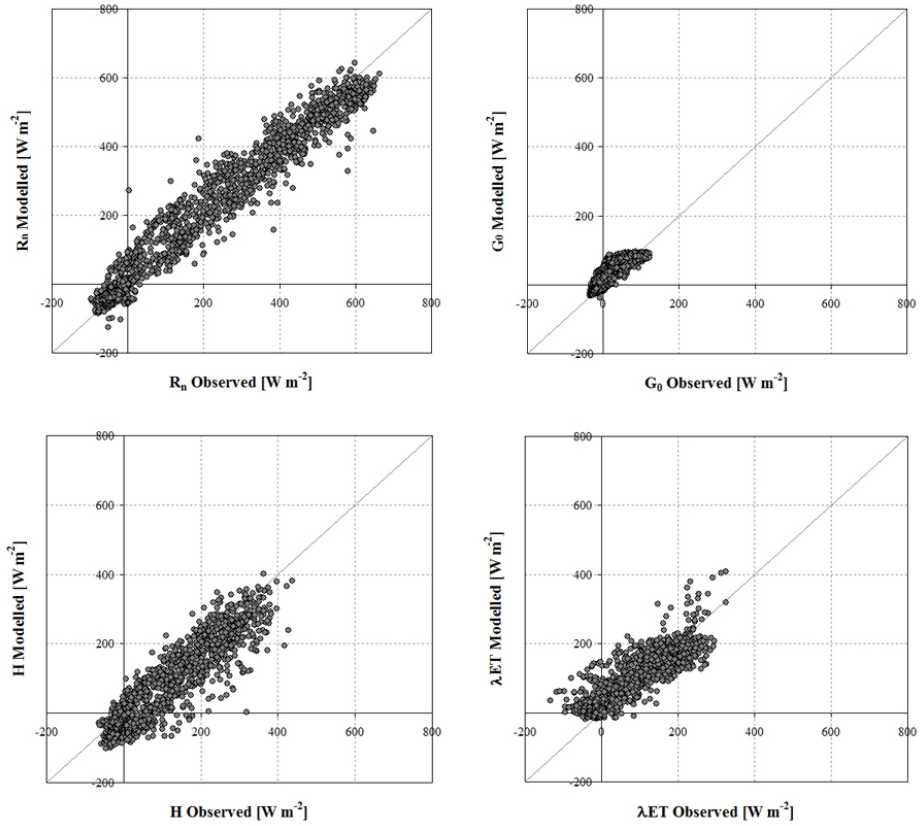

Figure 8.9: Scatterplots comparing the surface energy fluxes observed by EC1/SAS systems and modelled by SVAT at hourly scale. Upper line panels report the net radiation (left panel) and the soil heat flux (right panel); the lower lines panels report the sensible (left panel) and latent (right panel) heat fluxes.

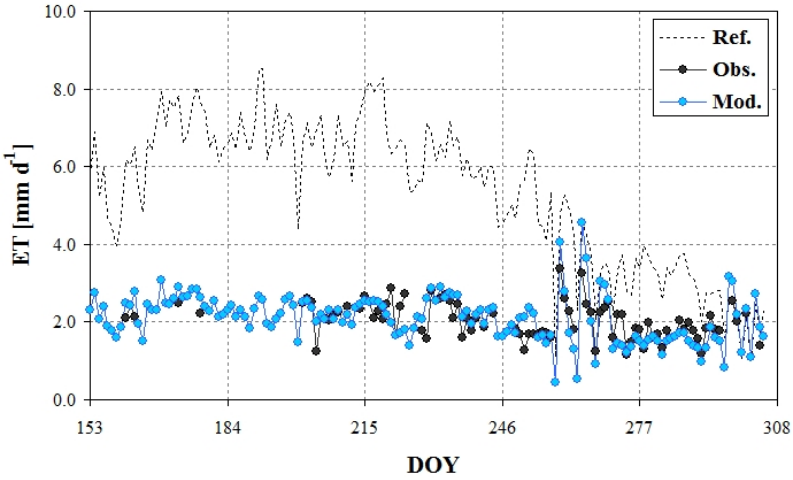

Figure 8.10: Temporal trend of daily evapotranspiration modelled by SVAT approach. The Obs. values correspond to the observations made by EC1/SAS systems; Mod. values are the ones modelled by means of two-source scheme and force restore approach; and Ref. values are the ET_0 derived applying the FAO-56 formulation on the locally observed weather data.

Validation at daily scale

The modelled latent heat flux was aggregated at daily scale and compared with the observed values. Figure 8.10 shows the comparison between measured and modelled daily evapotranspiration. As can be generally observed, the pattern of ET_{24} is well reproduced by the model both in terms of ranges of variability and temporal dynamic.

Analyzing in details the plot in Figure 8.10, it is possible to observe how no significant bias are present between modelled and observed values; this is confirmed by the analysis of model accuracy, assessed using RE, MAD and RMSD statistical indices, which reports values equal to 15.4%, 0.32 and 0.43 mm d^{-1}, respectively.

These RE, MAD and RMSD values are slightly lower to the ones corresponding to the measurements accuracy, and are also similar to those found for other applications of similar models (Crow *et al.*, 2008). Moreover, considering the high degree of water stress that occurs in the simulation period, the accuracy of this model seems to adequate reproduce

the values obtained from the measured data, as deeply discussed in the next sub-section.

8.4 Water stress modelling

The effective capability of the model to reproduce the evapotranspiration process can be evaluated also in terms of the capability to reconstruct the effective environmental stress condition (mainly due to soil water deficit). In fact, in practical applications the parameter of real interest is the reduction of the actual condition from the theoretical potential one, in order to quantify the stress induced by limited water availability.

In the specific case, on the basis of the analogy between K_cK_s and Λ measured terms reported in the sub-section 6.4.3, the indicator adopted to quantify the water stress is the ratio ET_{24}/ET_0 (equal to the product K_cK_s of the FAO-56 scheme).

To facilitate an objective analysis, in Table 8.3 are reported the statistical indices derived by the comparison of modelled ET_{24}/ET_0 values with the observed one across the whole study period.

First of all it is interesting to notice the quite small variability of MAD and RMSD indices for the different models, mainly due to the reduced variability of the adopted stress index (0–1). This consideration suggests how, differently from ET_{24} data, these indices are not suitable for the critical analysis of ET_{24}/ET_0 ratio in this study case.

Similarly, the efficiency index IA seems to return high values for all the models (with the exception of RS-based one), suggesting also in this case the non-optimality of the use of this statistical metric in the specific case.

After these preliminary considerations, the results in Table 8.3 show, as previously underlined in the above reported analyses on ET_{24}, the optimal performance obtained with the SVAT model which returns the best agreement both in terms of accuracy (RMSD, MAD and RE) and efficiency (E and IA).

Moreover, the SVAT model is the only one that obtained a satisfactory efficiency E (0.66); this means both small modelling errors and a good capability to reproduce the general behaviour of the stress index as well. This result is particularly significant if analyzed with the regression line which have a slope closer to the unity (0.97) with a R^2 of 0.75 and a

Table 8.3: Summary of statistical indices of modelled continuous stress factor. A description of the indices is reported in the Appendix B.

Index	ALEXI	PM-based	RS-based	2-CC	SVAT
Mean	0.39	0.44	0.39	0.42	0.46
MAD	0.12	0.15	0.19	0.11	0.07
RMSD	0.15	0.18	0.24	0.15	0.10
RE	25.5	32.3	42.5	24.7	16.1
E	0.28	-0.10	-0.97	0.30	0.66
IA	0.80	0.79	0.49	0.81	0.92

negligible intercept.

The analysis of the statistical indices highlights also how both the 2-CC and ALEXI/Dis-ALEXI approaches perform similarly in term of almost all the statistical metrics, as previously highlighted by ET_{24} data analysis. Unfortunately, both models return values of the efficiency E significantly smaller than the SVAT one, suggesting how the performance as slightly far from optimality.

Additionally, a significant difference between these two models is observable in terms of the average ET_{24} (or the ratio with ET_0), which is close to the observed one just for the 2-CC model. This behaviour is probably related to the above discussed underestimation of ALEXI/Dis-ALEXI between the DOY 225 and 260, after the irrigation supplies but before the rainfall events.

Finally, it is clear how the performance of the PM- and RS-based models is unsatisfactory, with RE, MAD and RSMD values significantly greater than measurements accuracy, and efficiency (both in terms of E and IA) inadequate for detailed application at field scale.

Another way to compare the performance of the different models in terms of water stress is the analysis of the cumulative ET values during the whole study period of 153 days. This approach allows to analyze the impact of the model errors on the total water lost in the irrigation period. This quantity is, in fact, strongly correlated with the irrigation requirements, representing the total amount of water returned in the atmosphere in a particular date due to the evapotranspiration process (and then subtracted from the root zone).

The plot in Figure 8.11 reports the cumulative ET for the 5 tested

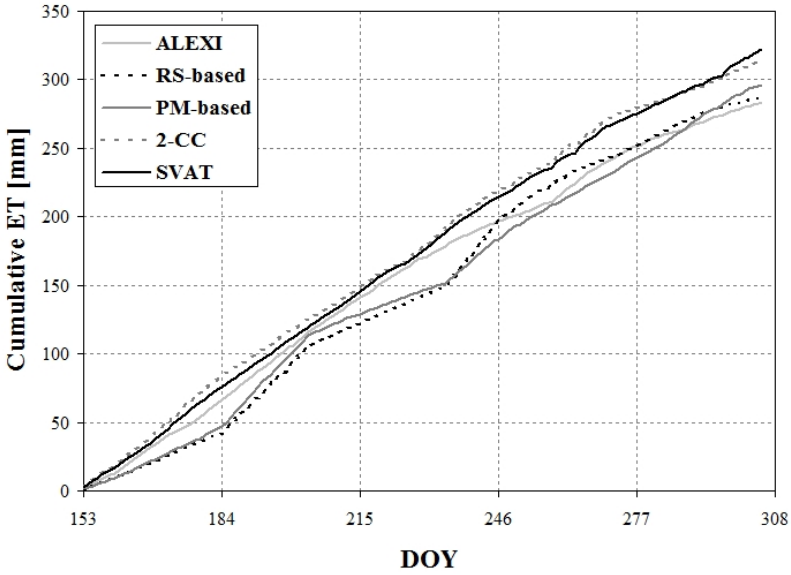

Figure 8.11: Cumulative curves for the evapotranspiration modelled by the analyzed models for the period June-October 2008 (153 days). The continuous black line represent the SVAT model, which is takes as a reference due to the closer results with the observed values.

models. In this analysis, due to the presence of missing value in the observations during the study period, the SVAT model was taken as the reference due to the better agreement with the measured values in all the previously reported analyses.

This graph highlights how the 2-CC model returns, at the end of the simulation a total amount of ET practically coincident with the SVAT one, with a difference quantifiable in about the 2.5%. Also the general trend of the two model is very close, and not show particularly discrepancies along the whole period.

Differently, the ALEXI/Dis-ALEXI model shows a good agreement with the SVAT in the first period of simulation, spacing out the SVAT after the DOY 225 and registering an underestimation of about 12% at the end of the simulation period.

A comparable amount of underestimation is observable for the PM- and RS- based models, which show a similar temporal trend characterized

by sub-periods of local underestimation and overestimation. Globally, the PM-based approach shows a slighly better final agreement, with an underestimation of about 8% of the SVAT cumulative ET.

The analysis of the temporal trends, statistical indices and cumulative values confirms the reliability of the results based on the LSM approaches, especially in the case of SVAT one which returns the higher performance in all the analyses. The SVAT model overcome the 2-CC in terms of RE, MAD and RMSD indices and cumulative ET, obtaining also a significant improvement in the Nash and Sutcliffe efficiency index in terms of quantification of water stress amount.

The consistency of these good performances is partially augmented by the requirement of root zone soil hydraulic parametrisation, which can be a limitation for the applicability in non-monitored wide areas. This particular problem will be partially discussed in the next sub-section.

The results obtained for the ALEXI/Dis-ALEXI procedure are potentially interesting, due to the similarity, in terms of statistical indices, with the 2-CC one. Nevertheless, the model underestimation after the irrigation supplies highlights the limitation on the applicability of this procedure in areas characterised by a considerable amount of external local water inputs.

The procedure seems promising in the case of large area (watershed scale) applications, due to the capability to catch the effective water stress conditions by means of continuous monitoring of the actual evapotranspiration (even if only at low spatial resolution).

Finally, the procedure based on the hot-spot estimation of ET_{24} made by TSEB model seems to drive to unacceptable results, mainly due to the small frequency of the thermal images (about 2 weeks) and the necessity to base the estimation for a long period on a single estimation of a stress coefficient; this last behaviour causes systematic errors in the values modelled between two consecutive acquisitions, magnifying the error obtained in the single hot-spot estimation.

Despite that, the remote estimations of ET_p look useful for the monitoring in absence of weather stations, suggesting the possibility to obtain better performance with more frequent high-resolution acquisitions. Unfortunately, nowadays there are no plan for moderate/high spatial resolution sensors on satellite platforms which could allow the availability of thermal

data with a frequency higher than 2 weeks.

8.5 Evaluation of data assimilation schemes

As result of the analysis reported in the previous sections, it is possible to affirm how in this study case the SVAT approach seems to be suitable for detailed continuous monitoring of ET at both hourly and daily scale. Despite that, as highlighted by the critical analysis of the results, the requirements of a sub-surface hydrological balance should limit the applicability of this methodology in absence of information on root zone depth or hydraulic characterisation of the soil. This problem is particular relevant for applications in wide areas, where remote sensing data do not provide support to these model parameters.

Another interesting feature of the SVAT model is the possibility to reconstruct the surface energy partitioning also in absence of surface temperature observations, due to the complete solution of the surface energy budget. This feature highlights the possibility to take advantage of the unused information in the thermal region for the improvement of the model performance in absence of detailed information characterizing the sub-surface.

In order to test the potentiality of this proposal, the data assimilation schemes introduced in the section 4.4 were applied. In particular, two different schemes were analyzed, both based on the ensemble Kalman filtering: the single filter for the state updating (1EnKF) and the dual state-parameter filtering (2EnKF).

However, in both cases, as briefly introduced in the sub-section 4.4.2, some characteristics of the ensemble (e.g., dimension, distribution of errors, assimilation frequency) should be defined. To reduce the efforts required by a detailed study of all these problematics, some assumption was made in order to focus the attention on the applicability of these methodologies in a real case:

- ensemble size equal to 50 replicates;
- errors in the model input (meteorological data) Gaussian with know variance;
- errors in the assimilable variables Gaussian with know variance;

- assimilation frequency of 10 days for the applications with synthetic data (comparable to the availability of moderate resolution remotely observed thermal data in practical applications);
- uncertainty in SVAT model parametrization limited to 1 parameter (the most sensible one).

Regarding the latter point, a preliminary sensitivity analysis was performed in order to establish the more sensible parameter of the SVAT approach, as discussed in the next sub-section.

8.5.1 SVAT sensitivity analysis

With the aim to detect the more sensitive parameter in the SVAT model not directly derivable from remotely-sensed data, a sensitivity analysis was performed using the meteorological dataset available for the seasons 2007 and 2008. In order to take into account the model behaviour for different crop types, 4 scenarios were analyzed:

1. a tall dense crop (e.g., citrus orchard or forest);
2. a tall sparse crop (e.g., olive trees);
3. a short dense crop (e.g., reference grass);
4. a short sparse crop (e.g., shrub).

For each scenario the parameters not interested by the sensitivity analysis were fixed, assuming the typical values for each one. The parameters included in the analysis should be subdivided into 2 classes: 1) lumped parameters, generally considered spatially invariable; 2) parameters that characterize the sub-surface system.

The sensitivity analysis was performed by varying the single parameter in the admissible range of variability (reported in Table 8.4) and assuming the others equal to the more plausible value for the considered crop type. This approach allows to analyze the effects related to errors in one parameter if it is the only source of error. For each parameter 5 values were considered, uniformly distributed within the admissible range.

The SVAT model sensitivity to each parameter was computed on the basis of the error in the modelled ET, assuming it as the variable of

Table 8.4: Summary of the sensitivity analysis of the SVAT model.

Parameter	Description	Range	Error [%]
κ	Radiation extinction coefficient	0.3–0.6	13
a'	Free convective velocity constant	0.004–0.011	13
b'	Empirical coefficient for r_s computation	0.012–0.024	8
C'	Coefficient for r_x computation	90–175	5
θ_{wl}	Residual soil water content	0.05–0.15	9
θ_{sat}	Saturated soil water content	0.35–0.55	35
$r_{c,\min}$	Stomatal resistance in absence of stress	100–450	40
d_{z2}	Root zone layer thickness	0.2–3.0	88

interest. In particular, the error associated to the parameter was computed averaging in time the ratio between the maximum range of variability of ET in the 5 simulations and their mean value. Afterwards, the error was expressed as percentage.

Table 8.4 reports the obtained results, limited to the most sensible parameters. The analysis of these data highlights three significantly sensible parameters: the saturated soil water content, the minimum stomatal resistance and the root zone layer thickness.

Nevertheless, it is clear how the model sensitivity to the root zone depth is 2 times greater than the other two. For this reason, as final consideration on these data, the analysis seems to suggests how the more sensitive parameter among the ones not retrievable from remotely-sensed data is the root zone depth, d_{z2}.

8.5.2 Critical analysis with synthetic data

Following the considerations obtained from the sensitivity analysis, the root zone depth was adopted as the parameters to be modified in order to evaluate the data assimilation approaches efficacy, in absence of information on model parametrization.

A preliminary test on the data assimilation schemes was performed using synthetic observations extracted from the SVAT simulated outputs reported in the previous sub-section. Assuming that simulation as the *optimal* one, synthetic observations of θ_2 and λET were extracted every 10 days at the 11 UTC starting from the 21/06/2008 (DOY 173). These

observations were considered as measures of the "*true*" state of the system, then unaffected by observation errors.

Moreover, the *optimal* simulation was taken as the reference one to analyze the performance of the assimilation schemes. Similarly, the simulations realized with the SVAT assuming d_{z2} equal to 0.2 and 3.0 m (named *open loop*) were considered as boundary conditions to evaluate the improvements related to data assimilation.

After that, the SVAT model joined with 1EnKF was applied 280 times assuming uniformly distributed starting values of the parameters d_{z2} in the range 0.2–3.0 m. Two different tests were performed: the first assimilating the "*perfect*" observation of θ_2 and the second one assimilating the "*perfect*" observation of λET.

These simulations were averaged in 14 classes (20 simulations for each class) for both the tests, and the results were plotted against the *optimal* and *open loop* simulations. The two tests return quite similar results; for this reason Figure 8.12 (left panel) reports the result relative to the λET case. This solution was indicated by the fact that λET observations are more easily obtainable from residual SEB model applications.

The results reported in Figure 8.12 (left panel) show how the 1EnKF assimilation procedure causes a reduction in the general dispersion of the simulation around the *optimal* case, especially if compared with the *open loop* ones. However, it is possible to notice how in some cases (i.e., around the DOY 235) the assimilation do not return significant improvements.

This behaviour can be partially justified by the fact that the 1EnKF do not modify the model parametrization, but just reinitialises the model state according to the latter available observation. For this reason, in proximity of localized water inputs (rainfall or irrigation) the previous update of the soil water content state can be followed by excessive/moderate modification in the system state independently from the assimilation renew process (e.g., excessive inputs in too small root zone reservoir). These errors affect the model simulations until the new assimilation, causing in some cases errors comparable to the *open loop* cases.

Another interesting feature can be observed by analysing the distribution of model's errors (assuming as reference the *optimal* case) as a function of the initial value of d_{z2}. These results are reported in the right panel of Figure 8.13, quantifying the errors by means of the MAD index.

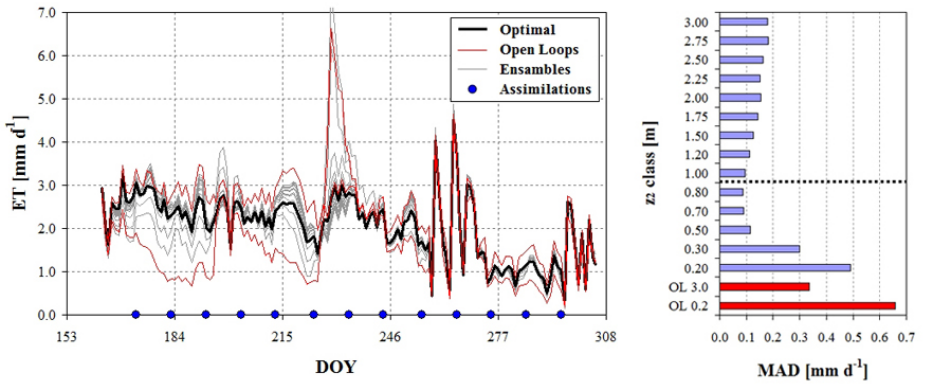

Figure 8.12: Analysis of daily evapotranspiration obtained with 1EnKF using synthetic perfect observations. Right panel reports the temporal trend of daily evapotranspiration modelled with SVAT applying the 1EnKF using synthetic perfect λET observations derived from optimal simulation (black line); red lines represent the open loop simulations realized without assimilation and root zone depth equal to 0.2 and 3.0 m; grey lines are the model replicates obtained with different initial values for the root zone depth; and the blue dots are the synthetic assimilation dates. Left panel reports the average MAD value for each class of initial root zone depth (d_{z2} class), assuming as reference the Optimal simulation; the red bars represents the MAD of the two open loop simulations; and black dashed line represents the optimal d_{z2} value.

It is possible to observe how the MAD value is a function of d_{z2}, assuming smaller value (better matching) in proximity of the *optimal* d_{z2} value (0.9 m). Moreover, the errors in the extremes of the range of variability of d_{z2} (especially the lower one) are consistent and not negligible, somewhat similar to the *open loop* ones. Despite that, on average, the differences result quite small for a large range of variability, approximately from root zone depth of 0.5 to 1.5 m.

An analogous analysis was performed adopting the 2EnKF approach, as summarized by the plots in Figure 8.13.

In this case, the analysis of the temporal trend of the ET (Figure 8.13, left panel) highlights how the dispersion around the *optimal* results is smaller than the case of the 1EnKF. Additionally, it is evident the absence of simulations with errors closer to the *open loop* cases, obtaining a quite

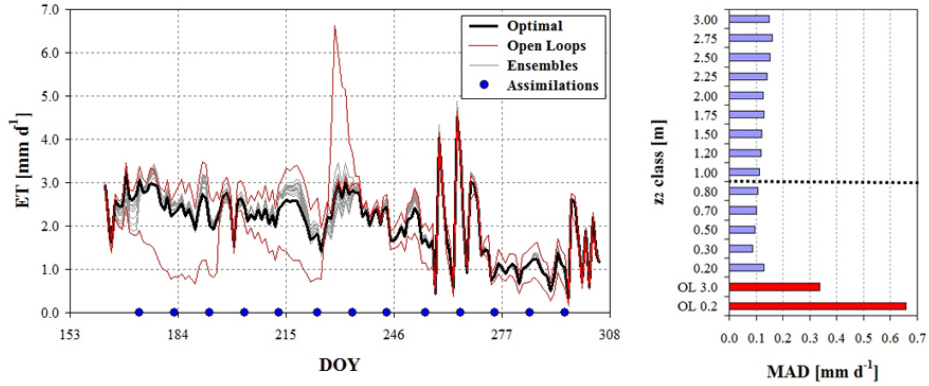

Figure 8.13: Analysis of daily evapotranspiration obtained with 2EnKF using synthetic perfect observations. Right panel reports the temporal trend of daily evapotranspiration modelled with SVAT applying the 2EnKF using synthetic perfect λET observations derived from optimal simulation (black line); red lines represent the open loop simulations realized without assimilation and root zone depth equal to 0.2 and 3.0 m; grey lines are the model replicates obtained with different initial values for the root zone depth; and the blue dots are the synthetic assimilation dates. Left panel reports the average MAD value for each class of initial root zone depth (d_{z2} class), assuming as reference the Optimal simulation; the red bars represents the MAD of the two open loop simulations; and black dashed line represents the optimal d_{z2} value.

small range of variability for ET.

The analysis of the errors reported in Figure 8.13 (right panel), shows, also in this case, how the MAD results weakly sensitive to the starting value assumed by d_{z2}, ranging between 0.1 and 0.15 mm d^{-1}. This latter result is particular interesting, because it highlights the possibility to obtain results close to the optimality independently for the initial parametrization of d_{z2}.

Another interesting consideration can be made by analyzing the evolution of the d_{z2} parameter during the simulations for the 14 classes of initial value, as reported by the plot in Figure 8.14.

This diagram shows how almost all the simulations converge in time to the value of d_{z2} adopted for the *optimal* simulation, and in particular, how the range of variability of the assumed d_{z2} is very small after just 3 assimilations. The velocity of this process is mainly due to the hypothesis

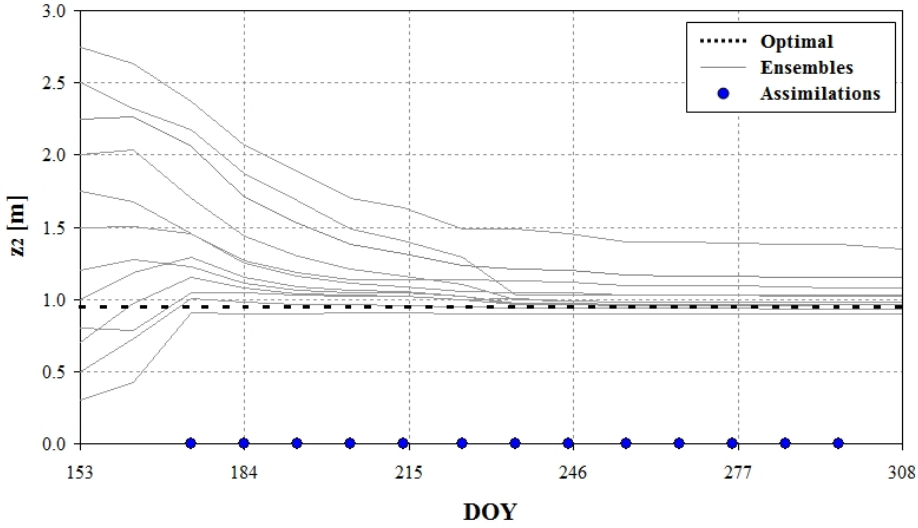

Figure 8.14: Temporal trend of the root zone depth modelled by 2EnKF starting from different initial value. Black dashed line represents the optimal value for the root zone depth obtained from *in-situ* observations; grey lines are the average of 20 replicates for each class of starting value of d_{z2}; and blue dots are the synthetic assimilation dates.

to assimilate "*perfect*" observations; in fact, the latter strongly forces the model to the *optimal* condition. The effects of real data assimilation will be discussed in the next sub-section.

8.5.3 Application to the study case

On the basis of the considerations reported in the previous sub-section, the 2EnKF was chosen as the ideal algorithm to incorporate the TSEB λET estimations in the SVAT model.

In this case, the assimilation frequency was not defined artificially, but was imposed by the availability of the airborne acquisitions. Moreover, the observed values were not assumed "*perfect*", but characterised by a Gaussian distribution with variance equal to 35 W m^{-2} (derived from the TSEB model uncertainty analysis reported in the sub-section 7.1.2).

Similarly to the case of the assimilation of "*perfect*" observations, the simulations realized with different initial values of d_{z2} return quite similar

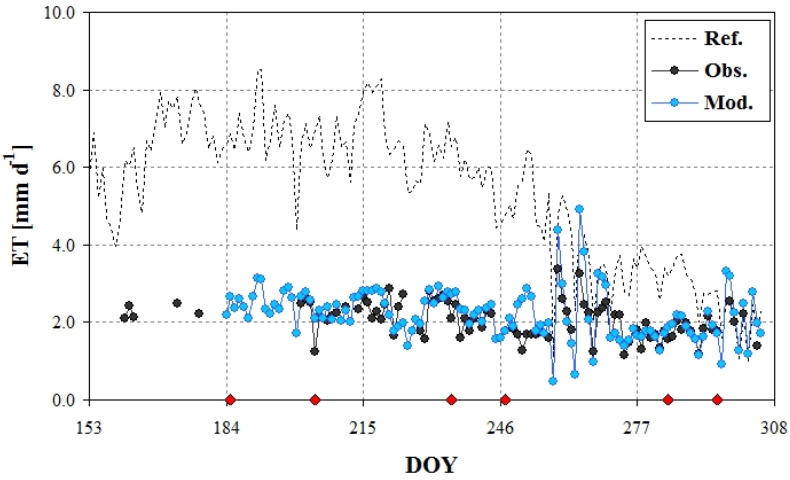

Figure 8.15: Temporal trend of daily evapotranspiration modelled by SVAT+2EnKF approach. The Obs. values correspond to the observations made by EC1/SAS systems; Mod. values are the average of all the replicates obtained with different initial parametrization of root zone depth; and Ref. values are the ET_0 derived applying the FAO-56 formulation on the locally observed weather data. Red rhombus represent the airborne images acquisition dates.

results just after the fist assimilation. For this reason, in Figure 8.15 is reported the ET temporal trend derived by the average of the 280 simulations starting from the day after the first assimilation.

Comparing the data in Figure 8.15 with the ones of Figure 8.10 (SVAT with the optimal parametrization) it is possible to observe how the results are very similar in both magnitude and temporal trend. The computation of the indices of agreements for this case allows to quantify the accuracy of the model in terms of RE, MAD and RMSD equal to 16%, 0.35 and 0.49 mm d^{-1}, respectively, just slightly worse than the *optimal* SVAT simulation.

Additionally, Table 8.5 reports the statistical indices relative to the hourly scale results, also in this case referring to the average of the 280 simulations from the day after the first assimilation.

Also this analysis highlights how the results are only very slightly worse than the one obtained with the *optimal* SVAT model (see Table 8.9), but

Table 8.5: Summary of hourly energy fluxes statistics derived from the comparison of SVAT+2EnKF modelled values (average of 280 simulations with different starting value of d_{z2}) and EC/SAS observed ones.

Flux	MAD [W m^2]	RMSD [W m^2]	E	IA
R_n	27	40	0.97	0.99
G_0	16	19	0.69	0.88
H	38	49	0.85	0.96
λET	36	46	0.81	0.93

obtained without the knowledge of the root zone depth.

On the basis of these considerations, the differences found in the comparison between *optimal* SVAT and SVAT+2EnKF should be considered practically negligible at both hourly and daily scale; moreover, the accuracy indices at daily scale result always better than the ones computed for the other analyzed models, also when it was hypothesized the absence of knowledge on the root zone depth. In this case, the dual state-parameter filter seems to be an useful tool to minimize the model uncertainties when reliable observations of latent heat flux were assimilated, also providing a sort of calibration of the model parameter, just after few assimilations independently from the assumed initial value.

Chapter 9

Summary and Conclusions

In the framework of the reduction of water waste, and in particular in the support of irrigation practice, the detailed modelling of water loss by means of evapotranspiration (ET) assessment assumes a central role.

The increased availability of remotely observed images drastically enhances the interest of scientific community in the improvements in the spatially distributed modelling of the hydrological main terms related to this novel source of data.

With this preface, the general context of this thesis can be identified in the support of remotely-observed data to hydrological models for high temporal and spatial resolution modelling of evapotranspiration.

9.1 Concluding remarks

In this thesis, the potentiality of short-wave (visible and near infrared) and thermal remotely-sensed data was explored, with particular regards to the assessment of evapotranspiration in sparse tall vegetated areas (i.e., olive orchard). Contextually, the capability of the micro-meteorological techniques to observe the energy fluxes exchange in the SPA was investigated, in order to obtain reference values on the reliability of these observations.

To this aim, a set of 7 airborne acquisitions was planned and realised;

then the acquired images were processed, analyzed and used to derive variables useful to characterize the land surface for hydrological applications.

Additionally, the test site was interested by numerous field measurement campaigns, including the monitoring of surface energy fluxes by means of two different micro-meteorological techniques: eddy correlation and scintillometry.

The main goals of this research can be summarized in three distinct objectives: i) the evaluation of micro-meteorological measurements accuracy in a sparse tall system; ii) the applicability of residual energy balance models in a typical Mediterranean landscape; iii) the suitability of remotely-sensed data for the high -spatial -temporal resolution modelling of water losses.

Evaluation of micro-meteorological measurements

Regarding to the observation of surface energy fluxes with micro-meteorological instruments, the first issue was related to the capability of the different techniques to provide comparable measurements, and in particular to return reliable estimations of the sensible heat flux.

This issue, of particular interest in the case of sparse and tall vegetation, was investigated comparing the fluxes observed by two stand-alone installations: an eddy covariance tower (EC1) and a scintillometer system (SAS). The comparison of the observed fluxes highlights the underestimation of the SAS observations, probably related to the presence of a significantly thick roughness sub-layer in the olive field.

The implementation and application of an alternative calibration procedure of the SAS data, which requires an additional measurement of the above canopy horizontal wind speed, allow to remove the biases between the observations realized by the two techniques obtaining indices of agreements in the order of 40 W m^{-2}.

The independent analysis of the proposed approach with a second eddy covariance system (EC2), located in the same study field, confirms the applicability of the suggested calibration approach, obtaining agreement indices slightly better than the EC1 case (30 W m^{-2}); this result is probably due to the better matching between the source areas of EC2 and SAS instruments. This latter result suggests that the discrepancies in the observed sensible heat fluxes are only partially attributable to the difference in footprint locations.

These fluxes were used, jointly with the observation of available energy, to evaluate the balance closure in this crop system. The results obtained from the analysis of budget closure ratio (CR) suggest that the terms neglected in the standard formulation of the surface energy budget are effectively negligible. The CR obtained for the EC1 and EC2 system were equal to 0.86 and 0.90, respectively, in the same order of the acceptable results suggested in literature.

Moreover, the analysis of EC2 data suggests how no substantial differences were found in the measured, residual and closure-forced latent heat fluxes when the observed data were accurately derived.

Further analyses on the observed data were focused on the validation of some hypotheses generally adopted by remote sensing-based modelling of ET for the daily integration procedure. In particular, the retrieval of daily net radiation with the FAO-56 formulation was critically analyzed for the sparse configuration of the olive trees, suggesting the need of an empirical correction to account the difference between daily-average air and surface temperatures.

Additionally, the daytime integration approach from instantaneous fluxes was analyzed, finding good results using the corrected evaporative fraction ($\Lambda' = 1.1\Lambda$) originally suggested by Anderson *et al.* (1997).

Finally, as a summary of all the uncertainties in the surface fluxes measurements, the accuracy of daily ET was computed by comparing the observations provided by the different installations. For this study case, an accuracy equals to 0.4 mm d^{-1} was found, similar to the values obtained in other studies on both dense and sparse crop systems.

Performance of residual SEB model

The principal application of thermal remotely-sensed data in the ET modelling is the so-called residual surface energy balance (SEB) approach, where the latent heat flux at the overpass time is derived as residual term of the energy budget and the daytime value is obtained by means of the self-preservation hypothesis on the evaporative fraction.

Among the residual SEB schemes, the TSEB (Two Source Energy Balance) model was tested in this study case. This choice was suggested by the strong clumping of the olive trees, which causes significant interactions between the fluxes generated by soil and canopy surfaces.

The TSEB model was tested on the olive orchard, at both instantaneous (overpass times) and daily scale, in correspondence of the 7 images acquisition dates. In particular, due to the sparse configuration of the crops in the study area, a detailed analysis of the impact of in-canopy wind profile was performed.

The analysis aims to quantify the effects of different in-canopy wind speed models on the sensible heat flux modelled by TSEB, by comparing three wind profile schemes: the exponential profile (Goudriaan, 1977), the hyperbolic-cosine profile (Massman, 1987) and an empirical corrected version of the latter one (Lalic *et al.*, 2003).

The comparison of the fluxes modelled using the three approaches, with the observed values at hourly scale, suggests the scarce impact of this component on the available energy, highlighting the higher sensitivity of the turbulent fluxes. In particular, it was observed how the Massman approach produced the lowest errors in sensible and latent heat fluxes, the Goudriaan approach, used in the standard implementation of the TSEB, also returns reasonable estimates, comparable with the measurement uncertainties. In contrast, the Lalic in-canopy wind profile model yields unacceptably high errors with respect to measured fluxes.

The additional parameter requested by Massman model (to model the roughness sub-layer of the underlying vegetated surface) suggests how this approach is applicable only when detailed information on canopy structure are available (i.e., small area applications).

Another analysis on the TSEB model was performed by considering the possibility to directly infer the surface fluxes also in absence of information on the local air temperature value above the vegetation. In fact, due to the difficulties in remotely-observed surface temperature calibration, significant biases has been found between radiometric temperature and locally observed air temperature. These biases directly affect the computation of surface-air temperature gradient and, as a consequence, the sensible heat flux estimations. Moreover, the availability of suitable air temperature observation are not always possible, due to imperfect localization (or absence) of weather stations.

For these reasons, two alternative approaches to the classical TSEB were implemented and tested: the first one is based on the internal calibration of the air temperature on the basis of the information directly available within

the image (TSEB-IC), and the second one is based on the downscaling procedure of the fluxes assessed at larger scale by the ALEXI model, named Dis-LEXI.

The analysis of these approaches was performed by comparing the retrieved air temperature and the assessed fluxes. Both these analyses suggested not relevant biases among the three models, with differences practically negligible at both instantaneous and daily scale.

These results are promising to enlarge the applicability of the TSEB scheme also in absence of air temperature measurements, or to minimize the errors related to eventual biases in the remotely-derived radiometric temperature maps.

Accuracy of continuous ET assessment

The efforts focused on the previously summarized topics were finally put together in the comparative analysis of the different approaches to retrieve continuous estimation of evapotranspiration at local scale.

In particular, the analyses on fluxes measurements were used to define the admissible threshold for models accuracy; instead, the temporal sparse TSEB estimations were used as an index of water stress conditions.

The tested approaches include methodologies that use remotely-sensed data in various way. It is possible to distinguish three different class of models:

- approaches based on continuous low-resolution assessment of ET and downscaling procedure;
- approaches based on continuous potential ET estimations and hot-spot stress indices;
- approaches based on continuous solution of the hydrological balance.

In the first class of model, the ALEXI/Dis-ALEXI procedure was tested. This method uses MSG data to continuously asses the ET at coarse spatial resolution, downscaling it by means of hot-spot high resolution estimations retrieved by Dis-ALEXI. In this approach the requested ancillary *in-situ* data are reduced to the wind speed measurements at the airborne overpasses time only.

In the second class of models, two approaches were tested: the first one is based on the direct solution of Penman-Monteith formula for the potetial ET assessment and the stress index derived from TSEB-IC; and the second one that uses a combination of remotely-observed reference ET (using the Priestley-Taylor approximation) and crop coefficient (from NDVI) to assess the potential ET.

Finally, the estimations based on the solution of hydrological balance adopt the scheme known as force-restore; in particular, this scheme was joined with two different models of the surface flux exchanges: the first one is based on the FAO-56 dual crop coefficients (2-CC), and the second one is based on the complete solution of the two-source energy budget (SVAT). These latter models do not use the information acquired in the thermal region, replacing the land surface temperature input with the modelling of water dynamic in the soil.

The model performances were firstly tested by comparing the daily ET estimations with the data observed by micro-meteorological stations. These comparisons highlighted the poor performance of both the approaches based on the continuous estimation of the potential ET. This results is manly due to the high degree of stress of the simulated crop, and by the low frequency of the airborne images ($\approx$ 15 days).

Better results were obtained with the ALEXI/Dis-ALEXI procedure and the dual crop coefficient approach; however, in both cases, the indices of agreement of the models were slightly higher than the measurements uncertainties (accuracy in the order of 0.5 mm d^{-1}).

These results were partially justified in the case of ALEXI/Dis-ALEXI application by the underestimation of ET during the irrigated period; this is mainly due to the inability of ALEXI model to reconstruct the local increase of water availability caused by irrigation supplies.

Instead, the slightly unsatisfactory performance of the dual crop coefficient approach can be partially justified by the excessive simplification of the soil-vegetation interactions made by this approximate scheme based on multiplicative reduction coefficients.

The best results in terms of daily ET were obtained with the application of the SVAT approach; in fact, this model returns indices of accuracy generally lower than the measurements uncertainties and it well reconstructs both the ET magnitude and small scale temporal trend. Moreover, the

analysis of the model at hourly scale provides also a good agreement at this temporal scale, with accuracy always comparable with measurements uncertainties.

Additionally, the analysis of the tested models capability to reconstruct the effective water stress status returns similar considerations, highlighting the good performance of the SVAT model.

As final test, the suitability of coupling data assimilation schemes with the SVAT model was tested, in order to limit the request of sub-surface parameters not directly derivable from remote-sensed data. With this aim, two data assimilation approaches based on the ensemble Kalman filtering were applied: the state updating and the dual state-parameter filtering.

The first one updates the soil water content taking into account the information provide by external observation, differently, the second one uses the observations to update both system status (soil water content) and model parameters.

In order to evaluate the two filtering techniques performances, the root zone depth was detected as the more sensitive parameter not retrievable from remote sensing. The capability of the data assimilation schemes to minimize the errors related to root zone depth uncertainties was analysed using both artificial un-biases observations and TSEB modelled ones.

The preliminary analysis of the two schemes with artificial un-biases observations highlights how the dual state-parameter approach provides good estimations independently from the initial value assumed for the root zone depth this because the capability of the approach to calibrate the model along the assimilation phase. Differently, the state updating filter provides results sensitive to the root depth adopted starting value, returning satisfactory results only in the 0.5–1.5 m root depths range.

The dual state-parameter method was then applied to the real study case to assimilate the latent heat flux estimations made by TSEB model. This application provides a validation of the data assimilation procedure; in fact, the obtained accuracy indices were very close to the ones computed for the locally parametrized SVAT application, at both daily and hourly scale. Additionally, the root zone depth returned by this approach results very similar to the one experimental observed, confirming the capability of the model to provides a calibration of the model parameter in absence of local information.

The combination of SVAT model and dual state-parameter data assimilation scheme allows to obtain reliable estimations of surface energy and water fluxes at both daily and hourly scale, limiting the model parameters not retrievable from remotely-sensed data as the soil hydraulic characteristics.

9.2 Further development

Within this research several methods to assess the ET at high -temporal and -spatial resolution were detailed tested. However, many routes for future researches are still open.

This research, in fact, limited the study to high resolution data and agricultural environment, with particular regards to the olive orchard. Further applications of these methodologies should be realized for other sparse cropped system, i.e., vineyard. In particular, the analysis on the effects of in-canopy wind speed profile has pointed out the importance of this issue in sparse system, but further analysis should be performed for rowed crops where also the wind direction variable can be relevant.

Additional analyses should be realized on the possibility to improve the capability of residual energy balance approaches by introducing information on the plant photosynthesis activity and carbon exchange with the atmosphere, as suggested by Anderson *et al.* (2008).

The applicability of the methodologies based on the resolution of hydrological balance should be furthermore tested in longer simulation periods, including wet season, to evaluate the suitability of the simple force restore scheme.

The extension of these methodologies to wider areas introduces further degrees of complexity to the modelling, related to the spatialization of meteorological data, and to the availability of detailed information on the soil type. Moreover, problematics related to the effects of the complex morphology should be studied in details when basin-scale applications are realised. In these applications, remotely sensed data could be an additional source for both model calibration and parameterization (Boulet *et al.*, 2000; Qin *et al.*, 2008; van der Keur *et al.*, 2001).

In the context of large scale applications, the approaches more directly based on the remote sensed data, as the ALEXI/Dis-ALEXI one, are

promising due to the limited amount of requested ancillary information. Nowadays, remotely sensed images provide optimum spatial information, although the temporal frequency is currently inadequate for moderate/high spatial resolution applications. However, the development of new mission, and the interest in data fusion approaches (see McCabe *et al.*, 2008; Renzullo *et al.*, 2008) seem to suggests the possibility to reduce this limitation in the next future.

In this future scenario, the integration of multi-resolution and multi-frequency data, by means of data fusion approaches, and the assimilation of information provided by different sources, including *in-situ* observations made by micro-meteorological networks, appear the natural development in this research field. Moreover, the numerous interactions among the different components of the land-atmosphere continuum seem to suggests the need of multi-disciplinary approaches development to better understand these mutual relationships.

Appendix A

Airborne images calibration and processing

In this appendix the procedures adopted to perform geometric and radiometric calibrations, and atmospheric correction are described.

A.1 Geometric and radiometric correction

The pre-processing phase, including geometric and radiometric corrections, was performed by Terrasystem s.r.l., which provides radiometrically calibrated data (in radiance) georeferenced images.

The acquisitions were performed by means of a series of single snap-shot with a defined minimum overlap for both *Duncan* and *Flir* sensors, by means of a series of strips performed approximately in north-south direction. In order to obtain a single multi-spectral/thermal image of the whole study area, as first step the snap-shot suitable for the mosaic were selected.

The selected snap-shots were then georeferenced by means of ground truth points (GCP) extracted from a high resolution orthophoto of the site. The selected georeferencing procedure was a first order polynomial transformation. A summary of the georeferencing performances are reported in Tables A.1 and A.2 for multi-spectral and thermal acquisitions, respectively.

Table A.1: Performance of georeferencing process for multi-spectral images. RMS represents the average error in X (east-west) and Y (north-south) directions in meters.

n. flight	Date	DOY	n. images	n. GCP	X RMS	Y RMS
1	11/06/2008	163	4	127	1.04	1.02
2	03/07/2008	185	4	116	1.11	0.99
3	22/07/2008	204	4	121	1.30	1.11
4	22/08/2008	235	4	80	0.75	0.77
5	03/09/2008	247	4	87	1.19	1.03
6	10/10/2008	284	4	110	1.62	1.50
7	21/10/2008	295	4	110	1.93	1.53

Table A.2: Performance of georeferencing process for thermal images. RMS represents the average error in X (east-west) and Y (north-south) directions in meters.

n. flight	Date	DOY	n. images	n. GCP	X RMS	Y RMS
1	11/06/2008	163	18	311	1.07	0.89
2	03/07/2008	185	17	316	1.24	1.05
3	22/07/2008	204	17	254	0.86	0.80
4	22/08/2008	235	16	181	0.80	0.77
5	03/09/2008	247	17	226	0.69	0.73
6	10/10/2008	284	20	220	0.54	0.54
7	21/10/2008	295	20	207	0.56	0.60

The data re-sampling, after the georeferencing procedure, were performed by means of nearest neighbour approach in order to maintain the DN value contained in the original raw images.

The radiometric correction of *Duncan* images was performed following two main steps:

- devignetting;
- conversion of raw DN in spectral radiance.

The devignetting phase is required as a consequence of the non-uniform illumination of the acquired scene, mainly due to dispersion of the light generated by point-source (sun), distortions in the shape of diaphram across the image and obliquity of the sun ray respect to the focal plane (Lelong *et al.*, 2008; Mikhail *et al.*, 2001). This non-uniform illumination is known in literature as vignetting.

For the *Duncan* camera the vignetting is different for each spectral band, then three independent devignettings are required. In particular, due to the particular position of optical prism, for the R and G bands was observed an inverse-vignetting with lower illumination in the image corners.

On the basis of measures made with a standard lamp (Schott DCR III) in a dark room, was possible to obtain a correction matrix for each spectral band for the most common diaphragms and exposition times.

Figure A.1 reports an example of a false colours composition (R=NIR, G=R, B=G) before (upper panel) and after (lower panel) the devignetting.

The conversion of raw DN in spectral radiance was performed on the basis of a first order regression between DN and spectroradiometric measures performed in dark room. Also in this case the calibration parameters were obtained for integration times (8, 10, 12, 15 ms). The obtained parameters are reliable only for DN <200, condition always respected for the 7 acquired scenes.

The *Flir* thermal data were transformed from DN to at-sensor radiance taking into account air temperature and humidity closer to the surface, distance sensor-surface and sensor internal temperature during the acquisition. The obtained emitted radiances were computed assuming a surface emissivity equal to 1.

A.2 Atmospheric correction of VIS and NIR data

As briefly introduced in sub-section 5.3.1, in order to perform empirical in-reflectance calibrations, several spectroradiometric measures on different types of field targets have been acquired during the study period, contextualy to the airborne acquisition.

The main aim of these campaigns was to characterize the heterogeneity of the study area at the scale of remotely-sensed images resolution. As example, Figure A.2 reports the spectral signatures of some targets acquired during the third acquisition (DOY 204). On the same plot (in grey) the spectral windows interested by *Duncan* bands are demarcated.

Thanks to the availability of these *in-situ* observations was possible to realize in a single step both the radiometrical calibration (conversion of radiance values in reflectance) and the correction of atmospheric influence.

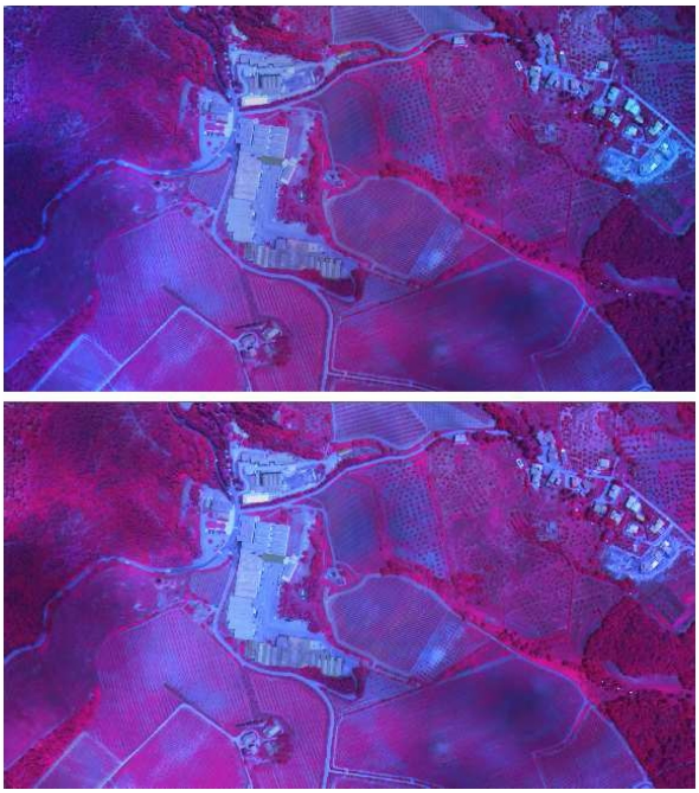

Figure A.1: Example of the result of devignetting procedure. Upper image shows a false color composition (R=NIR, G=R, B=G) obtained from original *Duncan* data. Lower panel shows the same composition after the devignetting. To be notice the reduction of blue component in the scene corner after the devignetting.

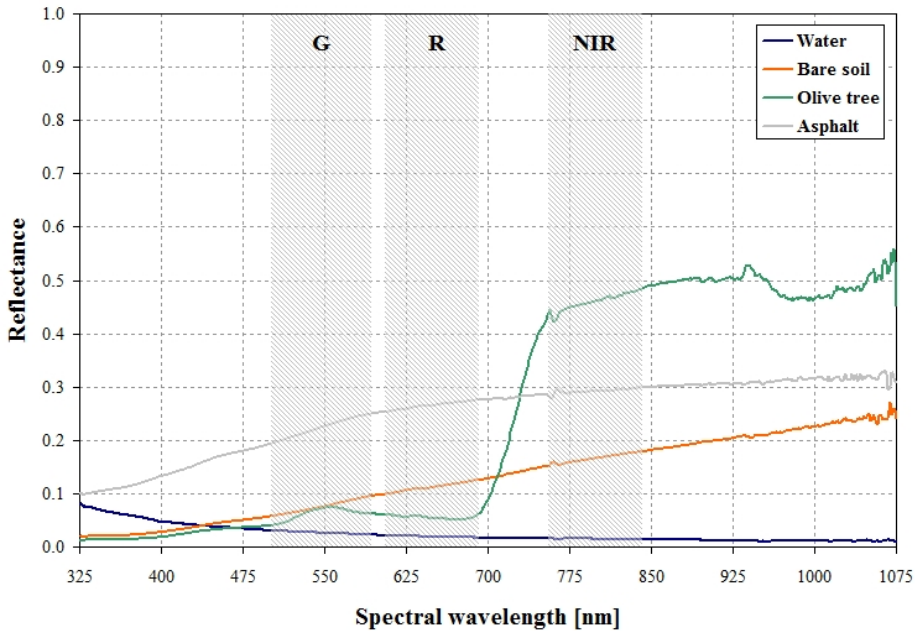

Figure A.2: Spectral signatures acquired on different targets during the third acquistion (DOY 204). Blue line represents a water body signature, green line represents an olive tree signature, orange line represents a bare soil signature and grey line represents an asphalted road signature. The vertical filled regions represent the three *Duncan* sensor spectral bands.

Table A.3: Summarize of the results of empirical line method. Slopes and intercepts for each band and date are obtained by means of least square regression fitting. R^2 represents the determination coefficient.

n. flight	Date	Band	Slope	Intercept	R^2
1	11/06/2008	G	0.077	-0.050	0.987
		R	0.073	-0.041	0.970
		NIR	0.077	-0.148	0.981
2	03/07/2008	G	0.085	-0.066	0.993
		R	0.072	-0.025	0.987
		NIR	0.068	-0.081	0.978
3	22/07/2008	G	0.079	-0.072	0.941
		R	0.065	-0.032	0.990
		NIR	0.063	-0.096	0.974
4	22/08/2008	G	0.076	-0.035	0.965
		R	0.064	-0.020	0.971
		NIR	0.063	-0.076	0.964
5	03/09/2008	G	0.094	-0.069	0.979
		R	0.088	-0.052	0.993
		NIR	0.079	-0.107	0.980
6	10/10/2008	G	0.096	-0.020	0.970
		R	0.098	-0.006	0.988
		NIR	0.099	-0.078	0.967
7	21/10/2008	G	0.105	-0.026	0.992
		R	0.108	-0.011	0.991
		NIR	0.100	-0.060	0.985

These corrections were performed by means of an empirical procedure, this consists on the assessment of in-reflectance images on the basis of an empirical linear relation between the at-sensor radiance and *in-situ* observed reflectance. This procedure, introduced by Slater *et al.* (1996), allows to perform in one step both in-reflectance calibration and atmospheric correction.

In particular, the *in-situ* reflectances were derived applying the sensor spectral responses to the observed signatures, obtaining 3 reflectance values for each acquired signature. The values adopted for the calibration were derived by means of an in-time interpolation of all the signatures acquired for the single target, extrapolating the values in correspondence of the

overpass time.

The spatial localization of the *in-situ* signatures, obtained by means of portable GPS system, was used to extract the at-sensor radiance in the same area. These data were used to perform a linear least square regression, allowing the calibration parameters assessment. These parameters, different for each band, were influenced by atmospheric conditions and then they differ also for each acquisition. The results of the application of empirical line method are reported in Table A.3.

The experimental points used for the calibration of empirical line method, and the derived calibration lines for each date and spectral bands are reported in Figure A.3.

Finally, Figure A.4 shows the images obtained afterwards the geometric corrections and calibration procedure. The images are false colour compositions where in red is represented the near-infrared band (NIR), in green the red spectral band (R) and in blue the green spectral band (G). These maps are in the original spatial resolution of 0.6 m and were used to derive all the surface characteristics of hydrological interest as reported in sub-section 5.3.1.

From the qualitative analysis of these images it is evident a general increase of vegetation presence in the last two acquisition, clearly highlighted by the increase in the red tone of these last images. This fact can be connected with the rainfall event occurred before the last two acquisitions which has supported the growth of the underlying vegetation.

A.3 Atmospheric correction of TIR data

The relation between observed radiance at-sensor level and the radiance emitted by the surface can be generally expressed by means of radiative transfer equation applied to a specific sensor wavelength:

$$L_{\text{sens}} = \Big[R^{\uparrow} + (1-\epsilon_0)L_{\text{dw}}\Big]\tau + L_{\text{up}} \tag{A.1}$$

where L_{dw} and L_{up} [W m^{-2} μm^{-1} sr^{-1}] are the downwelling (or hemispherical) and upwelling (or path) atmospheric radiances, respectively. In this equation the dependence of all variables for the wavelength was remove just to simplify the notation.

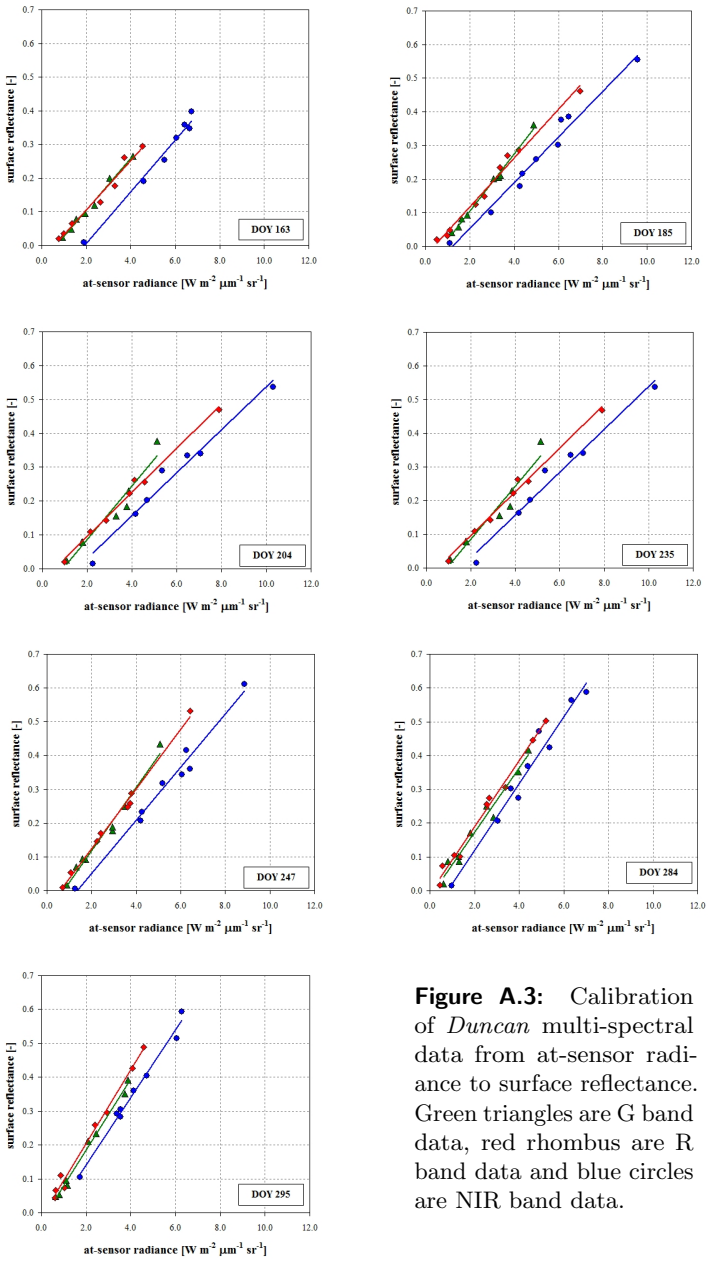

Figure A.3: Calibration of *Duncan* multi-spectral data from at-sensor radiance to surface reflectance. Green triangles are G band data, red rhombus are R band data and blue circles are NIR band data.

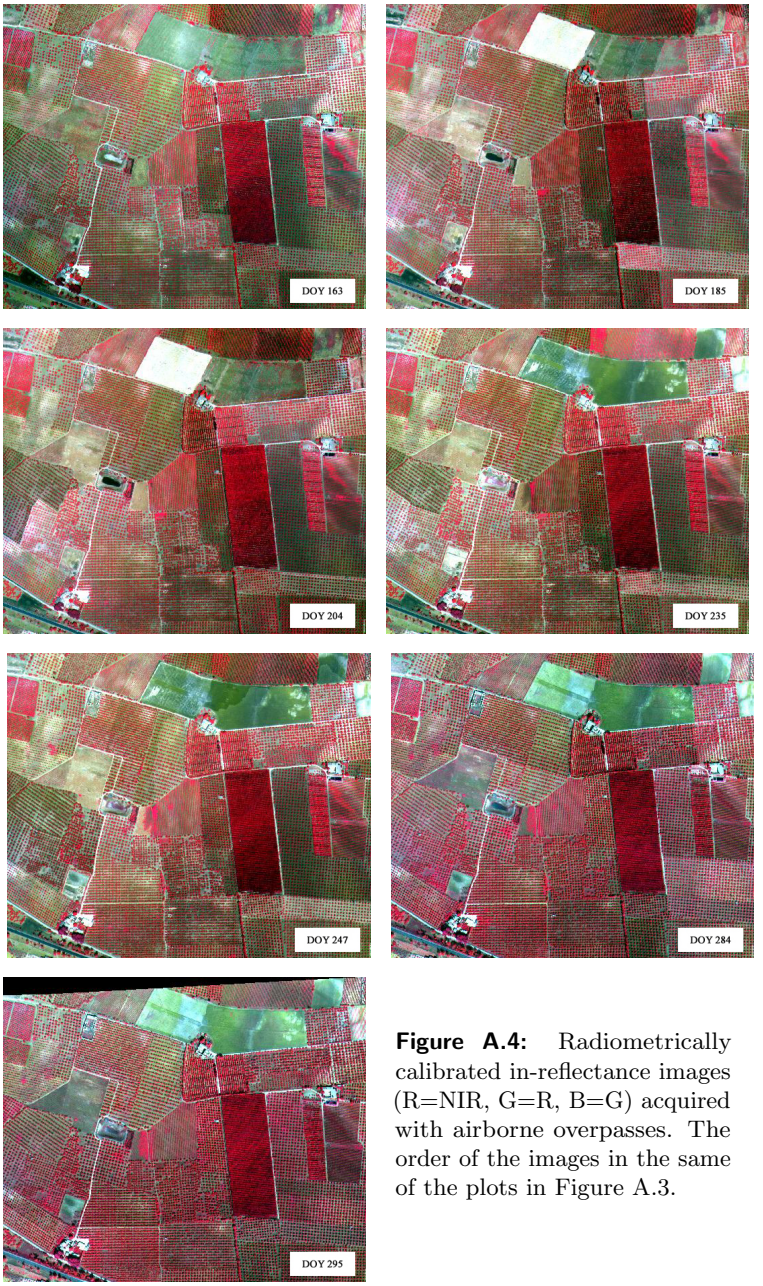

Figure A.4: Radiometrically calibrated in-reflectance images (R=NIR, G=R, B=G) acquired with airborne overpasses. The order of the images in the same of the plots in Figure A.3.

Equation (A.1) neglects the effect of the radiation emitted by the adjacent areas; additionally, this relationship represents only the transfer equation at a single wavelength, and then, in the case of measurements made in a band, a spectral integration procedure is required. Fortunately, the errors due to the integration are small and generally neglected (Gillespie *et al.*, 1998).

The analysis of atmospheric variables estimated by MODTRAN3 model, made by Gillespie *et al.* (1998) during summer clear days, highlights a typical order of magnitude of the atmospheric variables of about $\tau = 0.7$, $L_{\mathrm{dw}} = 3.7$ W m^{-2} μm^{-1} sr^{-1}, and $L_{\mathrm{up}} = 2.4$ W m^{-2} μm^{-1} sr^{-1}.

On the basis of this order of magnitude of the main variables, generally, for local application, it is possible to neglect the contribute of downwelling atmospheric radiance, due to the slight values of the term $(1 - \epsilon_0)$. Under this hypothesis, the surface-emitted radiance can be computed using the simple linear relationship:

$$R^{\uparrow} = \frac{1}{\tau} L_{\mathrm{sens}} + \frac{L_{\mathrm{up}}}{\tau} \tag{A.2}$$

The coefficients in Eq. (A.2) can be empirically derived by means of least square regression procedure based on *in-situ* observation of radiometric temperature.

The graphs reported in Figure A.5 show the calibration relationships for the acquired thermal images. The coefficient of determination (R^2) assumes in all cases values between 0.978 and 0.999, which highlight the quite good performance of the adopted calibration procedure.

Figure A.6 reports the images relative to the land surface temperature acquired in the 7 dates and calibrated as previously reported. This figure highlights the clear reduction in the scene-average surface temperature in the last two acquisitions (darker images) due to the increase in water availability. Moreover, the first acquisition appears definitely hotter than the others (lighter image) due to the relatively late overpass time.

The range of T_{RAD} changes, in fact, from 300–330 K in the first acquisitions to 290–315 K in the last two scenes. The choice to represent the images with the same grey scale (290–330 K) causes a slightly lost in single images dynamic, but it advantages the comparability of the different maps and the analysis on temporal dynamic.

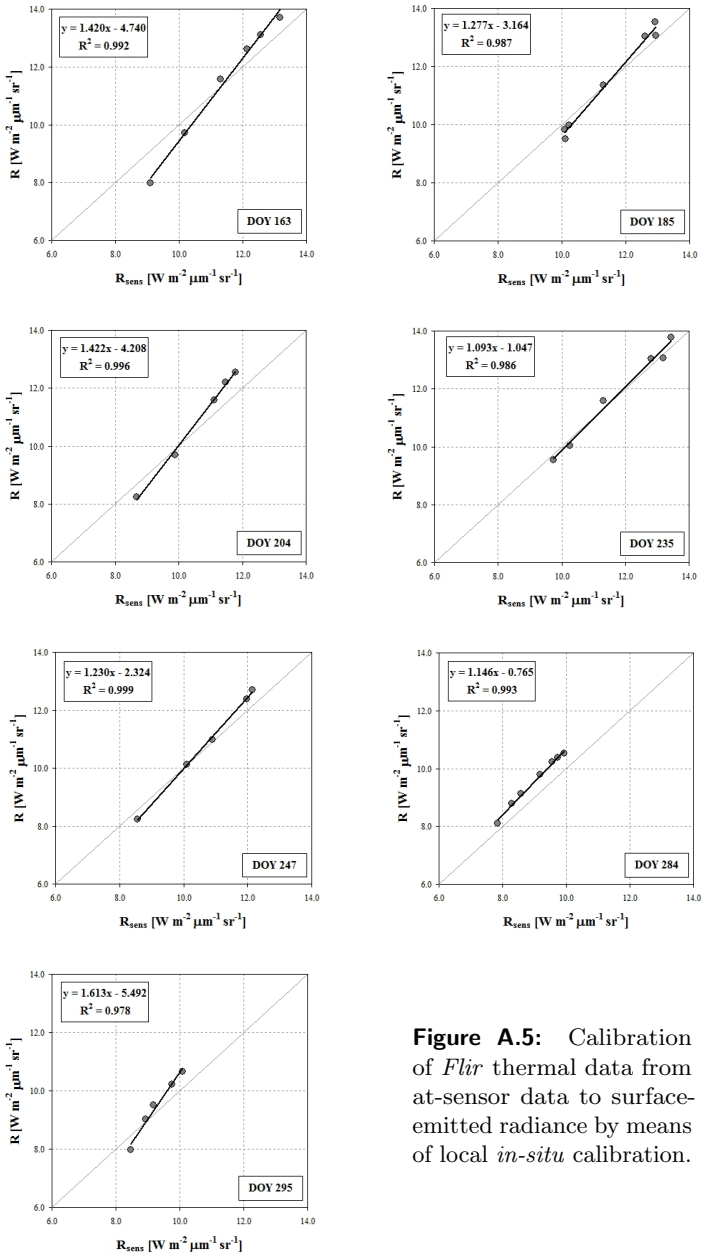

Figure A.5: Calibration of *Flir* thermal data from at-sensor data to surface-emitted radiance by means of local *in-situ* calibration.

Finally, some preliminary consideration can be made on the spatial variability of the observed land surface temperature. Regarding that, it is evident the presence, within the scene, of two different level of heterogeneity: the first one is related to the alternation of bare soil and full vegetated areas, representing an heterogeneity in the order of the fields characteristic dimension ($\sim 10^2$ m); the second one is related to the heterogeneity within the single field, mainly due to the sparse configuration of the trees (e.g., olive and grape), in the order of 10^0–10^1 m.

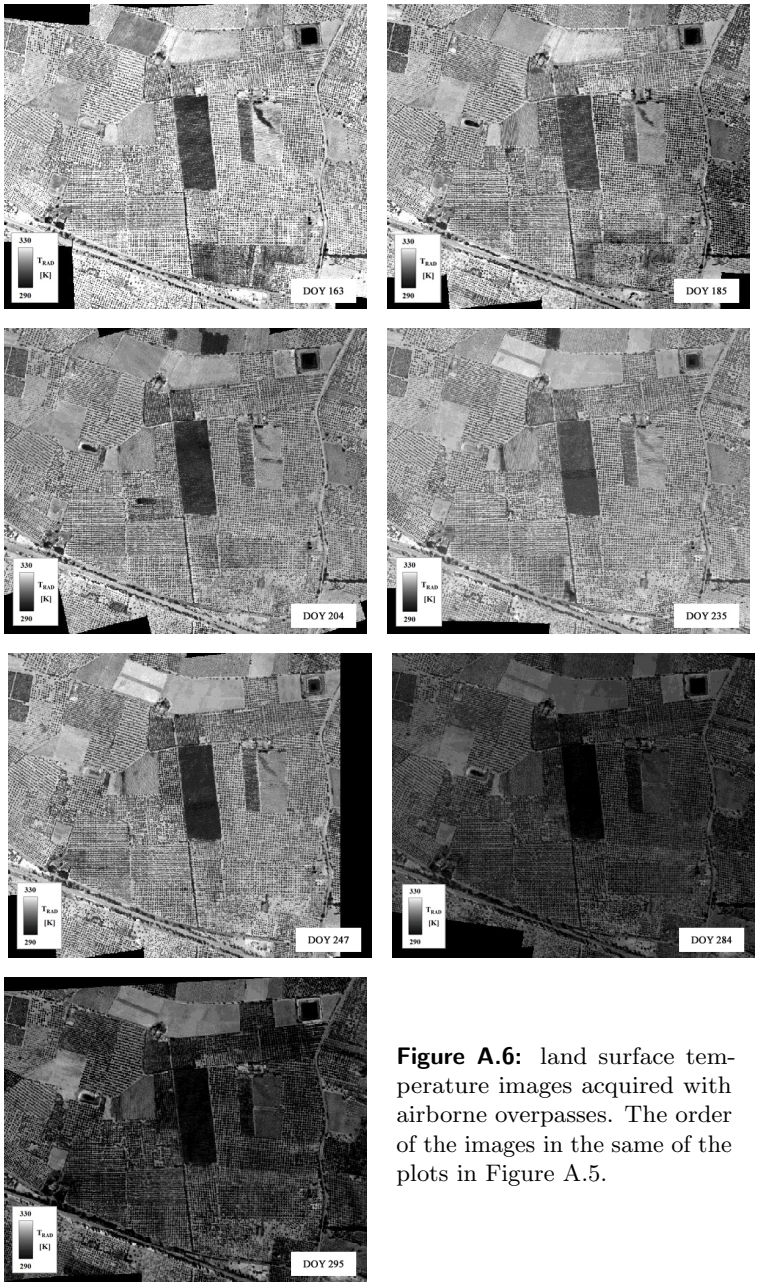

Figure A.6: land surface temperature images acquired with airborne overpasses. The order of the images in the same of the plots in Figure A.5.

Appendix B

Definition of the adopted statistical indices

Assuming N_0 as the size of the sample, O and M two series of observations and simulations of the same variable, respectively, M_i and O_i the i-th values of the relative series, is possible to define the following reported statistical indices. Generally, M assumes the meaning of modelled series and O of the observed series; however, in the cases of model *vs.* model (observed *vs.* observed) comparisons, both M and O referring to modelled (observed) values.

Sample Mean

$$\langle O \rangle = \frac{1}{N_0} \sum_{i=1}^{N_0} O_i \tag{B.1}$$

Mean Absolute Difference, MAD

$$\mathrm{MAD} = \frac{1}{N_0} \left(\sum_{i=1}^{N_0} |M_i - O_i| \right) \tag{B.2}$$

Root Mean Square Difference, RMSD

$$\mathrm{RMSD} = \sqrt{\frac{1}{N_0}\left[\sum_{i=1}^{N_0}(M_i - O_i)^2\right]} \tag{B.3}$$

Relative Error, RE

$$\mathrm{RE} = \frac{\mathrm{MAD}}{\langle O\rangle} \times 100 \tag{B.4}$$

Efficiency Index, E (Nash and Sutcliffe, 1970)

$$\mathrm{E} = 1 - \frac{\sum_{i=1}^{N_0}(M_i - O_i)^2}{\sum_{i=1}^{N_0}\big(O_i - \langle O\rangle\big)^2} \tag{B.5}$$

Index of Agreement, IA (Willmott, 1981)

$$\mathrm{IA} = 1 - \frac{\sum_{i=1}^{N_0}(M_i - O_i)^2}{\sum_{i=1}^{N_0}\big(|O_i - \langle O\rangle| + |M_i - \langle O\rangle|\big)^2} \tag{B.6}$$

Pearson correlation coefficient, R

$$\mathrm{R} = \frac{\sum_{i=1}^{N_0}\big(M_i - \langle M\rangle\big)\big(O_i - \langle O\rangle\big)}{\sqrt{\sum_{i=1}^{N_0}\big(M_i - \langle M\rangle\big)^2\big(O_i - \langle O\rangle\big)^2}} \tag{B.7}$$

References

M. Abrams and S. Hook. *ASTER User Handbook version 2.* Jet Propulsion Laboratory, California Istitute of Thecnology, USA, 2002.

R. G. Allen. Assessing integrity of weather data for use in reference evapotranspiration estimation. *J. Irrig. Drain. Eng.*, 122(2):97–106, 1996.

R. G. Allen, M. E. Jensen, J. L. Wright, and R. D. Barman. Operational estimates of evapotranspiration. *Agron. J.*, 81:650–662, 1989.

R. G. Allen, L. S. Pereira, D. Raes, and M. Smith. *Crop evapotranspiration. Guideline for computing crop water requirements.* FAO irrigation and drainage paper No. 56, Rome, Italy, 1998.

R. G. Allen, W. G. M. Bastiaanssen, M. Tasumi, R. Trezza, and R. Walters. *SEBAL Idaho implementation: advance training and users manual.* NASA EOSDIS Synergy grant from the Raytheon Company, through The Idaho Department of Water Resources, 2002.

R. G. Allen, R. Trezza, and M. Tasumi. Analytical integrated functions for daily solar radiation on slopes. *Agr. Forest Meteorol.*, 139(1-2):55–73, 2006.

R. G. Allen, M. Tasumi, and R. Trezza. Satellite-based energy balance for mapping evapotranspiration with internalized calibration (METRIC)-model. *J. Irrig. Drain. Eng.*, 133(4):380–394, 2007.

D. M. A. Aminou. MSG's SEVIRI instrument. *ESA bulletin*, 111:15–17, 2002.

K. Anandakumar. Sensible heat flux over a wheat canopy: optical scintillometer measurements and surface renewal analysis estimations. *Agr. Forest Meteorol.*, 96:145–156, 1999.

D. E. Anderson, S. B. Verma, and N. J. Rosenberg. Eddy correlation measurements of CO2, latent heat and sensible heat fluxes over a crop surface. *Boundary-Layer Meteorol.*, 29:263–272, 1984.

M. C. Anderson, J. M. Norman, J. R. Diak, W. P. Kustas, and J. R. Mecikalski. A two-source time-integrated model for estimating surface fluxes using thermal infrared remote sensing. *Remote Sens. Environ.*, 60 (2):195–216, 1997.

M. C. Anderson, C. M. U. Neale, F. Li, J. M. Norman, W. P. Kustas, H. Jayanthi, and J. Chavez. Upscaling ground observations of vegetation water content, canopy height, and leaf area index during SMEX02 using aircraft and Landsat imagery. *Remote Sens. Environ.*, 92(4):447–464, 2004.

M. C. Anderson, J. M. Norman, J. R. Mecikalski, J. P. Otkin, and W. P. Kustas. A climatological study of evapotranspiration and moisture stress across the continental U.S. based on thermal remote sensing: I. Model formulation. *J. Geophys. Res.*, 112(D10117), 2007a.

M. C. Anderson, J. M. Norman, J. R. Mecikalski, J. P. Otkin, and W. P. Kustas. A climatological study of evapotranspiration and moisture stress across the continental U.S. based on thermal remote sensing: II. Surface moisture climatology. *J. Geophys. Res.*, 112(D11112), 2007b.

M. C. Anderson, J. M. Norman, W. P. Kustas, R. Houborg, P. J. Starks, and N. Agam. A thermal-based remote sensing technique for routine mapping of land-surface carbon, water and energy fluxes from field to regional scales. *Remote Sens. Environ.*, 112(12):4227–4241, 2008.

M. C. Anderson, W. P. Kustas, J. M. Norman, C. R. Hain, J. R. Mecikalski, L. Schultz, M. P. Gonzàlez-Dugo, C. Cammalleri, G. D'Urso, A. Pimstein,

and F. Gao. Mapping daily evapotranspiration at field to continental scales using geostationary and polar orbiting satellite imagery. *Hydrol. Earth Syst. Sci.*, 15(1):223–239, 2011.

ASCE-EWRI. *The ASCE standardized reference evapotranspiration equation.* Environmental and Water Resources Institute (EWRI) of the American Society of Civil Engineers Task Committee on Standardization of reference Evapotranspiration Calculation, ASCE, Washington DC, USA, 2005.

W. G. M. Bastiaanssen. *Regionalization of surface flux densities and moisture indicators in composite terrain: a remote sensing approach under clear skies in Mediterranean climates.* PhD thesis, Wageningen Universitait, Den Haag, The Netherland, 1995.

W. G. M. Bastiaanssen. SEBAL-based sensible and latent heat fluxes in the irrigated Gediz Basin, Turkey. *J. Hydrol.*, 229(1-2):87–100, 2000.

W. G. M. Bastiaanssen, M. Menenti, R. A. Feddes, and A. A. M. Holtslag. A remote sensing surface energy balance algorithm for land (SEBAL). Part 1: Formulation. *J. Hydrol.*, 212-213:198–212, 1998a.

W. G. M. Bastiaanssen, H. Pelgrum, J. Wang, Y. Ma, J. F. Moreno, G. J. Roerink, and T. van der Wal. A remote sensing surface energy balance algorithm for land (SEBAL). Part 2: Validation. *J. Hydrol.*, 212-213: 213–229, 1998b.

F. Becker and Z. L. Li. Temperature-independent spectral indices in thermal infrared bands. *Remote Sens. Environ.*, 32:17–33, 1990.

A. Bennett and Y. C. Ho. *Inverse methods in physical oceanography.* Cambrige University Press, New York, USA, 1992.

A. K. Betts and J. H. Ball. Albedo over the boreal forest. *J. Geophys. Res.*, 102(D24):28901–28910, 1997.

K. Beven and J. Fisher. Remote sensing and scaling in hydrology. In J. B. Stewart, E. T. Engman, R. A. Feddes, and Y. Kerr, editors, *Scaling up in hydrology using remote sensing*, pages 1–18. John Wiley and Sons, Chichester, UK, 1996.

E. Boegh, H. Soegaard, and A. Thomsen. Evaluating evapotranspiration rates and surface conditions using Landsat TM to estimate atmospheric resistance and surface resistance. *Remote Sens. Environ.*, 79(2–3):329–343, 2002.

E. C. Boes. Fundamentals of solar radiation. In J. F. Kreider and F. Kreith, editors, *Solar Energy Handbook (Chapter 2)*, pages 2/1–2/78, 1981.

G. Boulet, J. D. Kalma, I. Braud, and M. Vauclin. Towards effective parametrization of soil physical and and surface properties in regional water balance studies. *J. Hydrol.*, 217:225–238, 1999.

G. Boulet, A. Chehbouni, I. Braud, M. Vauclin, M. Haverkamp, and C. Zammit. A simple water and energy balance model designed for regionalization and remote sensing data utilization. *Agr. Forest Meteorol.*, 105:117–132, 2000.

I. S. Bowen. The ratio of heat losses by conduction and by evaporation from any water surface. *Phys. Rev.*, 27:779–787, 1926.

H. Braden and T. Blanke. About the use of remotely sensed surface temperatures for controlling estimates of evapotranspiration. *Model Geo-Biosphere Process Ger.*, 2:53–66, 1993.

C. L. Brest and S. Goward. Deriving surface albedo measurements from narrowband satellite data. *Int. J. Remote Sens.*, 8:351–367, 1992.

A. Brisson, P. Le Borghe, and A. Marsouin. *Development of algorithms for surface solar irradiance retrieval at OSI SAF low and mid latitude.* Mètèo-France/CMS, Lannion, France, 1999.

W. Brutsaert. *Evaporation into the atmosphere: Theory, history and applications.* D. Reidel Publ. Co., Dordrecht, 1982.

W. Brutsaert. Aspects of bulk atmospheric boundary layer similarity under free-convective conditions. *Rev. Geophys.*, 31(37):439–451, 1999.

W. Brutsaert and M. Sugita. Regional surface fluxes from satellite-derived surface temperatures (AVHRR) and radiosonde profiles. *Boundary-Layer Meteorol.*, 58:355–366, 1992.

G. Burba and D. Anderson. *Introduction to the eddy covariance method: general guidelines and conventional workflow*. LI-COR, Inc., 2005.

A. Calera, J. Gonzàlez-Piqueras, and J. Melià. Monitoring barley and corn growth from remote sensing data at field scale. *Int. J. Remote Sens.*, 25: 97–109, 2004.

P. J. Camillo and R. J. Gurney. A resistance parameter for bare soil evaporation models. *Soil Sci.*, 141:95–105, 1986.

C. Cammalleri, M. C. Anderson, G. Ciraolo, G. D'Urso, W. P. Kustas, C. Hain, L. Schultz, and J. R. Mecikalski. Analysis of energy fluxes estimations over Italy using time-differencing models based on thermal remote sensing data. *IAHS Publ.*, 3xx:xxx–xxx, 2011.

G. S. Campbell. *Soil physics with Basic: transport models for soil-plant systems*. Elsevier, 1985.

G. S. Campbell and J. M. Norman. *An introduction to environmental biophysics*. Springer-Verlag, 1998.

Campbell-Inc. *Model HFP01SC self-calibrating soil heat flux plate: instruction manual*. Campbell Scientific Inc., 2007.

F. Caparrini, F. Castelli, and D. Entekhabi. Mapping of land-atmosphere heat fluxes and surface parameters with remote sensing data. *Boundary-Layer Meteorol.*, 107:605–633, 2003.

V. Caselles, E. Valor, C. Coll, and E. Rubio. Thermal band selection for the PRISM instrument. 1: Analysis of emissivity-temperature separation algorithms. *J. Geophys. Res.*, 102(D10):11145–11164, 1997.

L. Cavazza and A. Patruno. *Terreno agrario: il comportamento fisico*. Reda Edizioni, Torino, Italy, 2005.

P. Cayrol, L. Kergoat, S. Moulin, G. Dedieu, and A. Chehbouni. Calibrating a coupled SVAT-vegetation growth model with remotely sensed reflectance and surface temperature: a case study for the HAPEX-sahel grassland sites. *J. Appl. Meteorol.*, 39:2452–2472, 2000.

P. Cellier, G. Richard, and P. Robin. Partition of sensible heat fluxes into bare soil and the atmosphere. *Agr. Forest Meteorol.*, 82:245–265, 1996.

A. Chehbouni, Y. Nouvellon, J. P. Lhomme, C. Watts, G. Boulet, Y. H. Kerr, M. S. Moran, and D. C. Goodrich. Estimation of surface sensible heat flux using dual angle observations of radiative surface temperature. *Agr. Forest Meteorol.*, 108:55–65, 2001.

J. M. Chen and J. Cihlar. Quantifying the effect of canopy architecture on optical measurements of leaf area index using two gap size methods. *IEEE Trans. Geosci. Remote Sens.*, 33:777–787, 1995.

M. Choi, W. P. Kustas, M. C. Anderson, R. G. Allen, F. Li, and J. H. Kjaersgaard. An intercomparison of three remote sensing-based surface energy balance algorithms over a corn and soybean production region (Iowa, U.S.) during SMACEX. *Agr. Forest Meteorol.*, 149(12):2082–2097, 2009.

B. J. Choudhury. Relationships between vegetation indices, radiation absorbition, and net photosynthesis evaluated by a sensitivity analysis. *Remote Sens. Environ.*, 22:209–233, 1987.

B. J. Choudhury, S. B. Idso, and R. J. Reginato. Analysis of an empirical model for soil heat flux under a growing wheat crop for estimating evaporation by an infrared-temperature based energy balance equation. *Agr. Forest Meteorol.*, 39:283–297, 1987.

B. J. Choudhury, N. U. Ahmed, S. B. Idso, R. J. Reginato, and C. S. T. Daughtry. Relations between evaporation coefficients and vegetation indices studied by model simulations. *Remote Sens. Environ.*, 50:1–17, 1994.

R. B. Clapp and G. M. Hornberger. Empirical equations for some soil hydraulic properties. *Water Resour. Res.*, 14:601–604, 1978.

N. Clerbaux, C. Bertrand, D. Caprion, B. Depaepe, S. Dewitte, L. Gonzalez, and A. Ipe. Narrowband-to-Broadband conversions for SEVIRI. In *Proceedings of the 2005 EUMETSAT Meteorological Satellite Conference*, pages 351–357. Dubrovnik, 2005.

J. G. P. W. Clevers. The application of a weighted infrared-red vegetation index for estimating leaf area index by correcting for soil moisture. *Remote Sens. Environ.*, 29:25–37, 1989.

S. E. Cohn, N. S. Sivakumaran, and R. Todling. A fixed-lag Kalman smoother for retrospective data assimilation. *Mon. Weather Rev.*, 122: 2838–2867, 1994.

D. Couralt, B. Seguin, and A. Olioso. Review on estimation of evapotranspiration from remote sensing data: from empirical to numerical modelling approaches. *Irrig. Drain. Syst.*, 19:223–249, 2005.

P. Courtier, J. Derber, R. Errico, J. F. Louis, and T. Vukicevic. Important literature on the use of adjoint, variational methods and the Kalman filter in meteorology. *Tellus A*, 45:342–357, 1993.

R. D. Crago. Conservation and variability of the evaporative fraction during the daytime. *J. Hydrol.*, 180(1-4):173–194, 1996.

R. D. Crago and W. Brutsaert. Daytime evaporation and the self-preservation of the evaporative fraction and the Bowen ratio. *J. Hydrol.*, 178:241–255, 1996.

W. T. Crow, W. P. Kustas, and J. H. Prueger. Monitoring root-zone soil moisture through the assimilation of a thermal remote sensing-based soil moisture proxy into a water balance model. *Remote Sens. Environ.*, 112: 1268–1281, 2008.

A. D. Culf, T. Foken, and J. H. C. Gash. The energy balance closure problem. In P. Kabat, M. Claussen, P. A. Dirmeyer, and et al., editors, *Vegetation, water, humans and the climate. A new perspective on an interactive system*, pages 159–166. Springer, Berlin, Heidelberg, 2004.

H. A. R. de Bruin. From Penman to Makkink. *Den Haag. Proc. and Inform.*, 39:5–30, 1987.

H. A. R. de Bruin. Introduction : renaissance of scintillometry. *Boundary-Layer Meteorol.*, 105:1–4, 2002.

H. A. R. de Bruin, W. Kohsiek, and B. J. J. M. van den Hurk. A verification of some methods to determine the fluxes of momentum, sensible heat, and water vapour using standard deviation and structure parameter of scalar meteorological quantities. *Boundary-Layer Meteorol.*, 63:231–257, 1993.

K. de Ridder. Bulk transfer relations for the roughness sublayer. *Boundary-Layer Meteorol.*, 134:257–267, 2010.

J. W. Deardorff. A parameterization of ground surface moisture content for use in atmospheric prediction models. *J. Appl. Meteorol.*, 16:1182–1185, 1977.

R. E. Dickinson. Modelling evapotranspiration for three-dimensional climate models. In *Climate Processes and Climate sensitivity*, pages 58–72. Geophys. Monogr. No. 29, Am. Geophys. Union, 1984.

J. A. Duffie and W. A. Beckman. *Solar engineering of thermal process.* Wiley and Sons, NY, USA, 1980.

G. D'Urso and M. Menenti. Mapping crop coefficients in irrigated areas from Landsat TM images. In P. Europto, editor, *European Symposium on Satellite Remote Sensing II*, pages 41–47. SPIE, Intern. Soc. Optical Engineering vol. 2585, Bellingham, USA, 1995.

W. P. Elliott. The growth of the atmospheric internal boundary layer. *Trans. Amer. Geophys. Union*, 39:1048–1054, 1958.

G. F. Epema. Determination of planetary reflectance for landsat 5 thematic mapper tapes processed by earthnet. *ESA Journal Papers*, 14:101–108, 1990.

S. Er-Raki, A. Chehbouni, N. Guemouria, B. Duchemin, J. Ezzahar, and R. Hadria. Combining FAO-56 model and ground-based remote sensing to estimate water consumptions of wheat crops in a semi-arid region. *Agr. Water Manage.*, 87:41–54, 2007.

G. Evensen. Sequential data assimilation with a non-linear quasi-geostrophic model using Monte Carlo methods to forecast error statistics. *J. Geophys. Res.*, 99(C5):10143–10162, 1994.

G. Evensen and P. J. van Leeuwen. An ensemble Kalman smoother for nonlinear dynamics. *Mon. Weather Rev.*, 128:1852–1867, 2000.

J. Ezzahar, A. Chehbouni, J. Hoedjes, D. Ramier, N. Boulain, S. Boubkraoui, B. Cappelaere, L. Descroix, B. Mougenot, and F. Timouk. Combining scintillometer measurements and an aggregation scheme to estimate area-averaged latent heat flux during the AMMA experiment. *J. Hydrol.*, 375:217–226, 2009.

E. Falge, S. Reth, N. Brüggemann, K. Butterbach-Bahl, V. Goldberg, A. Oltchev, S. Schaaf, G. Spindler, B. Stiller, R. Queck, B. Köstner, and C. Bernhofer. Comparison of surface energy exchange models with eddy flux data in forest and grassland ecosystem of germany. *Ecological Modelling*, 188:174–216, 2005.

J. S. Famiglietti and E. F. Wood. Effects of spatial variability and scale on areally averaged evapotranspiration. *Water Resources Res.*, 31(3): 699–712, 1995.

J. E. Fernàndez, F. Moreno, I. F. Giròn, and O. M. Blàzquez. Stomatal control of water use in olive tree leaves. *Plant and Soil*, 190:179–192, 1997.

J. J. Finnigan, R. Clement, Y. Malhi, R. Leuning, and A. H. Cleugh. A re-evaluation of long-term flux measurement techniques part I: averaging and coordinate rotation. *Boundary-Layer Meteorol.*, 107:1–48, 2003.

T. Foken. 50 years of the Monin-Obukhov similarity theory. *Boundary-Layer Meteorol.*, 119(3):431–447, 2006.

T. Foken. *Micrometeorology.* Springer, Berlin, Germany, 2008.

T. Foken and B. Wichura. Tools for quality assessment of surface-based flux measurements. *Agr. Forest Meteorol.*, 78:83–105, 1996.

T. Foken, F. Wimmer, M. Mauder, C. Thomas, and C. Liebethal. Some aspects of the energy balance closure problem. *Atmos. Chem. Phys. Discuss.*, 6:3381–3402, 2006.

W. L. Fons. Influence of forest cover on wind velocity. *J. Forestry*, 38: 481–487, 1940.

R. A. Freeze and R. N. Harlan. Blueprint for a physically-based, digitally-simulated hydrologic response model. *J. Hydrol.*, 9(3):237–258, 1969.

R. Frehlich. Laser scintillation measurements of the temperature spectrum in the atmospheric surface layer. *J. Atmos. Sci.*, 49:1494–1509, 1992.

A. N. French, F. Jacob, M. C. Anderson, W. P. Kustas, W. J. Timmermans, A. Gieske, Z. Su, H. Su, M. F. McCabe, F. Li, J. Prueger, and N. Brunsell. Surface energy fluxes with the Advanced Spaceborne Thermal Emission and Reflection radiometer (ASTER) at the Iowa 2002 SMACEX site (USA). *Remote Sens. Environ.*, 99(1-2):55–65, 2005.

M. A. Friedl. Modelling land surface fluxes using a sparse canopy model and radiometric surface temperature measurements. *J. Geophys. Res.*, 16:25435–25446, 1995.

M. A. Friedl. Relationships among remotely sensed data, surface energy balance, and area-averaged fluxes over partially vegetated land surfaces. *J. Appl. Meteorol.*, 35:2091–2103, 1996.

M. A. Friedl and F. W. Davis. Sources of variation in radiometric surface temperature over a tallgrass prairie. *Remote Sens. Environ.*, 48:1–17, 1994.

R. D. Frouin, D. W. Lingner, C. Gautier, K. S. Baker, and R. C. Smith. A simple analytical formula to compute clear sky total and photosynthetically available solar irradiance at the ocean surface. *J. Geophys. Res.*, 94:9731–9742, 1989.

M. Fuchs and A. Hadas. The heat flux density in a non-homogeneous bare loessial soil. *Boundary-Layer Meteorol.*, 3:191–200, 1972.

F. Garcìa-Haro, S. Sommer, and T. Kemper. Variable multiple end member spectral mixture analysis (VMESMA). *Int. J. Remote Sens.*, 26:2135–2162, 2005.

B. J. Garner and A. Ohmura. A method for calculating direct shortwave radiation income of slopes. *J. Appl. Meteorol.*, 7:796–800, 1968.

J. R. Garratt. Flux profile relations above tall vegetation. *Q. J. Roy Meteorol. Soc.*, 104:199–211, 1978.

J. R. Garratt. Surface influence upon vertical profiles in the atmospheric near-surface layer. *Q. J. Roy Meteorol. Soc.*, 106:803–819, 1980.

J. R. Garratt and B. B. Hicks. Momentum, heat and water vapour transfer to and from natural and artificial surfaces. *Q. J. Roy Meteorol. Soc.*, 99: 680–687, 1973.

J. D. Garrison and G. P. Adler. Estimation of precipitable water over the United States for application to the division of solar radiation into its direct and diffuse components. *Solar Energy*, 44(4):225–241, 1990.

J. H. R. Gash. A note on estimating the effect of a limited fetch on micrometeorological evaporation measurements. *Boundary-Layer Meteorol.*, 35:409–413, 1986.

C. Gautier, G. Diak, and S. Masse. A simple physical model to estimate incident solar radiation at the surface from GOES satellite data. *J. Climate Appl. Meteorol.*, 19:1005–1012, 1980.

P. Gentine, D. Entekhabi, A. Chehbouni, G. Boulet, and B. Duchemin. Analysis of evaporative fraction diurnal behaviour. *Agr. Forest Meteorol.*, 143:13–29, 2007.

H. Gijzen and J. Goudriaan. A flexible and explanatory model of light distribution and photosynthesis in row crops. *Agr. Forest Meteorol.*, 48: 1–20, 1989.

A. Gillespie, S. Rokugawa, T. Matsunaga, J. S. Cothern, S. Hook, and A. B. Kahle. A temperature and emissivity separation algorithm for Advanced Spaceborne Thermal Emission and Reflection radiometer (ASTER) images. *IEEE Trans. on Geosc. and Remote Sensing*, 36(4): 1113–1126, 1998.

M. Göckede, T. Markkanen, M. Mauder, K. Arnold, J. Leps, and T. Foken. Validation of footprint models using natural tracer measurements from a field experiment. *Agr. Forest Meteorol.*, 135:314–325, 2005.

S. J. Goetz, R. N. Halthore, F. G. Hall, and B. L. Markham. Surface temperature retrieval in a temperate grassland with multiresolution sensors. *J. Geophys. Res.*, 100(D12):25397–25410, 1995.

M. P. Gonzàlez-Dugo and L. Mateos. Spectral vegetation indices for benchmarking water productivity of irrigated cotton and sugarbeet crops. *Agr. Water Manage.*, 95:48–58, 2008.

M. P. Gonzàlez-Dugo, C. Neal, L. Mateos, W. P. Kustas, J. H. Prueger, M. C. Anderson, and F. Li. A comparison of operational remote sensing-based models for estimating crop evapotranspiration. *Agr. Forest Meteorol.*, 149:1843–1853, 2009.

N. J. Gordon, D. J. Salmond, and A. M. F. Smith. Novel approach to non-linear/non-Gaussian Bayesian state estimation. *IEEE Proceedings-F*, 140:107–113, 1993.

J. Goudriaan. *Crop micrometeorology: a simulation study.* Center Agricoltural Publications and Documentation, Wageningen, The Netherlands, 1977.

J. Grace. Some effects of wind on plants. In J. Grace, E. Ford, and P. J. Jarvis, editors, *Plants and their atmospheric environment*, pages 31–56. Blackwell Scientific, London, 1981.

R. J. Gurney and A. Y. Hsu. Relating evaporative fraction to remotely sensed data at fife site. In *Symposium on FIFE: Fist ISLSCP field experiment*, pages 112–116. American Meteorological Society, Boston, 1990.

F. G. Hall, K. F. Huemmrich, S. J. Goetz, P. J. Sellers, and J. E. Nickerson. Satellite remote sensing of surface energy balance: Success, failures and unresolved issues in FIFE. *J. Geophys. Res.*, 97:19061–19089, 1992.

O. K. Hartogensis. *Exploring scintillometry in the stable atmospheric surface layer.* PhD thesis, Wageningen Universitait, Wageningen, The Netherlands, 2006.

O. K. Hartogensis, H. A. R. de Bruin, and B. J. H. van de Wiel. Displacement-beam small aperture scintillometer test. Part II: CASES-99 stable boundary-layer experiment. *Boundary-Layer Meteorol.*, 105: 149–176, 2002.

J. L. Hatfield, M. Vauclin, S. R. Vieira, and R. Bernard. Surface temperature variability patterns within irrigated fields. *Agr. Water Manage.*, 8: 429–437, 1984.

J. L. Heilman, W. E. Heilman, and D. G. Moore. Evaluating the crop coefficient using spectral reflectance. *Agron. J.*, 74:967–971, 1982.

R. J. Hill. Algorithms for obtaining atmospheric surface-layer fluxes from scintillation measurements. *J. Atmos. Oceanic Tech.*, 14:456–467, 1997.

R. J. Hill and S. F. Clifford. Modified spectrum of atmospheric temperature fluctuations and its application to optical propagation. *J. Opt. Soc. Am.*, 68:892–899, 1978.

R. J. Hill, S. F. Clifford, and R. S. Lawrence. Refractive index and absorption fluctuations in the infrared caused by temperature, humidity and pressure fluctuations. *J. Opt. Soc. Am.*, 70:1192–1205, 1980.

C. H. Huang. A theory of dispersion in turbulent shear flow. *Atmos. Environ.*, 13:453–463, 1979.

Hukseflux. *Application and specification of heat flux sensors.* Hukseflux Thermal Sensors, Delft, The Netherlands, 2000.

J. Idso, K. Aase, and R. D. Jackson. Net radiation-soil heat flux relations as influenced by soil water content variations. *Boundary-Layer Meteorol.*, 9:113–122, 1975.

M. Iqbal. *An Introduction to Solar Radiation*, volume XVIII. Academic Press, NY, USA, 1983.

R. D. Jackson, J. L. Hatfield, R. J. Reginato, S. B. Idso, and P. J. Pinter. Estimation of daily evapotranspiration from one time day measurements. *Agric. Water Manag.*, 7:351–362, 1983.

P. G. Jarvis. The interpretation of the variations in leaf water potential and stomatal conductance found in canopies in the field. *Phil. Trans. R. Soc. London Ser. B*, 273:563–610, 1976.

P. G. Jarvis and K. G. McNaughton. Stomatal control of transpiration. Scaling up from leaf to region. *Adv. Ecol. Res.*, 15:1–49, 1986.

O. Johansen. *Thermal conductivity of soils*. PhD thesis, University of Trondheim, Trondheim, Norway, 1975.

S. A. Josey, R. W. Pascal, P. K. Taylor, and M. J. Yelland. A new formula for determining the atmospheric longwave flux at ocean surface at mid-high latitudes. *J. Geophys. Res. Oceans*, 108(C4):3108, 2003.

B. A. Kader and A. M. Yaglom. Mean fields and fluctuation moments in unstably stratified turbulent boundary layers. *J. Fluid Mech.*, 212: 637–662, 1990.

J. C. Kaimal and J. J. Finnigan. *Atmospheric boundary layer flows*. Oxford University Press, NY, USA, 1994.

J. D. Kalma, T. R. McVicar, and M. F. McCabe. Estimating land surface evaporation: a review of methods using remotely sensed surface temperature data. *Surv. Geophys*, 29(4-5):421–469, 2008.

R. E. Kalman. A new approach to linear filtering and prediction problems. *Trans. AMSE J. Basic Eng.*, 82(1):35–45, 1960.

M. Kanda, A. Inagaki, M. O. Letzel, S. Raasch, and T. Watanabe. LES study of the energy imbalance problem with eddy covariance fluxes. *Boundary-Layer Meteorol.*, 110:381–404, 2004.

D. S. Kimes, S. B. Idso, P. J. Pinter, R. J. Reginato, and R. D. Jackson. View angle effects in the radiometric measurement of plant canopy temperatures. *Remote Sens. Environ.*, 10:273–284, 1980.

J. Kondo and S. Ishida. Sensible heat flux from the earth's surface under natural convective conditions. *J. Atmos. Sci.*, 54:498–509, 1997.

R. Kormann and F. X. Meixner. An analytical footprint model for non-neutral stratification. *Boundary-Layer Meteorol.*, 99:207–224, 2001.

W. P. Kustas and C. S. T. Daughtry. Estimation of the soil heat flux/net radiation ratio from spectral data. *Agr. Forest Meteorol.*, 49(3):205–223, 1990.

W. P. Kustas and J. M. Norman. Evaluation of soil and vegetation heat flux predictions using a simple two-source model with radiometric temperatures for partial canopy cover. *Agr. Forest Meteorol.*, 94(1): 13–29, 1999.

W. P. Kustas, E. M. Perry, P. C. Doraiswamy, and M. S. Moran. Using satellite remote sensing to extrapolate evapotranspiration estimates in time and space over a semiarid Rangeland basin. *Remote Sens. Environ.*, 49:224–238, 1994.

W. P. Kustas, X. Zhan, and T. J. Schmugge. Combining optical and microwave remote sensing for mapping energy fluxes in a semiarid watershed. *Remote Sens. Environ.*, 64:116–131, 1998.

W. P. Kustas, J. M. Norman, M. C. Anderson, and A. N. French. Estimating subpixel surface temperatures and energy fluxes from the vegetation index-radiometric temperature relationship. *Remote Sens. Environ.*, 85 (4):429–440, 2003.

B. Lalic, D. T. Mihailovic, B. Rajkovic, I. D. Arsenic, and D. Radlovic. Wind profile within the forest canopy and in the transition layer above it. *Environm. Modelling and Software*, 18:943–950, 2003.

M. Y. Leclerc and G. W. Thurtell. Footprint prediction of scalar fluxes using a Markovian analysis. *Boundary-Layer Meteorol.*, 52(3):247–258, 1990.

C. C. D. Lelong, P. Burger, G. Jubelin, B. Roux, S. Labbè, and F. Baret. Assessment of unmanned aerial vehicles imagery for quantitative monitoring of wheat crop in small plots. *Sensors*, 8:3557—3585, 2008.

J. M. Lewis. The story behind the bowen ratio. *Bull. Am. Meteorol. Soc.*, 76:2433–2443, 1995.

Z. Li and H. Leighton. Narrowband to broadband conversion with spatially autocorrelated reflectance measurements. *J. Appl. Meteorol.*, 31:421–432, 1992.

Z. L. Li, R. Tang, Z. Wan, Y. Bi, C. Zhou, B. Tang, G. Yan, and X. Zhang. A review of current methodologies for regional evapotranspiration estimation from remotely sensed data. *Sensors*, 9:3801–3853, 2009.

S. Liang. *Quantitative remote sensing of land surfaces*. Wiley and Sons, Hoboken, NJ, USA, 2004.

H. P. Liu and G. Peters. New equation for sonic temperature variance and buoyancy heat flux with an omni-directional sonic anemometer. *Boundary-Layer Meteorol.*, 100:459–468, 2001.

J. S. Liu and R. Chen. Sequential Monte Carlo methods for dynamic systems. *J. Am. Stat. Ass.*, 90:567–576, 1995.

Y. H. Liu and R. Jordan. The interrelationship and characteristic distribution of direct, diffuse and total solar radiation. *Solar Energy*, 4(3):1–19, 1960.

C. R. Lloyd. The effect of heterogeneous terrain on micrometeorological flux measurements: a case study from HAPEX-SAHEL. *Agr. Forest Meteorol.*, 73:209–216, 1995.

LSASAF. *Down-welling Surface Short-wave radiation Flux: product user manual*. Version 1.4, 1994.

LSASAF. *Land Surface Albedo: product user manual*. Version 1.3, 2005.

LSASAF. *Vegetation parameters (FVC, LAI, FAPAR): product user manual*. Version 2.1, 2008.

LSASAF. *Land Surface Temperature: product user manual*. Version 2.4, 2009.

LSASAF. *Down-welling Longwave Flux (DSLF): product user manual*. Version 3.0, 2010.

S. Lu, T. Ren, Y. Gong, and R. Horton. An improved model for predicting soil thermal conductivity from water content at room temperature. *Soil Sci. Soc. Am J.*, 71:8–14, 2007.

S. Lu, Z. Ju, T. Ren, and R. Horton. A general approach to estimate soil water content from thermal inertia. *Agr. Forest Meteorol.*, 149: 1693–1698, 2009.

L. Mahrt. Flux sampling errors for aircraft and towers. *J. Atmos. Ocean. Technol.*, 15:416–429, 1998.

N. C. Majumdar, B. L. Mathur, and S. B. Kaushik. Prediction of direct solar radiation for low atmospheric turbidity. *Solar Energy*, 13:383–394, 1972.

N. Manalo-Smith, G. L. Smith, S. N. Tiwari, and W. F. Staylor. Analytic forms of bi-directional reflectance functions for application to Earth radiation budget studies. *J. Geophys. Res.*, 103(D16):733–751, 1998.

G. Manca. *Analisi dei flussi di carbonio di una cronosequenza di cerro (Quercus Cerris L.) dell'Italia centrale attraverso la tecnica della correlazione turbolenta*. PhD thesis, Università degli Studi della Tuscia, Viterbo, Italy, 2003.

S. A. Margulis and D. Entekhabi. Boundary-layer entrainment estimation through assimilation of radiosonde and micrometeorological data into a mixed-layer model. *Boundary-Layer Meteorol.*, 110:405–433, 2004.

E. P. Marques-Filho, L. D. A. Sà, H. A. Karam, R. C. S. Alvalà, A. Souza, and M. M. R. Pereira. Atmospheric surface layer characteristics of turbulence above the Pantanal wetland regarding the similarity theory. *Agr. Forest Meteorol.*, 148:883–892, 2008.

W. J. Massman. A comparative study of some mathematical models of the mean wind structure and aerodynamic drag of plant canopies. *Boundary-Layer Meteorol.*, 40:179–197, 1987.

W. J. Massman. A model study of kB^{-1} for vegetated surfaces using localized near-field Lagrangian theory. *J. Hydrol.*, 223:27–43, 1999.

E. Masuoka, A. Fleig, R. E. Wolfe, and F. Patt. Key characteristics of MODIS data products. *IEEE T. Geosci. Remote*, 36(4):1313–1323, 1998.

M. F. McCabe, E. F. Wood, R. Wòjcik, M. Pan, J. Sheffield, and H. Gao. Hydrological consistency using multi-sensor remote sensing data for water and energy cycle studies. *Remote Sens. Environ.*, 112(2):430–444, 2008.

M. C. McCumber and R. A. Pielke. Simulation of the effects of surface fluxes of heat and moisture in a mesoscale numerical model. *J. Geophys. Res.*, 86:9929–9938, 1981.

D. McLaughlin. Recent developments in hydrologic data assimilation. *Rew. Geophys.*, 740:977–984, 1995.

D. McLaughlin. An integrated approach to hydrologic data assimilation: interpolation, smoothing and filtering. *Adv. Water Resour.*, 25:1275–1286, 2002.

K. G. McNaughton and T. W. Spriggs. A mixed-layer model for regional evaporation. *Boundary-Layer Meteorol.*, 34:243–262, 1986.

W. M. L. Meijninger. *Surface fluxes over natural landscape using scintillometry.* PhD thesis, Wageningen Universitait, Wageningen, The Netherlands, 2003.

W. M. L. Meijninger, O. K. Hartogensis, W. Kohsiek, J. C. B. Hoedjes, R. M. Zuurbier, and H. A. R. de Bruin. Determination of area averaged sensible heat fluxes with a large aperture scintillometer over a heterogeneous surface – Flevoland field experiment. *Boundary-Layer Meteorol.*, 105 (1-2):37–62, 2002.

J. F. Meirink and M. C. Bergamaschi, P. Krol. Four–dimensional variational data assimilation for inverse modelling of atmospheric methane emissions: method and comparison with synthesis inversion. *Atmos. Chem. Phys.*, 8:6341–6353, 2008.

T. P. Meyers and S. E. Hollinger. An assessment of storage terms in the surface energy balance of corn and soybean. *Agr. Forest Meteorol.*, 125: 105–115, 2004.

E. M. Mikhail, J. S. Bethel, and J. C. McGlone. *Modern Photogrammetry.* Wiley and Sons, Hoboken, NJ, USA, 2001.

R. N. Miller, M. Ghil, and F. Gauthiez. Advanced data assimilation in strongly nonlinear dynamical systems. *J. Atmos. Sci.*, 51:1037–1056, 1994.

M. Minacapilli, C. Agnese, F. Blanda, C. Cammalleri, G. Ciraolo, G. D'Urso, M. Iovino, D. Pumo, G. Provenzano, and G. Rallo. Estimation of actual evapotranspiration of Mediterranean perennial crops by means of remote-sensing based surface energy balance models. *Hydrol. Earth Syst. Sci.*, 13:1061–1074, 2009.

J. Moncrieff. Surface turbulent fluxes. In P. Kabat, M. Claussen, P. A. Dirmeyer, and et al., editors, *Vegetation, water, humans and the climate. A new perspective on an interactive system*, pages 173–182. Springer, Berlin, Heidelberg, 2004.

J. Moncrieff, R. Clement, J. Finnigan, and T. Meyers. Averaging, detrending, and filtering of eddy covariance time series. In X. Lee, M. W., and B. Law, editors, *Handbook of Micrometeorology (Chapter 2)*, pages 7–31. Kluwer Ac. Publ., The Netherlands, 2004.

J. B. Moncrieff, J. M. Massheder, H. A. R. de Bruin, T. Elbers, J. Friborg, B. Heusinkveld, P. Kabat, S. Scott, H. Soegaard, and A. Verhoef. A system to measure surface fluxes of momentum, sensible heat, water vapour and carbon dioxide. *J. Hydrol.*, 188–189:589–611, 1997.

J. L. Monteith. Evaporation and environment. In G. E. Fogg, editor, *The State and Movement of Water in Living Organisms*, pages 205–234. Proceedings of the XIX Symposium of the Society of Experimental Biology, University Press, Cambridge 19, 1965.

J. L. Monteith. *Principles of environmental physics*. Edward Arnold Press, London, UK, 1973.

H. Moradkhani, S. Sorooshian, H. V. Gupta, and P. R. Houser. Dual state-parameter estimation of hydrological models using ensemble Kalman filter. *Adv. Water Resour.*, 28:135–147, 2005.

G. V. Mostovoy, V. Anantharaj, R. L. King, and M. G. Filippova. Interpretation of the relationship between skin temperature and vegetation fraction: Effect of subpixel soil temperature variability. *Int. J. Remote Sens.*, 29(10):2819–2831, 2008.

T. Murray and A. Verhoef. Moving towards a more mechanistic approach in the determination of soil heat flux from remote measurements. I: A

universal approach to calculate thermal inertia. *Agr. Forest Meteorol.*, 147:80–87, 2007a.

T. Murray and A. Verhoef. Moving towards a more mechanistic approach in the determination of soil heat flux from remote measurements. II: Diurnal shape of soil heat flux. *Agr. Forest Meteorol.*, 147:88–97, 2007b.

J. E. Nash and J. V. Sutcliffe. River flow forecasting through the conceptual models, Part 1: A discussion of principles. *J. Hydrol.*, 10(3):282–290, 1970.

C. M. U. Neale, W. Bausch, and D. Heermann. Development of reflectance-based crop coefficients for corn. *Trans. ASAE*, 32:1891–1899, 1989.

P. S. Nobel. *Physicochemical and environmental plant physiology.* Elsevier, Burlington, MA, USA, 2005.

J. Noilhan and S. Planton. A simple parameterization of land surface processes for meteorological models. *Mon. Weather Rev.*, 117:536–549, 1989.

J. M. Norman and G. S. Campbell. *Application of a plant environment model to problems in irrigation.* Advances in Irrigation Academic Press, NY, USA, 1983.

J. M. Norman, J. Chen, and N. Goel. Thermal emissivity and infrared temperature dependence on plant canopy architecture and view angle. In *IGARSS '90 Remote Sens. Int. Geosci. Remote Sens. Symp.*, pages 1747–1750, 1990.

J. M. Norman, W. P. Kustas, and K. S. Humes. Source approach for estimating soil and vegetation energy fluxes in observations of directional radiometric surface temperature. *Agr. Forest Meteorol.*, 77(3-4):263–293, 1995.

J. M. Norman, W. P. Kustas, J. H. Prueger, and G. R. Diak. Surface flux estimation using radiometric temperature: A dual temperature-difference method to minimize measurement errors. *Water Resour. Res.*, 36(8): 2263–2274, 2000.

J. M. Norman, M. C. Anderson, W. P. Kustas, A. N. French, J. R. Mecikalski, R. D. Torn, G. R. Diak, T. J. Schmugge, and B. C. W. Tanner. Remote sensing of surface energy fluxes at 10^1-m pixel resolutions. *Water Resour. Res.*, 39(8):278–294, 2003.

J. M. Norman, M. C. Anderson, and W. Kustas. Are single-source, remote-sensing surface-flux models too simple? In G. D'Urso, M. A. Osann Jochum, and J. Moreno, editors, *Earth observation for vegetation monitoring and water management*, pages 170–177. AIP Conference proceeding 852, 2006.

A. Olioso, O. Taconet, M. Ben Mehrez, D. Nivoit, F. Promayon, and L. Rahmoune. Estimation of evapotranspiration using SVAT models and surface IR temperature. In *Proceedings of IGARSS 1995*, pages 516–518, Florence, Italy, 10–14 July 1995.

A. Olioso, Y. Inoue, J. Demarty, J. P. Wigneron, I. Braud, and S. Ortega-Farias. Assimilation of remote sensing data into crop simulation models and SVAT models. In J. A. Sobrino, editor, *Proceedings of 1st International Symposium on Recent Advances in Quantitative Remote Sensing*, pages 329–338, Valencia, Spain, 16–18 September 2002.

J. Overgaard, D. Rosbjerg, and M. B. Butts. Land-surface modelling in hydrological perspective – a review. *Biogeosciences*, 3:229–241, 2006.

P. R. Owen and W. R. Thomson. Heat transfer across rough surfaces. *J. Fluid Mech.*, 15:321–324, 1963.

T. Paço, M. Ferreira, and N. Conceicao. Peach orchard evapotranspiration in a sandy soil: Comparison between eddy covariance measurements and estimates by the FAO 56 approach. *Agric. Water Manag.*, 85(3): 305–313, 2006.

E. F. Pan, M. Wood, R. Wòjcik, and M. F. McCabe. Estimation of regional terrestrial water cycle using multi-sensor remote sensing observations and data assimilation. *Remote Sens. Environ.*, 112(3):1282–1294, 2008.

G. N. Panin, G. Tetzlaff, and A. Raabe. Inhomogeneity of the land surface and problems in the parameterization of surface fluxes in natural conditions. *Theor. Appl. Climat.*, 60:163–178, 1998.

D. Papale. Il progetto Carboitaly: una rete nazionale per la misura di sink forestali e agricoli italiani e lo sviluppo di un sistema di previsione dell'assorbimento dei gas serra. *Forest@*, 3(2):165–167, 2006.

F. Pasquill. *Atmospheric diffusion*. 2nd Ed., J. Wiley and Sons, NY, USA, 1974.

C. A. Paulson. The mathematical representation of wind speed and temperature profiles in the unstable atmospheric surface layer. *Appl. Meteorol.*, 9(2):857–861, 1970.

H. L. Penman. Natural evaporation from open water, bare soil and grass. *Proc. Roy. Soc. A.*, 193:120–146, 1948.

H. L. Penman. Estimating evaporation. *Trans. Amer. Geoph. Union*, 37: 43–46, 1956.

R. Perez, P. Ineiche, R. Seals, J. Michalsky, and R. Steward. Modelling daylight availability and irradiance components from direct and global irradiance. *Solar Energy*, 44:271–289, 1990.

C. Petit, T. M., and P. Valentin. Study of turbulent diffusion above and within a forest- application in the case of SO_2. *Atmospheric Environment*, 10:1057–1063, 1976.

A. Prata. A new long-wave formula for estimating downward clear-sky radiation at the surface. *Q. J. Roy. Meteor. Soc.*, 122:1121–1151, 1996.

J. C. Price. On the information content of soil spectra. *Remote Sens. Environ.*, 33:113–121, 1990.

C. H. B. Priestley and R. J. Taylor. On the assessment of surface heat flux and evaporation using large-scale parameters. *Mon. Weather Rev.*, 100: 81–92, 1972.

J. H. Prueger, J. L. Hatfield, W. P. Kustas, L. E. Hipps, J. I. MacPherson, and T. B. Parkin. Tower and aircraft eddy covariance measurements of water vapour, energy and carbon dioxide fluxes during SMACEX. *J. Hydrometeorol.*, 6(6):954–960, 2005.

C. Qin, Y. Jia, S. Z., Z. Zhou, J. Qiu, and S. Suhui. Integrating remote sensing information into a distributed hydrological model for improving water budget predictions in large-scale basins through data assimilation. *Sensors*, 8:4441–4465, 2008.

M. R. Raupach. A practical Lagrangian method for relating scalar concentrations to source distributions in vegetation canopies. *Quart. J. Roy. Meteorol. Soc.*, 115:609–632, 1989.

M. R. Raupach and A. S. Thom. Turbulence in and above plant canopies. *Ann. Rev. Fluid Mech.*, 13:97–129, 1981.

R. Reichle, D. McLaughlin, and D. Entekhabi. Hydrologic data assimilation with the ensemble Kalman filter. *Monthly Weather Rev.*, 130(1):103–114, 2002.

L. J. Renzullo, D. J. Barrett, A. S. Marks, M. J. Hill, J. P. Guerschman, and Q. Mu. Multi-sensor model-data fusion for estimation of hydrologic and energy flux parameters. *Remote Sens. Environ.*, 112:1306–119, 2008.

K. J. A. Revfeim. A simple procedure for estimating global daily radiation on any surface. *J. Appl. Meteorol.*, 17:1126–1131, 1978.

K. Richter and W. J. Timmermans. Physically based retrieval of crop characteristics for improved water use estimates. *Hydrol. Earth Syst. Sci.*, 13:663–674, 2009.

N. Robinson. *Solar radiation*. Elsevier, Amsterdam/London/NY, USA, 1966.

G. J. Roerink, Z. Su, and M. Menenti. S-SEBI: a simple remote sensing algorithm to estimate the surface energy balance. *Phys. Chem. Earth*, 25(2):147–157, 2000.

J. Ross. Radiative transfer in plant communities. In J. L. Monteith, editor, *Vegetation and atmosphere*, pages 13–55. Academic press, London, UK, 1975.

J. Ross. The radiation regime and architecture of plants. In H. Lieth, editor, *Tasks for vegetation sciences 3*, pages 1–391. Dr. W. Junk, The Hague, Netherlands, 1981.

J. W. Rouse, R. H. Haas, J. A. Schell, and D. W. Deering. Monitoring vegetation systems in the Great Plains with ERTS. *Third ERTS Symposium-NASA*, SP-351 I:309–317, 1973.

H. Saito, J. Šimůnek, and B. P. Mohanty. Numerical analysis of coupled water, vapour, and heat transport in the vadose zone. *Vadose Zone J.*, 5:784–800, 2006.

J. A. Santanello and M. A. Friedl. Diurnal covariation in soil heat flux and net radiation. *Am. Meteorol. Soc.*, 42:851–862, 2003.

T. J. Sauer. *Sensible and latent heat exchange at the soil surface beneath a maize canopy.* PhD thesis, University of Wisconsin, Madison, WI, USA, 1993.

T. J. Sauer, J. M. Norman, C. B. Tanner, and T. B. Wilson. Measurement of heat and vapour transfer at the soil surface beneath a maize canopy using source plates. *Agr. Forest Meteorol.*, 75:161–189, 1995.

R. W. Saunders. The determination of broadband surface albedo from AVHRR visible and near-infrared radiances. *Int. J. of Remote Sens.*, 11: 49–67, 1990.

M. J. Savage. Estimation of evaporation using a dual-beam surface layer scintillometer and component energy balance measurements. *Agr. Forest Meteorol.*, 149:501–517, 2008.

K. Schelde, F. M. Kelliher, W. J. Massman, and K. H. Jensen. Estimating sensible and latent heat fluxes from a temperate broad-leaved forest using the simple biosphere (SiB) model. *Agr. Forest Meteorol.*, 84:285–295, 1997.

H. P. Schmid. Source areas for scalars and scalar fluxes. *Boundary-Layer Meteorol.*, 67:293–318, 1994.

T. J. Schmugge, W. P. Kustas, J. C. Ritchie, T. J. Jackson, and A. Rango. Remote sensing in hydrology. *Adv. Water Resour.*, 25:1367–1385, 2002.

P. Schotanus, F. T. M. Nieuwstadt, and H. A. R. de Bruin. Temperature measurement with a sonic anemometer and its application to heat and moisture flux. *Boundary-Layer Meteorol.*, 26(1):81–93, 1983.

P. H. Schuepp, M. Y. Leclerc, J. I. MacPherson, and R. L. Desjardins. Footprint prediction of scalar fluxes from analytical solutions of the diffusion equation. *Boundary-Layer Meteorol.*, 50:355–373, 1990.

P. Schwerdtfeger. *Physical principles of micro-meteorological measurements.* Elsevier, The Netherlands, 1976.

Scintec. *Scintec surface layer scintillometer SLS20/SLS40 SLS20-A/SLS40-A user manual (including OEBMS1).* Scintec Atmospha renmesstechnik AG, Tu bingen, Germany, 2006.

P. J. Sellers. Simple biosphere model (SiB) for use within general circulation models. *J. Atmos. Sci.*, 43:505–531, 1986.

P. J. Sellers, M. D. Heiser, and F. G. Hall. Relations between surface conductance and spectral vegetation indices at intermediate (100 m^2 to 15 km^2) length scales. *J. Geophys. Res.*, 97(D-17):19033–19059, 1992.

R. H. Shaw. Secondary wind speed maxima inside plant canopies. *J. Appl. Meteorol.*, 16:514–521, 1977.

W. J. Shuttleworth. Evapotranspiration measurement methods. *Southwest Hydrology*, 7:22–23, 2008.

W. J. Shuttleworth and J. S. Wallace. Evaporation from sparse crops - an energy combination theory. *Q.J.R. Meteorol. Soc.*, 111:839–855, 1985.

W. J. Shuttleworth, R. J. Gurney, A. Y. Hsu, and J. P. Ormsby. FIFE: the variation in energy partition at surface flux sites. *IAHS Publ.*, 186: 67–74, 1989.

P. Slater, S. Biggar, K. Thome, D. Gellman, and P. Spyak. Vicarious radiometric calibrations of EOS sensors. *J. Atmos. Ocean Tech.*, 13: 349–359, 1996.

J. A. Sobrino and N. Raissouni. Toward remote sensing methods for land cover dynamic monitoring: Application to Morocco. *Int. J. Remote Sens.*, 21(2):353–366, 2000.

J. A. Sobrino, V. Caselles, and F. Becker. Significance of remotely sensed thermal infrared measurements obtained over a citrus orchard. *ISPRS Photogrammetric Engineering and Remote Sensing*, 44:343–354, 1990.

J. A. Sobrino, J. C. Jimènez-Munõz, G. Sòria, M. Romaguera, L. Guanter, and J. Moreno. Land surface emissivity retrieval from different VNIR and TIR sensors. *IEEE Trans. on Geosc. and Remote Sensing*, 46(2): 316–327, 2007.

G. Somma. *Synergistic use of energy and water balance approaches for improved hydrological modelling over heterogeneous agricultural landsacpes in water scarce areas.* PhD thesis, Università degli Studi di Napoli ¨Federico II″, Naples, Italy, 2003.

D. I. Stannard, J. H. Blanford, W. P. Kustas, W. D. Nichols, S. A. Amer, T. J. Schmugge, and M. A. Weltz. Interpretation of surface flux measurements in heterogeneous terrain during the Monsoon90 experiment. *Wat. Resour. Res.*, 30(5):1227–1239, 1994.

J. B. Stewart, W. P. Kustas, K. S. Hmes, W. D. Nichols, M. S. Moran, and H. A. R. de Bruin. Sensible heat flux-radiometric surface temperature relationships for eight semi-arid areas. *J. Appl. Meteorol.*, 33:1110–1117, 1994.

R. B. Stull. *An introduction to boundary layer meteorology.* Kluwer academic publishers, Dordrecht, 1988.

Z. Su. The Surface Energy Balance System (SEBS) for estimation of turbolent heat fluxes. *Hydrol. Earth Syst. Sci.*, 6(1):85–99, 2002.

M. Tasumi. *Progress in operational estimation of regional evapotranspiration using satellite imagery.* PhD thesis, Dept. Biological and Agricultural Engineering, Univ. Idaho, 2003.

V. I. Tatarskii. *Wave propagation in a turbulent medium.* Translated from Russian by R.S. Silverman, McGraw-Hill, NY, USA, 1961.

H. Tennekes. A model for the dynamics of the inversion above a convective boundary layer. *J. Atmos. Sci.*, 30:558–567, 1973.

V. Thiermann. A displaced-beam scintillometer for line-averaged measurements of surface layer turbulence. *Proceedings of the tenth symposium on turbulence and diffusion*, pages 244–247, 1992.

V. Thiermann and H. Grassl. The measurement of turbulent surface-layer fluxes by use of bichromatic scintillation. *Boundary-Layer Meteorol.*, 58: 367–389, 1992.

N. Thompson, M. Barrie, and A. Ayeles. The meteorological office rainfall and evapotranspiration calculation system: MORECS. *Hydrol. Mem.*, 45, 1981.

Y. Q. Tian, R. Davies-Colley, P. Gong, and B. W. Thorrold. Estimating solar radiation on slopes of arbitrary aspect. *Agr. Forest Meteorol.*, 109: 67–74, 2001.

D. Troufleau, J. P. Lhomme, B. Monteny, and A. Vidal. Sensible heat flux and radiometric temperature over sparse Sahelian vegetation. I: an experimental analysis of the kB^{-1} parameter. *J. Hydrol.*, 188-189(1-4): 815–838, 1997.

L. R. Tsvang, M. M. Feorov, B. A. Kader, S. L. Zubkovskii, T. Foken, S. H. Richter, and Y. Zeleny. Turbulent exchange over a surface with chessboard-type inhomogeneities. *Boundary-Layer Meteorol.*, 55:141–160, 1991.

T. E. Twine, W. P. Kustas, J. M. Norman, D. R. Cook, P. R. Houser, T. P. Meyers, J. H. Prueger, P. J. Starks, and M. L. Wesely. Correcting eddy-covariance flux underestimates over a grassland. *Agr. Forest Meteorol.*, 103(3):279–300, 2000.

Z. Uchijima and J. L. Wright. An experimental study of air flow in a corn plant-air layer. *Bull. Natn. Inst. Agric. Sci. Tokio*, Ser. A 11:19–66, 1964.

UNEP/MAP-PlanBleu. *State of the Environmental Development in the Mediterranean.* UNEP/MAP-PlanBleu, Athens, Greece, 2009.

B. J. J. M. van der Hurk, W. G. M. Bastiaanssen, H. Pelgrum, and E. van Meijgaard. A new methodology for assimilation of initial soil moisture

fields in weather prediction models using METEOSAT and NOAA data. *J. Appl. Meteorol.*, 36:1271–1283, 1997.

P. van der Keur, S. Hansen, K. Schelde, and A. Thomsen. Modification of DAISY SVAT model for potential use of remotely sensed data. *Agr. Forest Meteorol.*, 106:215–231, 2001.

W. R. van Wijk and D. A. de Vries. Periodic temperature variations in a homogeneous soil. In W. R. van Wijk, editor, *Physics of Plant Environment*, pages 103–143. North-Holland, Amsterdam, 1963.

M. Vazifedoust, J. C. van Dam, W. G. M. Bastiaanssen, and R. A. Feddes. Assimilation of satellite data into agrohydrological models to improve crop yield forecasts. *Int. J. Remote Sens.*, 30(10):2523–2545, 2009.

D. Vickers and L. Mahrt. Quality control and flux sampling for tower and aircraft data. *J. Atmos. Oceanic Tech.*, 14:512–526, 1997.

R. Vogt, A. Christen, and A. Pitacco. Scintillometer measurements in a cork oak and an olive tree plantation. In *26th Conference on Agricultural and Forest Meteorology*, Vancouver, BC, Canada, 23–27 August 2004.

Z. Wan and J. Dozier. A generalised split-window algorithm for retrieving land-surface temperature from space. *IEEE Trans. Geosci. Remote Sens.*, 34(34):892–905, 1996.

E. K. Webb. Profile relationships: the log-linear range, and extension to strong stability. *Q. J. Roy Meteorol. Soc.*, 96:67–90, 1970.

E. K. Webb, G. I. Pearman, and R. Leuning. Correction of flux measurements for density effects due to heat and water vapour transfer. *Q. J. Roy Meteorol. Soc.*, 106:85–100, 1980.

M. L. Wesely. The combined effect of temperature and humidity fluctuations on refractive index. *J. Appl. Meteorol.*, 15:43–49, 1976.

M. West. Mixture models, Monte Carlo, Bayesian updating and dynamic models. *Comput. Sci. Statist.*, 24:325–333, 1993a.

M. West. Approximating posterior distributions by mixtures. *J. Roy. Stat. Soc.*, 55:409–422, 1993b.

P. J. Wetzel, D. Atlas, and R. Woodward. Determining soil moisture from geosynchronous satellite infrared data: A feasibility study. *J. Clim. Appl. Meteorol.*, 23:375–391, 1984.

C. J. Willmott. On the validation of models. *Phys. Geogr.*, 2:184–194, 1981.

K. B. Wilson, P. J. Hanson, P. J. Mulholland, D. D. Baldocchi, and S. D. Wullschleger. A comparison of methods for determining forest evapotranspiration and its components: sap-flow, soil water budget, eddy covariance and catchment water balance. *Agr. Forest Meteorol.*, 106: 153–168, 2001.

K. B. Wilson, A. Goldstein, E. Falge, M. Aubinet, D. Baldocchi, P. Berbigiere, C. Bernhofer, R. Ceulemans, H. Dolman, C. Field, A. Grelle, A. Ibrom, B. E. Law, A. Kowalski, T. Meyers, J. Moncrieff, R. Monson, W. Oechel, J. Tenhunen, R. Valentini, and S. Verma. Energy balance closure at FLUXNET sites. *Agr. Forest Meteorol.*, 113:223–243, 2002.

J. C. Wyngaard, Y. Izumi, and S. A. Collins. Behaviour of the refractive index structure parameter near the ground. *J. Opt. Soc. Am.*, 61: 1646–1650, 1971.

thanks to (in no particular order): i miei genitori e la mia famiglia tutta (vicini anche da lontano), gc, mario minacap, i proff. agnese e la loggia, guido, nino & fulvio, gli elabbi, martha, bill, henk, giovanni ed i colleghi dell'itaf, tutti i soppalcati, i miei compagni di sventura: elisa (sempre presente, a differenze dei toast al bar), lizzie (e la maternità isterica), alida (stavolta senza pe-pem), vincenzo (ma soprattutto la sua canaletta), il corato (con cui dobbiamo ancora linearizzare), il nostro decano smemorato claudio, massimo ed i viaggi in pick-up, i colleghi dell'enea, l'azienda crescimanno, sergio di castelvetrano, i colleghi del dca e dell'ibimet di bologna, alessandra gagliano, la pausa crostino del mercoledì (e tutti i falsi mercoledì), l'upupa, la fila alla mensa, cetto la qualunque, il sig. franco di fronte accardi, il topolino di johnny, la pista da bowling, la pausa tè, i miei amici a canicattì (anche se non scendo mai), disgrazia, valeeè ed elulù, grace & ladyelena, lauretta, i miei coinquilini storici nino e luvici, lo zio alfredo the situation special guest star from p3 street, emi e la famiglia duck hards, marioman (anche la sede, il divano e la connessione internet), lo zio maurizio (e casa sua), quantos, giovanna super tur operetor, vitruvio, i puccios, linkdi, il verchio, l'ambasciatore e first lady, filippo e i suoi amici mitologici di baaria, i tatucci (necessari come l'antimateria), vv, le serate indie rock al lulù, i rum e pera a 1 €, il white russian, il cinemeloforum, il piano emiliano, u pani chi panelli, la forst, i water hummer, il digaspam, le emergenze, skincats, le teorie del sonno, all the guys at the usda, portbelly, chinabus, 9:30 club, black cat, pitchfork.com, breakfastjumpers, i simpsons (una frase per ogni circostanza), sheldon cooper, billy corgan, tutti i gruppi che ho ascoltato in questi anni (che sarebbero troppi da elencare), tutti coloro i quali hanno fatto parte della mia vita in questi tre anni (anche solo di passaggio) e tutti quelli che ho colpevolmente dimenticato. love, peace, empathy. 2011.

Università degli Studi di Palermo
Dipartimento di Ingegneria Civile, Ambientale e Aerospaziale (DICA)
Dipartimento dei Sistemi Agro-Ambientali (SAGA)
February, 2011